^{30}S BEAM DEVELOPMENT AND THE ^{30}S WAITING POINT IN TYPE I X-RAY BURSTS

McMaster University
The Graduate School

^{30}S BEAM DEVELOPMENT AND THE ^{30}S WAITING POINT IN TYPE I X-RAY BURSTS

A Thesis in
Physics & Astronomy
by

David Miles Kahl
B.Sc, Beloit College

Submitted to the School of Graduate Studies
in Partial Fulfillment of the Requirements
for the Degree

Master of Science

September 2008

MASTER OF SCIENCE (2008) McMaster University

(Physics & Astronomy) Hamilton, Ontario

TITLE: ^{30}S Beam Development and the ^{30}S Waiting Point in Type I X-Ray Bursts

AUTHOR: David Kahl, B.Sc. (Beloit College)

SUPERVISOR: Professor Alan A. Chen

NUMBER OF PAGES: xvi, 196

Abstract

Nuclear physics tells us a lot about astrophysics, particularly the energy generation in stars. The present work is a thesis in experimental nuclear physics, reporting the results of ^{30}S radioactive beam development for a future experiment directly measuring data to extrapolate the ^{30}S(α,p) stellar reaction rate in Type I X-ray bursts, a phenomena where nuclear explosions occur repeatedly on the surface of accreting neutron stars. On the astrophysics side, the work details basic stellar physics and stellar reaction formalism in Chapter 1, the behaviour of compact stars in Chapter 2, and a full literature review of Type I X-ray bursts in Chapter 3.

Nuclear experiments are non-trivial, and the results reported here were not accomplished by the author alone. Stable-beam experiments are technically challenging and involved, but for the case at hand, the halflife of ^{30}S is a mere 1.178 seconds, and in order to measure reaction cross-sections, we must make a beam of the radionuclide ^{30}S *in situ* and use these rare nuclei immediately in our measurement. Particle accelerator technology and radioactive ion production are treated in Chapter 4, and the experimental facility and nuclear measurement techniques are discussed in some detail in Chapter 5.

In order to perform a successful future experiment which allows us to calculate the stellar ^{30}S(α, p) reaction rate, calculations indicate we require a ^{30}S beam of $\sim 10^5$ particles per second at $\sim$ 32 MeV. Based on our recent beam development experiments in 2006 and 2008, it is believed that such a beam may be fabricated in 2009 according to the results presented in Chapters 6 and 7. We plan to measure the ^{4}He(^{30}S,p) cross-section at astrophysical energies in 2009, and some remarks on the planned (α,p) technique are also elucidated in Chapters 5, 6 and 7.

All hail goatface.

Acknowledgments

The enclosed work is academic, and shows little traces of the effort put forward by many people helping me in conducting this research and learning the necessary physics. The author worked primarily at the Physics & Astronomy Department of McMaster University in Hamilton, Ontario, Canada, although all the experimental work took place at RIKEN in collaboration with the Center for Nuclear Study of the University of Tokyo in Wakō, Saitama, Japan. Because the work was performed in both North America and Asia, where family and given names are customarily listed in a contrasting order, this thesis names all individuals as found in their homelands, where family names are indicated with SMALL CAPITAL LETTERS whenever both family name and given name are presented.

My thesis supervisor, Dr. Alan CHEN, deserves much credit for master-minding my thesis project and also my appreciation for taking me under his wing. Indeed, the original proposal for my thesis experiments was submitted before I applied for graduate studies in Physics & Astronomy at McMaster University. I pursued an educational path at Beloit College uncharacteristic of many graduate students of physics, and I am particularly grateful for Dr. Chen's willingness to bring me to work with him and assist me with the many challenges I faced completing the required course-work. Without such an opportunity, I doubt I could have remained in physics.

My interest in physics came quite late in my undergraduate career, and I must express much gratitude to Dr. J. Patrick POLLEY for assisting me to undertake a major in Physics & Astronomy in merely three semesters. I was immediately

fascinated with both nuclear physics and astronomy, likely due to my access to a small accelerator and other nuclear experiment tools and an optical observatory, which I was able to get my hands dirty playing with due to being at a small liberal arts school. I became interested in experimental nuclear astrophysics the first time I met Dr. K. Ernst REHM at a workshop on the Rare Isotope Acçelerator, held at Monmouth College, which Pat POLLEY drove a few of us down to attend. In the beginning of Dr. Rehm's talk, he described his work in experimental nuclear astrophysics, and from this time on, I have not had any doubts about the academic path I wish to pursue. He later supervised me as a summer student at Argonne National Laboratory in 2005, where I was able to gain valuable experience calibrating an ionization chamber for a measurement of the β-delayed α decay of ^{16}N, with ramifications for the *holy grail* of nuclear astrophysics, the ^{12}C(α,γ) stellar reaction rate. In a rare case for a summer student, I was also able to participate in the experiment itself, conducted later in October 2005.

The amount of work required in undertaking radioactive ion beam experiments is rather immense, and the beam facilities themselves require years of planning and construction. As an outside user of the Nishina Center of RIKEN, one must be pleased the facility is already constructed and fully functional upon arrival in a foregin land. The local professors, researchers, and students take care of everything when you're not there, so one actually has to make an active effort to contribute to the planning, setup, and running of a given experiment. Professor KUBONO Shigeru officially serves as our liaison at the Center for Nuclear Study of the University of Tokyo, but in reality he oversees the entire experiment preparation, ensures the online data results are properly interpreted, convinces the beam operators to give us extra beam time, and, among other feats, assists in the physical interpretation of experimental results. Professor YAMAGUCHI Hidetoshi has such a mastery of the operation of the CRIB experimental hall and data collection room that sometimes he gets a mobile call during his dinner break to solve problems which arose in the half hour of his absence. The research associates Dr. Wakabayashi and Dr. Hashimoto show clear leadership skills in experimental preparation and shift operation, as well as calibrating and installing many of the beam line detectors. The graduate students of the CNS astrophysics group, Hayakawa-san, Kurihara-san, and Binh perform much of the particular experimental setups such as wiring and checking a massive amount of electronics, as well as the calibration of many of the detectors used. Although I have not personally interacted with many of the beam operators, members of the cyclotron group, and the individuals who work with the ion sources, this work would not be possible without stable ^{28}Si beams, which these people provided around-the-clock during the experimental work reported here, which I am very thankful for. Although I've flow to Japan to perform my thesis research, I do not speak any Japanese, and I am very ashamed, and yet very happy, that my Japanese colleagues can speak to a dumb American in my own native language, even though we work in their homeland. Many others have also been involved with the experimental work reported here, particularly the graduate students LEE Nam Hee and KIM Aram of Dr. HAHN's research group of Ewha Womans University of Seoul, Korea.

The other graduate students in my own research group at McMaster, CHEN Jun and Kiana SETOODEH NIA, fly across the Pacific Ocean to stay awake late hours on experimental shifts. Of equal importance is how much my colleagues have helped me with physics generally, as Jun tells me everything I need to know about the operation of my analysis code and the data, and I'd never have passed all my required courses without constantly pestering Kiana for assistance. Our post-doctoral research associate, Dr. Christian OUELLET has served both of these positions aptly, helping me with the ROOT data analysis package and many physics topics. I thank all my officemates for putting up with me on a daily basis, despite my disruptive behaviour and outspoken personality. Although I am sad to leave McMaster as I move to Tokyo in the coming weeks, I hope that at least the productivity may increase around our office without all my antics.

I've had the opportunity to participate in many other nuclear experiments, summer schools, and conferences, where I met many other physicists and had productive dialogue — I've tried to cite as many individuals as I can for particularly helpful ideas and suggestions throughout the text. Dr. Jacob Lund FISKER, in particular, has been a great resource on this thesis work, and he has taken his own time to edit my writing and answer my many questions. Although we cannot choose our colleagues and co-workers, one reason I hope to never stray far from the field of nuclear astrophysics is because of the great community of people, and the people who've helped me with this work seem to be friends more than merely people I work with. However, in regard to my friends who I do not work with, you are all friends by nothing other than choice, and I hope you will not be offended at the omission of any names, as the list would quickly grow out of control.

My parents Mary Lou and Joe are very supportive, and are likely the only people who the work would be physically impossible without.

I am grateful for the members of my thesis supervisory committee, Dr. Bill HARRIS and Dr. Jim WADDINGTON, whose wisdom greatly assisted in the quality of the work.

Table of Contents

List of Figures

List of Tables

List of Symbols

acronym or abbreviation — What the Letters Represent(: association)

ADC — analog to digital converter: signal processing
ANAPAW — Online Analysis combined with the Physics Analysis Workstation: Computer software package
ATLAS — Argonne Tandem Linear Accelerator System: Argonne National Laboratory
AVF — azimuthally varying field: cyclotron
B^{2}FH — The authors of a famous 1957 paper on stellar nucleosynthesis; Margaret BURBIDGE, Geoffrey BURBIDGE, William FOWLER and Fred HOYLE: Bibliographic item [B^{2}FH]
CFD — constant fraction discriminator: signal processing
CINT — C++ Interpreter: Computer software routine
CMB — cosmic microwave background: Big Bang
CNS — Center for Nuclear Study: University of Tokyo
CRIB — CNS Radioactive Ion Beam: separator facility
DAQ — data acquisition: computer routine
EC — electron capture: nuclear decay
ECR — electron cyclotron resonance: ion source
enA — electrical nano Amperes: beam current
ESTU — Extended Stretched TransUranium: tandem accelerator at Yale University
FWHM — full width half maximum: Gaussian distributions
GMSTPC — gated multiple-sampling and tracking proportional chamber
HMXB — high mass X-ray binary
HRIBF — Holifield Radioactive Ion Beam Facility: Oak Ridge National Laboratory INS — Institute for Nuclear Study: University of Tokyo
IS — ion source
ISM – interstellar medium

ISOL — isotope separation online
KEK — The High Energy Accelerator organization: Japanese national laboratory
linac — linear accelerators
LIS — Laser ion sources
LMXB — low mass X-ray binary
MRI — magneto-rotational-instability: accretion disks
P-10 — percent 10 methane, 90% argon: detector fill gas
PAC — Project Approval Committee: nuclear laboratories
PAW — Physics Analysis Workstation: Computer software package
PI — primary investigator
PID — particle identification
pnA — particle nano Amperes: beam current
PPAC — Parallel plate avalanche counter
pps — particles per second: beam particle frequency
PSD — Position sensitive detector
PSSD — Position sensitive silicon detector
pulsars — pulsating stars: neutron stars
r process — rapid neutron capture process: nucleosynthesis
rp process — rapid proton capture process: nucleosynthesis
RARF — RIKEN Accelerator Research Facility
rdf — raw data file: computer file extension
RF — radiofrequency: various
RI — radioactive ion
RIB — radioactive ion beam
RIKEN — The Institute for Physical and Chemical Research: Japanese national laboratory
SRAFAP — student running as fast as possible
SSD — Silicon strip detector
TDC — time to digital converter: signal processing
ToF — time of flight
WF — Wien filter: velocity separation
WNSL — Wright Nuclear Structure Laboratory: Yale University
XRB — X-ray burster: accreting neutron star

Chapter 1

Introduction

1.1 History of Thought on Atomic Matter

The nature, building blocks, and origin of matter has been of much interest throughout human history. In ancient Greece, it was held that all matter is composed of earth, air, fire, and water; whereas in China, the elements were held to be earth, air, fire, water, and gold — the Chinese at least got one element correct. To the credit of the Greeks, the philosopher Democritus reasoned that if one were to iterate cutting a piece of matter in half, eventually the matter could not be divided further. Being indivisible, Democritus coined this state *atoma*, or uncuttable. Fourteen years after Democritus's death, a highly influential philosopher was born — Aristotle. Long after his death, Aristotle is still one of the most respected Western philosophers, even though a number of his ideas have been disproven. Aristotelian dogma dominated Western thought for more than 17 centuries, and a vast majority in the Western world was content to take many of his bolder claims at face value with no need for proof. As science emerged, many of Aristotle's ideas — such as the geocentric universe, the immutability of the cosmos, and the notion that more massive objects fall faster than less massive objects — did not withstand the tests of observation and experimentation. Aristotle argued that all matter was composed of the four elements (except for stars, which were immutable and thus made of æther) as well as four forms — hot, cold, wet, and dry — along with an immaterial form.

While Galileo GALILEI (1564–1642) is often cited as the first scientist, or *experimental philosopher* by his own reckoning, Daniel SENNERT (1572–1637, an alchemist, who also deserve credit for using experimental technique to gain insight into the universe [NEW06]. Alchemists believed sulfur and mercury are elements, and they strove to turn lead into gold and prolong life. Sennert's experiment 'reduction to a pristine state' indicated that silver is an element, or at the very least that Aristotelian immaterial forms are not destroyed by chemical reactions. This simple experiment was later made famous by Robert BOYLE: Fully dissolve silver in nitric acid, then add potassium carbonate, and finally heat the resulting precipitate to 1 x 10^3 C, and the result is a crucible of silver [NEW06].

In the 19th century, John DALTON recorded many properties of matter, and came up with an atomic theory for molecules, and soon after Dmitri MENDELEEV compiled what is regarded as the first periodic table of elements due to its predictive powers. By the end of the 19th century, J. J. THOMSON showed that DALTON's 'atoms' were not fundamental building blocks by discovering cathode-rays, or electrons. 15 years later, Ernest RUTHERFORD discovered the atomic nucleus [RUT11], and then it did not take Henry MOSELEY long to deduce that different elements have a unique nuclear charge [MOS13]. Contemporary nuclear theory emerged shortly after James CHADWICK discovered the neutron in 1932 [CHA32].

While nuclear science is a subsection of physics, the alchemists might claim this discipline as their own, because around half of the diagnostic and therapeutic techniques used in hospitals to prolong life are nuclear technologies, and using basic nuclear theory, one may show how to turn lead into gold.

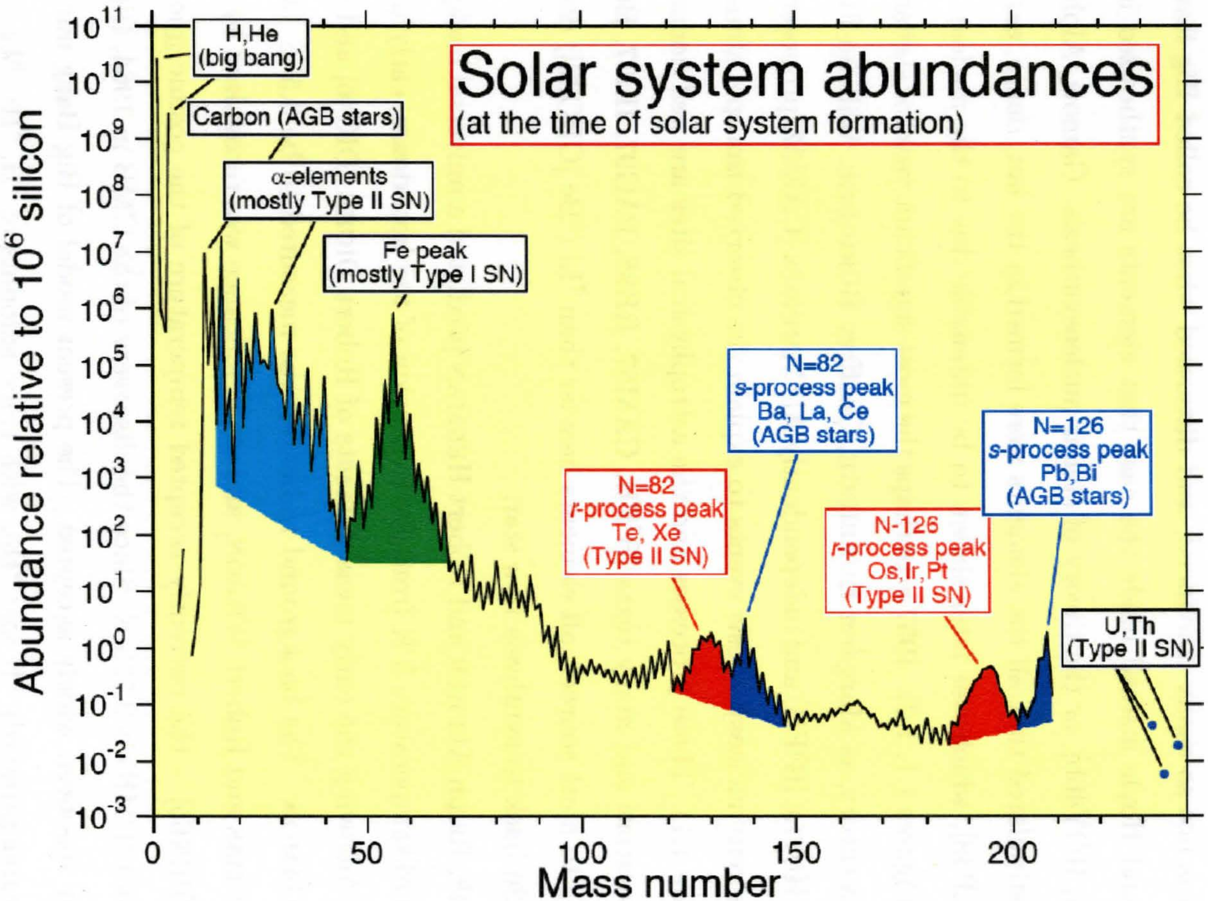

Figure 1.1: The plot shows the nucleon number (A) of stable (unstable isotopes are indicated with points) nuclear isotopes along the abscissa against the logarithmic solar system abundance with the ordinate normalized to make silicon 10^6 [DIE08]. Some elements are much more abundant than others (some 12 orders of magnitude separates hydrogen from uranium). Nuclear formation processes are indicated, with candidate astrophysical locations also listed.

Newtonian steady state cosmology was not absolutely disproven until Edwin Hubble demonstrated in 1929 that the universe is expanding [HUB29]. The notion of an expanding universe led physicists such as George Gamow to argue that all matter in the universe must have a common origin in space and time. Fred Hoyle was not so easily convinced, and dismissed what he called Big Bang cosmology, and Hoyle instead made the case that elements are synthesized in stars [HOY46a, HOY46b], or the theory of stellar nucleosynthesis. Gamow, Alpher and Herman stipulated that all the elements were formed in the hot, dense, early universe [ALP48], which was later shown to be untenable due to the nuclear mass 8 gap (see Figures 1.1, 1.2). 1957 is perhaps the most significant year for stellar nucleosynthesis theory, as Margaret Burbidge, Geoffrey Burbidge, William Fowler and Fred Hoyle [B^{2}FH] and independently Al Cameron [CAM57] proposed a theory of discrete nucleosynthesis events to explain the observed isotopic abundances (see Figure 1.1). These processes and the astrophysical sites are well documented in the literature and many texts [B^{2}FH, CAM57, RR88, PAG97, ILI07, BOY08]. According to most sources, all elements heavier than ^{7}Li (^{9}Be [GRO02]) can trace their origin back to synthesis in a star.

In 1948, Ralph Alpher and Robert Herman predicted a universal background radiation of temperature 5 K from the expansion of the hot, dense, early universe [ALP49], following the early measurements of Robert Dicke [DIC46] and predictions of Gamow. The background radiation was measured to be 3.5 $\pm$ 1.0 K by Arno Penzias and Robert Wilson, and its significance was recognized by Bernie Burke [PEN65] – the currently accepted temperature of the cosmic microwave background (CMB) is 2.725 K. Since the discovery of the CMB in 1964, Big Bang cosmology has been widely accepted. The present model of Big Bang nucleosynthesis creates primarily ^{1}H and ^{4}He, with trace amounts of ^{2}H, ^{3}He, ^{6}Li and ^{7}Li. While Hoyle's cosmological model is no longer taken seriously by most members of the scientific community, his theory of stellar nucleosynthesis is corroborated by astronomical observations, astrophysics theory and nuclear experimental work.

The theory of stellar nucleosynthesis predicted the detection of the radioactive element technetium in stellar spectra (the lightest element with no stable isotopes), the detection of solar neutrinos, the detection of neutrinos from supernova 1987a, and the detection of galactic gamma emitters such as ^{26}Al and ^{44}Ti.

The field of nuclear astrophysics focuses on the origin and synthesis of all the isotopes of the chemical elements and the energy generation of stars. The present work focuses primarily on the thermonuclear energy generation mechanism in X-ray bursts, which is not believed to contribute significantly to the galactic chemical evolution (because the synthesized elements are not ejected into the interstellar medium (ISM)), but are "the most common thermonuclear explosions in the universe" [FIS08a]! Because most elements relevant to life on Earth are synthesized in stars, and half the elements heavier than iron are made in explosive environments, if one wishes to understand the processes and mechanisms of stellar nucleosynthesis, one ought to study those explosive events which occur with the most frequency and provide the best observational statistics of thermonuclear energy release — X-ray bursts.

1.2 Nuclear Astrophysics

1.2.1 Stellar Equation of State

Stars are understood to be in a state of hydrostatic equilibrium, where the kinetic gas pressure P as a function of radius r is set equal and opposite to the gravitational potential G of the mass confined within that radius M_r and local gas density ρ as[1]

$$\frac{dP}{dr} = -G\frac{M_r \rho}{r^2} \; . \tag{1.1}$$

[1]The proper relativistic form of the equation for hydrostatic equilibrium, applicable to white dwarfs and neutron stars, is given by the Oppenheimer-Volkoff equation.

In the kinetic theory of gas[2], the pressure results from the collision of energetic particles with root-mean-square velocity v_{rms} given by

$$P = \frac{1}{3}\rho v_{rms}^2 \ . \tag{1.2}$$

In a quiescent star the equation of state can be approximated by the ideal gas law

$$PV = nRT \ , \tag{1.3}$$

where P is pressure, V is volume, n is the number of moles of gas, R is the universal gas constant and T is the absolute temperature. When energy is added to a confined ideal gas, the energy causes individual gas particles to have a higher average velocity, and through the Maxwell-Boltzmann statistics, one may understand the temperature of a non-degenerate gas by considering the velocity distribution of thermal molecules. The probability $\phi(v)$ for a particle to have a particular velocity v is given by the Maxwell-Boltzmann velocity distribution

$$\phi(v) = 4\pi v^2 \left(\frac{m}{2\pi kT}\right)^{3/2} \exp\left(-\frac{mv^2}{2kT}\right) \tag{1.4}$$

where m is the mass of the particle of interest, k is Boltzmann's constant, and T is the gas temperature. It is assumed the function has been normalized to unity ($\int_0^\infty \phi(v)dv = 1$). In the non-relativistic limit, $E = \frac{1}{2}mv^2$, and so the velocity distribution can be written in terms of the energy [RR88]

$$\phi(E) \propto E \ \exp\left(-\frac{E}{kT}\right) \ . \tag{1.5}$$

Thermonuclear reactions within the star convert mass to energy at a constant rate (see Sections 1.2.2, 1.3 and Appendix A). The infusion of nuclear energy into the stellar matter prevents further gravitational contraction to densities where

[2]Matter at the core of a star is in a plasma state, but the kinetic gas model (of non-ionized gas) provides a simple and fairly accurate description of the physics.

the kinetic theory of gas is no longer applicable. The thermonuclear reactions at the core of a star convert nuclear mass into thermal energy and radiation. The emitted radiation comes into equilibrium with the stellar matter, leading to the observed stellar surface luminosity. A star may be modeled as a blackbody, an ideal emitter of electromagnetic radiation that absorbs all incident radiation. Individual particles in a blackbody obey the Maxwell-Boltzmann statistics as in our above stellar model, and the radiation is emitted preferentially at a peak energy. The energy E of a wave of light is related to its wavelength λ by Planck's constant h and the speed of light c

$$E = \frac{hc}{\lambda} . \tag{1.6}$$

Spectroscopic technology of the early 20th century enabled astronomers to make precise measurements of the intensity of light at different wavelengths, and hence stellar temperature by Wien's displacement law:

$$\lambda_{max} T = 0.002897755\, m\, K , \tag{1.7}$$

where λ_{max} is the blackbody peak wavelength, and T is surface temperature. One may then calculate the stellar radius using the Stefan-Boltzmann law:

$$L = 4\pi R^2 \sigma T_e^4 , \tag{1.8}$$

where L is stellar luminosity, R is radius, σ is the Stefan-Boltzmann constant, and T_e is the effective temperature (since stars are not perfect blackbodies). Using the Stefan-Boltzmann law, one may compute the pressure exerted by radiation P_{rad}:

$$P_{rad} = \frac{4\sigma T^4}{3c} , \tag{1.9}$$

a result previously omitted in the conditions for stellar hydrostatic equilibrium. Radiation pressure does not significantly contribute to the stellar equation of state until the luminosity becomes very large, as will become important later in the discussion of accreting compact stars.

1.2.2 Quiescent Nuclear Burning

The source of stellar energy has interested scholars in the physics community for many years. If the Sun were powered by a chemical reaction, such as the oxidation of coal, based on its mass, radius, and luminosity, the Sun's lifetime would be under 4,000 years, inconsistent with historical records of human civilization. In the nineteenth century, it was argued by many, such as Mayer, Waterson, von Helmholtz and Kelvin, that the Sun radiated energy by merit of converting gravitational potential energy into heat. According to the virial theorem, the thermal energy E_T is half the time-averaged gravitational potential energy $\bar{U}_G$ [RR88, CAR06]

$$E_T = -\frac{1}{2}\bar{U}_G \ . \tag{1.10}$$

The thermal energy may be radiated away at the surface over a timescale $\tau = \frac{E_T}{L}$ [RR88]. Given the luminosity, mass, and radius of the Sun, such a source of energy yields a solar lifetime of merely 19 million years, which sparked a series of debates with biologists, geologists, and physicists who did not accept such a young age for the solar system. Discoveries near the turn of the century by Becquerel, Curie, and Rutherford immediately led many to postulate radioactivity as a possible source of stellar energy, but the materials and mechanism were unknown, as the Sun did not appear to contain large amounts of radioactive elements.

In 1920, Francis ASTON experimentally demonstrated that the mass of a helium atom is less than four times the mass of a hydrogen atom, which, later that same year, led Sir Arthur EDDINGTON to postulate that in the core of the Sun, hydrogen is transmuted into helium, and the mass excess is released as energy [EDD19, EDD20]; converting hydrogen to helium releases ~6.7 MeV per nucleon (see Figure 1.2). However, the mechanism for stellar nuclear burning proved theoretically challenging, because interactions between the charged nuclei involved should be

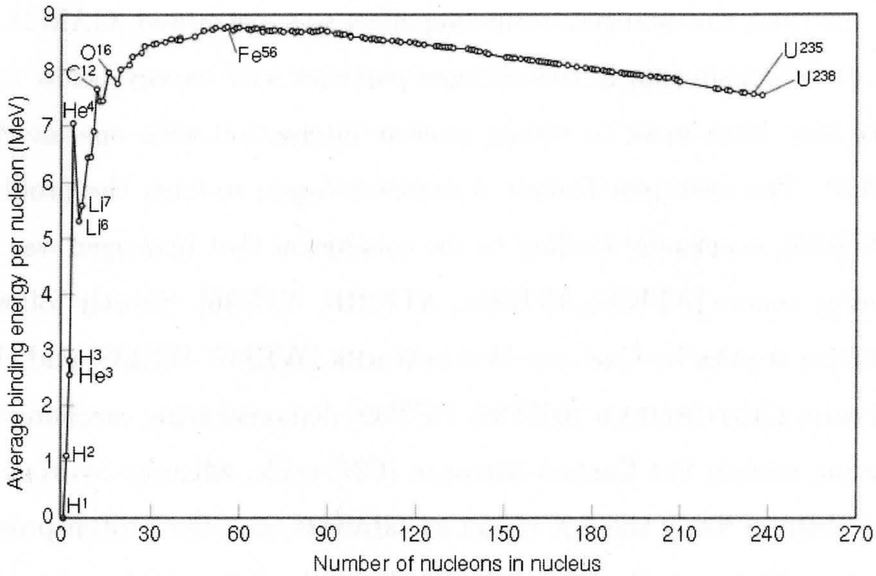

Figure 1.2: The plot shows the number of nucleons (A) in selected stable or long-lived nuclei along the abscissa against the average binding energy per nucleon in million electron volts on the ordinate [WIK08b]. One can infer the mass gaps at $A = 5, 8$; hydrogen fusion into helium liberates ~7 MeV per nucleon; ^{56}Fe is the most tightly bound nucleus — exothermic fusion cannot proceed past the iron peak. It is also evident the α-nuclei ^{12}C and ^{16}O are tightly bound. (α-nuclei are those with $N = Z$ and A evenly divisible by 4.)

inhibited by the electrostatic potential U_{Coul}, the Coulomb barrier

$$U_{Coul} = \frac{1}{4\pi\epsilon_0}\frac{Z_1 Z_2 e^2}{r}, \tag{1.11}$$

where ϵ_0 is the permittivity of free space, e is the elementary unit of charge, Z_1 and Z_2 are the electric charge of the two nuclei involved, and r is the distance between the interacting nucleons. A quick calculation shows that for two protons to touch at the surface, the Coulomb potential is ~900 keV. The Maxwell-Boltzmann energy distribution (Equation 1.5) has a peak at $E = kT$, which for the sun ($T = 1.5\ x\ 10^7$ K) is 1.3 keV. From this simple calculation, one can see the Coulomb barrier is nearly two orders of magnitude higher than the most probable thermal energy of protons in the solar interior.

In 1928, the quantum tunneling effect was discovered [GAM28, GUR29], which is a mechanism that allows charged particles with energy below the Coulomb barrier may have weak or strong nuclear interaction with one another (see Section 1.3.3). The next year Robert ATKINSON began to treat the problem qualitatively [ATK29], eventually leading to the conclusion that hydrogen was the main stellar energy source [ATK29, ATK31a, ATK31b, ATK36]. Shortly following were quantitative studies by Carl von WEIZSÄCKER [WEI37, WEI38] and Hans BETHE and Charles CRITCHFIELD [BET38, BET39] demonstrating mechanisms for hydrogen fusion, namely the Carbon-Nitrogen (CN) cycle, whereby hydrogen could be fused into helium using the CN nuclei as catalysts, and the proton-proton (*pp*) burning chains. These studies also calculated the dependence of nuclear fusion on stellar luminosity, mass, and temperature [BET39]. The *pp* chains operate at the lowest stellar temperatures from 10^6 - 10^7 K. The Bethe-Weizsäcker cycle, or cold-CN cycle, operates above 2 x 10^7 K, and the timescale is set by the slowest proton capture in the sequence, ^{14}N+p $\rightarrow$ ^{15}O+γ. At temperatures above 10^8 K, the CNO cycle reaction path and timescale are set by nuclei of relatively long β^+ (positron) decay lifetimes [HOY65, FRI73], called *waiting point nuclei.* For specific details of hydrogen burning, see Appendix A.

1.3 Stellar Reaction Rates

1.3.1 Nuclear Reaction Nomenclature

When discussing specific reactions, the notation $A(a,b)B$ is used (see Figure 1.3), where the two inputs are the target nucleus A and *projectile*, or beam nucleus, a, and the outputs are the *ejectile* b and the recoiling nucleus B. For astrophysics, the beam/target ejectile/recoil notation is irrelevant, and from nuclear experiments, it is customary to list the light input nucleus as the beam a, due to the advent of light ion accelerators prior to heavy ion accelerators, and call the ejecta b, because

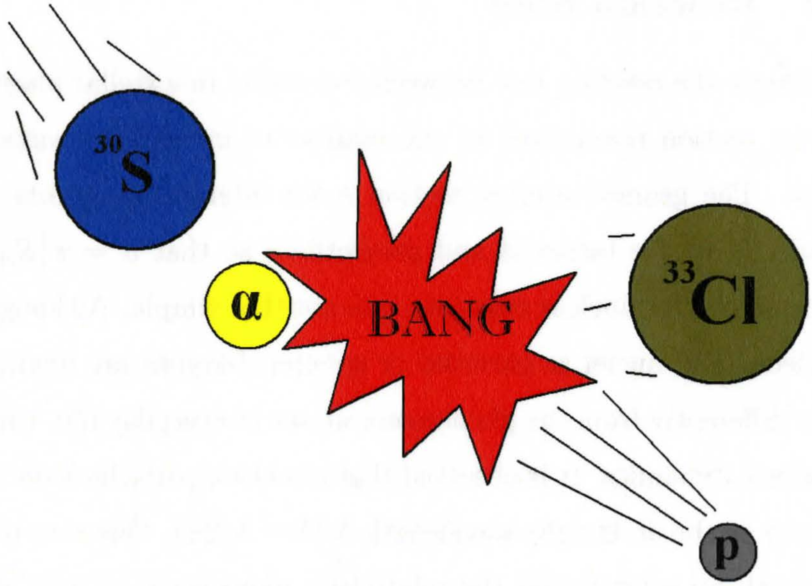

Figure 1.3: A cartoon of the ^{4}He(^{30}S,p)^{33}Cl reaction, where ^{30}S is the beam in the laboratory, the ^{4}He nucleus, or α particle, is the target, the proton is measured in the laboratory, and the recoiling ^{33}Cl is typically not detected. For astrophysics, this is usually written as ^{30}S(α,p)^{33}Cl, because both the input nuclei have kinetic energy, and one can easily recognize the light input and output nuclei (α,p) as part of the αp process.

due to momentum conservation, the ejectile is easier to detect in nuclear experiments. [Some more sophisticated experiments will detect the recoiling nucleus in coincidence with the ejectile.] Weak decays may also use this notation, with the initial nucleus A, the final nucleus B, and leptons as a and b in the case of electron captures (EC), and as b_1 and b_2 (both particles are ejecta) in the case of $\beta^{+/-}$ decay. For example, EC on ^{30}S (t$_{1/2}$=1.178 seconds) is written ^{30}S(e$^-$,ν_e)^{30}P, and the positron emission of ^{30}S is denoted ^{30}S(e$^+$ ν_e)^{30}P.

The Q-value of a reaction is defined to be the mass difference of the inputs and outputs, so that in an exothermic nuclear reaction, the Q-value is positive, and in an endothermic nuclear reaction, the Q-value is negative.

1.3.2 Reaction Rate

To calculate the reaction rate between two nuclei in a stellar plasma, we only need the cross section normalized to the number of interacting particles in the star's interior. The geometric cross section σ for interacting objects just depends on the radii R_i of the target A and projectile a so that $\sigma = \pi(R_A + R_a)^2$ [RR88]. Unfortunately, for nuclear reactions it is not that simple. Although we often speak of nucleons and nuclei as particles or spheres, baryons are quantum objects, and behave differently from the phenomena we see in everyday life, which are described by classical dynamics. It is observed that quantum particles have wave-like properties, such as the de Broglie wavelength $\lambda\!\!\!^{-}$ ($\lambda\!\!\!^{-} = \lambda/2\pi$). One may obtain a particle's wavelength by substituting the relativistic momentum of light $p = E/c$ into the light energy-wavelength relation (Equation 1.6) yielding

$$\lambda\!\!\!^{-} = \frac{\hbar}{p} \tag{1.12}$$

where $\hbar$ is Dirac's version of Planck's constant ($\hbar = h/2\pi$). For a non-relativistic projectile a on target A, we can then write [RR88]

$$\lambda\!\!\!^{-} = \frac{m_a + m_A}{m_A} \frac{\hbar}{\sqrt{2 m_a E_{lab}}}. \tag{1.13}$$

Thus, the radii in the geometrical cross section must be replaced with the de Broglie wavelength of the projectile so that the cross section σ

$$\sigma(E) = \pi \lambda\!\!\!^{-2} \tag{1.14}$$

becomes a function of energy — $\sigma \propto E^{-1}$ [RR88].

As we have seen, particles in a stellar plasma have a distribution of velocities (Equation 1.4), and the cross section depends on the properties of both interacting particles. It is preferable to use the relative velocity between two interacting particles in the centre-of-mass frame so that one does not need be concerned with the individual velocities of the interacting particles, v_A and v_a. In the centre-of-mass frame, the total mass is $M = m_A + m_a$, the reduced mass of the system is $\mu = \frac{m_A m_a}{M}$, and the centre-of-mass frame velocity V depends on the momenta of the interacting particles and the mass of the system as $V = \frac{p_A + p_a}{M}$ [RR88]. The centre-of-mass energy is then just $E_{cm} = \frac{\mu}{m_A} E_{lab} = \frac{1}{2}\mu\nu^2$, where ν is the velocity of both particles approaching one another in the centre-of-mass frame.

Because of the distribution of velocities, one must include a variable reaction rate per particle pair $\langle \sigma\nu \rangle$ summed over all velocities, cross sections, and the velocity probability function $\phi(\nu)$ (Equation 1.4) [RR88]

$$\langle \sigma\nu \rangle = \int_0^\infty \phi(\nu)\nu\sigma(\nu)d\nu. \tag{1.15}$$

Using the individual particle velocities v_A and v_a requires a double integral over both velocity distributions, which is avoided here because in the centre-of-mass frame, $V \equiv 0$ and $\int_0^\infty \phi(V)dV = 1$. Using the Maxwell-Boltzmann velocity distribution and the centre-of-mass energy, one may get [ILI07]

$$\langle \sigma\nu \rangle = \left(\frac{8}{\pi\mu}\right)^{1/2} (kT)^{-3/2} \int_0^\infty \sigma(E) E \exp\left(-\frac{E}{kT}\right) dE. \tag{1.16}$$

The stellar rate r for a given thermonuclear reaction is just the number of interacting nuclei of species A and a, N_A and N_a, multiplied by the variable reaction rate per particle pair $\langle \sigma\nu \rangle$ [ILI07]

$$r = \frac{N_a N_a \langle \sigma\nu \rangle}{1 + \delta_{Aa}} \tag{1.17}$$

where δ_{Aa}=0 for non-identical particles, and δ_{Aa}=1 for identical particles [RR88]. As two particles approach one another, they may interact via the electromagnetic, weak, or strong forces, and cross sections are calculated for specific cases.

To calculate the stellar reaction rate, one only need determine the temperature T and the energy dependent cross section $\sigma(E)$. The stellar reaction rate is essentially the fraction of the total collision rate between any two ions in a stellar plasma when specific nuclear interactions take place. The part of the cross section which increases gradually with energy we attribute to nonresonant reactions, and when there is a sharp rise and sunsequent drop in cross section with increasing energy, we attribute this phenomena to a physical resonance at a particular energy.

1.3.3 Nonresonant Charged-Particle Reactions

When two nuclei interact, if the impact parameter is large, the nuclei only interact peripherally, in which case only one or two nucleons within either nucleus may participate, called a direct reaction. Direct reactions have fast transit time 10^{-22}, and include transfer reactions where one nucleon is lost/gained, knock-out reactions, *etc.* *Direct reactions* should not be confused with *direct capture*, which is a total fusion of projectile and target, governed by the electromagnetic force. Direct captures may be resonant or nonresonant, where as direct reactions are never resonant reactions.

For charged particle interactions, one must consider the Coulomb barrier, and the tunneling (see Section 1.2.2) probability when $E < U_{Coul}$. For the case when $E \ll U_{Coul}$, the probability P for tunneling through the Coulomb barrier (see Equation 1.11) is roughly [RR88]

$$P = \exp(-2\pi\eta). \tag{1.18}$$

The variable η is the Sommerfeld parameter

$$\eta = \frac{Z_A Z_a e^2}{\hbar\nu} = \frac{Z_A Z_a e^2 \sqrt{\mu}}{\hbar\sqrt{2E}}. \tag{1.19}$$

However, for particular cases, one should compute the penetration factors directly from known information about the Coulomb wave function [ILI07].

If one combines the nuclear properties of the cross section, such as the spin and parity of the excited states in the compound nucleus, into a function $S(E)$, one may then write the energy-dependent nuclear reaction cross section as [RR88]

$$\sigma(E) = \frac{S(E)}{E} \exp(-2\pi\eta). \tag{1.20}$$

The quantity $S(E)$ is the astrophysical S-factor, and for nonresonant reactions (those that do not proceed via a particular excited state in the compound nucleus), it varies smoothly with energy, making it much more useful for extrapolating astrophysical cross sections than the cross section itself, which varies exponentially [RR88]. One may then calculate the nonresonant charged particle reaction rate per particle $\langle\sigma\nu\rangle$ substituting Equation 1.20 into Equation 1.16

$$\langle\sigma\nu\rangle = \left(\frac{8}{\pi\mu}\right)^{1/2} (kT)^{-3/2} \int_0^\infty S(E) \exp\left(-\frac{E}{kT} - 2\pi\eta\right) dE \tag{1.21}$$

recalling that η depends on energy (Equation 1.19), the equation is typically rewritten for clarity

$$\langle\sigma\nu\rangle = \left(\frac{8}{\pi\mu}\right)^{1/2} (kT)^{-3/2} \int_0^\infty S(E) \exp\left(-\frac{E}{kT} - \frac{b}{\sqrt{E}}\right) dE \tag{1.22}$$

where b is the Gamow factor

$$b = \sqrt{2\mu}\pi e^2 Z_a Z_A \hbar^{-1} . \tag{1.23}$$

Although the most probable particle energy is $E = kT$ in an ensemble described by Maxwell-Boltzmann statistics (Equation 1.4), the most probable energy for a particle to induce a nuclear reaction is shifted by the Gamow parameter to E_0, the Gamow peak. The width of this function is Δ, corresponding to the energy range in which nonresonant charge particle reactions will occur in a star. Upon knowing the relevant energies, one may measure a reaction cross section in the laboratory and attempt to extrapolate the astrophysical S-factor down to stellar

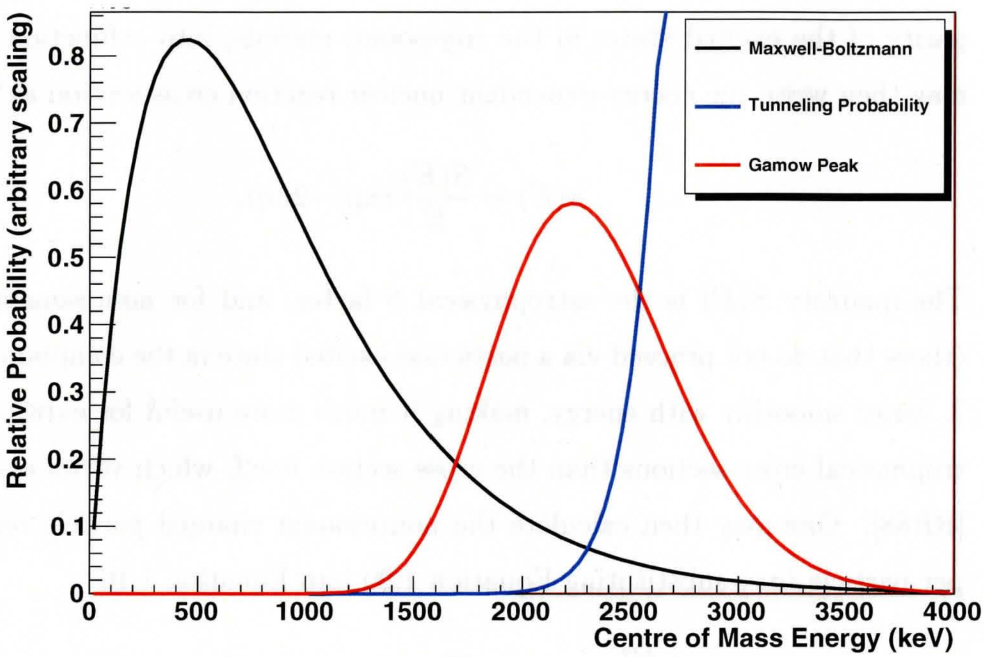

Figure 1.4: The figure shows the Gamow window for the interaction of ^{30}S + α at 1.3×10^9 K, plotted by the author. The centre-of-mass energy is plotted along the abscissa in thousands of electron volts against arbitrary probability on the ordinate. The probability scaling spans some twenty orders of magnitude so that all three plots are simultaneously visible, as is customary in plots of the Gamow window. The Gamow peak is at E_0=2.23 MeV, with a width Δ=1.15 MeV, indicating the astrophysically important centre-of-mass energies for the ^{30}S(α,p) reaction at 1.3 GK, the maximum energy achieved in Type I X-ray bursts [WOO04, FIS08a].

temperatures; in a select few cases, cross section measurements have been made directly at the Gamow peak [LUNA06].

1.3.4 Resonant Reactions

Nuclear reactions with a small impact parameter, when the collision is head-on, particularly at low energy, proceed via a compound nucleus C that is temporarily formed [BOH37]. We may write the interaction informally as $A + a \rightarrow C \rightarrow B + b$, where $A + a$ is the entrance channel and $B + b$ is the exit channel. In this two stage process, the compound nucleus de-excites without regard to how the excited state was populated in the entrance channel, although quantities like energy and angular momentum must be conserved throughout the process. Compound nuclear reactions are slow compared to other nuclear interactions, taking place on timescales of the order 10^{-16} to 10^{-18} seconds.

Spatial and time properties are quantized on the smallest scales, so that a nucleus may only be excited in discrete quantities of energy, and may only have particular values of angular momentum. Quantum objects are more accurately described as wave-packets than particles, and so when a nucleus is excited with energy above its ground state potential, it may emit one or more packets of energy (particles) to de-exite. Nuclear de-excitation energy is manifested in various forms, such as: high-frequency electromagnetic radiation (γ-rays), other nucleons (protons or neutrons) or nuclei (α particles or fission fragments), nuclear energy directly transferred to an atomic electron (internal conversion); or the weak nuclear force may convert neutrons to protons and vice versa ($\beta^{+/-}-$decay). However, these quantized energy levels have some width Γ in energy, given by the sum of the partial widths Γ_i for emission or absorption of different forms of quantized radiation

$$\Gamma = \sum_i \Gamma_i \tag{1.24}$$

where the Γ_i's, and hence Γ, are energy dependent. Quantum states have an energy width based on the lifetime of the level through the time-energy uncertainty relation [SAK93]

$$\Delta t \Delta E \approx \hbar \ . \tag{1.25}$$

As $\hbar \approx 6.58\ x\ 10^{-16}$ eV s, short-lived states may have widths on the order of keV (10^{-3} smaller than typical excitation energies).

The resonant reaction is special because it is populated through a particular excited state in the compound nucleus of energy E_R, which can only occur if $E_R \pm \Gamma_a/2 = E + Q$, that is, if the incoming energy through channel a falls within the width of a resonance in the compound nucleus. The density of states near E_R needs to be low enough that consecutive levels do not overlap in the compound nucleus, otherwise the behaviour cannot be described through single resonant mechanics.

Because total angular momentum is also conserved, the angular momenta of the projectile (J_a), target (J_A) and compound nuclear excited state (J_R) must also be accounted for in the interaction cross section statistical spin factor ω, which quantifies the different allowed spins from each level and any degeneracy [ILI07]

$$\omega \equiv \frac{2J_R + 1}{(2J_A + 1)(2J_a + 1)} \,. \tag{1.26}$$

Finally, one can modify the general cross section (Equation 1.14) to the case of radiative capture with a narrow resonance, or the Breit-Wigner formula [ILI07]

$$\sigma(E) = \lambda\!\!\!^{-2}\pi\omega \frac{\Gamma_a \Gamma_b}{(E - E_R)^2 + (\Gamma/2)^2} \tag{1.27}$$

where the width of the entrance channel through the projectile a is Γ_a, and the width of the exit channel through ejectile b is Γ_b.

One may then calculate the reaction rate per particle $\langle\sigma\nu\rangle$ substituting Equation 1.27 into Equation 1.16 [ILI07]

$$\langle\sigma\nu\rangle = \left(\frac{8}{\pi\mu}\right)^{1/2} (kT)^{-3/2} \int_0^\infty \lambda\!\!\!^{-2}\pi\omega \frac{\Gamma_a \Gamma_b}{(E - E_R)^2 + (\Gamma/2)^2} E \exp\left(-\frac{E}{kT}\right) dE. \tag{1.28}$$

For narrow resonances (defined when $\Gamma \ll E_R$), the tail-end of the Maxwell-Boltzmann distribution (Equation 1.5) changes very little over the resonance, and its value at $E = E_R$ can be taken outside the integral, and one can assume the partial widths Γ_i are approximately constant over the total resonance width. Thus, if we also re-write the de Broglie wavelength (Equation 1.13) in the centre-of-mass system [RR88]

$$\langle\sigma\nu\rangle = \frac{\sqrt{2\pi}\hbar^2}{(\mu kT)^{3/2}}\exp\left(-\frac{E_R}{kT}\right)\omega\Gamma_a\Gamma_b\int_0^\infty\frac{1}{(E-E_R)^2+(\Gamma/2)^2}dE. \tag{1.29}$$

The integral is a known Gaussian which evaluates to $2\pi/\Gamma$, and so we define the reduced width γ as

$$\gamma \equiv \frac{\Gamma_a\Gamma_b}{\Gamma} \tag{1.30}$$

and identify $\omega\gamma$ with the *resonance strength*, allowing us to finally write the stellar reaction rate per particle pair for a narrow resonance [RR88]

$$\langle\sigma\nu\rangle = \left(\frac{2\pi}{\mu kT}\right)^{3/2}\hbar^2\omega\gamma\exp\left(-\frac{E_R}{kT}\right) . \tag{1.31}$$

Thus, to determine the experimental cross section of a narrow resonance, one must measure or calculate the resonance strength $\omega\gamma$ based on laboratory data, along with measuring the resonance energy E_R. The resonance energy E_R and Gamow peak energy E_0 are derived independently, but we hope to find resonances in compound nuclei in the astrophysically relevant energy regimes. However, knowing the important burning energy regime may help identify any important resonances which likely enhance the stellar reaction rate [RR88].

1.3.5 Hauser-Feshbach Statistical Model

Nuclear experimental data indicate that with increasing excitation energy, the level density in a compound nucleus increases rapidly. In a given nucleus, below ~5 MeV there may be only a handful of discrete excitation levels, whereas above ~10 MeV there may be more than 10 levels per MeV. One may understand this property of nuclei by considering that for small amounts of energy, there is only just enough energy to power an excitation mode, such as a single particle excitation, a rotation, a vibration, a deformation, and so on with a list of classical analogies to explain quantized nuclear behaviour. However, as more energy is added, these different modes may mix with one another, leading to many permutations of precise ways to distribute nearly the same amount of energy, resulting in many closely spaced levels. Thus, for low energy resonant nuclear reactions, it is meaningful to consider the possible contributions from individual resonant levels, but at very high energy, there exists a virtual continuum of levels, and calculating the contribution from each level becomes cumbersome. Hauser and Feshbach were the first to work on such a statistical model of nuclear reactions [HAU52], and so the method is named after these physicists. However, these calculations are rarely done by hand, and the code NON-SMOKER has been developed which allows one to easily get Hauser-Feshbach cross-section of interest at astrophysical temperatures [RAU00, RAU01, RAU04]. Giving the statistical reaction rate formalism is thus outside the scope of this thesis.

Although experimentally measuring nuclear reaction cross section may seem onerous, it is useful to consider an example where nuclear data provide key astrophysical parameters.

1.3.6 ^{14}N(p,γ) Reaction

For the cold CN cycle, it was mentioned that the limiting reaction is ^{14}N(p,γ)^{15}O, which was directly measured at stellar temperatures for the first time at the LUNA facility in 2006 [LUNA06]. The stellar reaction rate (see Section 1.3) was decreased by a factor of 2 compared to the previously extrapolated rate from higher energy experimental data. Because the ^{14}N(p,γ) reaction sets the timescale for hydrogen burning in the CN cycle, a decrease in the reaction cross section increases the calculated lifetime of a star [in particular the main-sequence turn-off]. Prior to the LUNA measurement, the calculated age of globular clusters was 13.4 $\pm$ 1.2 Gyrs [CHA95, KRA03], which is increased by 0.5-1 Gyrs based on the new ^{14}N(p,γ) experimental data [ANG05], possibly bringing globular cluster lifetimes into closer agreement with the Wilkinson Microwave Anisotropy Probe (WMAP) results for the age of the universe 13.8 $\pm$ 0.3 Gyrs [DEB08]. From the ^{14}N(p,γ) experiment, one can understand that directly measuring key nuclear cross sections at stellar energies yields critical input data for astrophysics calculations. We will return to this point later on in discussion of the $^{30}S(\alpha,p)$ reaction in x-ray bursters.

Once an equilibrium is established in the number of CNO seed nuclei [CAU62], the CNO cycles (or the *pp* chains) release energy at a constant rate by converting hydrogen into helium, allowing stars to exist in a state of hydrostatic equilibrium, until the hydrogen is exhausted in the burning region. Without a source of energy to counteract gravitational pressure, the star's core will contract until helium ignites. Helium has a higher ignition temperature than hydrogen due to the Coulomb barrier (Equations 1.11, 1.18). As the helium fuel is exhausted, the core will contract further, allowing for the burning of the heavier elements. Exothermic nuclear fusion may continue in stellar core and shell, starting from carbon and the oxygen, and the burning may eventually proceed up to as far as ^{56}Fe, the most tightly bound nucleus (see Figure 1.2), after which all subsequent fusion reaction are endothermic. It is then interesting to ask what happens when nucleosynthesis is turned off within a star after the nuclear fuel runs out.

Chapter 2

Compact Objects

2.1 The Last Phase of Stellar Evolution

Compact objects represent the final phase of evolution of solitary star systems. However, only three configurations of high density baryonic matter are stable: black holes, neutron stars, and white dwarfs [WHE66], listed in order of decreasing density. Super-hyperon and/or quark stars have been postulated [XU06, NAK08][1], and there are also theories about observed stars that may fit the quark star ticket (see Section 2.4.1). These exotic stellar objects have also been dubbed 'dead stars' [LON94], but such a title does not do justice to the rich physics of matter at extreme densities and gravitational pressure found only here. As these compact objects are not stabilized by the release of thermonuclear energy, without stellar evolution theory, it would not even be proper to label these objects as stars at all.

Stellar mass black holes and neutron stars are likely formed in core collapse supernovæ ($\approx 10^{44}$ J [THI01]) , which are spectrally labeled Type II and identified by hydrogen Balmer absorption lines; white dwarfs are also formed in this manner. It is important to note that massive black holes may be formed in ways unrelated to stellar evolution, such.as galactic collisions, but white dwarfs and neutron stars

[1]John WHEELER's work indicates that there is not another stable configuration of cold catalyzed matter without a yet unknown equation of state [WHE66].

are created strictly as by-products of dead stars. There is no continuous transition that can take place from a white dwarf to a neutron star [WHE66].

2.2 Black Holes

Although a detailed understanding of the dynamics near black holes requires a delicate interplay of general relativity and quantum mechanics, in principle a black hole is a gravitating object with an imaginary surface (often called the event horizon) at radius r from is centre, within which the escape velocity exceeds the speed of light. Karl SCHWARZSCHILD first calculated the radius of such an object of mass M [SCH16]. Using a simple Newtonian mechanics model, the gravitational potential needed to prevent a test particle of mass m with speed c from escaping (because not even a massless particle can exceed the speed of light) the potential induced by the black hole yields

$$\frac{1}{2}mv^2 = \frac{GMm}{r} \ . \tag{2.1}$$

The dependence of the mass m of the test particle drops, and if the equation is algebraically rearranged, one may define the Schwarzchild radius:

$$r_{Sch} \equiv \frac{2GM}{c^2} \ . \tag{2.2}$$

To treat this subject with rigor requires a formal analysis of the problem in the framework of electromagnetism, general relativity, and quantum mechanics, but for the purposes here we may consider John WHEELER's famous statement that, "Black holes have no hair," even though he omitted quantum effects[2]. The *no-hair* theorem insists that the only external properties, or observables, of a black hole are its mass, charge, and angular momentum. With the exception of some accreting

[2]Pair production at the event horizon may result in Berkenstein-Hawking radiation, for example, yielding a finite entropy in agreement with the 2^{nd} law of thermodynamics.

black hole binaries (discussed later in Section 3.1), thermonuclear energy release is not relevant to the physics of black holes and black-hole systems.

2.3 White dwarfs

Observations indicate that a vast majority of stars are not massive enough to complete nucleosynthesis up to iron, leaving behind a hot core, or white dwarf. Unlike the other compact objects, white dwarfs were observed before they were theoretically predicted, thus creating a bit of a shake up in the astronomy community. Such as the observation by Friedrich Wilhelm HERSCHEL in 1783 of the triple-star system 40 Eridani [HER85] and Friedrich Wilhelm BESSEL predicited in 1838 that Sirius is a binary star system [HER44], which was confirmed by Alvan Graham CLARK in 1862 [CAR06]. Spectral observations of 40 Eridani B and Sirius B were conducted by Walter ADAMS in 1914 [ADA14] and 1915 [ADA15]. Using Wien's displancement law (Equation 1.7) and the Stefan-Boltzmann law (Equation 1.8), astronomers computed from these high resolution spectral observations that white dwarfs ought to have radii smaller than Earth, despite having masses comparable to the Sun! It is little surprise that for some time these data were regarded as erroneous. However, white dwarfs are now fairly well characterized, as their composition is largely some blend of α-nuclei ranging from ^{12}C to ^{24}Mg, supported by electron degeneracy pressure (the electron abundance, $Y_e \equiv \frac{Z}{A}$ for charge-neutral ensembles, of a white dwarf is thus 0.5).

Since electrons are Fermions, they are subject to the Pauli Exclusion Principle and cannot occupy the same quantum state. R. H. FOWLER first explained white dwarfs as supported by electron degeneracy pressure using Fermi-Dirac statistics [FOW26]. In a collapsing proto white dwarf, the density of occupied quantum states increases for all particles, but due to the light mass of the electron m_e compared to the mass of a nucleon m_n ($\frac{m_e}{m_n} \simeq \frac{1}{500}$), the number of available low energy states reaches a critical value for electrons before nucleons. In a normal star like the Sun, electrons also fill quantum states, but the density of states is so high that we may treat the problem in the classical limit; thus, adding or removing a single electron from the Sun is fairly irrelevant. However, because all the low energy states are occupied in a white dwarf, adding (removing) an electron from the system requires (releases) the Fermi energy ϵ_F

$$\epsilon_F = \frac{\hbar^2 k_F^2}{2m_e} , \tag{2.3}$$

where $\hbar$ is Planck's constant over 2π and k_F is the Fermi wave vector

$$k_F = (\frac{3\pi^2 N}{V})^{\frac{1}{3}} , \tag{2.4}$$

with N electrons in volume V (the generalized wave number $k = \lambda^{-1}$ (Equation 1.13)). The total electron kinetic energy E_{kin} in such a system arising from degeneracy is

$$E_{kin} = 2\int_0^{k_F} D(k)\epsilon(k)dk = \frac{3}{5}N\epsilon_F , \tag{2.5}$$

where the factor of 2 is included because there are two electron spin states ($\sigma = \frac{1}{2}, -\frac{1}{2}$), and the density of states $D(k)$ for a standing wave in $\vec{k}$-space in three dimension is given by

$$D(k) = \frac{Vk^2}{2\pi^2} . \tag{2.6}$$

The energetic electrons thus exert a pressure against further collapse in a gravitational potential E_{pot}

$$E_{pot} \simeq -\frac{3GM^2}{5R} , \tag{2.7}$$

and it is straight-forward to solve for the maximum stable mass. Subrahmanyan CHANDRASEKHAR was the first to arrive at this result [CHA31], so the critical white dwarf mass is honorifically called the Chandrasekhar mass M_{Ch}, which is found to be

$$M_{Ch} \simeq 1.4M_\odot , \tag{2.8}$$

where $M_\odot$ is one solar mass ($M_\odot \approx 1.98x10^{30}kg$); a classmate once lamented that Chandrasekhar received the Nobel Prize for modeling electrons in a box [MCG07], though one is inclined to see the elegance of such a simple solution and novel idea. These results indicate that the mass M of the star and its radius R go as $M \propto R^{-3}$, indicating that larger mass degenerate stars have smaller radii. Above the Chandrasekhar mass, the electron mass m_e increases, decreasing the Fermi energy (see Equation 2.3), and enough pressure is not generated by the degenerate electron gas to prevent further gravitational contraction. In the next stable state of cold catalyzed matter[3] the system becomes supported by neutron degeneracy pressure.

2.4 Neutron Stars

One year after Chandrasekhar published his results about white dwarfs, Chadwick discovered the neutron [CHA32], subsequently leading Walter BAADE and Fritz ZWICKY to suggest that a supernova is a transition between a normal star and a neutron star [BAA34]. One may immediately estimate the maximum stable mass of a neutron star using Chandrasekhar's method, where the Fermi energy (Equation 2.3) is calculated with the neutron mass, yielding around $6\mathrm{M}_\odot$ — an over-estimate due to relativistic effects. Several years later, Robert OPPENHEIMER and George VOLKOFF modeled neutron stars under general relativity as a cold Fermi gas of neutrons, and they deduced that only three configurations are stable, all below $0.7\mathrm{M}_\odot$. [OPP39]. Despite much effort, the neutron star equation of state is still a mystery nearly 70 years later. However, it is clear why a white dwarf or neutron star does not collapse into a black hole based on John WHEELER's spring analogy: "With further increase in density the net energy becomes more and more positive, like the energy of a spring tightly compressed and ready to expand explosively if released" [WHE66].

[3]The matter is considered cold because all the available quantum ground states are filled, despite the fact that the temperature may be well above 10^6 K.

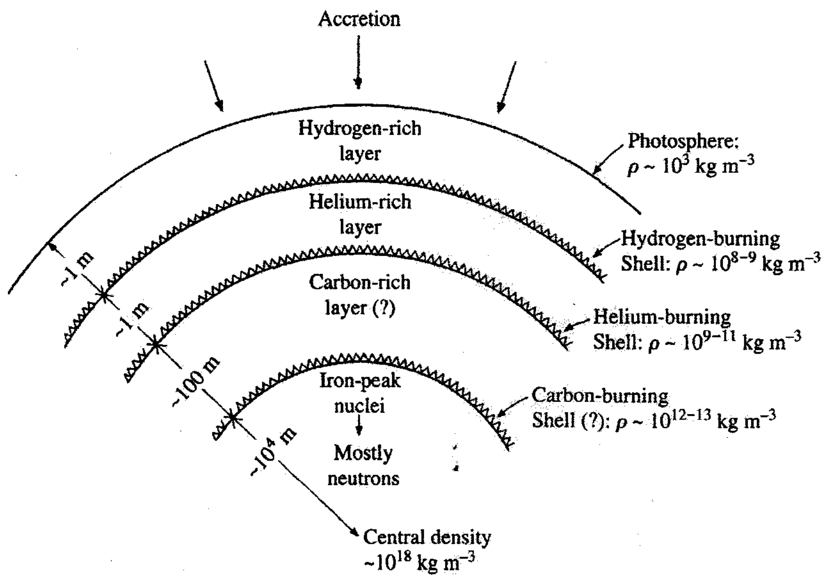

Figure 2.1: The figure shows inferred crustal structure and core composition of an accreting neutron star [CAR06]. Note the logarithmic radius length scale on the left. Accreting systems are discussed in Chapter 3.

In neutron stars, a majority of the electrons have been captured (see Appendix A) by free protons and iron group nuclei, so that $Y_e \approx 0.1$ [THI01]. Although $t_{1/2}$=10.24 minutes for neutrons in free space, in a neutron star, there are no vacant low energy states for the emitted electron to occupy [CAR06], hence the very low electron abundance Y_e. In the crust layers, these neutrons are captured by Fe seed nuclei up to the neutron drip line (see Figure 2.1). Towards the core, the matter density approaches nuclear densities, and so attempting to distinguish nuclei in this neutron-rich sea of particles is fairly asinine.

It is important to consider general relativistic effects when considering neutron star observations, as most quantities are gravitationally red-shifted (denoted z) by an amount

$$z = \frac{\lambda_\infty - \lambda_*}{\lambda_*} , \tag{2.9}$$

where λ_∞ is the wavelength of radiation measured by a distant observer and λ_* is the proper wavelength, or the wavelength of the radiation as measured in the star's reference frame. The correction factor $(1+z)$ is assumed to be

$$1+z \approx 1+z_s = \left(1-\frac{2GM_*}{R_*c^2}\right)^{-1/2}, \tag{2.10}$$

where z is the red-shift to the center of the star, z_s is the red-shift to a point on the surface of the star, M_* is the proper mass of the star, R_* is the proper radius of the star, G is the universal gravitational constant, and c the speed of light [AYA82]. The observed radius R_∞ is thus larger than the proper radius by an amount

$$R_\infty = \frac{R_*}{\sqrt{1-\frac{2GM_*}{R_*c^2}}}, \tag{2.11}$$

and the measured gravitational mass M_∞ far away from the object must be less than the sum of the constituent baryons and leptons ($M_\infty < M_*$) because, like white dwarfs (see Section 2.3), the neutron star radius is inversely proportional to its mass. The exact neutron star mass/radius relationship is unknown. R_* and M_* are usually quoted in the literature as R and M, and the subscript $_\infty$ is specified for observed values. Oddly, when observing a neutron star from any angle, due to the warping of spacetime, one actually sees something like part of the back of the neutron star [CUM08].

If the masses and radii of neutron stars can be well measured, this will constrain their mass/radius relationship, and one may then evaluate the matter composition inside a neutron star [ZHA07a], perhaps yielding an equation of state. There is not yet a way to directly measure the radii of any neutron stars [ZHA07a]. One can observe thermal neutron star emission in some low mass X-ray binary transients (see Chapter 3) during periods of non-accretion — the emission is isotropic and results from deep crustal heating, and so there should be a radius/luminosity relation [BRO98]. Such spectra have been fit to a pure hydrogen atmosphere model [PAV91, ZAV96] to extract mass/radius relationships. Selected neutron star radii are listed in Table 2.4 [RUT05], although these values are model-dependent,

Reference object	Satellite	Radius_∞ (km)	Distance kpc	kT^{∞}_{eff} eV	Reference
omega Cen	Chandra	13.5 ± 2.1 [4]	$5.36 \pm 6\%$	66^{+4}_{-5}	[RUT02]
	XMM	13.6 ± 0.3	$5.36 \pm 6\%$	67 ± 2	[GEN03a]
M13	XMM	12.8 ± 0.4	$7.80 \pm 2\%$	76 ± 3	[GEN03b]
47 Tuc X7	Chandra	$14.5^{+1.8}_{-1.6}$	$5.13 \pm 4\%$	105 ± 6	[HEI06]
M28	Chandra	$14.5^{+6.9}_{-3.8}$	$5.5 \pm 10\%$	90^{+30}_{-10}	[BEC03]

Table 2.1: Calculated radii for select neutron stars in quiescent low mass X-ray binary transients. The extrapolated effective temperature and assumed distances used for the computation are also given.

assuming $M_{Nstar} = 1.4M_\odot$ and distances are taken from [CAR00, THO01].

The observed neutron star mass range is presently $M_{Nstar} = 1.35 \pm 0.04M_\odot$ [THO99], which comes from radio pulsating stars (pulsars).

2.4.1 Radio Pulsars

Radio pulsars were first observed in 1967 [HEW68] and explained as rotating neutron stars shortly thereafter [GOL68]. As a consequence of the properties of the proto neutron star formed during core-collapse supernovæ, neutron stars are often born rotating rapidly with strong embedded magnetic fields. However, as this magnetic field is embedded and not driven by a rotational dynamo in the neutron star core, the magnetic dipole axis is often not aligned with the axis of rotation, as shown in Figure 2.2. Electrons and other charged particles emitted near the magnetic poles are quickly accelerated to relativistic speeds by the induced electric field [CAR06]. As the electrons spiral around the $\vec{B}$-field lines, they may decrease their energy by emitting curvature radiation [CAR06], or high energy γ-rays. This process is more of an electron-gamma shower, where the high energy gamma rays

[4] Recalculated from original reported value of 14.3 ± 2.1 km based on updated distance data [RUT05].

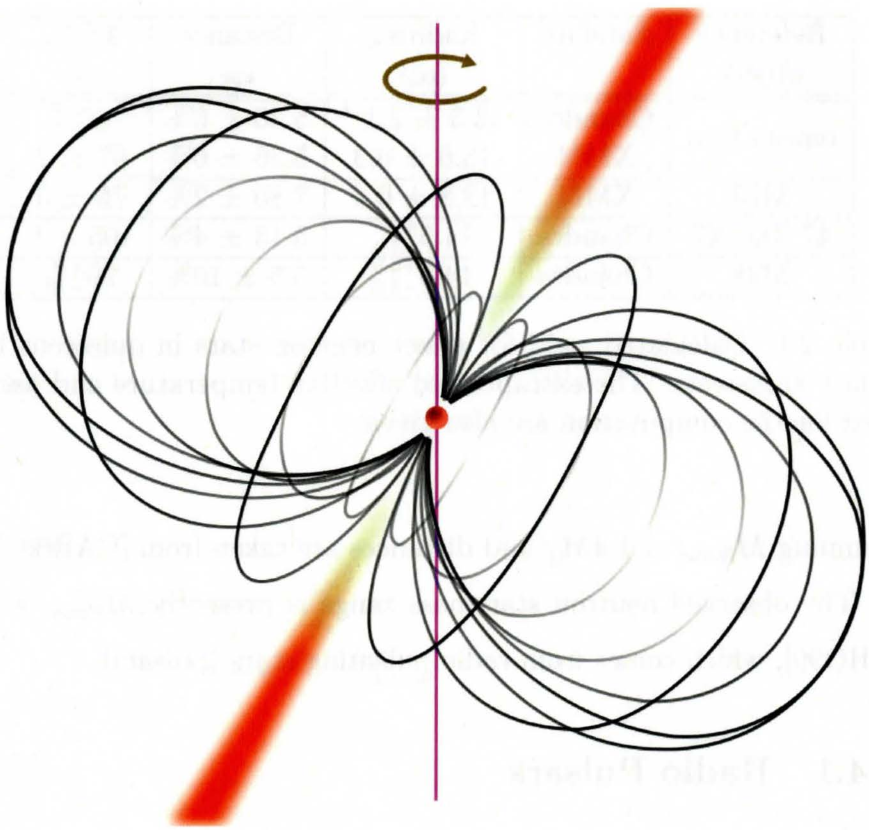

Figure 2.2: The figure depicts a toy model of a central neutron star rotating rapidly about the blue vertical axis with an embedded off-axis magnetic dipole field [WIK08d]. Red jets are drawn emerging from the magnetic poles of the neutron star, and the $\vec{B}$-field lines of a magnetosphere are sketched out.

($E_\gamma \geq$1022 MeV) can then transform to charged particles via pair-production

$$\gamma \rightarrow e^- + e^+ , \tag{2.12}$$

and these electrons and positrons may also annihilate via the time-reversal of pair-production

$$e^- + e^+ \rightarrow \gamma + \gamma , \tag{2.13}$$

where two γ's must be emitted to conserve momentum in the centre-of-mass frame. All the while, the charged particles also decrease their kinetic energy by emitting synchrotron radiation tangentially to their trajectory with a frequency equal to the red-shifted orbital frequency of the electrons about the field lines — synchrotron radiation is relativistic cyclotron radiation (see Section 4.2.3 for a discussion of how charged particles behave in a magnetic field). This mechanism provides the bright radio source in these pulsars. The radio emission appears to be periodic because, like a lighthouse, while the beacon is always illuminated, it is not always directed at a stationary observer. Because the neutron stars in radio pulsars lose angular momentum to the emitted charged particles, their period decreases with time. However, these stars do not actually pulse. Some pulsars are possible candidates for quark stars [ZHA07b, YUE08, XU08].

In 1942, the Crab nebula was associated with the remnant from the supernova of 1054 [DUY42, MAY42], and the so-called *south preceeding star* was deduced to be the dead stellar core from the explosion [BAA42, MIN42]. The collapsed star associated with the Crab nebula was later determined to be a radio pulsar [COC69], confirming the predicted connection between supernovæ and neutron stars [BAA34]. Radio pulsars in binary star systems, particularly when both stars are radio pulsars, allow for quite precise calculations of the stellar masses, detailed in [THO99]. Binary star systems containing compact objects may also involve accretion, a rich astrophysical site for the study of thermonuclear explosions — the subject of the next chapter.

Chapter 3

X-Ray Emission In Accreting Neutron Star Binaries

The first chapter treated quiescent stellar nucleosynthesis, where it is appropriate to apply equilibrium statistical physics. Most of the α-nuclei, the iron group nuclei, and half the elements heavier than iron are produced in entropy dominated explosive stellar nucleosynthesis (refer to Figure 1.1, which shows what astrophysical processes create heavy elements). Thermonuclear reactions also provide the energy for the explosive stellar phenomena in accreting binary star systems, so we consider these environments in more detail.

3.1 Accretion

Accretion in astrophysics is when the change of mass $\dot{M}$ in a system is positive ($\dot{M} > 0$). Accretion happens on many astrophysical scales. For example, galaxies may accrete matter from neighboring galaxies or the intergalactic medium, supermassive black holes accrete material in galactic centres, matter may be transferred from one star to another in binary stellar systems (see Figure 3.1), *etc.* Mass transfer in binary star systems has interesting consequences for stellar evolution, but also enables thermonuclear powered explosions in compact object binaries, such as

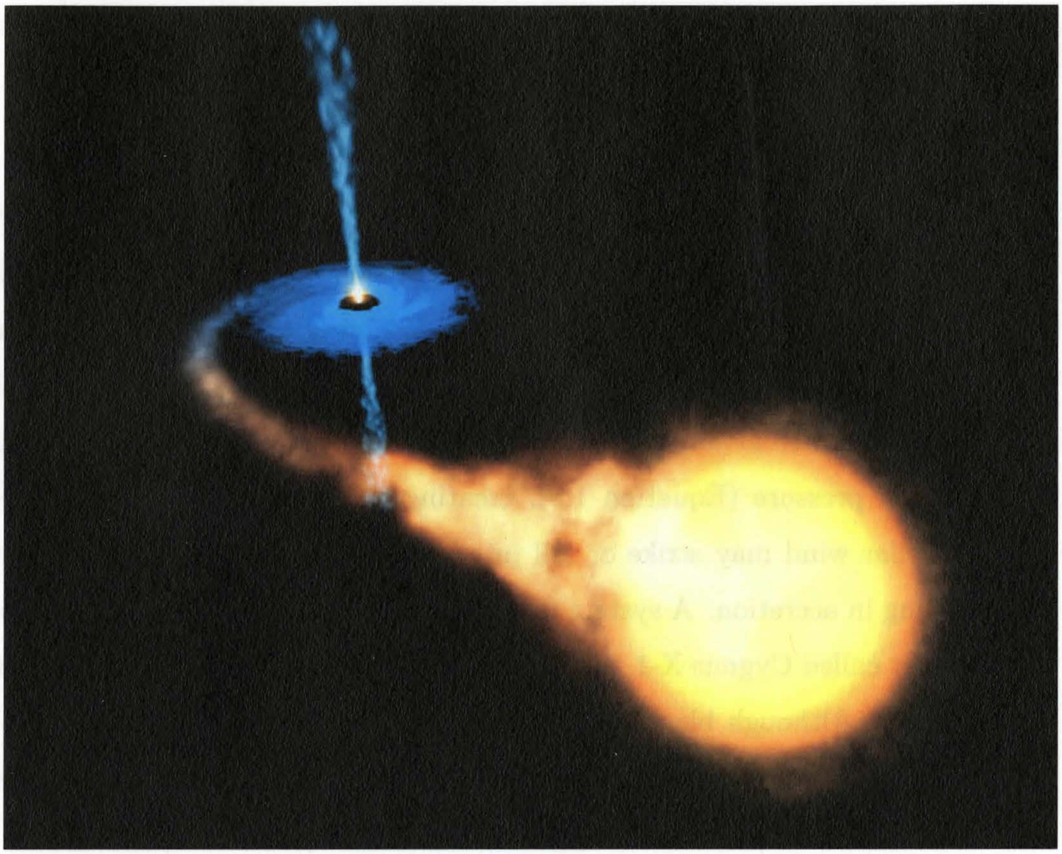

Figure 3.1: Artist's conception of accretion in a binary star system with a compact object [CIE08]. The accretion disk and bi-polar jets are clearly visible near the compact object in the upper left side. The companion, or donor star, can be seen in a non-spherical state in the lower right corner.

novæ, Type Ia supernovæ, and X-ray bursters (XRBs).

The power involved in accretion processes is one of the most energetic phenomena known in the universe. Dropping a nucleon from infinity onto a neutron star releases roughly 180 MeV when the nucleon impacts the neutron star's surface. Compared to the ~6.7 MeV/u released in burning hydrogen to helium, accretion releases an order of magnitude more energy than thermonuclear processes [LEW93].

The binary fraction, or percent of star systems that involve two stars, is around 50%. Accretion occurs through two mechanisms in binary stars: radiation pressure driven mass loss and Roche lobe overflow. Eddington first calculated the maximum radiative luminosity L_{Edd} a star of mass M can have and still remain in hydrostatic equilibrium (Equation 1.1)

$$L_{Edd} = \frac{4\pi Gc}{\bar{\kappa}} M \ , \tag{3.1}$$

where G is the universal constant of gravitation, c is the speed of light, and $\bar{\kappa}$ is the opacity of the photosphere averaged over the spectrum. Stars exceeding L_{edd} must undergo radiation pressure driven mass loss, and so this maximum luminosity is dubbed the *Eddington limit.* In massive binary systems, one or both of the stars may fail to attain hydrostatic equilibrium and undergo mass loss driven by radiation pressure (Equation 1.9), creating a fierce stellar wind. Matter within the stellar wind may strike or fall into shallow orbits about the companion star, resulting in accretion. A system first observed in 1964 turned out to be an XRB of this sort called Cygnus X-1, a stellar mass black hole with a supergiant companion [ODA71]. Although black holes exist in some X-ray binaries, black hole systems are powered by accretion and not thermonuclear burning, although there may be some *rp* process occuring in the inner accretion disk.

To understand Roche lobe overflow, consider the gravitational potential in a binary star system. In a rotating reference frame, shells of gravitational equipotential surround each star like Russian nesting dolls of infinitesimal thickness. These shells of potential each comprise of points in space with identical gravitational potential. Very close to either star, the shells are spherical, but they are quickly distorted into rain-drop shaped surfaces in the region between the two stars. Although the equipotential surfaces become more distorted further away from the stars, the point between the two stars where the equipotential surfaces meet is important. Now imagine placing a test particle at such a specific point between the two stars where the gravitational force experienced by the test particle is equal and opposite. This specific location is one of three points where a test particle feels no gravitational force, called the inner Lagrange point [CAR06]. Matter from the less massive star may escape at this joining point, where it can fall into the deeper gravitational potential of the binary companion [THI94].

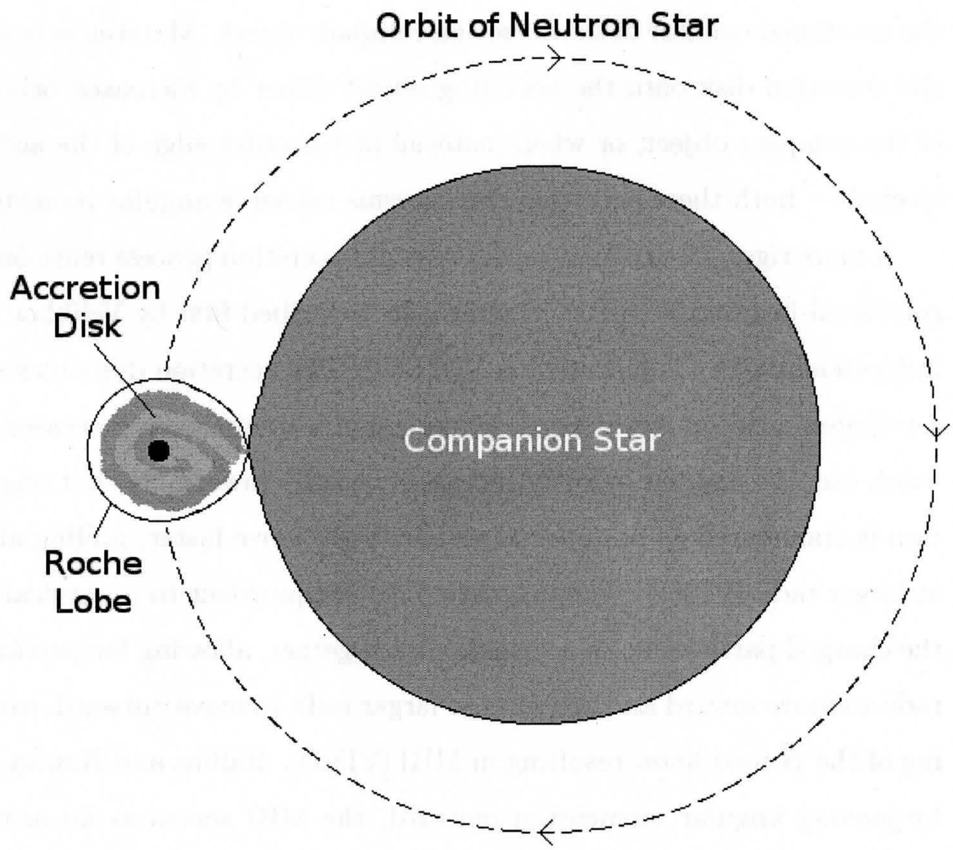

Figure 3.2: A schematic drawing of a companion star filling the Roche lobe in a binary star system, where the primary star is a neutron star. The stars orbit each other about the inner Lagrange point (see the text), but in this diagram, the neutron star's rotational path is drawn in the frame of the companion star for clarity. Material may fall from the inner Lagrange point from the companion star into orbit about the neutron star, forming an accretion disk.

In close or extremely massive binary star systems, one (or both) of the stars may extend to the inner Lagrange point in a rain drop shape, where mass transfer from the envelope of the donor secondary star to the primary star occurs (or a contact binary exists if the stars share a common envelope [LON94]). The rain drop equipotential surface is called the Roche lobe, drawn for a neutron star binary system in Figure 3.2. In an accreting binary where the primary star is a compact object, there is either a small surface or no surface for the material to strike, and from conservation of angular momentum, the accreted material forms a disk about the rotational equator of the accreting compact object. Material is transferred from the accretion disk onto the accreting object either by increased orbital frequency of the compact object, or when material at the outer edge of the accretion disk is ejected — both these accretion mechanisms conserve angular momentum.

A more rigorous explanation of the latter accretion process relies on the magneto-rotational-instability (MRI), theoretically described first by Velikhov [VEL59] and independently by Chandrasekhar [CHA60]. The accretion dynamics are similar to a tethered satellite experiment, where angular momentum increases radially outward, but the angular velocity increases radially inward, so that angular momentum is transferred as particles at smaller radii move faster, pulling along particles at larger radii [VIS08]. The magnetic field is equivalent to a physical tether, tying the charged particles in an accretion disk together, allowing for particles at smaller radii to move inward and particles at larger radii to move outward, causing stretching of the $\vec{B}$-field lines, resulting in MRI [VIS08]. Balbus and Hawley realized that by moving angular momentum outward, the MRI serves as an accretion engine in these disks, as gravitational energy is released as (nonlinear) heat dissipation [BAL90, BAL91a, BAL91b, BAL92a, BAL92b]. However, the natural strength of the $\vec{B}$-field in accretion disks is a controversial topic in astrophysics, and no consensus exists [VIS08].

The full power of accretion is only realized when matter hits a solid surface. In the case of an accreting black hole, there is no surface for the material to strike. Even for the case of a white dwarf or neutron star, accreted material will decelerate significantly in the atmosphere and often come into low orbits rather than strike the crust. At low accretion rates, the flow is optically thin and much of the gravitation energy is released and radiated away before the material reaches the photosphere, making it have a smaller impact on the thermonuclear physics [FUJ81]. In accreting white dwarf or neutron star systems, accretion is significant primarily as a source of hydrogen and helium, which often make up more than 98% of the infalling material. These nuclear fuels power thermonuclear explosions in an environment where light elements were long exhausted by fusion in these dead stars.

In a fixed volume, the temperature in an ideal gas is stabilized by pressure (see Equation 1.3). But in a star, heat is often exchanged through radiative transfer. Because heat exchange processes are statistical in nature, one can imagine that thermal fluctuations often arise in any small volume. In the case of an ideal gas in a fixed volume, the pressure increases linearly with temperature, and thermal anomalies are stabilized quickly by pressure work. Nuclear reactions are also probabilistic, and so the instantaneous local rate of nuclear energy release may vary from the system average, temporarily disrupting thermal equilibrium.

The situation is starkly different in an electron degenerate gas where pressure and temperature are de-coupled. With radiation pressure and heat transfer as the only mechanism counteracting temperature increase in a degenerate gas, small fluctuations in local temperature may result in large scale thermal instabilities when the thermonuclear energy generation rate surpasses the rate of conductive cooling. Because nuclear reaction cross sections are extremely energy dependent, even small increases in temperature increases the energy generation rate, creating a positive feedback loop resulting in a runaway thermonuclear explosion.

3.2 Explosive Nucleosynthesis

With the exception of core-collapse supernovæ, accreting compact binaries (which are also the origin of supernovæ of Type Ia) are the only source of active explosive nucleosynthesis, where nucleosynthesis refers to any release of thermonuclear energy altering the local abundances (not necessarily ejected in the interstellar medium). Type II supernovæ are the predominant candidate location for the formation of the α nuclei, the rapid neutron capture process (r process) (responsible for the production of half the elements heavier than iron as in Figure 1.1), as well as the birth place of neutron stars.

The r process was first proposed in 1957 [B^{2}FH] to explain the abundance peaks (see Figure 1.1) below closed neutron shells near Ge, Xe, and Pt. Seed nuclei (presumed in most cases to be Fe-group) capture neutrons up to the neutron drip line, or (n,γ)–(γ,n) equilibrium, in an environment of high neutron flux, and then decay back to stability. The sites for the r process are still unknown, but it has been observed that at least two different sites are required [WAS96, SNE00]. Type II supernovæ are generally accepted as the main r process site, ejecting an average of 10^{-5} $M_\odot$ r process elements per event [THI05]. The second (heavy) r process site may be neutron star ejecta [LAT77, THI05], as the proton to neutron ratio, or electron abundance Y_e, of neutron stars is about right at $Y_e \sim 0.1$ [THI01]. Also, the crustal composition of elements from $56 \leq A \leq 106$ naturally serve as seed nuclei for an accreting neutron star [SCH99] (or lighter elements for a primordial neutron star crust [PET95]). Neutron star mergers [EIC89, FRE99] are the most favoured heavy r process site, perhaps ejecting as much as 10^{-2} $M_\odot$ r process elements per event [THI05], but the low probability of occurrence has yet to receive a satisfactory answer.

Novæ are understood as explosive hydrogen burning on the degenerate surfaces of accreting white dwarves. These explosions on white dwarves do not necessarily disrupt the binary system, and so they may repeat on timescales typically greater than 1,000 years. The nova burning path is outlined in Appendix A, beginning at Section A.2.2. In such a system, it is also possible for the white dwarf to accrete sufficient mass to slowly exceed the Chandrasekhar limit (Equation 2.8), and after about 100,000 years of simmering will result in a Type Ia supernova explosion, triggered by explosive carbon burning. These accretion-induced supernovæ are the primary source of the iron peak nuclei (see Figure 1.1).

If a white dwarf in an accreting binary system exceeding the Chandrasekhar mass limit leads to explosive nucleosynthesis, one wonders if a similar situation occurs with accreting neutron stars as well. If any of the material from an accretion-induced collapse of a neutron star is ejected into the interstellar medium, it is a candidate location for the heavy r process. It is unknown if such a transition is visible, which primarily depends on whether or not there is a third stable form of cold condensed matter in between a neutron star and a black hole, such as a quark star. Without a proto quark star for the collapsing neutron star to "bounce" off, the neutron star may undergo an uneventful collapse to within its own Schwarzschild radius (see Equation 2.2), in a smooth transition to a singularity. Recent work indicates that a significant amount of matter can be ejected from the hydrodynamic collapse of a neutron star from a hadron-quark phase transition [MAR08], but the authors do not consider the nucleosynthetic implications of such an event, nor the accretion-induced collapse mechanism (which seems more robust). There are many known X-ray transient systems with accreting neutron stars—over 100 XRBs alone, though X-ray pulsars, and other neutron star binary systems with higher accretion rates, are more favoured as sites for accretion-induced collapse. Many X-ray transients are understood as hydrogen and helium burning on the surface of an accreting neutron star, which are a type of X-ray binary system.

3.3 X-ray Binaries

An X-ray transient is any astrophysical source with peak wavelength 0.1 – 10 nm exhibiting significant fluctuations in luminosity over time. In 1962, the first evidence for X-ray sources outside the solar system was observed by detectors strapped to a sounding rocket [GIA62], which initiated the field of X-ray astronomy. Accretion onto a compact object was an early suggested source of powerful X-rays [ZEL64, SAL64, SHK67]. In 1971, the first X-ray pulsar was discovered [GIA71] and the system was deduced to be an accreting binary with a compact object [SCH71]. The Einstein X-Ray Observatory showed that all classes of stars emit X-rays, so here we consider the systems with peak emission in the X-ray [LON94].

In 1975, two groups independently reported findings of X-ray sources exhibiting bursting behaviour, where the luminosity would increase by at least an order of magnitude and then decline [GRI76, BEL76]. As soon as astronomers started looking, many similar sources were found, dubbed X-ray bursters (XRBs), and by 1977, some fifteen burst sources were known [LEW77]. XRBs were almost immediately explained theoretically as thermonuclear flashes on accreting neutron stars [WOO76, MAR77], as postulated prior to the discoveries of XRBs [ROS73, VAN74, HAN75]. While other explanations for XRBs involving black holes were also proposed, blackbody radii measured during bursts indicated neutron stars as the source [SWA77, HOF77a, HOF77b, VAN78]. All of the sources exhibited bursts with hourly, daily, or more extended regularity, and after a sharp rise time (1–10 seconds), show a thermal decline and a softening of the X-ray spectrum (spectral softening is a property of cooling blackbodies) – this behaviour is classified as Type I and results from thermonuclear burning (see Section 3.4.3 for a more detailed treatment of X-ray burst spectra) [HOF78]. Particular rare systems, such as the Rapid Burster [LEW76a], also show extremely rapid fluctuation in hard X-ray luminosity – this behaviour is classified as Type II and results from accretion instabilities [HOF78].

Of principal interest to this thesis are neutron stars in binary systems. Although the binary fraction is typically around 50%, only around 5% of neutron stars are in binary systems, due to their formation process through core collapse supernovæ. Supernovæ are often asymmetric, which can give a kick to the proto-neutron star; the average formation velocity $\langle V \rangle$ has a Gaussian distribution around $0 \leq \langle V \rangle \leq 550$ km s^{-1} [POP00], and with the possibility of a kick to the neutron star and ejection of mass from the system, many core-collapse supernova in binary star systems do not result in a neutron star binary. The results of neutron star accretion are variable, depending on parameters such as the mass of the companion star, the binary orbital radius, the neutron star's magnetic field, and to a lesser extent the chemical composition of the companion star.

If the neutron star's magnetic field is high enough ($> 10^{11}$ G [LEW93]), then it will funnel material from the accretion disk directly onto the star's magnetic poles.

Like radio pulsars in Section 2.4.1, these neutron stars often have axially unaligned embedded magnetic fields, and the accretion induced stable thermonuclear burning at the magnetic poles is observed as an X-ray pulsar. The magnetic poles of the accreting neutron star are heated tremendously by the anisotropic infall of matter, and energy is released from thermonuclear burning of hydrogen and helium, to be described in Sections 3.4.1 and 3.4.2. However, because matter is falling onto the neutron star, its angular momentum increases over time, and so the rotational frequency of X-ray pulsars increases over time as the pulsar is spun up. X-ray pulsars are found in high mass X-ray binaries (HMXB) (*massive* describes when the secondary, or donor, star is greater than $10M_\odot$ [LEW93]), and about half of all HMXBs are X-ray pulsars [CAR06]. Steady state burning occurs under high local accretion rates, which is the reason the systems do not exhibit bursts [JOS80, BIL97].

In the case of accreting neutron stars with lower magnetic fields ($<10^{10-11}$ G [LEW93]), the accreted material is not funneled to the star's magnetic poles, and as material passes through the accretion disk, it settles on the surface of the neutron star, forming an atmosphere rich in hydrogen and helium. The material has an abundance of light elements because it is accreted from the surface layers of the companion star, which is generally a main sequence star (though in some cases no hydrogen is present in the accreted material [LEW95]). After sufficient material accumulates on the surface of the neutron star, a thermonuclear explosion will occur. Observationally, the result is an X-ray burst, and because the accretion process is not disrupted during these outbursts, X-ray bursts are recurrent, and such systems are known as X-ray bursters. Accretion onto these neutron stars produces a steady luminosity of order 10^{37} ergs [AYA82], and so the ratio of burst flux to persistent flux α (not to be confused with the ^{4}He nucleus) ranges between 10 and 10^3, usually closer to 100 for most systems [LEW93]. These burst sources are low mass X-ray binaries (LMXBs) (low mass describes when the secondary, or donor, star is less than 1 $M_\odot$ [LEW93], which makes one wonder how a medium mass

X-ray binary behaves). The mass of the companion star in X-ray binary systems is determined by optical observations [VAN80, THO78, KOY81]. No HMXBs have been observed to exhibit distinct bursting behaviour[1], and no LMXB is observed to show pulsations [LEW93]. As the magnetic field is buried in HMXBs over time, and the mass of the companion decreases through accretion, HMXBs may evolve into LMXBs. LMXBs make up an older population of stars and have been accreting much longer than HMXBs [BHA97]. LMXBs should be more than 10^4 years old because there is no supernova remnant associated with any LMXB systems [FUJ81]. However, more recent theoretical work indicates that highly magnetized neutron stars may show bursting behaviour, theoretically understood as runaway thermonuclear burning initiated at the magnetic poles spreading as a detonation wave (faster than the local sound speed) around the surface of the neutron star, in contrast to the deflagration burning (slower than the local sound speed) initiated in X-ray bursts on neutron stars with low magnetic fields [LAM00].

3.4 Thermonuclear Flash Model

Early XRB simulations either used simple one-zone models to estimate the explosion conditions and burning pathway, using the parameters (ρ, T, X), where ρ is the density, T is the temperature, and X is the mass fraction array [TAA80, FUJ81, HAN82, HAN83, KOI99], or more sophisticated one-dimensional (1D) multizone models with limited nuclear reaction networks [JOS78, TAA79, WAL82, AYA82, FUJ87]. Most models have still not progressed past 1D, and the thin burning shell has been assumed to be spherically symmetric over the surface of the neutron star, which is a fair approximation since the accreted envelope is less than 1% of the neutron star radius [FUS87]. Only recent models are able to successfully include extended nuclear reaction networks and realistic burning conditions [WOO04, FIS04, FIS06]. 1D models are a problem because localized burning is

[1]Although the emissions from HMXBs are not constant.

anticipated at the onset of X-ray bursts [STR01]. Some recent models have been made in 2D, showing that the flame front propagation on the neutron star surface is consistent with burst rise times[ZIN01]. However, for those interested in the relevant nuclear reactions in X-ray bursts, these models are still lacking, including either extremely few isotopes compared to current 1D models [ZIN01] or no nuclear reaction network at all [SPI02].

Simulations quickly indicated that the accretion rate is the most important burst parameter [FUJ81, FUS87], determining the regime of nuclear burning [WOO04]. At the highest accretion rates $\dot{M} > 4 \times 10^{-8}$ $M_\odot$ yr^{-1}, stable hydrogen burning occurs, which is the case for X-ray pulsars [FIS03]. In XRBs there are two accretion regimes: $\dot{M}$ ~2×10^{-8} – 4×10^{-10} $M_\odot$ yr^{-1} leads to combined helium and hydrogen shell flash; and $\dot{M}$ ~2×10^{-10} – 1×10^{-9} $M_\odot$ yr^{-1} leads to a pure helium shell flash (and also weak hydrogen shell flashes) [WOO04]; the accretion $\dot{M}$ regimes overlap due to the effects of the metallicity of the accreted material (see Section 3.4.4). Typical accretion rates generally range from $\dot{M}$ ~10^{-10} – 1×10^{-9} $M_\odot$ yr^{-1} [TAA85, TAA96].

In the first proposed nuclear flash model for XRBs [WOO76], the infalling matter is heated to 10^8 K [FIS08a] by impact on the neutron star and fully ionized. The material is compressed in this electron degenerate environment as material continues to accrete on top, leading to a thin shell instability that triggers thermonuclear runaway [VAN74, HAN75]. Hydrogen shell burning via the HCNO cycles (see Section A.2.2) is stable shortly after the onset of accretion due to temperatures above 10^7 K [TAA80], so a pure hydrogen shell flash generally cannot occur (the HCNO cycles are β^+-limited by ^{14}O ($t_{1/2}$=70.641 seconds), ^{15}O ($t_{1/2}$=122.24 seconds), and ^{18}Ne ($t_{1/2}$=1.672 seconds)) [JOS77, LAM78].

It was originally proposed that the burning proceeded via the HCNO cycles (described in Section A.2.2) triggered by a helium shell flash. If the accretion rate is low enough, the HCNO cycles may exhaust hydrogen locally, leading to a zone depleted of hydrogen called the helium shell [BIL98]. Pure helium burning is inhibited because ^{8}Be is alpha-unbound, and so helium burning may only proceed via the so-called triple-α reaction

$$\alpha + \alpha \rightleftharpoons {}^8Be + \alpha \rightarrow {}^{12}C \tag{3.2}$$

which requires high densities ($\sim 10^9$ kg m^{-3} [LEW93]) so that electron screening enhances the reaction rate [SAL69]. Because helium burning does not rely on any weak interactions, it is not β-limited, and the burning may be thermally unstable [LEW93]. In a pure helium shell flash, the burning continues via (α,γ) reactions starting with ^{12}C and continuing no farther than ^{40}Ca [FIS08b]. But unlike in quiescent nuclear burning, hydrogen and helium burning may occur simultaneously as the convective region of helium burning mixes into the hydrogen shell [TAA79], and helium burning serves as the trigger for explosive hydrogen burning [SCH99].

At high accretion rates, burning may ignite before a helium shell can form (see Equation A.10), leading to a combined helium and hydrogen shell flash, which is triggered by break-out from the HCNO cycles or the triple α process [WIE00, THI01]. As a result, the ^{12}C created by the triple-α in combined helium and hydrogen shell flashes immediately captures two protons, becoming ^{14}O [FIS08a], rather than the burning proceeding via ^{12}C(α,γ)^{16}O. The ignition temperature for ^{14}O(α,p) is 4×10^8 K, whereas it is above 10^9 K for ^{12}C(α,γ) [FUJ81]. Although the triple-α reaction initially causes the rise in luminosity, its reaction rate levels off around 10^9 K (due to the strong resonant contribution from the Hoyle state [HOY54] in ^{12}C at 7.65 MeV), so its overall contribution to the energy generation rate in XRBs is small [AYA82].

3.4.1 The *rp* process

Starting in 1981, models indicated that the thermonuclear burning path breaks-out from the HCNO cycles [WIE99] and the triple α reaction [WHE98], and nucleosynthesis proceeds at least up to the iron-peak nuclei, releasing energy at a rate more than 100 times greater than the HCNO cycles alone [WAL81]. The burning pathway predominately involves rapid proton capture (*rp* process) on HCNO break-out seed nuclei (typically ^{19}Ne and ^{21}Na) [WAL81], moving the flow of material towards the proton drip line. The proton drip line is the boundary where nuclei become proton-unbound, which occurs when the proton capture Q_p drops below 0. However, the (p,γ) cross section is identical to the time-reversed reaction (γ,p), where a γ-ray photodisintegrates the nucleus [ILI99]. At XRB temperatures of 10^9 K, the tail of the Maxwell-Boltzmann distributed photons (see Equation 1.4) is energetic enough to photodisintegrate all nuclei produced through reactions with $Q_p < 3$ MeV [THI94], preventing the *rp* process from reaching the proton drip line, and burning can only proceed after a β-decay which is temperature independent causing further thermonuclear burning to come to a roadblock, waiting for the duration of the β halflife [BRO02]. These nuclei in (p,γ)–(γ,p) equilibrium are called *waiting point* nuclei as in the HCNO cycle (see Sections 1.2.2, A.2.2) . But the *rp* process cannot be explained in a straight-forward way, since the various waiting points and exact reaction flow path depend on burst conditions [THI94], and much of the nuclear properties are unknown.

Stable *rp* process burning occurs in X-ray pulsars, but previous reaction networks did not include nuclei above $A > 56$ [SCH99]. Stable burning occurs when the nuclear fuel is consumed at the same rate it is accreted, which begins at a critical accretion rate of $\sim 3.2 \times 10^{-8}\ M_{\odot}\ yr^{-1}$ for isotropically accreting LMXBs [FIS03]. At high accretion rates, the *rp* process cannot proceed beyond the SnSbTe cycle, because ^{107}Te is α-unbound, and so the ^{107}Te(γ,α)^{103}Sn photodisintegration prevents further proton captures [SCH01a, SCH01b], allowing for steady hydrogen burning to helium even at the highest accretion rates. The originally proposed SnSbTe cycle is [SCH01a, SCH01b]

$$^{103}Sn(e^+\nu)^{103}In(p,\gamma)^{104}Sn(e^+\nu)^{104}In(p,\gamma)^{105}Sn(p,\gamma)^{106}Sb(p,\gamma)^{107}Te(\gamma,\alpha)^{103}Sn\ . \tag{3.3}$$

The SnSbTe cycle may be cutoff at lower A, depending on the existence of lighter, α-decaying tellurium isotopes, and this limit was originally thought to be ^{107}Te [SCH01a, SCH01b]. ^{106}Te is now a known ground state α emitter, and ^{103}Sb is also known to be particle bound; ^{105}Te is also bound and has a positive α-decay Q value, but ^{102}Sb has yet to be observed. The only way to by-pass the SnSbTe cycle would be a pulsed *rp* process [SCH01b], but this is not likely in steady accretion scenarios in X-ray pulsars, and more recent work has shown that in XRBs, the reaction flow stops on even-even nuclei near $A \sim 60$ (specifically, the ^{64}Ge halflife is $t_{1/2} = 63.4$ s, predicted to truncate the burning at A=63 for most X-ray burst conditions [FIS08b]) [WOO04, FIS08a]; of course, for the steady *rp* burning in X-ray pulsars, which can by-pass the ^{64}Ge waiting point, the SnSbTe cycle is the ultimate end-point.

3.4.2 The αp process

The *rp* process timescale is set by the sum of the β decay halflives involved [VAN94], but may be dominated by the sum of the halflives of the waiting point nuclei, specifically. In mixed compositions of hydrogen and helium at these high temperatures and densities, β^+ decay timescales lose in competition with (α,p) reactions [FUJ81] on $T_z = -1$ nuclei up to ^{34}Ar, after which alpha captures are generally unimportant at Z$\geq$20 due to the strong Coulomb barrier and decreasing Q values [THI94]. The *rp* process is altered by a sequence of $(\alpha,\mathrm{p})(\mathrm{p},\gamma)^2$ reactions that bridge the β^+-decays at waiting point nuclei between $18 \leq A \leq 40$ [WAL81], called the αp process. Although the αp process involves proton captures, it does not change the overall hydrogen abundance and so may be considered a pure helium burning chain. The initial HCNO break-out is via ^{15}O(α,γ)^{19}Ne (at T=2 x 10^8 K) while the reaction flow is dominated by ^{18}Ne(e$^+$ ν)^{18}F(p,α)^{15}O, but eventually ^{18}Ne(α,p) becomes the primary destruction mechanism for ^{18}Ne (at T=9 x 10^8 K)

[2] $^{A}\mathbf{N}(\alpha,\mathrm{p})^{A+3}\mathbf{N}{+}1(\mathrm{p},\gamma)^{A+4}\mathbf{N}{+}2$ (where A is the number of nucleons and **N** is the nuclear species, determined by the number of protons Z, not the number of neutrons N).

[WAL81, FIS05]. The original $^{14,15}O$ seed nuclei are exhausted as thermonuclear runaway initiates, and the burning proceeds via [WOO04]

$$3\alpha \rightarrow\ ^{12}C(p,\gamma)^{13}N(p,\gamma)^{14}O(\alpha,p)^{17}F(p,\gamma)^{18}Ne(\alpha,p)^{21}Na(p,\gamma)^{22}Mg(\alpha,p)^{25}Al\ . \tag{3.4}$$

The αp process may continue as

$$^{25}Al(p,\gamma)^{26}Si(\alpha,p)^{29}P(p,\gamma)^{30}S(\alpha,p)^{33}Cl(p,\gamma)^{34}Ar(\alpha,p)^{37}K(p,\gamma)^{38}Ca\ , \tag{3.5}$$

at which point the Coulomb barrier becomes too large. Once the αp process commences (some 1.5 seconds after the onset of thermonuclear runaway [WAL81]), the energy generation rate jumps by as much as 3 orders of magnitude in one second [WAL81]. In consequence, one should note that, due to the competing αp process, the *rp* process effectively involves the consumption of hydrogen and helium [AYA82].

It is not possible or necessary to directly measure all of the thousands of nuclear cross sections involved, and so one must rely on models to indicate which nuclei and reactions are most relevant. Unknown cross sections are estimated using the Hauser-Feshbach model. Except for $^{14}O(\alpha$,p) and $^{18}Ne(\alpha$,p), all (α,p) reaction rates are based on Hauser-Feshbach predictions [THI05]. One may then simulate bursts and consider which nuclei are abundant as a function of burst time (see Figure 3.3). There are inferred waiting points at a number of nuclei, including ^{21}Mg, ^{30}S, ^{34}Ar, ^{38}Ca, ^{56}Ni, ^{60}Zn, ^{64}Ge, ^{68}Se, ^{72}Kr, ^{76}Sr, ^{80}Zr [KOI99, FIS08a], and a newly released software package `Computational Infrastructure for Nuclear Astrophysics` allows users to specify waiting point parameters, the program then finding nuclei satisfying the criteria [NUC08].

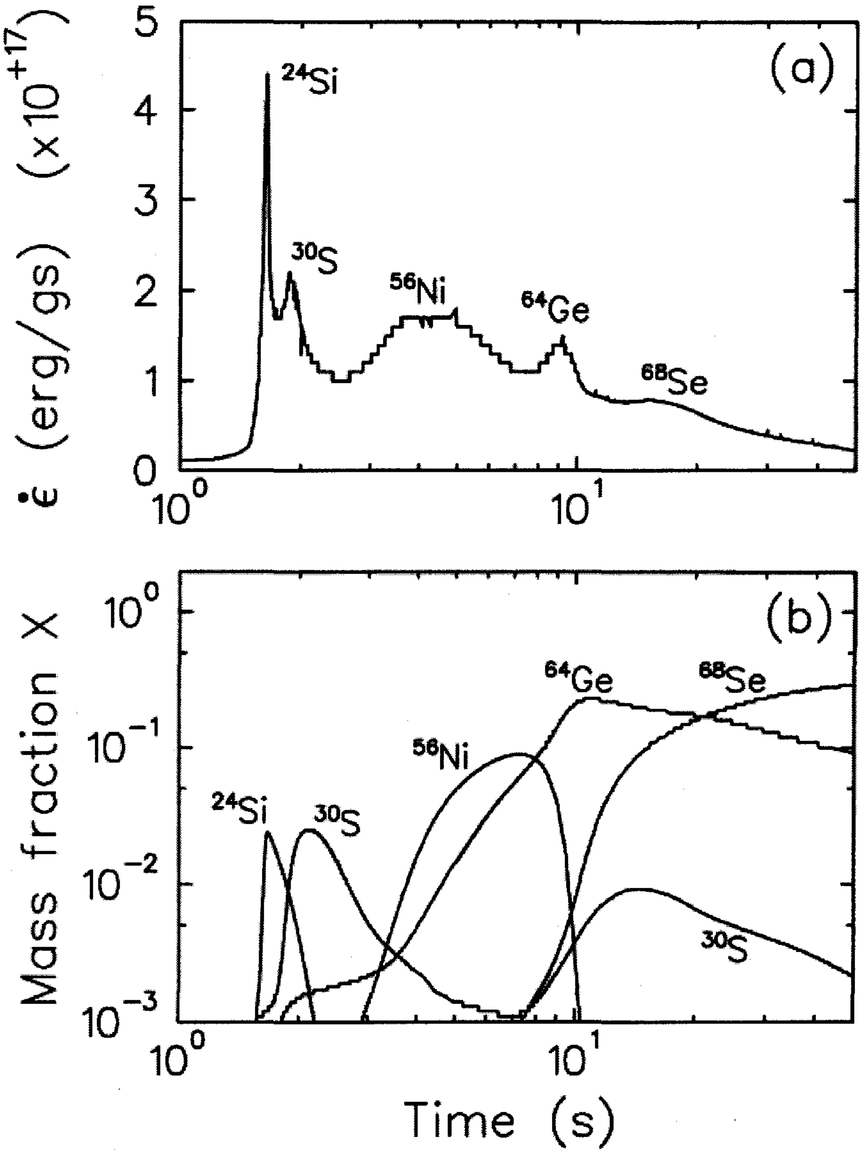

Figure 3.3: Plots of energy generation rate $\dot{\epsilon}$ in ergs per gram second and mass fraction $X \equiv \frac{N_i M_i}{\rho N_A}$ (where N_i is the number density of selected nuclei i, M_i is the relative atomic mass of species i, ρ is the mass density, and N_A is Avogadro's number [ILI07]) on the ordinate, against logarithmic burst time in a simulation [ILI99]. The mass fraction is high for a number of nuclei, indicating they are possible waiting points. The energy generation rate has local maxima when waiting point nuclei mass fraction varies most sharply [ILI99].

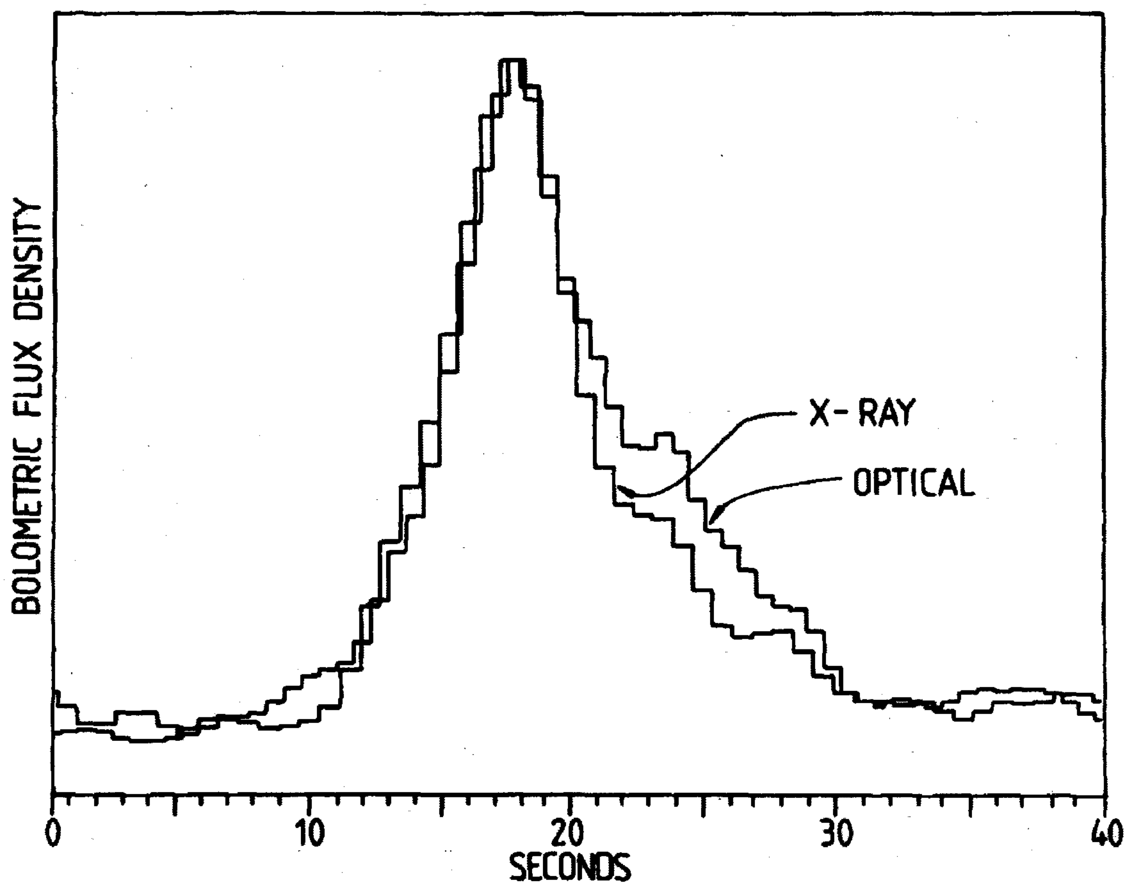

Figure 3.4: Extracted bolometric luminosity from the X-ray burster 4U/MXB 1636-53 [LAW83], as a function of burst time in seconds, showing the optical and X-ray components. Notice the sharp rise time on the order of seconds. The burst shows a single, well-defined peak. The burster system is chosen because bolometrically double-peaked bursts have also been observed from this system (see Section 3.4.5.

3.4.3 X-Ray Burst Spectra

The burning proceeds, subsequently heating the atmosphere to a maximum of 1.3 x 10^9 K [FIS08a] and releasing energy which is eventually transported to the surface, observed as a brief emission of X-rays. The prompt X-ray emission is 80% of all the nuclear energy released in the thermonuclear runaway (omitting the energy taken away by neutrinos) [AYA82] — the rest heats the neutron star, which is later radiated during X-ray burst quiescence. The burst rise time results from radiative diffusion in the neutron star envelope [TAA80]

The X-ray luminosity quickly reaches its peak (from less than one second [GOT86] up to around 10 seconds [DAY90]), and then the luminosity decreases exponentially as the atmosphere cools [FIS08a]. Pure He shell flashes have short rise times ($\sim$ 1 second) due to less dependence on the slow weak force than combined H/He shell flashes, which release energy on a longer time scale (10–100 seconds) [KUU02]. This model describes the observed XRB spectra quite remarkably [JOS78, TAA80], including the integrated flux (or fluence), the burst rise and decay timescales, recurrence times, and energetics ($\sim 10^{39-40}$ ergs [LEW93]) (see Figure 3.4), although weak bursts with recurrence times of 5-20 minutes are yet to be explained [ILI99]. Unfortunately, the ashes of burning are opaque to γ-rays, due to the high gravitational field on the surface of a neutron star [WAL81], and the only spectral feature common to many systems is a mysterious absorption line at 4.1 keV [LEW93]. Pure He shell flashes are more powerful than combined H/He shell flashes. Because He shell flashes occur for lower accretion rates, it will take a longer time to accrete adequate material to achieve ignition temperature and density compared to a combined H/He flash. But because He shell flashes are more powerful than H/He shell flashes, burst fluence is correlated with recurrence time, consistent with observations [HOF77b]. The HCNO cycles are also dependent on the mass fraction of catalytic material Z_{CNO} (see Equation A.10), and so hydrogen is converted to helium at a faster rate with an increased metallicity. The ignition temperature T_{ig} is shown to depend on the abundance of CNO nuclei as $T_{ig} \propto Z_{CNO}^{1/9}$ [BIL98]. In consequence, neutron stars accreting material with a higher Z_{CNO} may form a helium shell more rapidly by local depletion of hydrogen, leading to a pure He shell flash instead of a combined H/He shell flash. Thus, burst power also correlates with the metallicity of the accreted material [TAA96].

3.4.4 Compositional Inertia

In the preceding discussion of thermonuclear burning, catalytic material has been assumed. However, calculations indicate that nuclei heavier than helium accreted onto a neutron star are largely destroyed (survival rate of 1 in 10^3) by atmospheric spallation reactions [BIL92], and assuming accretion of solar composition, the mass fraction of elements heavier than helium Z is only 0.02% initially [AND89]. Spallation may play a smaller role at higher accretion rates, because the ion kinetic energy is decreased by lower effective gravity [TAA96]. This mechanism is not always favoured, as pure He shell flashes cannot occur if no CNO material is accreted [LEW93], theoretically limiting the number of ways to easily explain variations in burst behaviour [LEW95].

The Coulomb stopping length for a nucleus containing Z protons and A nucleons in the atmosphere of a neutron star goes as A/Z^2, so that protons and α particles have the furthest penetration depth [BIL92]. The result is that the mean molecular weight in the neutron star atmosphere is higher above the proton stopping point than below it, resulting in the Raleigh-Taylor instability [BIL92] of a heavier fluid accelerated into a lighter advection region [RAY83]. For neutron star magnetic fields below $B < 10^8$ G, the Raleigh-Taylor instability growth rate is faster than the diffusive mixing rate [BIL92], transporting heat and making the nuclear abundances more homogenous. An inverted mean molecular weight also occurs during thermonuclear runaway, but it is stabilized by an inverted temperature gradient [WOO84].

If no catalytic material is available, the above description is not accurate, and burning may proceed via the *pp* chains fueled by electron capture (EC) (see Equation A.2) at densities above 2 x 10^{10} kg m^{-3} [TAA96, BIL98]. However, the ashes of previous bursts include many heavy elements [TAA96], and so recurrent bursts rely on thermal and compositional inertia [TAA80], where the ashes of previous bursts serve as catalysts in future bursts and the residual heat reduces the recurrence time of subsequent bursts [WOO04]. Each modeled case is followed until a

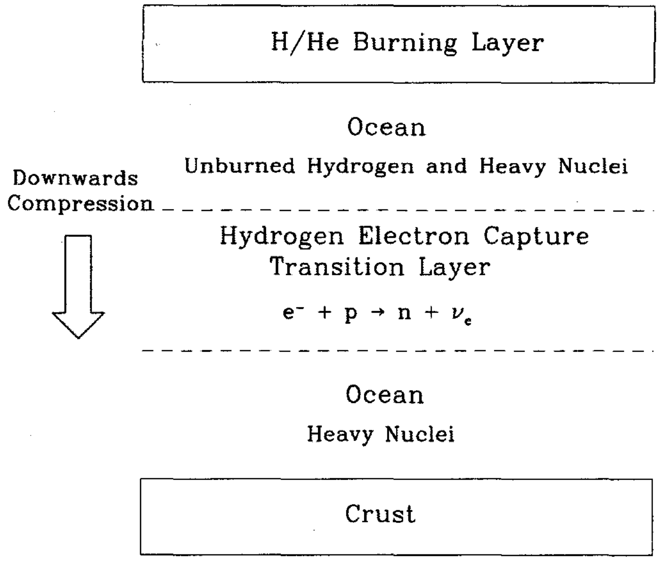

Figure 3.5: Schematic of the upper layers in an accreting neutron star [BIL98]. It is disputed as to whether or not there is any hydrogen remaining after bursts [SCH99]. The crust connects with other layers down to the core as in Figure 2.1.

limit cycle equilibrium is reached, in as few as 15 consecutive bursts in one case [AYA82, TAA93]. We can see that the oceanic and crustal compositions of a neutron star influence the burst behaviour; in particular, the compositional inertia decreases the burst recurrence time [WOO04].

LMXBs accrete enough material to replace their entire crusts, down to the crust/core interface [RAV94, SCH99]. As a result, the composition of an accreting neutron star ocean and crust deviates significantly from the primordial neutron star [PET95], and may include many elements heavier than iron [SCH99] which may capture neutrons created by proton EC (see Figure 3.5) [BIL98]. The crust comprises a lattice of nuclei, and lattice vibrations may also lead to nuclear fusion. Ground state oscillations in a Coulomb lattice lead to tunneling at densities exceeding ρ=10^{16} kg m^{-3}, called pycnonuclear burning [FUS87, YAK05]. Pycnonuclear burning can ignite helium burning [CAM59] in XRBs [LEW93], and may also lead to carbon lattice burning, which may be a way to explain especially powerful superbursts in LMXB systems (1000 times more powerful and longer than previous bursts in the same system) first observed in 2000 [COR00, WOO76, TAA78, BRO98, CUM01, SCH03, WEI06, WEI07].

3.4.5 Double Peaked X-Ray Bursts

The apparent double-peaked spectra of some XRBs, where the double-peak is only observed in the X-ray spectrum, is well documented [LEW76b, HOF80]. *Double-peaked* here refers to two maxima in the peak wavelength, and not in the bolometric fluence (discussed later), or total radiated energy (as in Equation 1.7). The double-peak was explained first as Compton scattering [HOF80], but this was never reproduced in any models. Upon the modeling of combined hydrogen and helium shell flashes, the postulate that double-peaks arise from the incomplete burning of hydrogen in previous bursts was considered in some detail [AYA82] (which is no longer believed to be the case); however, [AYA82] also predicted that high luminosities could lead to photospheric expansion, a phenomena later considered in more detail by others [TAA82, WAL82, HAN82, KAT83, EBI83]. Radial expansion was followed up in a later model, which reproduced the double-peaked structure of the X-ray spectrum while preserving the single-peak structure of the overall light-curve [PAC83]. Another model showed that the double-peaked structure during extreme luminosities is caused by mass loss and not radial expansion [EBI84]. The model of residual hydrogen burning was cast into doubt later when models showed that there is no persistence of hydrogen after the compositional inertia stabilizes [WOO84]. However, the radial expansion model was corroborated by many studies [TAA82, WAL82, HAN82, KAT83, EBI83]. If the peak burst luminosity approaches the Eddington limit (Equation 3.1), which may happen if pure helium shell burning is ignited at high density ($> 10^6$g cm^{-3} [LEW95]), the accreting neutron star will undergo photospheric radius expansion [HAN82]. As the photosphere expands, the temperature declines and the peak X-ray wavelength decreases. The photosphere quickly contracts again, increasing the temperature, and the peak X-ray wavelength once again achieves its previous value, causing the second peak [LEW93]. An impedance of the radiation transfer was found in a two-zone model, which could explain the double-peaks [REG84], but this effect disappears when 25 or more zones are included in the model [FIS04]. In some less common XRBs, a double-peak is observed in the bolometric luminosity (4U/MXB 1636–53 [SZT85], 4U 1608–52 [PEN89] (see Figure 3.6), and GX 17+2 [KUU02]) — and the unique triple peak from 4U/MXB 1636–53 [VAN86]. The bolometrically double-peak bursts are also set apart from the rest because they are weak bursts, which calls into question a model of radius expansion resulting from extreme luminosities for these cases [SZT85]. It was postulated that these bursts could result from the slow spreading of the flame front compared to the rotation rate of the accreting neutron star, but this idea was not favoured compared to multiple release of nuclear energy or a radiation transport impedance [SZT85]. Later analysis also indicated that spatially localized burning is a possible explanation, but that the frequency of these weak bolometrically double-peaked bursts is too infrequent for such a case [VAN86]. Instead, more support was given to the theory that bolometrically double-peaked XRBs result from multiple release of nuclear energy [VAN86, FUJ87]. The possibility of the burst light attenuating on a burst-induced accretion disk corona was proposed to explain the spectra of 4U/MXB 1636–53 [MEL87]. Within six months, the accretion disk corona model was shown to be inconsistent with other bursts from the same source that appeared to be unattenuated — in an unusual case where the original title of the work advocating the model [MEL87] was used, having changed *evidence for* into *evidence against*, the results being submitted to editors of the same journal [PEN87].

Although the multiple release of nuclear energy is the only explanation consistent with current observational data and burst models, the cause for a delay in the energy release is still an outstanding question. The idea of mixing combustible layers after the initial burst was proposed [WOO84], but the separation timescales are too long by a factor of 100 [SZT85]. Instabilities arising from differential rotation were proposed to mix material up into the burning region, which modeled

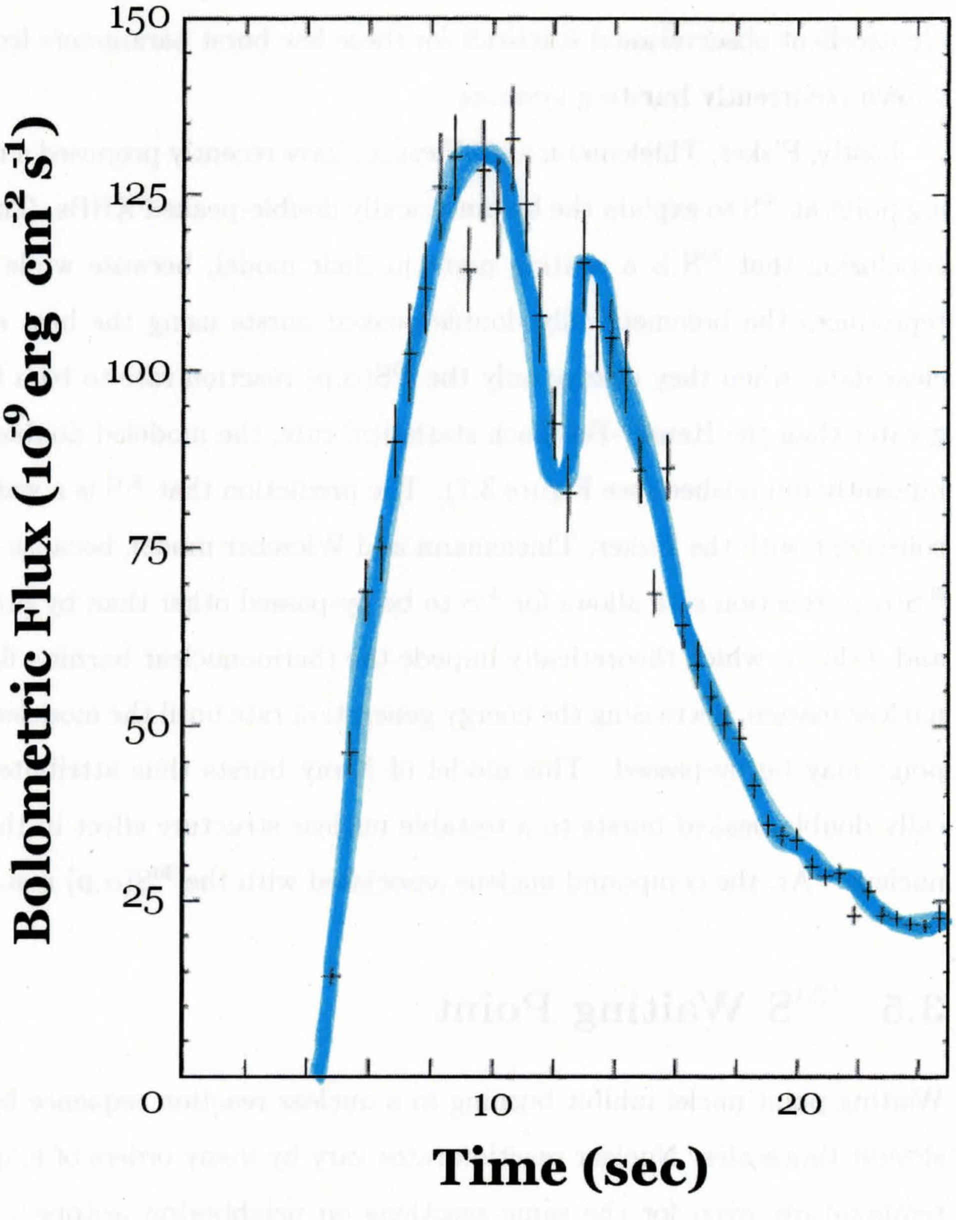

Figure 3.6: Extracted bolometric luminosity from the X-ray burster 4U 1608–52 [PEN89] as a function of burst time in seconds, where the blue line is strictly a visual guide and not a fit to the data. Notice the sharp rise time on the order of seconds, and the 25% decrease in luminosity mid-burst. Compare to Figure 3.4

consistent burst rise times for both peaks [FUJ88]. It is critical for burst models to precisely reproduce observed burst profiles, because although observation of XRBs is limited to the burst rise/decay times, peak wavelength and burst fluence, there are excellent observational statistics for these few burst parameters from the ~100 known recurrently bursting systems.

Lastly, Fisker, Thielemann and Wiescher have recently proposed a nuclear waiting point at ^{30}S to explain the bolometrically double-peaked XRBs. They reach the conclusion that ^{30}S is a waiting point in their model, because while their model reproduces the bolometrically double-peaked bursts using the best available nuclear data, when they change only the ^{30}S(α,p) reaction rate to be a factor of 100 greater than the Hauser-Feshbach statistical rate, the modeled double-peak is significantly diminished (see Figure 3.7). The prediction that ^{30}S is a waiting point is consistent with the Fisker, Thielemann and Wiescher model, because an increased ^{30}S(α,p) reaction rate allows for ^{30}S to be by-passed other than by proton capture and β-decay, which theoretically impede the thermonuclear burning flow to higher nuclear masses, decreasing the energy generation rate until the modeled ^{30}S waiting point may be by-passed. This model of X-ray bursts thus attributes bolometrically double-peaked bursts to a testable nuclear structure effect in the compound nucleus ^{34}Ar, the compound nucleus associated with the ^{30}S(α,p) reaction [FIS04].

3.5 ^{30}S Waiting Point

Waiting point nuclei inhibit burning in a nuclear reaction sequence by having the slowest timescales. Nuclear reaction rates vary by many orders of magnitude with temperature, even for the same reactions on neighboring isotopes, isobars, and isotones on the chart of nuclides. Variation in reaction rates ensures that some reaction channels will be accelerated or retarded compared to the average rate in a given burning pathway. However, the average rate is not important when the process is limited by one or more key reactions that may be many orders of magnitude lower. Indeed, one may essentially regard all but the limiting reactions involving waiting point nuclei as instantaneous.

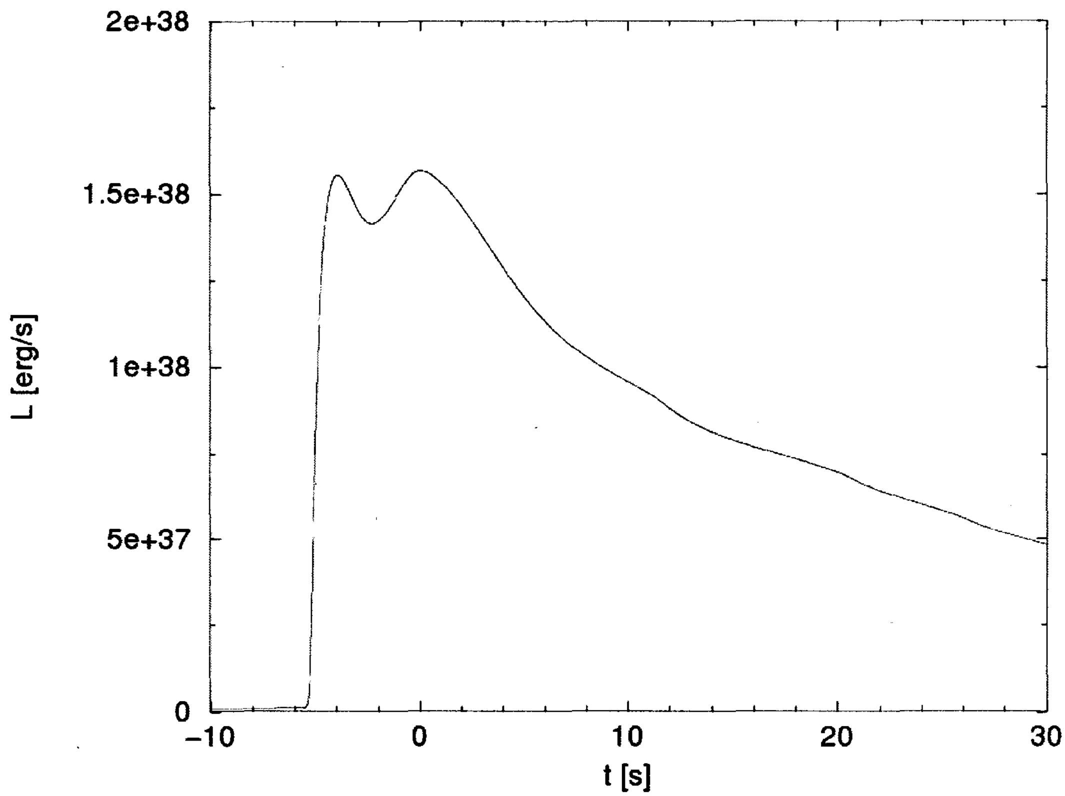

Figure 3.7: The figure shows a model X-ray burst of bolometric luminosity versus time in seconds [THI05]. The model [FIS04] assumes a pure helium shell flash and relatively low accretion rate (see the text). Compared to Figure 3.6, the peak heights are not realistic, but the rise and decay times reproduce observed quantities.

As pointed out in Section 3.4.2, there are many proposed waiting point nuclei involved in the *rp* and αp processes. These waiting points must be inferred from simulations of thermonuclear outbursts, because experimental nuclear data concerning short-lived, proton-rich nuclei are often not available. Furthermore, explosions powering X-ray bursts are generated by a large grouping of hydrogen and helium rich thermonuclear burning pathways, and the exact path in any given case (thus the important waiting points) are heavily dependent on physical conditions. As the temperature and density vary during a given X-ray burst, the relevant waiting point nuclei evolve as a function of burst time.

A ^{30}S waiting point was proposed in pure He shell flash X-ray bursts with low accretion rates ($\dot{M} \sim 8\ x\ 10^{-10}\ M_{\odot}\ yr^{-1}$) in LMXBs [FIS04], so this section will neglect the waiting points relevant to steady *rp* burning in X-ray pulsars at higher accretion rates. In the lower accretion rate He flash scenario, the nucleosynthetic path is typically truncated at $A \sim 64$ [WOO04, FIS08a], meaning the waiting point nuclei above germanium are not germane. The importance of $T_z = -1$ nuclei (^{14}O, ^{18}Ne, ^{22}Mg, ^{26}Si, ^{30}S, ^{34}Ar, ^{38}Ca, ...) as waiting points for β^+-decay is well-established in the *rp* process [VAN94]. Indeed, these nuclei comprise the target nuclei in the (α,p) part of the αp process [WAL81]. Helium shell flash X-ray burst rise times are typically on the order of one second, and the $T_z = -1$ nuclei all have half-lives longer than one second (except ^{34}Ar, $t_{1/2} = 844.5$ ms). The energy released by proton capture Q_p on these nuclei are all less than 1 MeV ($Q_p < 0$ for ^{14}O and ^{18}Ne), and so these nuclei are difficult to by-pass via (p,γ) reactions due to photodisintegration. From a nuclear structure perspective, the nucleon added by a (p,γ) reaction on a $T_z = -1$ target is unpaired, and so it[3] is not tightly bound and may easily be knocked out by relatively low energy γ-rays.

In both He and H/He shell flashes, after break-out from the HCNO cycles, the *rp* process competes with the αp process (see Section 3.4.2). The high temperature and hydrogen abundance ensure that the burning pathway is shifted towards the proton drip line. Nuclear physics intuition suggests that at higher temperatures, more burning flow ought happen to charged-particle reactions, such as proton capture, but in extremely hot environments, this is not true due to the effects of photodisintegration. Particularly at $T \sim 10^9$ K, the increased temperature decreases the (p,γ)/(γ,p) ratio because there are more energetic photons to disassociate nuclei, inhibiting burning and resulting in higher (p,γ)/(γ,p) ratios at $T \sim 10^8$ K, and thus a decreased nuclear flow through proton capture reactions at 10^9 K compared to 10^8 K [THI94].

[3] Of course, there is no distinction between any of the identical protons in a nucleus, so any one of the protons may be knocked out.

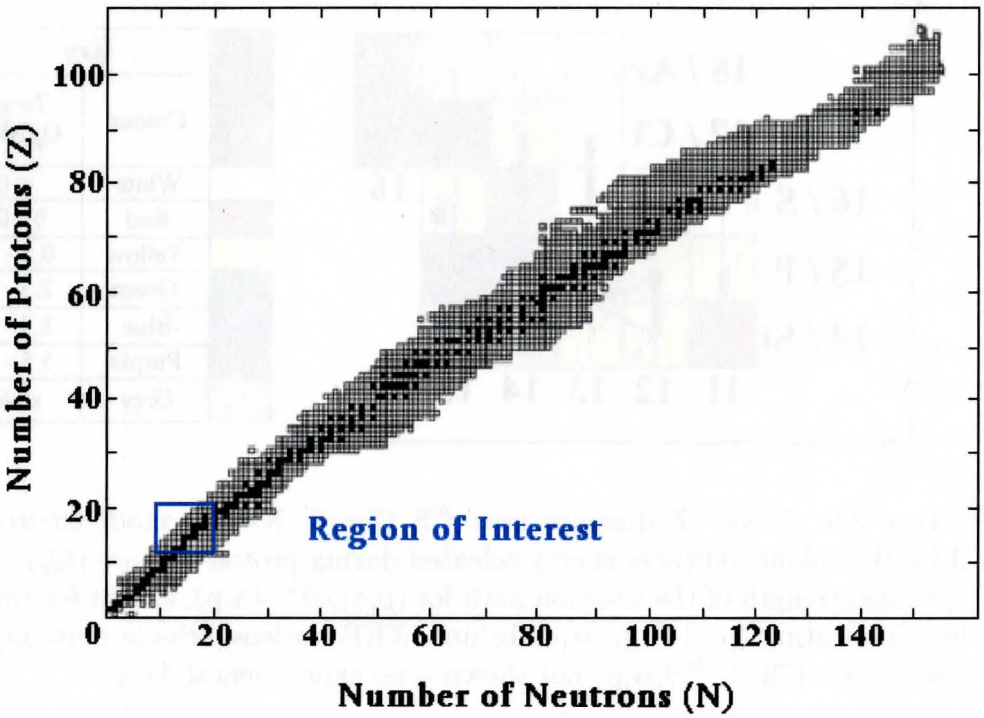

Figure 3.8: Number of neutrons is plotted on the abscissa against the number of protons on the ordinate, comprising a standard chart of nuclides or N vs. Z diagram. The region near ^{30}S is highlighted, to contextualize Figure 3.9.

For $A < 56$, one model with accreted material of solar composition [AND89] indicates ^{24}Si and ^{30}S as the only waiting point nuclei in the *rp* and αp processes (see Figure 3.3) [ILI99], although this model does not follow the compositional inertia of multiple bursts. In a study on stable burning in X-ray pulsars, ^{30}S(α,p) is identified as one of roughly fifteen of the most important nuclear input parameters below ^{56}Ni [SCH99]. Recent work has reviewed the temperature-density versus time profiles of three models [SCH01a, KOI04, FIS08a], showing that for models with metallicity roughly ten times the solar value ($Z_{CNO} \sim 0.20$), both the β^+ decay of ^{30}S and the ^{30}S(α,p) reaction are important [PAR08]. ^{30}S(α,p) is identified as one of the twenty-eight (nine are below ^{56}Ni) of the most influential nuclear processes, and one of seventeen (eight are below ^{56}Ni) nuclear processes affecting the energy generation by more than 5% [PAR08].

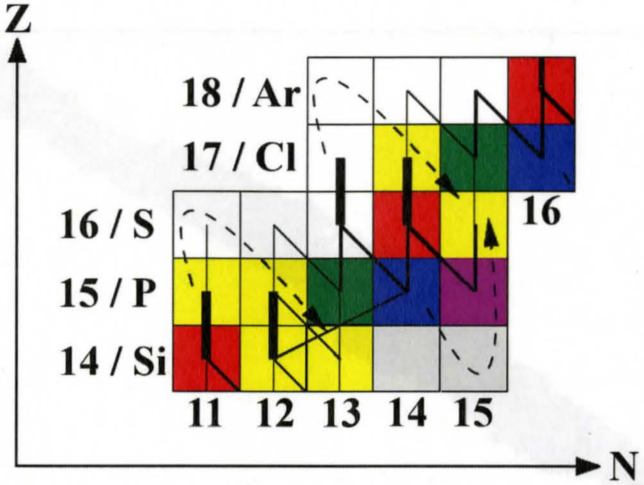

Key	
Colour	Target Q_p(MeV)
White	< 0
Red	0 - 0.5
Yellow	0.5 - 2.5
Green	2.5 - 3.5
Blue	3.5 - 5.0
Purple	5.5 - 8.0
Grey	stable

Figure 3.9: N vs. Z diagram near ^{30}S (Z=16, N=14), modified from original [FIS04]. Colour indicates energy released during proton-capture (Q_p). Black lines indicate strength of the reaction path for (p,γ), β^+, (α,p), except for thick vertical lines indicating (p,γ)-(γ,p) equilibrium. XRB nucleosynthesis must pass through ^{30}S($t_{1/2}$=1.178 s). ^{30}S(α,p) not shown – no experimental data.

The $T_z = -1$ nuclei between ^{22}Mg and ^{34}Ar were specifically studied as possible waiting point nuclei responsible for bolometrically double-peaked X-ray bursts, for the above-mentioned nuclear structure reasons, and because the flow must pass through these nuclei (see Figures 3.8 and 3.9) [FIS04]. Due to the slower rise time of combined H/He shell flashes [AYA82, HAN84], such a double-peak is not observationally separable, and so the model considers pure He flash ignition. Fisker, Thielemann and Wiescher's model also assumes solar composition [AND89, FIS04], and so one notices that ^{30}S is perhaps most relevant to X-ray bursts in systems accreting material of high metallicity. ^{26}Si is dismissed as a possible waiting point, because $Q_p = 859$ keV, and so it is not photodisintegrated to such an extent that material flow is prohibited from the burning path ^{26}Si(p,γ)^{27}P($e^+\nu_e$)^{27}Si [FIS04]. By plotting in a temperature versus density plot (see Figure 3.10) the condition

$$\lambda_{\beta+} = N_A \rho Y_\alpha \Delta(T) \langle \sigma \nu \rangle_{(\alpha,p)}, \tag{3.6}$$

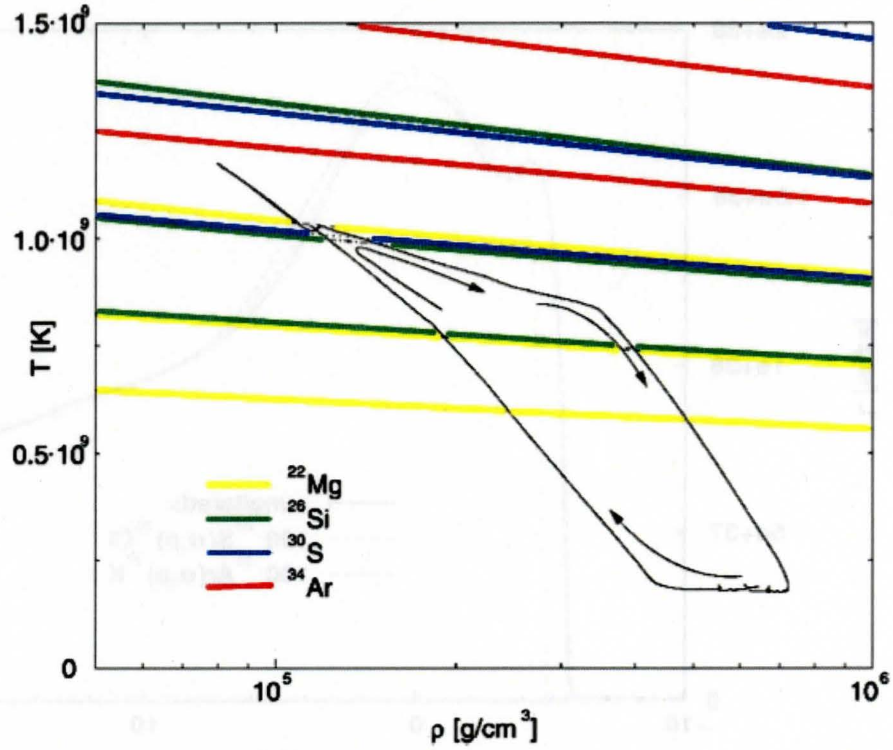

Figure 3.10: Plot of $\lambda_{\beta^+} = N_A \rho Y_\alpha \Delta(T) \langle\sigma\nu\rangle_{(\alpha,p)}$, in a temperature versus density plot [FIS04]. Each potential waiting point (α,p) reaction is plotted three times (except for ^{34}Ar(α,p) for Δ(T)=100, which falls outside the plot), for the cases where Δ(T)$= -100, 1, 100$. The temperature and density pathway in an X-ray burst is shown. We can see that increasing ^{30}S(α,p) by a factor of 100 is the only rate variation that results in significant change in X-ray burst conditions.

where the β^+ lifetime λ_{β^+} is equal to Avogadro's number N_A multiplied by the density ρ, the helium abundance Y_α, a constant uncertainty function $\Delta(T)$, and the (α,p) reaction rate per particle pair $\langle\sigma\nu\rangle_{(\alpha,p)}$ (the timescale for (α,p) reactions to occur), it is shown by Fisker, Thielemann and Wiescher that ^{22}Mg is an unlikely waiting point in the model [FIS04]. They then computed luminosity curves (see Figure 3.11) assuming the ^{30}S(α,p) and ^{34}Ar(α,p) Hauser-Feshbach reaction rates are underestimated by a factor of 100 (i.e. $\Delta(T) = 100$), indicating that if the ^{30}S(α,p) reaction were faster, the double-peak is significantly diminished [FIS04].

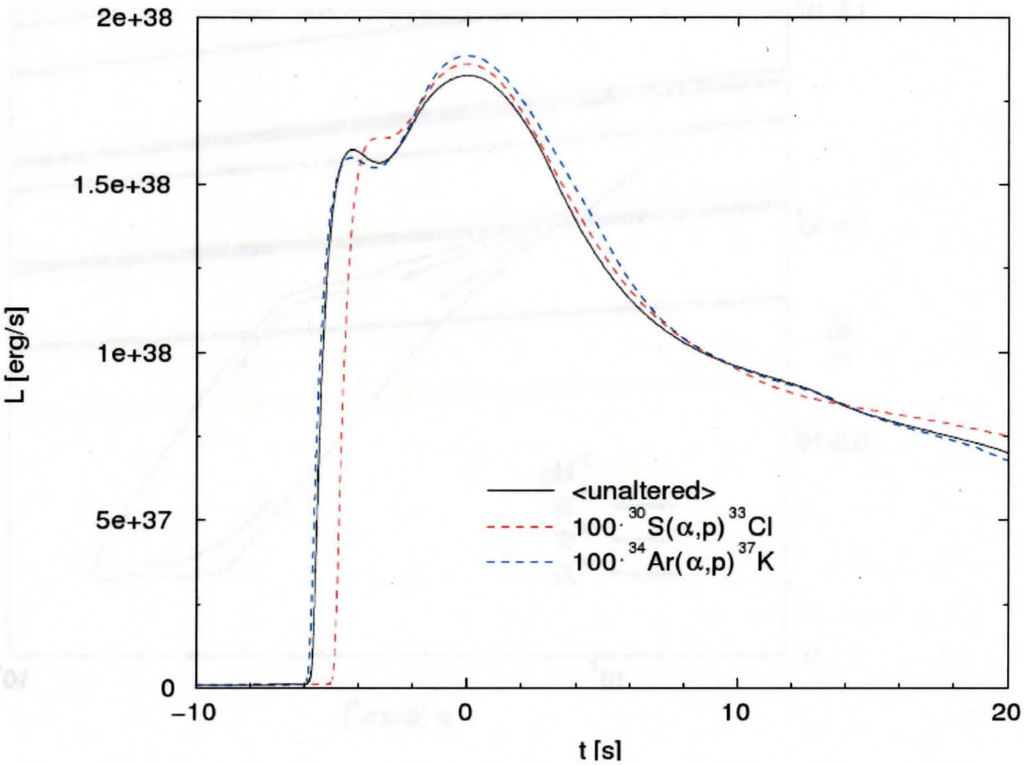

Figure 3.11: Similar to Figure 3.7, where the figure shows a model X-ray burst of bolometric luminosity versus time in seconds [FIS04]. Two plots are superimposed, for when ^{30}S(α,p) or ^{34}Ar(α,p) are increased by a factor of 100 from the Hauser-Feshbach rate.

3.6 ^{30}S(α,p) Reaction

As discussed, models of X-ray bursts, particularly for high accretion metallicity, indicate the ^{30}S(α,p) reaction is important to the thermonuclear energy generation. However, the ^{30}S(α,p) cross section has never been experimentally measured. One can often use indirect experimental techniques to infer if resonances exist in the compound nucleus at energies appropriate to astrophysical environments of interest. The ^{30}S(α,p) reaction proceeds via the ^{34}Ar compound nucleus, and very little information exists above the α threshold, with no known levels at X-ray burst energies (see Figure 3.12) [END90, END98]. It is important to know if there are strong α resonances in ^{34}Ar, because in this case the Hauser-Feshbach statistical

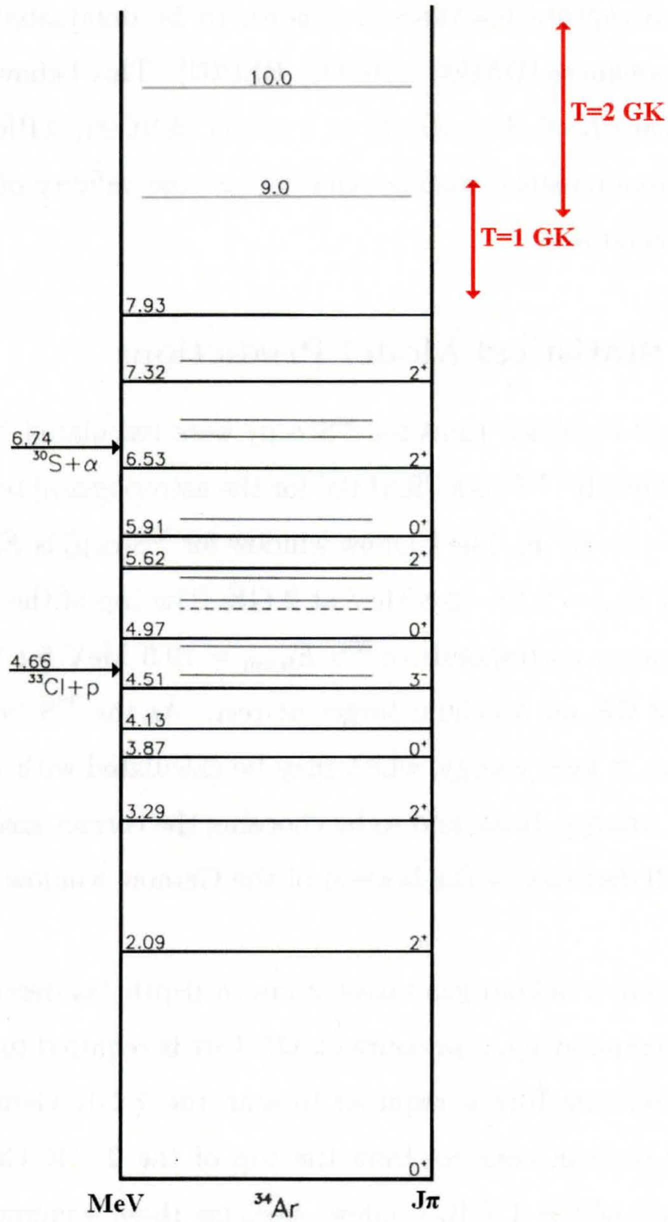

Figure 3.12: Level scheme of ^{34}Ar, the compound nucleus for the ^{30}S(α,p) reaction, modified from original [END90]. The α and proton thresholds are shown on the left in black, and the important astrophysical energies in the Gamow window are shown on the right in red. Notice how there are no known levels in the Gamow windows.

model will not give reliable reaction rate predictions. In $T_z = 1, -1$ nuclei with $A = 18$, α-capture reactions are shown to be dominated by natural parity[4] α-cluster resonances [DAB03, GRO02, BER03]. This behaviour is also observed in higher mass ($22 \leq A \leq 30$) $T_z = 1$ nuclei [ANG99, APR05], motivating experimental measurements, such as ours, to test the validity of Hauser-Feshbach rates for (α,p) reactions.

3.6.1 Statistical Model Predictions

The Hauser-Feshbach rates for ^{30}S(α,p) were calculated by the author using the NON-SMOKER^{WEB} code [RAU08] for the astrophysical temperatures $T = 1 \times 10^9$ K and $T = 2 \times 10^9$ K. The Gamow window for ^{30}S(α,p) is $E_{cm} = 1.41 - 2.34$ MeV at 1 GK and $E_{cm} = 2.15 - 3.8$ MeV at 2 GK. The top of the Gamow window centre-of-mass energy corresponds to ^{30}S $E_{beam} = 19.9$ MeV for 1 GK and $E_{beam} = 32.3$ MeV for 2 GK on a helium target at rest. As the ^{30}S beam passes through the helium gas, it loses energy, which may be calculated with the FORTRAN package `code_for_energy_loss`, and so by choosing the correct gas cell pressure, the beam energy will decrease to the bottom of the Gamow window after traversing the gas target.

Assuming a helium gas target 3 cm in depth (as described in Section 5.5) at ambient temperature, a pressure of 425 Torr is required to scan the 1 GK Gamow window and 760 Torr is required to scan the 2 GK Gamow window (1100 Torr is needed to scan energies from the top of the 2 GK Gamow window down to the bottom of the 1 GK window, because these windows overlap). Measuring a reaction cross section by this method is called the thick target technique (as opposed to a thin target technique where instead the beam energy is varied). By assuming a ^{30}S beam intensity of 1 $\times 10^5$ particles per second (pps) and the above ^{30}S beam and ^{4}He gas target parameters, the NON-SMOKER^{WEB} code predicts

[4] Natural parity is when the partiy has value $(-1)^J$, and unnatural parity a value $(-1)^{J+1}$. For example, 2^+ is natural parity and 3^+ is unnatural.

the yields tabulated in Table 3.1 for 1 GK and in Table 3.2 for 2 GK. Although the relevant X-ray burst temperatures are $T = 0.4 - 1.3$ GK, the Hauser-Feshbach model predicts merely 1 reaction per week of beam time for the 1 GK window under the assumed conditions, but 4.2×10^3 reactions in 11 days of beam time (the approved beam time for the ^{4}He(^{30}S,p) experiment) for the 2 GK window under the assumed conditions; because the statistical ^{30}S(α,p) reaction rate decreases exponentially with temperature, we do not consider experimentally measuring the cross section down to 0.4 GK at this time. One would then measure the ^{4}He(^{30}S,p) cross section from the top of the 2 GK Gamow window down to the bottom of the 1 GK Gamow window; if no data are observed at lower energies, the experimental cross section would need to be extrapolated to lower energies to the the X-ray burst ^{30}S(α,p) reaction rate. The successful ^{30}S(α,p) cross section measurement experiment should thus have a ^{30}S beam intensity $\geq 1 \times 10^5$ and a beam energy on target of $E = 32.3$ MeV — here *beam energy on target* refers to the beam energy as it begins to interact with helium nuclei, not the beam energy incident on the target entrance window.

3.7 Conclusion

There are many uncertainties in X-ray burst models. For the Fisker, Thielemann and Wiescher model, limitations of spherical symmetry due to the possibility of spatially localized burning and flame front propagation, inferred accretion rates and metallicity, the hydrodynamics determining the appropriate temperature and density, and (α,p) reactions are the main sources of uncertainty [FIS04, THI07]. As a result, these models should be experimentally and observationally constrained

[5] The barn is a measurement of area equal to 10^{-28} m^2 and corresponds approximately to the neutron-induced fission cross section of ^{235}U for medium energy neutrons (like those ejected in fission). In the Manhattan Project, this cross section was observed to be like 'hitting the broad side of a barn' compared to other reaction cross sections, which are much smaller. The unit was originally used as part of the Manhattan Project's colloquial code language, but is now widely used in nuclear physics.

E_{cm} (MeV)	$\sigma_{\alpha,p}$ (barns) [5]	Δx (mm)	yield (Hz)	yield (per day)	yield (per month)
2.3	1.54×10^{-6}	4.3	9.26×10^{-7}	8.00×10^{-2}	2.40
2.2	6.77×10^{-7}	3.1	2.94×10^{-7}	2.54×10^{-2}	7.63×10^{-1}
2.1	2.93×10^{-7}	3.1	1.27×10^{-7}	1.10×10^{-2}	3.29×10^{-1}
2.01	1.24×10^{-7}	2.8	4.86×10^{-8}	4.20×10^{-3}	1.26×10^{-1}
1.92	5.13×10^{-8}	2.8	2.01×10^{-8}	1.74×10^{-3}	5.22×10^{-2}
1.83	2.09×10^{-8}	2.7	7.89×10^{-9}	6.82×10^{-4}	2.04×10^{-2}
1.75	8.31×10^{-9}	2.6	3.03×10^{-9}	2.61×10^{-4}	7.84×10^{-3}
1.67	3.24×10^{-9}	2.4	1.09×10^{-9}	9.42×10^{-5}	2.83×10^{-3}
1.6	1.24×10^{-9}	2.3	4.00×10^{-10}	3.46×10^{-5}	1.04×10^{-3}
1.53	4.66×10^{-10}	2.4	1.57×10^{-10}	1.35×10^{-5}	4.06×10^{-4}
1.46	1.72×10^{-10}	1.5	3.61×10^{-11}	3.12×10^{-6}	9.36×10^{-5}
1.4	6.21×10^{-11}	0			
	Totals	30	1.43×10^{-6}	1.23×10^{-1}	3.70

Table 3.1: The table lists the yield predicted by the NON-SMOKER^{WEB} code for the ^{30}S(α,p) at T = 1 GK. The helium gas in the lab is assumed to be at T = 293 K and ρ = 9.31 $\times$ 10^{-5} g/cm^3, and the ^{30}S beam is assumed to be at an intensity of 1 $\times 10^5$ pps. The NON-SMOKER^{WEB} code gives discretized energies, and the ^{30}S beam loses energy as it traverses the helium gas, altering the cross section. The beam energy loss is calculated for each discretized energy with `code_for_energy_loss`, giving a distance the beam travels during each segment of energy loss. The isotropic yield is listed for each discretized energy by assuming the cross section is constant over each energy segment, resulting in an overestimate in the yield. The yield is listed three times for different time periods. Under 4 reactions are predicted to occur per month of beam time under these conditions, to say nothing about the experimental setup's detection capability.

whenever possible. The interpretation of ^{30}S as a waiting point impedance resulting in bolometrically double-peaked X-ray bursts is only consistent with Fisker, Thielemann and Wiescher's model for ^{30}S(α,p) reaction rates significantly less than two orders of magnitude greater than the Hauser-Feshbach rate, because in such a case, the double-peak is not well reproduced by the model. Experimentalists may test the prediction of the ^{30}S waiting point impedance model by performing a direct measurement of the ^{4}He(^{30}S,p) cross section at X-ray burst energies, and compare the astrophysical reaction rate extracted from experimental data to

E_{cm} (MeV)	$\sigma_{\alpha,p}$ (barns)	Δx (mm)	yield (Hz)	yield (per day)	yield (per month)
3.88	3.11×10^{-3}	2	1.56×10^{-3}	1.35×10^{2}	4.04×10^{3}
3.7	1.74×10^{-3}	3.4	1.48×10^{-3}	1.28×10^{2}	3.84×10^{3}
3.52	9.51×10^{-4}	2.9	6.91×10^{-4}	5.97×10^{1}	1.79×10^{3}
3.36	5.08×10^{-4}	2.9	3.69×10^{-4}	3.19×10^{1}	9.56×10^{2}
3.2	2.65×10^{-4}	2.5	1.66×10^{-4}	1.43×10^{1}	4.30×10^{2}
3.06	1.35×10^{-4}	2.7	9.15×10^{-5}	7.91	2.37×10^{2}
2.91	6.76×10^{-5}	2.3	3.90×10^{-5}	3.37	1.01×10^{2}
2.78	3.31×10^{-5}	2.3	1.91×10^{-5}	1.65	4.94×10^{1}
2.65	1.59×10^{-5}	2.1	8.34×10^{-6}	7.21×10^{-1}	2.16×10^{1}
2.53	7.43×10^{-6}	2.2	4.10×10^{-6}	3.54×10^{-1}	1.06×10^{1}
2.41	3.42×10^{-6}	1.9	1.63×10^{-6}	1.40×10^{-1}	4.21
2.3	1.54×10^{-6}	1.8	6.93×10^{-7}	5.99×10^{-2}	1.80
2.2	6.77×10^{-7}	1	1.70×10^{-7}	1.47×10^{-2}	4.40×10^{-1}
2.1	2.93×10^{-7}				
	Totals	30	4.43×10^{-3}	3.83×10^{2}	1.15×10^{4}

Table 3.2: The table lists the yield predicted by the NON-SMOKER^{WEB} code for the ^{30}S(α,p) at T = 2 GK. The helium gas in the is lab assumed to be at T = 293 K and ρ = 1.66 × 10^{-4} g/cm^3, and the ^{30}S beam is assumed to be at an intensity of 1 ×10^5 pps. The NON-SMOKER^{WEB} code gives discretized energies, and the ^{30}S beam loses energy as it traverses the helium gas, altering the cross section. The beam energy loss is calculated for each discretized energy with `code_for_energy_loss`, giving a distance the beam travels during each segment of energy loss. The isotropic yield is listed for each discretized energy by assuming the cross section is constant over each energy segment, resulting in an overestimate in the yield. The yield is listed three times for different time periods. 383 reactions are predicted to occur per day of beam time under these conditions, but the detector solid angle must be taken into account to determine how many protons can be anticipated.

the Hauser-Feshbach statistical reaction rate. However, in order to conduct such a measurement, one prerequisite is a radioactive ion beam of ^{30}S of high intensity and purity. The next chapter deals with the subject of radioactive ion beam production.

Chapter 4

Radioactive Ion Beam Development

4.1 Radioactive Ion Beam Techniques

If one wishes to do nuclear physics experiments involving short-lived nuclei, one is forced to use the radioactive species as the beam ion. "Short-lived" here is strictly relative, but will include anything with a half-life on the order of days or less; indeed, longer-lived radioactive ions have been implanted in solid material and used successfully as targets. Thus the limiting nuclear target lifetime is constrained by experimental setup, experiment duration, and the delay-time between implantation and experiment (minimized with the student running as fast as possible (SRAFAP) method). Longer-lived radioactive nuclei may also be made into radioactive ion beams (RIBs or RI beams) in a manner identical to stable beams (described below). The present research focuses on reactions involving ^{30}S, with the property $t_{\frac{1}{2}} = 1.178\,s$ — a half-life undoubtedly prohibitive to implantation for use as a target or direct acceleration by conventional means. As such, this chapter is dedicated to the properties of RIBs and the required physics, with an emphasis on application to developing a low-energy RIB of ^{30}S.

At present, four techniques exist for the production of intensity $> 10^3$ particles per second (pps) RIBs of short-lived nuclei: isotope separation online (ISOL), induced fission, fragmentation, and in-flight separation. In subsequent discussions of RIB production, *primary beam* refers to the stable beam striking a production target to make the RIB, or *secondary beam.* (Discussion of RIB techniques involving induced fission are omitted here, as this method is only applicable to the production of medium to heavy mass ($70 \lesssim$ A $\lesssim 170$), neutron-rich nuclei centered around $A = 95, 140$ and becoming broader with increasing E_{cm} [LET99].)

4.1.1 ISOL Technique

The ISOL method of RIB production uses ordinary laboratory kinematics, impinging a beam of light nuclei (p, n, or α) of high energy (≈ 0.5 GeV/u) on a heavy target and creating radionuclides by spallation. However, ISOL is set apart from the other methods by employing chemical methods to isolate the nuclear species of interest. Because ISOL requires detailed knowledge of real-time, *in situ*, hot, nuclear chemistry, it is considered to be somewhat a 'black art' (i.e., sorcery) even by experts in the field; this section will omit all but the most basic information regarding the inputs and outputs of ISOL.

An ISOL production target must have at least as many protons and neutrons as the desired secondary beam, but this restriction is the only hard rule in choice of an ISOL target element. By use of a light beam on a heavy target, reaction products are nearly distributed isotropically in the laboratory system, leading to a number of important consequences. Most importantly, the reaction products come into thermodynamic equilibrium within the target, allowing one to use chemical separation techniques. In order to successfully extract isotopes of interest, these particles ought to have significant kinetic energy to escape the target, requiring the target to be quite hot. While ISOL targets are externally heated, it is a convenience that ISOL targets are required to be high temperature ($> 10^3 K$) as all the primary beam energy is also deposited in the target material. Thus, a successful ISOL target material should have a high heat capacity. The target chemical compound clearly affects the isotope separation chemistry and therefore much care and testing are required in target choice.

Because the primary beam comes to rest within the ISOL production target, the resulting RIB must be reaccelerated for experimental purposes involving direct nuclear reaction measurements. It is straightforward to reaccelerate ISOL beams, once the ions are extracted and ionized, and so ISOL is a good tool for astrophysical application. However, up to the isotope production and extraction limits, there is a correlation of RIB intensity with half-life. Chemical separation is extremely slow compared to nuclear time-scales, and the radioactive nuclear species of interest must be extracted from the ISOL production target before it decays. For example, the CERN ISOLDE and TRIUMF ISAC facilities report maximum intensities of order 10^4 pps for ^{11}Li ($t_{\frac{1}{2}} = 8.5\,ms$), 10^8 pps for ^{8}Li ($t_{\frac{1}{2}} = 838\,ms$), and 10^{10} pps for ^{7}Li (stable) [DOM08, MIL01]. Species with $t_{\frac{1}{2}} \gtrsim 10\,s$ yield ISOL intensities comparable to those of stable nuclei. For this reason, one would expect ^{30}S intensities some two orders of magnitude lower than a stable (or long-lived) species of sulfur (A=32, 33, 34, 36). The ISOL method is advantageous because of the excellent beam characteristics, such as the beam spot-size and variable beam energy of good resolution.

However, chemical properties are likely the most influential factor in the successful production of a particular RIB via ISOL. For example, RIBs of many alkali metals, alkaline earth metals, halogens, and poor metals have been successfully produced at a number of ISOL facilities [DOM08, MIL01, HRIBF07]. Unfortunately, only ISOLDE reports production of any sulfur (chemically nonmetal) isotope, and then only the neutron-rich isotope ^{38}S ($t_{\frac{1}{2}} = 170.3\,m$) at slightly below 10^4 pps [MIL01]. Thus, the ISOL technique is excluded from consideration by use of this or any other project desiring an RIB of proton-rich sulfur at the time of writing.

4.1.2 In-flight Separation

4.1.2.1 Beam Fragmentation Technique

Fragmentation is performed in inverse laboratory kinematics, where a stable primary beam of heavy ions is impinged on a light target at high energy ($>$ 100 MeV/u), resulting in the break-up of the beam ions into lighter species; many of these fragments are radioactive, and ions of interest are separated from other fragments with electrostatic beam-line components (electric and/or magnetic dipoles). The fragmentation process is not easily described by the physics of nuclear reactions and is better understood in terms of the abrasion-ablation model [BEN98]. Thus, fragmentation necessarily requires a high primary beam energy, or the interaction between the beam and target will follow the canon of nuclear reaction physics *a la* in-flight separation (see below).

A fragmentation target ought to have: low Z, high density, and low chemical volatility. Low nuclear charge is required or else Coulomb repulsion will begin to inhibit beam-target interaction. High target densities, such as those found in any non-gaseous substance, are preferred in order to maximize interaction probability. Thus, beryllium and aluminium are frequently employed as targets for nuclear beam fragmentation. One may vary the target thickness to alter the amount and type of specific nuclear fragments produced.

Fragments have a net forward momentum in the laboratory system, by merit of using a heavy primary beam, resulting in high fragment collection efficiencies. The primary beam species chosen is typically the lightest feasible stable beam containing as many protons and neutrons as the fragment of interest. Unfortunately, by requiring high primary beam energies, conservation of energy and linear momentum require the fragmentation technique to produce only high energy secondary beams that are unsuitable for direct astrophysical application. Facilities using fragmentation, such as the National Superconducting Cyclotron Laboratory (NSCL) of Michigan State University, are presently considering upgrades involving gas-stopping targets coupled with low energy linear accelerators to circumvent this disadvantage; however, at the time of writing, no such nuclear facility is available for experimentation. Beam fragmentation is useful for many types of nuclear experiments, because many nuclear species may be produced this way, particularly very short-lived nuclei for mass measurements and decay studies that do not require high intensities, or longer-lived nuclei of high energy (>100 MeV/u) and high intensity (up to $106-8$ pps) which are used to probe nuclear structure far from stability. But until fragmentation facilities are upgraded, the fragmentation technique is excluded from consideration for use by this or any other project desiring a low energy RIB.

4.1.2.2 Low Energy In-flight Separation Technique

The in-flight RIB production method may be used for with lower energy (1 MeV/u $< E_{beam} <$ 10 MeV/u) primary beams. Just as for beam fragmentation, the low energy in-flight technique is performed in inverse laboratory kinematics, where a beam of heavy ions is impinged on a light target; as noted above, inverse kinematics are used for increased efficiency in collecting reaction products, which are then separated by electrostatic beam-line components. In this energy regime, the RIB production mechanism is best described by canonical nuclear reaction physics. Thus, the primary beam and production target nuclear species are chosen with a particular production reaction in mind to create the RIB of interest. The RIBs have a maximum intensity comparable to fragmentation of around 10^7 pps and but much lower energy (at maximum ~100 MeV. Many beams lighter than species of Z=13 have been successfully produced, such as (but not limited to) ^{7}Be, ^{11}C, ^{14}O, ^{21}Na, ^{22}Mg, and ^{25}Al. Since the in-flight technique typically relies on direct reaction physics, the targets are, with few exceptions, isotopes of hydrogen and helium. However, compound reactions may also be used, and in this case, targets up to $Z = 6$ may be employed; in principle one could use even heavier targets, but from Coulomb barrier considerations, the secondary beam yield drops dramatically as Z increases. The remaining discussion will focus on in-flight RIB production via direct nuclear reactions.

A H or He production target is typically gaseous by necessity, since the alternatives involve either extreme cooling or introduction of possible contaminants to make a solid chemical compound. Target gas must be prevented from dispersing into the accelerator beam-line, which is kept under high vacuum, most obviously accomplished by employment of solid target windows. One may fairly ask, "How can a thin foil window confine target gas from escaping into the beam-line vacuum system and yet allow a nuclear beam to pass through?" The answer is quite straight-forward. The nuclear beam is impeded by the gas target window and loses energy according to statistical formulæ governing charged particle radiative interaction with matter, which depends on the beam species's nuclear charge and energy, and the target material's nuclear charge and thickness; this energy loss is described by the Bragg curve (see Figure 4.1) after William Henry BRAGG (1903). However, the nuclear beam energy is many orders higher than the average kinetic energy of target gas particles, which abide by the Maxwell-Boltzmann statistics in the kinetic theory of gases. As such, the window foil imposes an energy barrier to any incident particles, which the beam particles overcome and the target gas particles do not surmount.

Under ideal circumstances, the best window is no window at all (except in real estate). Indeed, windowless gas targets are successfully used at many laboratories worldwide to study nuclear reactions. These systems use a complicated array of powerful vacuum pumps arranged in such a way as to collect the target gas before it may jeopardize the beam-line vacuum integrity. In this case, the target gas does not have a constant density throughout, due to sharp pressure gradients in the front and rear, making it difficult to control the exact target thickness. While windowless targets are quite suitable for low target thicknesses (corresponding to gas pressures of several tens of Torr), they may be problematic for gas at higher pressure (significant fractions of an atmosphere and above).

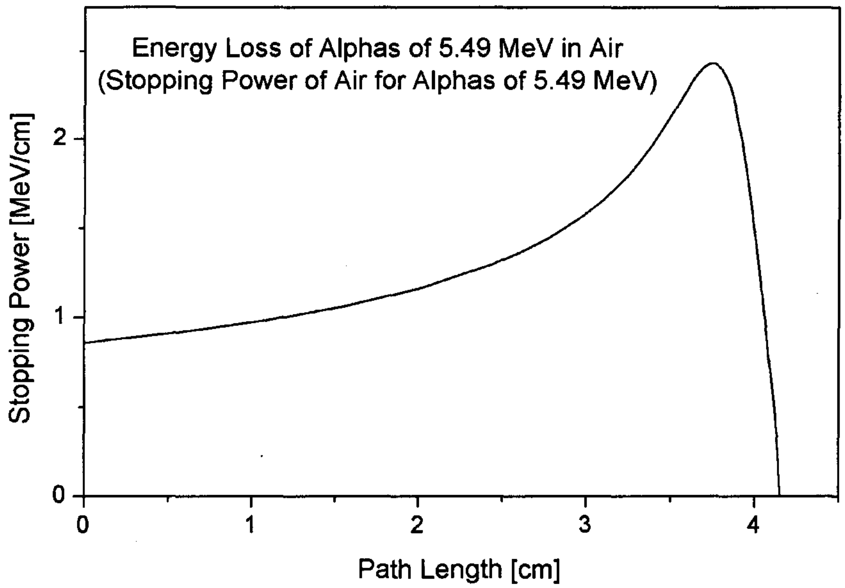

Figure 4.1: The plot shows α-particle penetration depth in air along the abscissa in centimetres against the stopping power of air in million electron volts per centimeter on the ordinate [WIK08c]. A pronounced peak in energy loss is observed, because radiative stopping power is a non-monotonic function of incident particle energy; that is, the charged-particle/material interaction cross-section increases dramatically at lower charged particle incident energies. The stopping power drop-off at high path length indicates the incident charged particle has come into thermal equilibrium with the target material (ie: the radiation is stopped).

Choosing the correct production target thickness is an optimization of RIB yield versus momentum dispersion. A thicker target will contain more target nuclei, thus increasing the probability of a single primary beam ion inducing a nuclear reaction within the target material. The reaction cross-section and detection efficiency of the planned RIB-induced reaction will set a lower limit for the on-target intensity, in order to collect sufficient experimental statistics. But a thicker target will also induce more energy straggling of reaction-products (and ultimately stop the beam all together), increasing the momentum spread between the highest and lowest energy ions of a particular species emerging from the production target. The beam-line components comprising the separator facility set an upper limit on $\frac{\Delta p}{p}$

for RIB cocktail separation and transmission. Our experimental results (detailed in Chapter 5) indicate that secondary beam-on-target yield is maximized by at least 400 Torr (at 80 K) gas pressure in the production target (but we never tested higher pressures). As a result, a windowless gas target will be too thin to achieve optimum on-target RIB intensity in virtually all imaginable cases.

The above account demonstrates that with present technology and available nuclear experimental facilities, the in-flight technique is the only suitable ^{30}S RIB production method via ^{28}Si(^{3}He,n) in inverse kinematics (see Production Mechanism below). With that in mind, it is appropriate to take a step back and consider the ion source and accelerator system providing the ^{28}Si primary beam.

4.2 Particle Accelerators

While nuclear scientists are no more a violent people than anyone else, we have found that the best way to study nuclei is to hurl them together at high speed, and hence the common aphorism that nuclear accelerators are "atom smashers" is not far from the truth (we prefer to smash nuclei). Although the topic of this thesis is nuclear astrophysics, a notoriously "low-energy" nuclear science, we may still employ particles at fractions ($\sim$10%) of the speed of light for experimentation. These particles are accelerated by subjection to high electric potentials. However, if left alone, atoms will acquire or release electrons to achieve neutrality (like Switzerland), and so they must be ionized (see Ion Sources below). With the exception of tandem accelerators, which require incident particles of negative charge (cations), most accelerators use positive ions (anions) by removing, or stripping, atomic electrons. It is difficult to make a cation with $q < -1$, since extra electrons (past the number to make the atom or molecule neutral) are weakly bound. However, as the nucleus has a positive charge Z (the number of protons), anions up to $q = Z$ can be made by stripping electrons. Ion charge qe is important to its acceleration, because the energy E gained by a charged particle crossing a given electric potential V is

$E = qeV$.

Nuclear accelerators can be broken into three general categories: electrostatic accelerators, linear accelerators (linac), and cyclotrons. It is important to remember that Gauss's law stipulates that there is no electric field inside a conductor, because accelerator systems often take advantage of this fact. For the project detailed herein, a monoenergetic ^{28}Si primary beam of $E \gtrsim 200\,MeV$ ($\sim 7\,MeV/u$) is required (see Chapter 5). The spread in primary beam energy may be neglected, due to the statistical energy straggling, which is much larger than ΔE_{beam}, of the primary beam in the RIB production target.

4.2.1 Electrostatic Accelerators

Van de Graaff, Cockcroft-Walton, and Dynimatron accelerators all locate a positive ion source on a platform and use some clever means to charge the terminal to a high negative voltage [RR88], thereby accelerating the particles through a single electrostatic potential. As the conducting terminal surrounds the ion source and controlling electronics, Gauss's law indicates that the terminal charge will not adversely affect the operation of these devices. However, this accelerating method involves two apparent disadvantages. For one, all controlling electronics must also be kept at high potential, because the platform must be electrically isolated to retain its charge; the control electronics are not readily accessible for operators to make changes or correct errors during operation. The need for electric isolation extends to the intervening accelerator beam-line, typically constructed from conducting material such as seamless stainless steel piping; however, this problem is surmounted by constructing that portion of the beam-line from a series of interlocked glass rings (although this compromises the quality of the maximum achievable vacuum). Secondly, the resistivity of air is finite, and spark discharging places an upper limit on the terminal voltage (and hence the accelerating potential). One may increase this limit by placing the high voltage terminal in a tank filled with high resistivity gas, such as sulfur hexafluoride (SF_6—dielectric constant roughly 2.5 times greater than air). Unfortunately, surrounding material will not eliminate the high voltage ceiling and further complicates access to the control systems and ion source, although SF_6 is still employed to this end.

A variant of the electrostatic accelerator is the tandem concept, which uses the terminal voltage twice (as the name suggests). A tandem accelerator works by instead using a positive high voltage, locating a negative ion source outside the platform (an added benefit for on-line maintenance) [RR88]. The cations are stripped of electrons with a foil (see Charge State Booster, chapter 5) located at the terminal (a misleading name in tandem accelerators). Because ion sources are limited to producing cations of charge -1, the emerging beam particles have energy $E = eV(1 + q)$, where q is the anion charge emerging from the terminal stripper foil. But for large q, $E \simeq qeV$, and not all chemical elements are readily made into cationic atoms or molecules. The Extended Stretched TransUranium (ESTU) tandem accelerator at the Wright Nuclear Structure Laboratory (WNSL) of Yale University reports beam acceleration through terminal voltage up to 22 MV [HYD88, SET07, WNSL08]. The Holifield RIB Facility (HRIBF) tandem reports terminal voltages up to 25 MV. Assuming the silicon beam may be stripped up to a 10+ charge state at the terminal with a carbon foil (see Section 6.7), corresponding to a maximum ^{28}Si beam energy $\sim$ 250 MeV ($\sim$ 9 MeV/u). Thus, a tandem accelerator could be used for this project, if the beam intensity may reach 10 pnA. There are also facilities coupling an electrostatic accelerator with another accelerator, such as the Argonne Tandem Linear Accelerator System (ATLAS), is not precluded in principle (although a proposal to study ^{33}Cl(p,α)^{30}S in inverse kinematics was turned down by the ATLAS Project Approval Committee (PAC) several years ago for concerns about the astrophysical modeling involved (see Chapter 2) [REH08]).

4.2.2 Linear Accelerators

A linear accelerator (linac) produces energetic nuclear beams by subjecting particles emerging from a positive ion source to a series of oscillating electric potentials along the beam-line [RR88], a method invented by Wideroe in 1928 [WID28]. The control system oscillates the electric field of each cavity with the goal that as a particle approaches a cavity, it sees a negative potential and is accelerated forward. Then, when that beam particle is within the conducting cavity, by Gauss's law the electric field is zero, and the cavity potential is switched to positive, so that by the time the beam particle emerges at the opposite end, it is repelled by the same cavity to which it was formerly attracted. This process is repeated all the way down the beam line, with the consequence that if the anions emerged from the ion source at a time-independent rate, at the end of the linac, the ions arrive in bunches with a frequency (f) equal to the radiofrequency (RF) of the oscillating electric potential. For convenience in nomenclature, this series of particle packets is still considered a nuclear beam. The final beam energy E for anions of charge qe in a linac with N oscillating cavities of electric potential V is thus $E = NqeV$ [RR88].

The clever reader will realize that with a constant rf source, the cavity length L must continue to double all the way down the linac, as the distance travelled by a beam particle depends on its increasing velocity v: $L = \frac{v}{2f}$ [RR88]. Early linacs experienced limitations of accelerator length and requisite construction material imposed by use of a constant rf source connected to all cavities. In particular, early linacs were only suitable for heavy ions, because the length of the tubes was impractical for the high speeds of light particles [LAW34]. Modern linacs employ appropriately controlled varying rf electric fields so that the cavity length is fixed and the electric field polarity is switched at the time when each particle packet is within an rf cavity, all the way down the accelerator line. While the maximum beam energy is still limited by the number of cavities (or available construction space), existing linacs provide the needed ^{28}Si primary beam energy. However, heavy ion linacs are often upgrades to existing electrostatic accelerator facilities, making it difficult to quote a specific ^{28}Si beam energy arising from a linac alone. The ATLAS facility reports ^{28}Si maximum $E_{beam} = 430\,MeV$ ($\sim 15.4\,MeV/u$) at 100 particle nA (pnA[1]) or $6\,MeV/u$ at >1000 pnA [ANL08].

4.2.3 Cyclotrons

Wideroe's use of time-dependent electric field cavities controlled by an rf source in his linac design inspired Lawrence to create a new type of accelerator in 1930, the cyclotron [LAW30]. Instead of allowing the particles to travel through a sequence of rectilinear electrode cavities, Lawrence had the idea to confine the particles in a cylindrical vacuum system with an axial magnetic field (see Figure 4.2). Thus, instead of using a long array of cavities, the cyclotron uses just two semi-circular electrodes, called D's or "dees" due to their shape. When a beam particle is inside either of the conducting electrodes, Gauss's law indicates that the particle will not be subjected to any external electric fields because in Lawrence's design, "the diametrical edges of the (dees) are crossed by a grid of wires" [LAW30]. Hence within either dee, an ion is just acted on by the axial magnetic field B, causing the particle to orbit in a circle of radius r depending on the ion's mass m, velocity v, and charge qe [RR88]:

$$\frac{mv^2}{r} = qevB \tag{4.1}$$

The frequency (f) of these circular orbits is just:

$$f = \frac{v}{2\pi r} = \frac{qeB}{2\pi m} \tag{4.2}$$

[1]Beam intensities are typically quoted as electric current, either in electric Amperes or particle Amperes. Since primary beam currents usually range from 10^{-9} to 10^{-6} Amperes, these units are typically quoted in the format enA, $p\mu A$, *et c.* A distinction is made between electric Amperes (standard units of current) and particle Amperes, because unlike ordinary electric current, where the charge carrier has $q = \pm 1$, beam particles may have charge up to $q = Z$; particle Amperes are generally preferred so that it is unnecessary to know the charge state of the beam. To convert to units of particles per second (pps), one must simply divide the beam current in pA by the elementary charge, e.

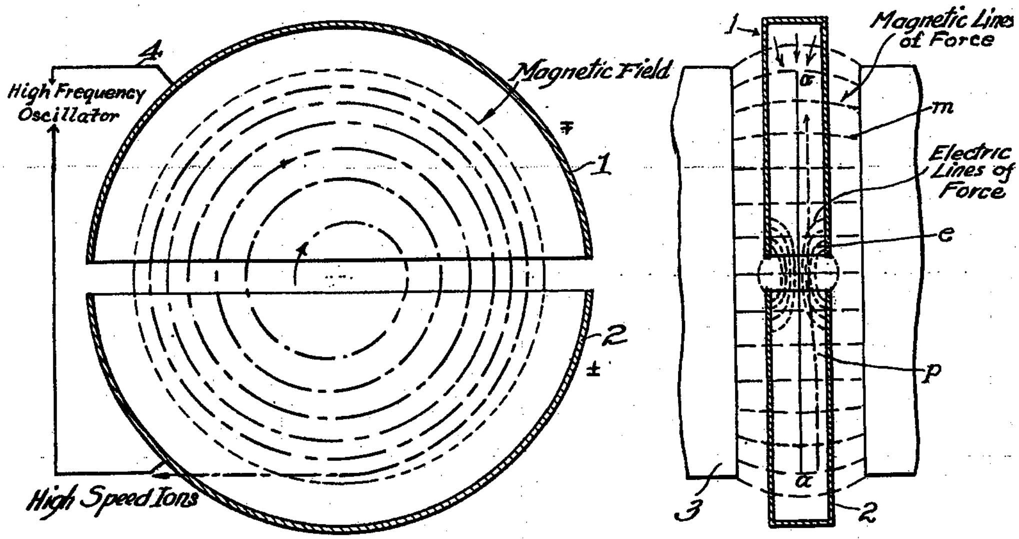

Figure 4.2: The image shows Lawrence's original drawing of the cyclotron concept, as submitted to the United States patent office in 1934 [LAW34, WIK08e]. The drawing on the left is a top-down schematic of the cyclotron, showing two 'D' shaped electrodes (**1** and **2**, respectively) connected by a **high frequency oscillator**, or rf source, (**4**) with opposite electric polarity ($\pm$). There is an axial **magnetic field** about α indicated in both drawings. The drawing on the right is a side view, where there are **electric lines of force** between the electrode gap between the two electrodes (**1** and **2** again). The area inside the electrodes (**3**) contains only magnetic field lines, and a particle of mass **m** will trace out an orbit of α perpendicular to the $\vec{B}$-field.

making the cyclotron a magnetic resonance accelerator [RR88]. Inspection of Equation (4.2) reveals that the resonance frequency f is independent of the ion velocity v or radius of orbit r (in the non-relativistic limit). The magnetic field strength B and the electric field controlling rf are synchronized such that the time it takes a beam particle to complete a half orbit is the same time the rf source oscillates the electric field polarity. Thus, when an ion cross the gap between the D's — the only time it experiences a force from the electric field emitted by the electrodes — it is repelled by the electrode it leaves and attracted to the electrode it enters. During each orbital cycle, a particle is accelerated across the gap twice, and the ion's increasing velocity causes it's orbital radius to increase as dictated by Equation (4.1). One may get the resultant energy E for a particle orbiting at final radius R

(limited by the size of the axial magnet) which crossed the electrode gap N times:

$$E = NqeV = \frac{(qeRB)^2}{2m} \tag{4.3}$$

Thus, the emerging energy depends on the square of the charge state. The RIKEN AVF cyclotron presently provides $^{28}Si^{9+}$ beams at 6.9 MeV/u at 1200 enA and $^{28}Si^{10+}$ beams at 7.54 MeV/u at 100 enA, although the 10+ beam is expected to reach intensities up to 300 enA (see Chapter 5). The particles are bunched into packets before being injected into the cyclotron, either by the ion source extractor, or by an rf buncher just prior to the cyclotron injector.

The cyclotron is quite a clever invention, because it allows one to accelerate both light and heavy ions to a high velocity with only the use of two low-potential electrodes in a confined space. Thus it avoids the spark discharging of electrostatic accelerators and the size limitations imposed by linac technology. Initially, ion energy output by a cyclotron was limited by relativistic effects which require that mass increase as the ion's velocity approaches the speed of light c. The true cyclotron resonance frequency f_r is related to the classical frequency f_c presented in Equation (4.2) by the ion's relativistic velocity ($\beta \equiv \frac{v}{c}$):

$$f_r = f_c\sqrt{1-\beta^2} \tag{4.4}$$

These relativistic problems were originally rectified by adapting the electrode oscillation rf to the particles' relativistic mass gain, this machine being called a synchrocyclotron. However, synchrocyclotrons had limiting beam intensities since they could only accelerate one packet of particles at a time. Contemporary laboratories employ cyclotrons with increasing magnetic field strength as a function of radius, known as azimuthally varying field (AVF), or isochronous, cyclotrons. The radial gradient in the $\vec{B}$-field has a de-focusing effect, which is corrected by grooves carved on the magnet faces, causing the field to vary azimuthally as well as radially (hence the name *AVF*).

With knowledge of the various means by which nuclei may be accelerated in the laboratory, it is appropriate to finally delve into the important subject of where the accelerated ions originate.

4.3 Ion Sources

While there are many methods of creating ions, such as dumping table salt (NaCl) into water (H_2O), since this thesis is concerned with nuclear reactions involving heavy anion beams (here heavy means $Z > 2$), the focus of this section will be the production of heavy ions to be injected into a particle accelerator. The above section indicates that the cyclotron is an excellent acceleration method for the presently described research, and because the ion energy emerging from a cyclotron goes as the square of the charge qe (see above), for cyclotrons it is particularly important that the ion source (IS) yield multiply charged anions for the production of high energy beams. However, as discussed in Chapter 3, it is also important for the IS to have high currents. The relatively late discussion of ISs within this thesis ought not detract from their importance to experimental nuclear physics; indeed, ISs are the bread and butter of any nuclear ion beam facility, and the available beam currents rely almost solely on the IS and subsequent transmission efficiency.

Ion sources may be grouped into two general categories: 1) vacuum electron beam sources and 2) plasma sources [APA75] (where we have neglected the production of cations, such as the sputter source). Electron beam sources include electron impact sources and arc-discharge sources, and this type may produce very high charge states at limited currents [APA75]. As the name suggests, an electron beam IS passes an electron beam through a gas to ionize the molecules, with a maximum ionization realized by employment of electron beams with energy three times higher than the atomic ionization energy of interest [RR88]. The types of plasma sources are more numerous, including duoplasmatron, rf, Penning, hollow-cathode [RR88], laser, and electron cyclotron resonance (ECR) sources [APA75]. Plasma sources historically produce only moderately high charge states, but at higher currents than the electron beam method [APA75]. Laser ion sources (LIS) are the youngest branch [LET99] but have still been known about for some time [TAM72]. Since the atomic excitation energies are unique for each element, resonant lasers may be used to remove electrons from the ion of choice [LET99], often performed in two or three steps [RAV92] to create a plasma. Many of these sources, however, are "not always satisfactory for the purpose of basic research" [ISH75], particularly when one wishes to have varied yet controlled beam parameters [ISH75], and so the focus will now shift specifically to the ECRIS.

4.3.1 ECR Ion Sources

ECRISs are now widely used for the production of heavy anion beams, to such an extent that we may avoid overly concerning ourselves with other methods. Such favouritism was not so true 20 years ago, but ECR technology improved dramatically during the intervening time; the widely-regarded text on nuclear astrophysics *Cauldrons in the Cosmos* by Rolf & Rodney, first published in 1988, details the mechanics of seven ion sources, none of which is of the ECR type [RR88]. The ECR effect in ISs was first noticed in the late 1940s, although it was only applied to the acceleration of light, singly-charged ions [THO46, RUT47, HAL48, OGA62]. The first reports of multiply charged ECR sources appeared in 1972-3 [TAM72, APA73], but not until 1974 were substantial beams available in Grenoble [DRE94]. However, the Grenoble ECRIS Supermafios required 3 MW of power to operate, making this type of IS unappealing to many laboratories until the introduction of Micromafios in 1979, reducing power consumption to 100 kW by using permanent magnetic materials (Nd alloys) [GEL80, DRE94].

ECRISs produce highly charged ions via repeated electron collisions with plasma particles (although not necessarily the same electrons or the same ions in each collision, see below). The plasma chamber is surrounded by solenoids creating an axial magnetic field, as well as a sextupole magnet of permanent magnetic ma-

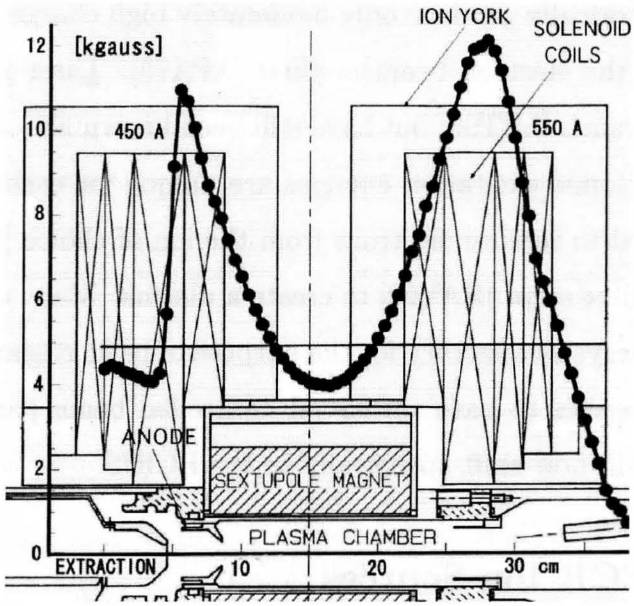

Figure 4.3: Schematic drawing of the 14 GHz HyperECR source of the Center for Nuclear Study (CNS) of the University of Tokyo, located at RIKEN and constructed at the former Institute for Nuclear Study (INS) [DRE94, OHS03]. The overlayed plot shows the mirror B field distribution used for production of the ions $^{12}C^{5+}$ and $^{14}N^{6+}$. The image cuts off display of the sextupole and solenoid coils below the plasma chamber. There is a typographical error in the figure, and *ion york* should be *iron yolk.*

terial (see Figure 4.3), such that there is a closed surface at which an electron will gyrate, or go in circles, about the field lines, just like ions in a cyclotron [RUT47, DRE94] (the cyclotron was invented prior to the observation of this effect [LAW30, THO46]). The electron "cyclotron frequency" in principle follows the same relation as expressed in Equation (4.2), although in practice it seems to be a factor of two greater due to harmonic or parametric resonances [OGA62], and is typically of the order GHz. Off-centre in the axial direction, microwaves at rf frequency equal to the electron cyclotron frequency are shot into the plasma chamber; these photons have microwave energy and frequency but are injected with regularity dictated by an rf source set to the electron cyclotron frequency [DRE94]. The gyrating electrons absorb this microwave energy in resonance with their orbital frequency, allowing them to create ions by successive collisions [APA75], and hence this method is called an electron cyclotron resonance ion source.

Due to the low plasma pressure (between 10^{-7} and 10^{-3} Torr, though typically closer to 10^{-5} [BAR65, TAM72, OKA72, BRI75]) in the chamber, one must account for highly stripped ions through single collision processes; although step-by-step ionizations may occur in the case of long ion lifetimes [BRI75]. Auger cascades and shake-off effects appear to be the main phenomena at work [APA73, BRI75]. When an electron collides with an ion, it may knock out an electron, creating an orbital vacancy. This vacancy may be filled either by a radiative transition or an Auger process, where a higher-orbital electron is ejected to reduce the atomic excitation energy [CAR66]. This transition or electron removal may not fully de-excite the atom, and so the process continues [SNE55]. High-charge states are preferentially populated through Auger cascades when a K-shell electron is initially knocked-out [SNE58], but any inner orbital knock-out may contribute, although the contribution to high-charge states by knock-out of upper-orbital electrons is negligible [SNE58]. These vacancy cascades take place on the order of 10^{-15} seconds [CAR66]. An ion may also shake-off an electron in an outer-most orbital to de-excite, particularly in the case of a sudden change in effective charge [CAR66], which is clearly applicable if the atom remains excited, yet there are no orbital holes to facilitate further Auger electron removal.

An ECRIS creates its own plasma in this way, when provided with an injection gas. However, the start-up electron density may be insufficient, and increased performances are reported by coating the chamber wall, using an electron gun, or applying a biased electrode to produce additional electrons [DRE94]. While an ECRIS may create ions from any gas, the production of ions from solid materials requires specialized techniques, often involving ceramic rods, containing or coated in a powder of the element of interest, inserted radially into the plasma chamber.

Given the above generalized account of RIB production mechanisms, ion beam accelerators, and ion sources, it is now appropriate to delve into the specific RIB physics relevant to this thesis, presented in Chapter 5.

Chapter 5

Experimental Facility and Technique

5.1 The CRIB Separator Facility

After the closure of the Institute for Nuclear Study (INS) of the University of Tokyo in the late 1990s, there was a desire to continue low-energy nuclear research in Japan, complementary to the facilities located at KEK (The High Energy Accelerator organization). Thus was born the Center for Nuclear Study (CNS) of the University of Tokyo in collaboration with RIKEN (The Institute of Physical and Chemical Research). A new CNS building was erected on the RIKEN main campus in Wakō in Saitama, a prefecture adjacent and to the northwest of the Tokyo Prefecture. Shortly thereafter, a new, low-energy, in-flight radioactive ion beam (RIB) separator was built at the Nishina Center of RIKEN, called the CNS RIB (CRIB) separator [KUB02, YAN05] located in Experimental hall 7 (E7). The beams supplied to the CRIB are produced by the HyperECR and accelerated by the RIKEN AVF cyclotron (see Figure 5.1).

5.1.1 CRIB Beam Optics and Focal Planes

The CRIB separator consists of four focal planes, denoted F0, F1, F2, and F3, respectively (see Figure 5.2). The production target of the secondary beam is

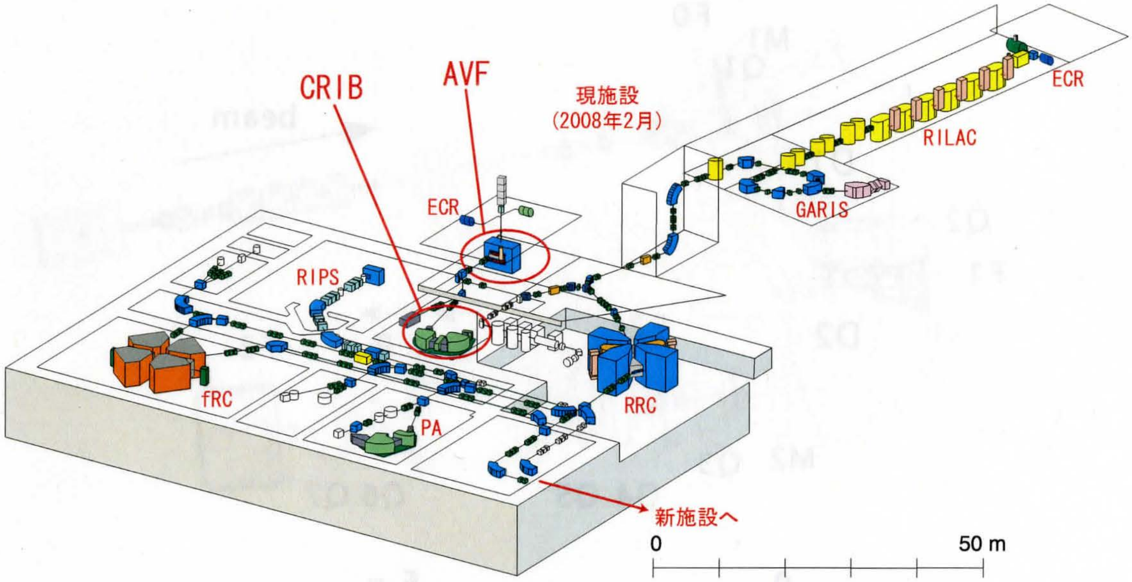

Figure 5.1: Schematic view of the Nishina Accelerator Center at RIKEN, current as of February 2008. The apparatuses of interest to this thesis are the ECR ion source, AVF cyclotron, and CRIB separator facility.

located at F0. For the subsequent discussion of beam optics and separation physics, the beam is assumed to travel in the positive $\hat{\mathbf{z}}$ direction, with the $\mathbf{x}$-axis crossing laterally, and the y-axis going orthogonally up and down. After the first magnetic dipole is the momentum dispersive focal plane, F1. The magnetic dipoles D1 and D2 consist of two pole pieces which produce a uniform magnetic field. In the non-relativistic limit (applicable to low-energy heavy ion separation), a beam ion of momentum p traversing a magnetic dipole is deflected along a circular path with radius ρ [RR88]:

$$\rho = \frac{mv}{qB} = \frac{p}{qB} = \frac{\sqrt{2mE}}{qB} \tag{5.1}$$

Equation (5.2) allows us to define a special parameter called the magnetic rigidity (quoted in Tesla-metres):

$$B\rho = \frac{p}{q} \tag{5.2}$$

For a fixed dipole strength, particles of the same magnetic rigidity will traverse a unique path through the dipole; equivalently, particles of the same energy with

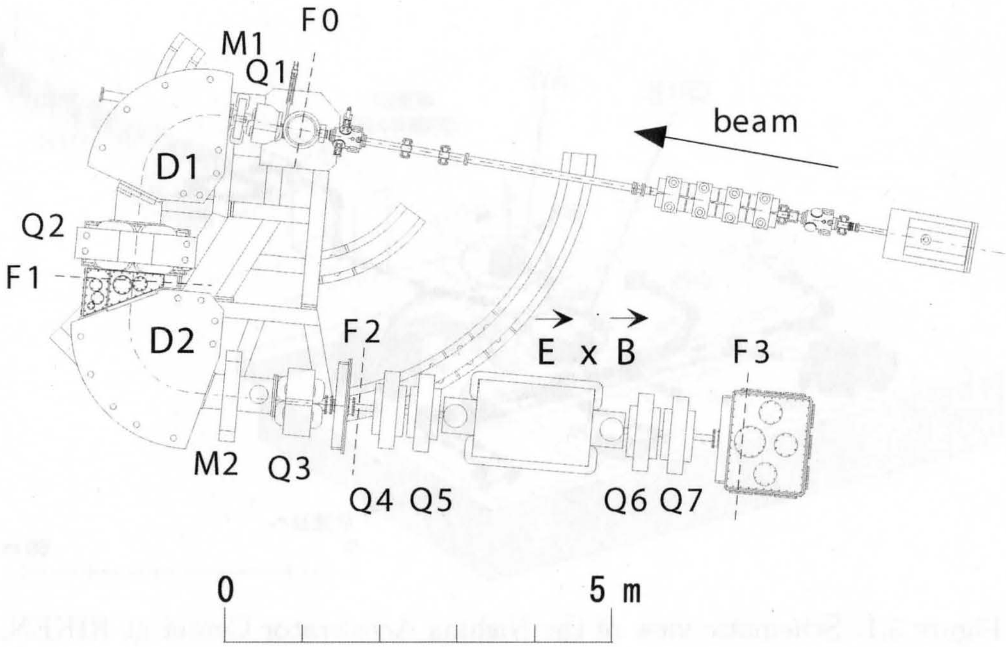

Figure 5.2: Schematic overhead view of the CRIB separator facility. The beam enters at the top right and experiments are conducted at F3. In the diagram, 'F' stands for focal plane, 'Q' for magnetic quadrupole, 'M' for magnetic multipole, 'D' for magnetic dipole, and $\vec{E} \times \vec{B}$ is a Wien (velocity) Filter (see the text).

a different charge-to-mass ratio $\frac{m}{q}$ will be separated by a magnetic dipole. At F1, there is a set of lateral slits which may be used to select particles with a given $B\rho$. A magnetic dipole also has focusing properties for particles having the same momentum and dipole entry location but different horizontal trajectories [RR88]. Lateral dipole focusing occurs because the amount a particle is bent depends not only on its $B\rho$ value, but also the amount of time it spends traversing the magnetic field. A particle with inward trajectory will spend less time inside the dipole and hence be deflected by a smaller amount than a particle with an outward trajectory, causing both particles to emerge from the dipole and intersect at a point diametrically opposite to their identical point of entry.

F1 is followed by a doubly achromatic focal plane F2; here an analogy to optics (because these particles do not have optical colours to be *(a)chromatic* is used to describe the beam focusing, based on the de Broglie hypothesis that

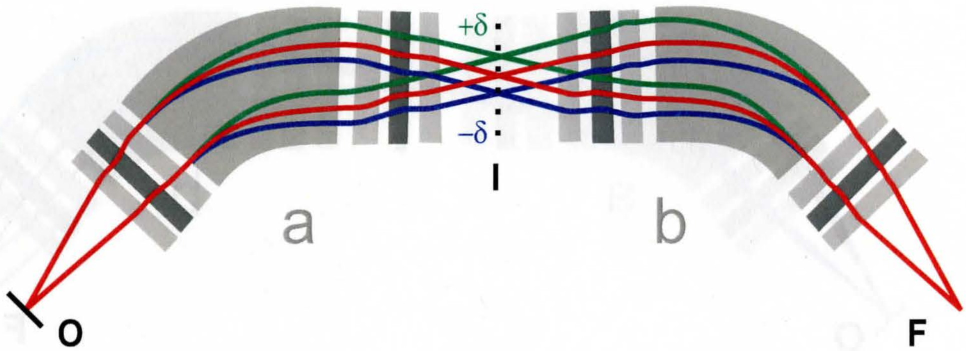

Figure 5.3: The image starts with beam particles at some common origin (**O**) and after passing through four sets of focusing magnets and two magnetic dipoles (**a** and **b**) have a momentum spread requiring that they pass between the magnets at different positions in physical space ranging from $\pm\delta$ and coming back to focus (**F**) [BAU07]. Within each of the initial and final red lines, representing two possible sets of particle trajectories, the green particles have a relatively higher $B\rho$ and the blue group a relatively lower $B\rho$.

matter has a wave-particle duality such that frequency is proportional to kinetic energy, and momentum is inversely proportional to wavelength meaning particles can be separated or focused 'optically' based on wavelength, just like visible light traversing a series of glass lenses. It is easy to understand how the second dipole D2 causes lateral focusing, as D1 and D2 are customarily set to the same field strength, and so as a mirror image of D1, D2 will undo the dispersion caused by D1 at F1 (see Figure 5.3).

A magnetic quadrupole can focus the beam in one transverse direction ($\hat{\mathbf{x}}$ or $\hat{\mathbf{y}}$) without bending the beam; at least two consecutive quadrupoles are required to focus the beam in two directions ($\hat{\mathbf{x}}$ and $\hat{\mathbf{y}}$). The focusing magnets Q1 and M1 are used to direct as many of the reaction products emerging from the production target at F0 into D1 as possible; should any of these reaction products be undesirable, there are vertical and horizontal slits which may be narrowed after the production target at F0. The subsequent beam optics components Q2, M2 and Q3 ensure that the beam is focused in the $\hat{\mathbf{y}}$ direction at F2 so that F2 is a doubly achromatic focal plane. A delay-line parallel plate avalanche counter and a

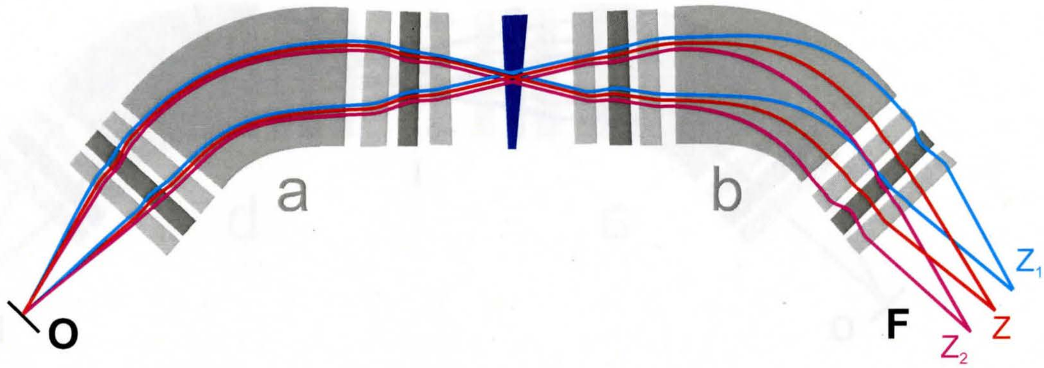

Figure 5.4: The image starts with beam particles at some common origin (**O**) and after passing through four sets of focusing magnets and two magnetic dipoles (**a** and **b**) separated by a wedge, coming to separate foci (**F**) depending on the nuclear charge Z [BAU07]. The trajectories of three different isotopes with same $\frac{m}{q}$ and velocity are shown to end up at different focal points.

silicon strip detector (see Section 5.3) may be inserted at F2 to analyze the beam properties, so that the D1 and D2 magnetic rigidities may be optimized.

F2 is followed by a Wien filter (WF) with two beam-focusing quadrupoles on each side (Q4, Q5, Q6, and Q7 respectively) before the experimental scattering chamber, F3. The WF is a velocity selector, which works by setting the force exerted on a particle by an electric field $\vec{E}$ equal to the force exerted by a magnetic field $\vec{B}$:

$$F = q\vec{E} = q(v \times \vec{B}) \tag{5.3}$$

However, if $\vec{E}$, $\vec{B}$, and $\hat{\mathbf{z}}$ (the beam direction) are mutually orthogonal, then from Equation (5.4 we can get (after cancelling the particle charge, q):

$$\frac{E}{B} = v \tag{5.4}$$

or a velocity filter (since the experimentalist may control E and B), increasing the RIB species purity (see Chapter 5) of interest by a factor of order 10^2. This high order discrimination is possible because at F2 with tight F1 slit settings, D1 and D2 have selected a single $B\rho$ value, and by further imposing a velocity constraint,

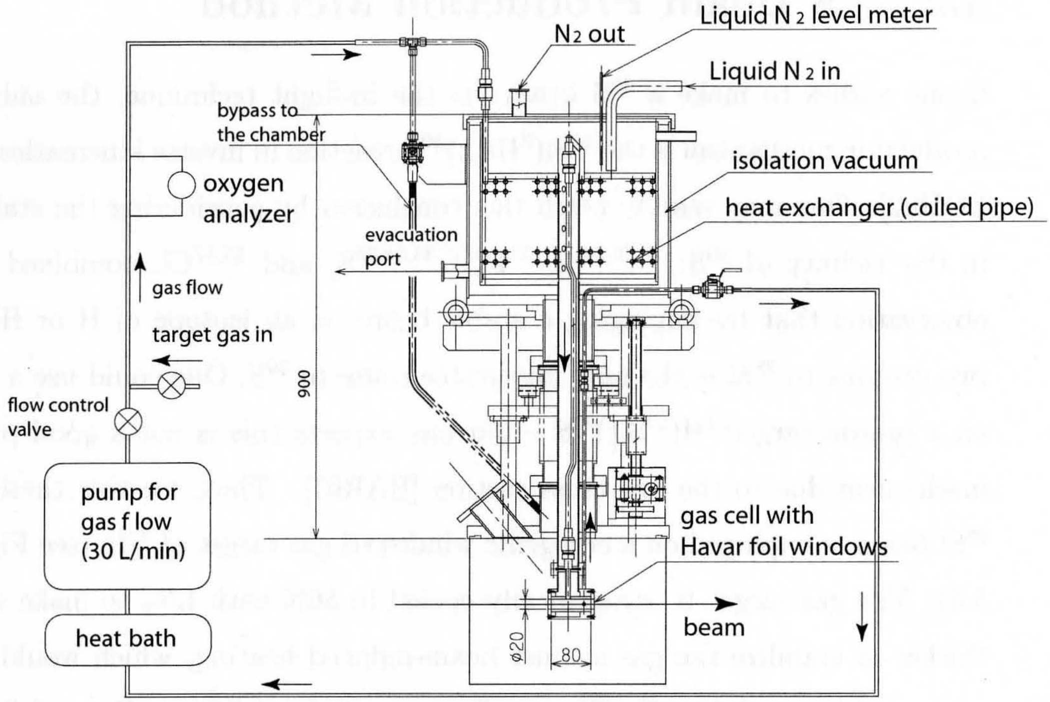

Figure 5.5: Schematic side view of the CRIB cryogenic gas target cooling system.

we select a specific $\frac{m}{q}$ value at a single energy emerging from F0.

One may further separate production target reaction products with the same $\frac{m}{q}$ and velocity by employment of a degrader or wedge placed at F1 (see Figure 5.4). A homogenous degrader will destroy the achromaticity of F2, but a wedge will preserve it for a nuclear charge Z of interest [DUF86]. This wedge will cause the particles to lose momentum differentially according to the A and Z values [DUF86] as seen in Figure 4.1. However, the requisite wedge-shaped degrader is much too thin for our low energy purposes, so when a degrader is used at the CRIB facility, we must rely on a homogenous degrader with beam optics tuned to achieve achromaticity at F2 [YAN05].

5.2 ^{30}S Beam Production Method

If one wishes to make a ^{30}S beam via the in-flight technique, the only feasible production mechanism is the ^{28}Si(^{3}He,n)^{30}S reaction in inverse kinematics [HAG68, BOH82]. One may readily reach this conclusion by considering the stable nuclei in the vicinity of ^{30}S: ^{28,29,30}Si, ^{31}P, ^{32,33,34,36}S, and ^{35,37}Cl, combined with the observation that by impinging a stable beam on an isotope of H or He, adding two protons to ^{28}Si is the only favourable route to ^{30}S. One could use a ^{32}S beam on a proton target ^{1}H(^{32}S,t)^{30}S – but one expects this is not a good production mechanism due to the low cross section [BAR07]. Thus, for this thesis work, a ^{28}Si beam is impinged on a cryogenic windowed gas target of ^{3}He (see Figures 5.5, 5.6). The gas target is cryogenically cooled to 80K with LN_2 to make the target thicker to stabilize the gas against beam-induced heating, which would alter the target thickness [YAM07]. The windows are made of 2.2 μm Havar foil, which is a popular window foil in nuclear physics.

The nickel-group alloy Havar has high tensile strength, high heat capacity, and most of its constituent nuclei have 24>Z>28. High tensile strength is important for window foils because not only may the pressure gradient across the window be 1 atmosphere or more, but the foil should be as thin as possible to minimize energy loss and straggling of particles traversing the window. Accelerated nuclear beams deposit large quantities of heat within any material impeding the flight path, and we avoid rupturing the windows by selecting a high heat capacity window material. It is preferable that the beam not induce a significant number of nuclear reactions within the window material, and to this end, experimentalists may choose a window material with high nuclear charge so that Coulomb repulsion decreases the probability of a nuclear interaction; conversely, if the nuclear charge is too high, it will increase energy straggling. Havar satisfies all these criteria, with a tensile strength of 1.86×10^{9} Pa and a composition of Be (0.3%), C (1.0%), Cr (22.2%), Mn (1.7%), Fe (18.1%), Co (41.6%), Ni (12.8%), Mo (1.4%) and W (0.9%).

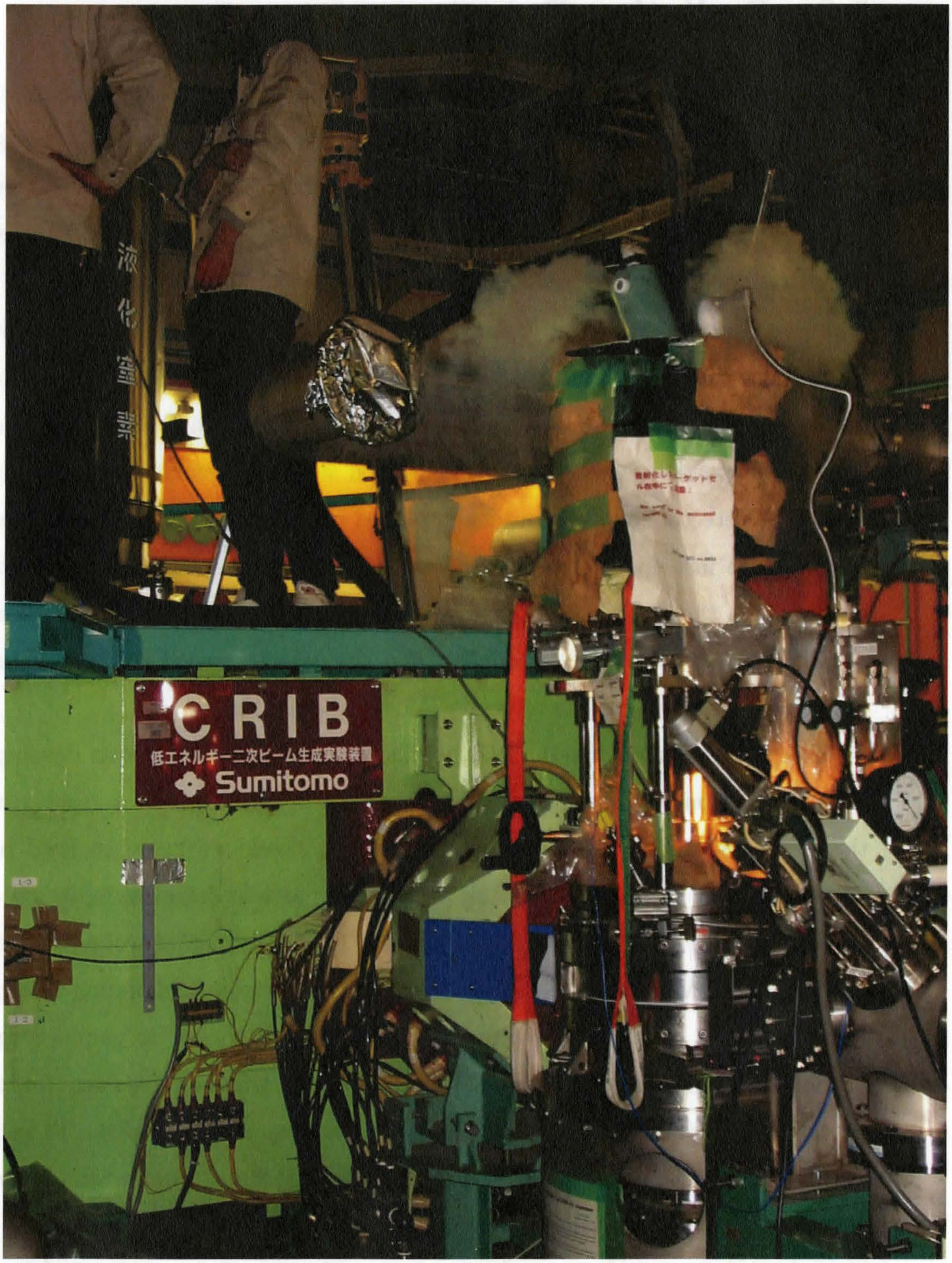

Figure 5.6: A photograph of the F0 production target and part of the D1 magnetic dipole, where LEE Nam Hee (right) and HAYAKAWA Seiya (left) can be mostly seen standing on D1, as they adjust the flow of LN_2 into the cryogenic production target. Gaseous nitrogen can be seen emerging from the crygenic target vents.

5.3 Radiation Detectors

There are three pieces of information a data analyst likes to know about the radiation used for and resulting from nuclear experiments: position, timing, and energy. Basic position information is obtained from placement of detectors with respect to the beam line and target(s). Segmented detectors, or detectors with many components and/or channels, yield more specific position information about radiation striking these particular detectors. If radiation strikes consecutive detectors, one may reconstruct particle trajectories during offline analysis. Although the experiments discussed in this thesis involve results from beam intensities up to around 10^6 particles per second (pps), which seems extremely fast to the human mind, the detectors and computers employed to record information about incident particles are fast enough to process such signals on an event-by-event basis. As will be seen, the flight time of particles through the CRIB facility is on the order of nanoseconds (ns, or 10^{-9} seconds), and the detectors used can distinguish one particle from another if the intensity is below $\sim 10^6$ Hz.

The work detailed herein, RIB production and (α,p) technique development, is primarily concerned with detection of charged particles. As a result, most of the detectors at the CRIB facility used in this thesis work are charged particle detectors. The present description of charged particle detectors is by no means exhaustive, and serves primarily to elucidate the experimental techniques relevent to this thesis. While it is possible to obtain both energy and timing information from the same detector, detectors are typically optimized for good energy resolution or good timing data. The reason for this trade-off between timing and energy is straight-forward, as will be shown with specific examples. To know the energy deposited in a detector, one must collect all the signal carriers, which will not arrive at the same time. In order to get good timing information, one would like a well-defined and sharp signal, which will not include all the signal carriers generated by the incident radiation. The time and energy dichotomy results from signal production and collection and is not related to the quantum energy-time uncertainty relation (see Equation 1.25); certainly quantum mechanics places ultimate limits on the timing and energy information one might obtain about a single particle, but present detectors are far from this limit.

One may wish to get either the energy loss ΔE, the full energy E, or both ΔE and E for experimentally-relevant radiation or beam ions. Whenever radiation passes through matter, energy is transferred from the radiation to the target matter. Such energy transfer is often referred to as energy loss, which, if not detected by an electronic system, the energy is 'lost' to thermal heating of the target. As was seen previously (see Figure 4.1), the energy loss of radiation in matter depends on the radiation energy, but it also depends on the nuclear charge Z of the radiation, because the energy is transferred primarily by Coulomb interactions between the radiation and the target matter. Because ΔE depends on Z, experiments typically use energy loss as a way of identifying the nuclear charge, or chemical element, which deposited the energy. However, to get the full kinetic energy of a particle, one must typically stop the particle within a detector[1]. Solid detector materials are often preferred to gaseous detectors for energetic particles and confined spaces, because solids are a factor of 10^3 more dense than gases [KNO00]. First, we consider semiconductor diode detectors made of silicon.

5.3.1 Silicon Strip Detectors

In order to get good energy resolution, one is concerned with the ionization energy, or energy to excite or knock-out one electron, of the detection matter. The ionization energy of semiconductors is on the order of 3 eV, whereas for gases

[1]There are many exceptions to the requirement of stopping radiation to get the energy. If one knows the charge and mass of the radiation, one may use a magnetic dipole, and the resulting magnetic rigidity $B\rho$ to deduce the energy (see Equation 5.2). If one knows the mass of the particle, one could measure the velocity to deduce the energy — a way to get energy information from two (or more) timing signals. Unfortunately, as will be discussed in Section 5.3.2, obtaining timing signals often alters (decreases) the beam energy, making energy measurements from timing signals impractical in most cases.

it is around 30 eV [KNO00], or an order of magnitude higher. One determines the energy deposited by the number of charge carriers collected multiplied by the ionization energy. The more charge carriers created by each incident particle, the better the obtainable energy resolution due to smaller statistcal fluctuations in the number of charge carriers collected for the same energy deposition.

A semiconductor is a material which has properties somewhere in between a conductor and an insulator. In a conductor, like a metal, there are many free electrons available to carry charge which are not associated with any lattice bonding points or particular nuclei. Accordingly, these electrons are considered to reside in the conduction band. In an insulator, there is a large gap between the valence band, or the least bound electrons associated with a particular atom, and the conduction band — the gap is typically greater than 5 eV [KNO00]. In a semiconductor, there are no electrons in the conduction band at zero temperature, but the band gap is much smaller than in an insulator — typically on the order of 1 eV or less [KNO00]. Although thermal excitations at room temperature may lead to electrons in the conduction band of a semiconductor, an equilibrium is established between the rate electrons are elevated to the conduction band and the rate electrons recombine with atoms in the lattice [KNO00]. In a conductor like copper, electrons are the (negative) charge carriers. However, in a conductor such as zinc, the absence of electrons, or electron holes, are (positive) charge carriers. The charge carrier in a conductor (electron or electron-hole) can be determined in many ways, like measuring the Hall effect, or the voltage across a conductor in a magnetic field. In a semiconductor, whenever an electron is elevated to the conduction band, an electron-hole pair is created, where both the electron and electron-hole serve as conduction mechanisms.

Although semiconductors may have a sparse number of conduction electrons due to thermal excitations alone, in the presence of an electric field $\vec{E}$ or applied electric potential V, electrons may be elevated to the conduction band and caused to flow, or drift, in the direction opposite the electric field lines. Semiconductors are typically in Group IV in the Periodic Table. However, semiconductors are rarely pure (impurities may be a few in a part per million), or semiconductors may also be intentionally contaminated, or doped, with other elements. If the contaminants are of Group V in the Periodic Table, there are extra electrons not associated with holes, and the results of this doping is called an n type semiconductor [KNO00]. If the contaminants are of Group III in the Periodic Table, there are extra holes not associated with electrons, called a p type semiconductor [KNO00].

When charged particle radiation passes through a semiconductor, a number of electron-hole pairs are created proportional to the energy deposited [KNO00], which is why cosmic rays often cause glitches or data corruption in consumer electronics. With an applied electric bias across the semiconductor, the electrons and holes drift in opposite directions, and may be collected and counted. The number of signal carriers detected is proportional to deposited energy and generally independent of the type of incident radiation, although heavy ions will create a higher density of electron-hole pairs, some of which may recombine at a higher rate and circumvent detection [KNO00]. The higher the applied voltage, the lower the recombination rate. Because signal carriers show some dependence on the type of radiation, silicon detectors used for experiments at the CRIB facility are calibrated with high energy ions, protons of many energies, and low energy α particles.

Because semiconductors are solid materials, they are very useful for obtaining the full energy of particles[2], because radiation is often stopped completely within the detectors. For example, a proton must have around 16 MeV (nearly 2% the speed of light) to pass through a silicon detector just 1.5 mm thick. Semiconductor detectors have some disadvantages, such as dead-layers and the capacity to sustain radiation damage over time [KNO00], and poor timing information. Semiconductors have poor time resolution because the electrons and electron-holes must also move through the solid material, which, for example, takes much more time than

[2]The energy resolution of semiconductors is always superb ($\frac{\Delta E}{E} \lesssim 1\%$), regardless of whether one obtains E or ΔE.

a free electron in a diffuse gaseous detector. Thus, in order to collect all the signal carriers, one must have relatively long collection times, and individual signal arrival times are thus not well defined. As a consequence, semiconductor detectors do not provide especially fantastic timing resolution. But the small size and good energy resolution of silicon (and other semiconductor) detectors makes them a good laboratory tool.

Silicon strip detectors (SSDs) are used at the CRIB facility to obtain diagnostic primary or secondary beam energy, as well as the energy of charged particles emerging from beam-induced creations. Position sensitive silicon detectors (PSSDs or PSDs) are also used, which are SSDs where the electron-hole collection electronics are broken into segments, as the surface of the silicon wafer is etched to create small inactive lines to divide the detector into smaller sections, where the effect is a segmented detector. Typically in a rectangular PSSD, a single silicon wafer will have y signal carrier detectors vertically on one side and x signal carrier detectors horizontally on the opposite face, making an effective $x \times y$ pixelation to determine the location of incident radiation. The SSDs and PSSDs used at the CRIB facility are 5 cm $\times$ 5 cm detectors, and the applied voltages (always negative) range from a few volts up to 330 volts (depending on the thickness of the particular silicon wafer). The double-sided, position sensitive SSDs (a long abbreviation) used for this work are 16 $\times$ 16 channels and either 69 or 400 μm thick.

5.3.2 Parallel Plate Avalanche Counters

It is useful to obtain the position and timing of beam ions in nuclear experiments. A particle's position after emerging from a magnetic dipole provides information about its magnetic rigidity (see Equation 5.2), and two consecutive position measurements allows one to extrapolate the particle's trajectory. Two timing signals may be used to determine a particle's velocity, or time of flight (ToF). However, beam diagnostic tools should interfere with the beam properties as little as possible. Unlike the full energy measurement method of SSDs, which requires one to completely stop the incident radiation, the ion beam is rather useless if stopped, and one tries not to molest the beam whenever possible.

Parallel plate avalanche counters (PPACs) are a type of gas-filled proportional counter, which are structurally similar to ionization chambers — another type of gas-filled detector with a more telling name. Gas detectors and semiconductor diode detectors (see Section 5.3.1) are similar, because as charged-particles pass through the fill-gas (specific gases are detailed in a later paragraph), the radiation may ionize gas atoms/molecules, creating ion-electron pairs (ion pairs for short), much like the electron-hole pairs created in semiconductors. Also like semiconductor diode detectors, the charged signal carriers are collected by applying a bias or voltage to the gas volume. The drift time of electrons in an $\vec{E}$-field is much faster than ions due to the low mass (and point-size) of the electron, and so typically electrons are collected at a cathode (positive terminal) and the ion signal, although it necessarily accumulates at the anode, is neglected.

Proportional counters differ from ionization chambers primarily by using higher electric potentials to collect the electrons. Just like in the semiconductor diode detectors, a single incident charged-particle may produce many ion pairs (electron-hole pairs in semiconductors). However, under a high $\vec{E}$-field, the free electrons are accelerated to an energy above the ionization energy of the fill-gas. The result of significant electron acceleration is that an initial ion pair created by the incident radiation may lead to secondary ionization, called a Townsend avalanche [KNO00] and leading to the name 'proportional counter,' because the number of electrons collected is proportional to the applied field more than the intrinsic properties of the incident radiation itself.

The multiplication of electrons also depends on the properties of the fill-gas, which in turn depends on the migration of the electrons within the gas [KNO00]. One also ought choose a fill gas with a low electron attachment coefficient [KNO00], because otherwise electrons may recombine with gas atoms/molecules, circumventing detection at the cathode. Below multiplication factors of 100, pure noble gases are popular fill-gases. However, as ionization may leave the atom/molecule in an excited state (see Section 4.3.1), the gas may de-excite by emitting photons, often in the ultra-violet region of the electromagnetic spectrum, which may also lead to secondary ionization. However, the timescale for atomic de-excitation and location of photon absorption are not well correlated with the incident radiation itself, unlike secondary ionization resulting from a Townsend avalanche. In such a case of high electron multiplication, a quench gas that is opaque to UV radiation, such as methane (CH_4), is added in with the noble gas [KNO00] to prevent UV ionization. Because argon is the least expensive noble gas (largely due to underground potassium deposits[3] and the β-decay of the naturally-occuring isotope ^{40}K), a widely-used fill gas is 90% argon and 10% methane, or *P-10* (short for percent 10 methane). Gaseous hydrocarbons, like methane, ethylene (C_2H_4), isobutane (C_4H_{10}) and isooctane/trimethylpentane (C_8H_{18}), themselves are used as proportional counter fill gases (in addition to quench gases), particularly when stopping power[4] is not an issue [KNO00]. However, octafluoropropane (C_3F_8) is becoming more prominent as a fill-gas for delay-line PPACs, because of the large stopping power, the fast signal rise time, and the absence of hydrogen [KUM01]; hydrogen is flammable, which is a laboratory safety issue during handling but not important to the physics. C_3F_8 is used as a fill-gas for this work at a pressure of 30 Torr, with high flow rates (between 5 and 10 litres/hour) for stable operation [KUM01].

There are two types of PPACs: charge-division and delay-line. In a charge-division PPAC, the position is determined by the charge distributed to the four different corners of a single cathode [YAM08]. Charge-division PPACs theoretically have better position resolution, but require time to integrate the charges, and so the maximum intensity of incident ions before these PPACs electrically discharge is 10^{3-4} Hz [KUM01]. The F1 PPAC at the CRIB facility is of the

[3]In other words, argon is cheap for the same reasons many foods, such as bananas, potatoes, avocados and many beans, are modestly radioactive.

[4]Stopping power is related to mass.

charge-division type, because position information is most important at the dispersive focal plane, and the F1 PPAC is used primarily for beam development and not during experiments, making the low counting limit less important. A delay-line PPAC uses two cathodes (one for horizontal position and the other for vertical position), and position is determined by time differences from the four signals (i.e. a wire in the x cathode has a signal on both ends, x_1 and x_2, and the same for the y cathode) [YAM08]. The time differences would not be noticeable without a delay-line. Delay-line PPACs can handle intensities upwards of 10^6 Hz [KUM01], and the F2 and F3 PPACs are of this type, because in these cases, precise position measurements are less important than high count rate tolerances. However, there is not a noticeable difference in the precision of position measurements between the different PPACs at the CRIB separator [YAM08]. Most of the experimental results presented here are obtained using the delay-line PPACs, so a detailed description is warranted.

The delay-line PPACs used at the CRIB facility were designed at RIKEN, and the design has been published [KUM01]. There are two cathodes spaced 8 mm apart, one used for x position and the other for y position, with a biased anode (negative terminal) placed between the two cathodes. In this work, the anode is set to around -800 V, although the design permits up to ~ -2000 V. Each cathode has 40 conducting strips 2.40 mm wide, with 0.15 mm between strips, providing a sensitive area of 10×10 cm^2 [KUM01]. The conductive strips are 30 nm of aluminium evaporated on 1.5 μm Mylar foil (bi-axially oriented $C_{10}H_8O_4$) [KUM01]; although evaporated gold was also tested, it showed more damage during discharge, or sparking [KUM01], likely because gold is a softer metal than aluminium. Because the PPACs use Mylar, they are a source of proton background, because the beam often knocks protons out of the Mylar foil; if Mylar foils were not used, the fact that the octafluoropropane fill-gas does not contain hydrogen would be experimentally relevant, but the Mylar windows contain much more hydrogen than any fill-gases at 30 Torr in the detector volume. Aluminized mylar is also used for the gas-confining entrance and exit windows of the PPACs, since the detectors are used in a vacuum.

The PPAC at F2 has an equivalent thickness of 13.78 μm Mylar, and the F3 PPACs have an equivalent thickness of 9.5 μm Mylar[5], which is useful information for quick energy loss calculations wishing to avoid adding the thickness of 5 aluminized mylar foils interspaced with C_3F_8 gas; energy loss calculations are rarely done for the F1 PPAC. For the beams discussed in this thesis, the beam particles lose on average $\sim$ 20 MeV traversing a single PPAC. The typical PPAC position resolution is 1.0 mm, with a timing resolution of 1.2 ns, both quoted at full width half maximum (FWHM) [KUM01], although only 5 channels are required for each PPAC. The position resolution is read continuously by comparing the time signals from opposite sides of the cathode [KUM01], so the detector has better than 40×40 pixelation resolution.

5.3.3 Measured Quantities of Interest

Particle energy is a useful quantity by itself, and the usefulness of knowing the energy of beam ions is described later for particular cases. However, unlike train arrival time, which tells a commuter what time to board from the platform based on a schedule, particle arrival time by itself is not especially enlightening. But two timing signals for the same particle indicates the flight time of the particle from one location to another position within the CRIB facility, which is useful. One timing signal is used to start the flight time clock, and another timing signal is used to stop the clock. There are four detectors in the CRIB with good timing properties (although they are never all inserted into the beam-line at once): the F1 PPAC, the F2 PPAC, and the F3 PPACs, denoted *a* and *b*. Supposing one obtains a timing signal from both F3 PPACs for a single particle, one may use these signals to get the particles time of flight (ToF) between F3 PPACa and PPACb.

[5]All the PPACs used have the same gas pressure and cathode setup, but different confining window thickness.

Because the primary beam is accelerated by a cyclotron, which outputs beam ions in discrete packets, the cyclotron radiofrequency (*RF*) signal may also be used to start the clock. Suppose one obtains timing signals for different nuclear species at F2 from a delay-line PPAC. Because all the primary beam ions have the same flight time from the cyclotron to the F0 position in the CRIB separator, the flight time clock is started for each packet of particles by the cyclotron RF signal, indicating another packet of particles arrived at the F0 position. However, after passing through the cryogenic gas target at F0, where nuclear transmutation and electron exchange take place, various beam ions have not only a different speed exiting the production target, but also have different flight paths through the magnetic dipoles D1 and D2, depending on their momentum, nuclear charge, electric charge, emission angle, and so on. The delay-line PPAC timing signal at F2 can then be used to stop the clock which started when the particles arrived at F0, indicating individual particle flight times from F0 to F2. Such a timing signal that is started by the cyclotron RF is called the particle's *RF time.*

The RF time is technically also a particle ToF, but these two quantities are distingushed from one another, because the RF time always begins counting the flight time from F0 to the first PPAC encountered, and the ToF measures the flight time between two PPACs. The RF time and ToF are necessarily different, because during a particle's RF time, it passed through at least one magnetic dipole, altering the particle's flight according to its magnetic rigidity. However, the ToF is measured in a region relatively free of trajectory-altering electro-magnetic fields, simply yielding the particle's velocity though that space. Identical particles will have the same RF time, even if they traverse the CRIB separator many hours apart from each other.

But the RF timing signal cannot run on forever, so it must be stopped and restarted regularly, or else a particle would be recorded to have an RF time of many millions of nanoseconds by the end of an experiment. The resetting time is always chosen to be longer than the cyclotron RF to ensure that no particles go unaccounted for. Thus, during a single cycle of the RF time clock, the next packet of particles will have arrived at F0 from the cyclotron and will be counted in the tail-end of the previous cyclotron packet RF time, leading to an unrealistically long RF time measurement (but still on the order of nanoseconds). Resetting the RF clock to 0 itself takes time, and so two RF timing measurements are made, denoted $RF0$ and $RF1$, offset from one another, to ensure that when one clock is resetting and not measuring particle flight time, an RF time signal is still produced for each beam ion. The above information about the RF time clocks is critical, because if one were interested to know how many particles have a particular RF time, one must multiply the recorded value by a factor of 2, since both RF clocks run for slightly more than one cyclotron RF cycle. The factor of 2 is not a direct consequence of having two RF clocks[6], but because the RF clock resetting frequency is longer than a single cyclotron RF cycle!

5.4 Detector Electronics and Signal Processing

Signal processing in nuclear physics (and high energy physics) is non-trivial, and typical CRIB experiments use 200 channels, or different signals input to the data acquisition computer. Some individual channels represent many electronic signal channels that have been reduced in number, such as timing from PSSDs, which start as 16 channels (32 including both sides) and are reduced to one timing signal for each side of the detector. A complete set of CRIB electronics diagrams can be found in Appendix B, which details exactly how the different electronics are wired. A qualitative description of the silicon detector and PPAC electronics is given presently, to elucidate the purpose of various components.

Because the signal carriers of interest are electrons (or electron-holes), the raw signals are quite weak, because the elementary charge is merely 1.6×10^{-19} C. Thus, a pre-amplifier (preamp) is used to enhance the raw detector signal, and

[6]Indeed, we could have many thousands of RF clocks if we chose (even though there is no reason to do so in practice), and the multiplicative factor is still 2.

the preamp is placed as close to the detector as possible, because even conducting wires have finite resistance which may impede the raw signal. The pre-amplified signal is then sent to an amplifier, which must be a fast amplifier for timing signals. One might fairly ask why two signal amplifiers are used, or why a pre-amplifier is used if the signal is amplified in any case. Firstly, the pre-amplifier is typically located in or near the detector, so that the signal is received and processed before it becomes indistinguishable from background electronic signals, or noise. But preamps can also be found in some consumer electronics, such as signal processing for phonographic turntables. Weak electronic signals must necessarily be pre-amplified, otherwise the signal would not be processable, or not processed properly. Another way to think about the situation is that amplifiers have adjustable gains, or amplification level, whereas preamps typically operate at the same amplification — one does not want to reduce the amplification to below the functional processing baseline. Whether the signal is initially weak or strong, it must be preamplified before it is fully attenuated, and subsequently sent on to the amplifier, where we may set the gain according to the signal energy range.

After the preamp, energy signals are simply amplified and sent to the data collection room, called J1. The full dynamic range of a given detector typically cannot be used for a given experiment, so amplifiers have adjustable gains to set the collection sensitivity to the particles of interest. For example, if one is interested in lower energy particles, the signal should be amplified much more than if one were interested in high energy particles.

Timing signals require slightly more processing before being sent to the data collection room. These signals are also amplified by a fast amplifier. As mentioned in Section 5.3, one does not need to collect the entire signal to extract timing, only the rise to maximum to extract the start time of the signal. As such, for timing purposes, one may quickly amplify only the leading edge of the signal. Unfortunately, the start of the signal is buried beneath noise. One may extract the start time based on the slope of the timing signal, but the pulse shape varies depending on the strength, or amplitude, of the signal. High amplitude signals have a more abrupt and steep rise than low amplitude signals. For pulses with the same shape, one may pick-off the signal start time after the leading edge of the pulse has passed a constant fraction of the total amplitude, yielding a pick-off time independent of amplitude [KNO00]. Because our timing signals have the same pulse shape, we use a constant fraction discriminator (CFD) module to analyze the signal arrival time. CFDs thus delay the signal while the pulse amplitude is determined, and the result is sent to the data room.

Once the detector signals are sent to J1, they are analyzed by logic electronics (see Appendix B) and converted to digital signals recordable by a computer. In the case of energy signals, analog to digital converters (ADCs) are used, and for timing signals, time to digital converters (TDCs) are used. The logic electronics discriminate true events from background, for example by requiring that consecutive PPACs trigger (otherwise the incident radiation has left the beam axis or was not a true beam event), or for silicon detectors, requiring that the PPACs have recorded a beam signal within an appropriate time window. However, converting analog signals to digital signals takes some time, and the appropriate ADC/TDC may be busy processing an earlier event when a good event arrives. The number of events occuring, or *triggers presented*, is recorded as the number of *ungated* events. The number of events occuring which were properly processed by the ADC/TDC are recorded as *gated* events, or *triggers acquired*. The leading PPAC is always used for the initial event trigger sequence, and without this trigger, no data are recorded.

5.4.1 Data Acquisition and Analysis Software

A majority of the author's computer work is performed in a Linux operating system. Having used Windows XP, Mac OS X and Linux quite extensively, the author recommends Linux to anyone undertaking similar work whenever possible. Some programs written strictly for Windows are not easily emulated, requiring occasional use of Windows. However, the data analysis tools and packages are found to install and run best in Linux systems, particularly because Mac OS X releases for Intel chips do not ship with a FORTRAN compiler (as well as shipping with an extremely old C compiler), and upon installing one's own compiler, one may come across a virtually infinite number of library linking issues (known as dependency hell). The author found it took less time to compile an entire Gentoo Linux operating system from source code for a proprietary hardware system than to fix the Mac OS X FORTRAN library issues.

The data collected at the CRIB facility is written to disk using the Babarl data acquisition (DAQ) program, written by BABA Hidetada and SAITO Akito. The details of the DAQ are mostly important to the experimentalist when something breaks, which did not occur during any of this work. The online data analysis is done in real time with an upgrade from CERN's Physics Analysis Workstation (PAW) called ANAPAW (both written in FORTRAN), created by TAKEUCHI Satoshi. Offline analysis is done using CERN's more contemporary package ROOT (written in C++), lead by René BRUN and Fons RADEMAKERS; the C++ Interpreter (CINT) was written by GOTO Masa. ROOT's histogram package is faster and more efficient than the FORTRAN HBOOK package since four months after its inception in 1995 [ROO08]. The data analysis relevant to this thesis is almost entirely histogram sorting and plotting, so a good histogramming program is desireable. However, since the online data is analyzed using ANAPAW, a program converting the raw data files (rdf) into ROOT format is necessary; such a program was written by Jonty PEARSON, a former research associate of our group, called `rdf2root`[7]. The data conversion code uses a MySQL database for detector calibration and runs in the ROOT environment.

The beam development results presented in this thesis do not require overly sophisticated analysis, as one simply wishes to know things like the beam-spot size, intensity, purity, and energy, most of which can be read straight from the

[7] `rdf2root` was apparently written in just one week!

calibrated data after setting a few gates. As such, using ANAPAW to analyze beam production data collected at the CRIB separator in the future is recommended, particularly for new users with no experience, because converting the data to ROOT takes a substantial amount of time, due to the fact that there is no user manual for the `rdf2root` package (although the code is very well written). Nearly all the analysis code already exists for ANAPAW as well, whereas the author had to make significant modifications to a colleague's ROOT code for his own analysis. It can be said that learning ROOT is a very useful skill, however, because ROOT is used at laboratories world-wide[8], whereas the author is unaware of any usage of ANAPAW outside Japanese laboratories.

Having completed a description of the tools used for experimentation, it is time to consider the originally proposed setup for the ^{4}He(^{30}S,p) cross section measurement.

5.5 (α,p) Measurement Technique, Completed Work

The originally proposed experimental setup involves a ^{30}S beam passing through two PPACs and impinging on a helium gas target, with protons detected downsteam in $\Delta E - E$ silicon telescopes, so that reactions of interest may be reconstructed on an event-by-event basis. The original experimental setup submitted to the Nishina Accelerator Center Proposal Approval Committee (PAC) is shown in Figure 5.7. The experiment is a future project, and has been approved by the PAC. More details about the planned experiment are given in Chapter 7.

5.5.1 Gas Target

The gas cell was designed by the author's graduate supervisor, with improvements by the author, and fabricated at the McMaster Science and Engineering Machine

[8]TRIUMF in Canada, Argonne National Laboratory in the USA, a majority of European laboratories, and the Chinese Institute of Atomic Energy are known by the author to use ROOT.

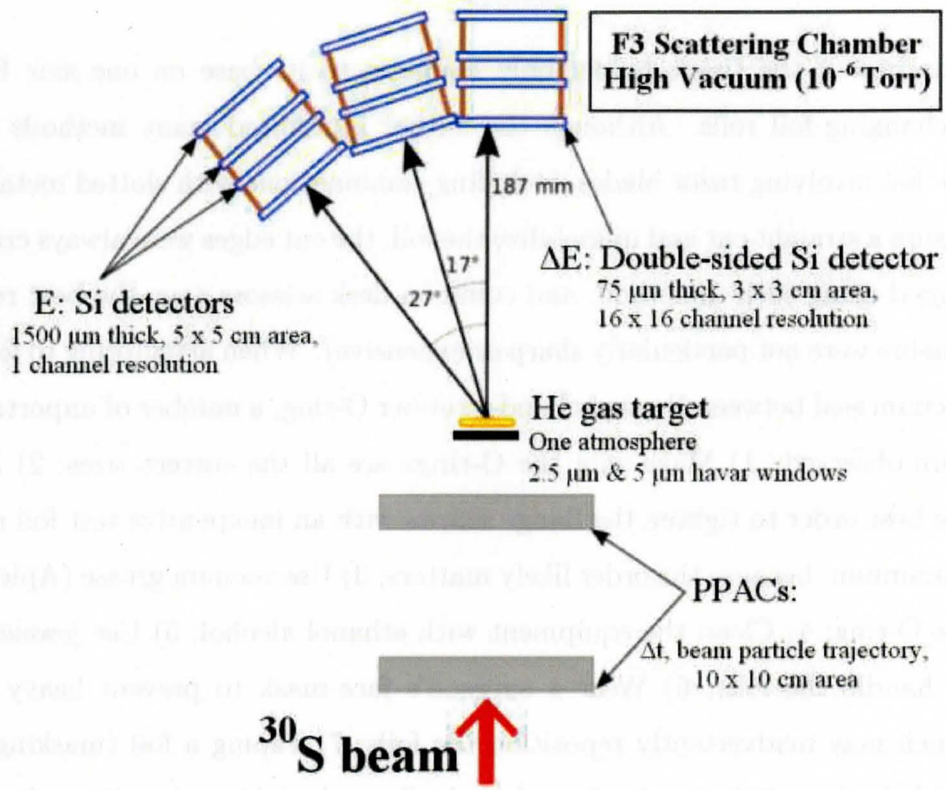

Figure 5.7: A diagram of the originally proposed setup for the ^{4}He(^{30}S,p) experiment. The drawing is not to scale. A similar detector setup was used for an elastic proton scattering experiment ^{1}H(^{25}Al,p) (using a solid polyethylene (CH_2) target), and for that case the solid angle of each silicon telescope was ~ 0.0497 sr [CHE08]. This setup was only used with the gas cell and the 0° with ^{30}S beam, but the data were lost.

Shop in 2006. The gas cell is made from aluminium, and is a semi-cylindrical shape with a 3.8 mm radius and a width of 6.7 mm. The front window is circular with a 1.0 cm diameter, and the curved exit window is also 1.0 cm high. Havar windows were used, 2.5 μm thick for the entrance window and 5 μm thick for the exit window to fully stop the beam (so the beam does not hit the 0° silicon detectors). The exit window is curved so that emerging protons traverse the same thickness of helium gas independent of the lateral angle.

Havar foil is quite expensive (some \$1000 per foot), and it is found that, when the foil is shipped on a roll, an effective way to dispense it is a household bathroom tissue holder attached to a heavy block of wood placed on the laboratory bench;

it is best if the tissue holder only connects to its base on one side for ease of exchanging foil rolls. Although the author attempted many methods of cutting the foil involving razor blades, including combinations with slotted metal sheets to ensure a straight cut and immobilize the foil, the cut edges were always crimped and jagged using such a method, and common desk scissors gave the best results (the scissors were not particularly sharp or expensive). When attempting to form a good vacuum seal between Havar foil and a rubber O-ring, a number of important factors were observed: 1) Make sure the O-rings are all the correct sizes; 2) Determine the best order to tighten the flange screws with an inexpensive test foil made from aluminium, because the order likely matters; 3) Use vacuum grease (Apiezon M) on the O-ring; 4) Clean the equipment with ethanol alcohol; 5) Use jeweler's forceps to handle the foils; 6) Wear a surgeon's face-mask to prevent heavy breathing which may inadvertently reposition the foils; 7) Taping a foil (masking tape will do) helps keep it from crimping when the flange is tightened and is easier to remove than glue; 8) If the foil is on a roll, and the desired foil is not square or circular, carefully consider the best direction to cut the foil keeping in mind the foil will bend back to the shape of the roll. The vacuum seal quality was tested a number of times at the McMaster Nuclear Research Building by John AVELAR and Jim MCANDREW, who provided many useful suggestions. Combining these methods with patience lead to a seal that leaked $\sim$ 360 Torr over two and a half days, starting at 1520 Torr over-pressure in a vacuum, or around 1 Torr every 4 hours. However, aspects of the gas handling system in the F3 experimental scattering chamber at the CRIB facility had an order of magnitude higher leak rate (11 Torr in 4 hours). The high leak rate of gas handling system in the F3 chamber was corroborated with a different gas target during a previous experiment [KIM06].

We determined the ^{30}S beam diameter on target is $\sim$ 1.5 cm during the December 2006 RI beam experiment, so the gas cell was subsequently modified to have an entrance window diameter of 2.4 cm, and the exit window an equal height of 2.4 cm (see Figure 5.8).

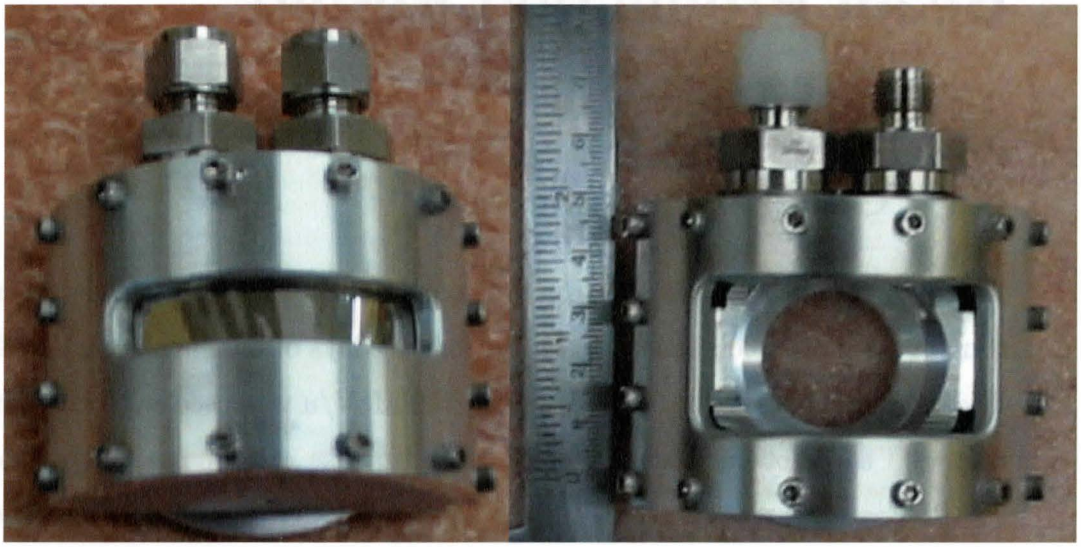

Figure 5.8: The two photographs show the rear view of the Havar-windowed ^{4}He gas cell before (left) and after (right) the windows were enlarged. A ruler is shown for scale. The left picture shows the gas target with 1.0 cm high windows and the Havar windows inserted, and the right picture shows the gas target as it is now, with 2.4 cm high windows, with no Havar windows in place to show the front of the cell.

Chapter 6

Beam Production Results

6.1 General Parameters

We conducted two ^{30}S beam production experiments, the first for two days of beam-time in December 2006 and the second for two days of beam-time in May 2008. In December 2006, a ^{28}Si^{9+} beam of energy 6.9 MeV/u was used with intensity ~100 pnA and a cyclotron frequency 16.2 MHz (inverse of 61.7 ns), and we analyzed the RI beam charge states ^{30}S$^{15+,16+}$. In May 2008, a ^{28}Si^{10+} beam of energy 7.5 MeV/u was used with intensity ~10 pnA and a cyclotron frequency 16.9 MHz (inverse of 59.2 ns), and we analyzed the RI beam charge states ^{30}S$^{14+,16+}$. The ^{28}Si ions are extracted from the Hyper ECR ion source, and as discussed in Section 4.2.3, the cyclotron beam energy goes as the square of the ion charge, resulting in the higher primary beam energy for the 10+ charge state used in May 2008. The higher charge state is extracted at a lower intensity from the ECRIS, resulting in an order of magnitude lower beam intensity of ^{28}Si^{10+} compared to ^{28}Si^{9+}. The Hyper ECRIS should be able to extract ^{28}Si^{10+} at a higher rate, resulting in intensities at F0 up to 30 pnA, but the beam operators had some difficulty with the ion source operation in May 2008. The AVF cyclotron group has reported the possibility to accelerate ^{28}Si^{10+} up to 8 MeV/u, but contamination arising from ^{14}N^{5+} is a concern. The nitrogen gas is used in the Hyper ECRIS to assist in the extraction

Centroid channels	$E_{predicted}$ MeV	F0 Target In/Out	F2 PPAC In/Out	F0 Havar In/Out
3739	211	Out	Out	Out
3429	193	Out	Out	In
2870	160.4	In	In	Out
2438	138.9	In	In	In

Table 6.1: The table shows the centroid, in raw channels, from the F2 SSD for different conditions and the predicted energy from `code_for_energy_loss`. When there are no targets, and hence no beam energy loss, the energy is obtained from the magnetic rigidity (see Equation 5.2) of the beam passing through D1 and D2. When the F0 target is empty, two 2.5 μm Havar foils induce energy loss. The F2 PPAC has an equivalent thickness of 13.78 μm of Mylar. The F0 Havar stripper foil is 2.2 μm thick.

of silicon. This higher beam energy would result from keeping the $^{28}Si^{10+}$ in the cyclotron for more turns and is anticipated for the next experiment. Because the same charge state will be extracted from the ion source, the theoretical beam intensity does not decrease.

6.1.1 SSD Energy Calibration for Heavy Ions

The first thing to do in any CRIB experiment is to send the primary beam all the way through the system, to test the detectors and calibrate the F2 SSD and the 0° F3 silicon telescope. Sending the ^{28}Si beam through without any targets gives one data point, and other data points are obtained by inserting other components to induce energy loss, such as the F0 target without any gas (the Havar entrance and exit windows induce energy loss), the F2 PPAC, and any other targets, such as stripper foils, that are present at F0 (see Table 6.1). The FORTRAN package `code_for_energy_loss` predicts energy loss of ions in matter, and by plotting the predicted energy loss versus energy channels in the SSD, we can get a good linear fit (see Figure 6.1) to calibrate the silicon detectors for high energy ions. Thus, energy calibration is done individually for each experiment, making us confident in our energy results for heavy ions.

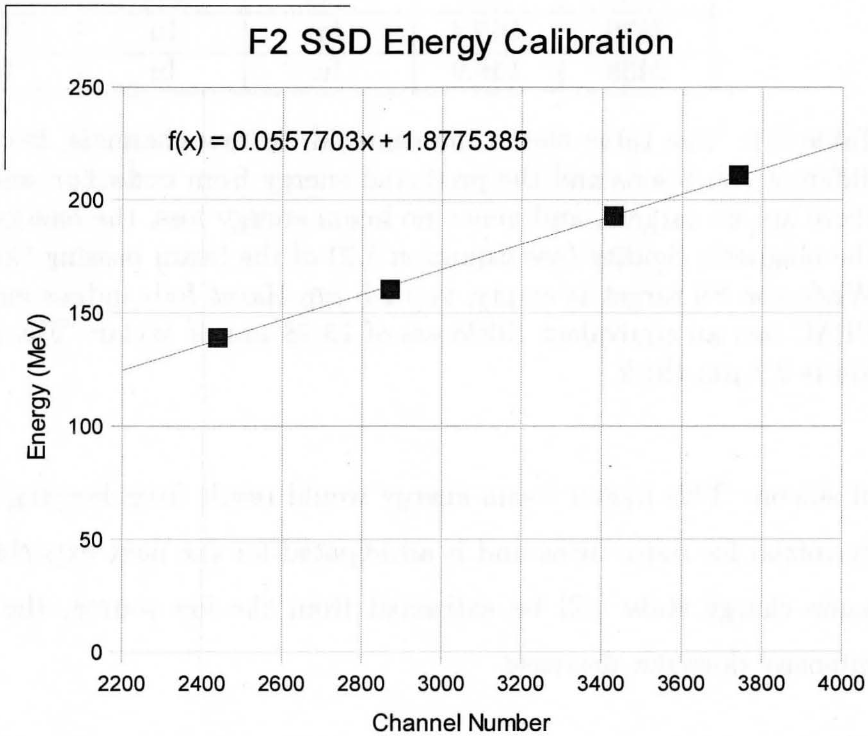

Figure 6.1: The plot shows the linear energy calibration of the F2 SSD from May 2008, using the data presented in Table 6.1. Centroid channel number is plotted along the abscissa, and the predicted energy from `code_for_energy_loss` in million electron volts is plotted on the ordinate. The offset is the y-intercept, which is non-zero because extremely low energy particles will not induce a signal. The energy per channel is given by the slope.

6.1.2 Unmixing the Cocktail Beam

By impinging accelerated ^{28}Si ions on ^{3}He gas, we necessarily create ^{30}S via the ^{3}He(^{28}Si,^{30}S)n reaction, but many other reactions are also induced, creating many isotopes of silicon, phosphorous and sulfur (among other reaction products), and the majority of primary beam ions do not induce any nuclear interactions within the helium gas and emerge from the F0 cryogenic target. To get a ^{30}S beam of high intensity and purity, we must optimize the magnetic rigidities of the magnetic

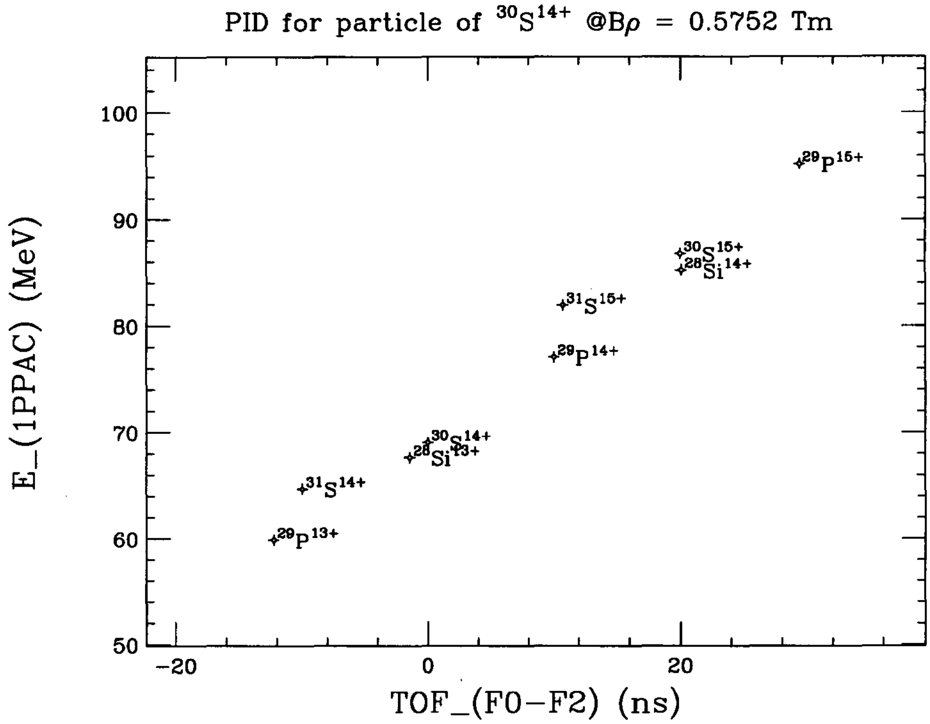

Figure 6.2: The plot shows predicted time of flight (corresponding to $RF0$) on the abscissa and energy on the ordinate for various charge-states of nuclear species in the cocktail beam after traversing the dipoles D1 and D2 and the F2 PPAC. The plot is calculated and generated by the CRIB Optimizer program. The species of interest, $^{30}S^{14+}$, is very close to the primary beam charge-state $^{28}Si^{13+}$ due to similar $\frac{A}{q}$. The CRIB Optimizer does not predict the intensity of beam ions.

dipoles D1 and D2 and the slit position at F1 in between the magnets to block other reaction products. We predict the optimum magnetic rigidities using beam kinematic tools available in the computer programs CRIB Optimizer and LISE++. However, for these calculations, we must assume an energy for the ^{30}S ions, which emerge with a spread in energy, depending on where in the production target they are produced.

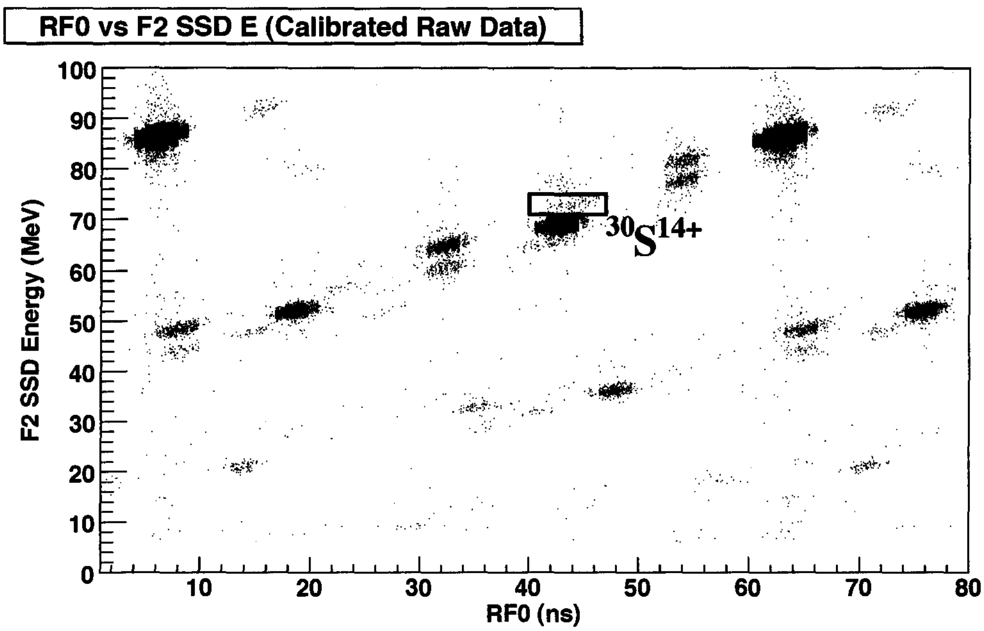

Figure 6.3: The plot shows *RF time* in nanoseconds on the abscissa and SSD energy in million electron volts on the ordinate for various charge-states of nuclear species in the cocktail beam after traversing the dipoles D1 and D2 and the F2 PPAC during run 152 in May 2008. The species of interest, $^{30}S^{14+}$, is indicated. The data collection period is 456 seconds, and a total of 184,615 particles are detected.

6.2 Particle Identification at F2

We perform particle identification (PID) at F2 with a delay-line PPAC and SSD, giving us particle *RF time* and energy, respectively. We then vary the F1 slit position to find the optimum magnetic rigidity for ^{30}S RI beam transmission. Varying the center of the F1 slit is equivalent to changing the magnetic fields, because magnetic rigidity calculations (see Equation 5.2) assume the ions traverse a central path through the magnets. Because electromagnets show hysteresis, it is easier and more reliable to move the F1 slits to see particles traversing non-central paths through the magnets than changing the magnetic field. A 16 mm positive/negative shift of the F1 slit position corresponds to a 1% increase/decrease of the D1 field setting, and a 50 mm positive/negative shift of the F1 slit position corresponds to a 1% increase/decrease of the D2 field setting.

For most experiments performed at the CRIB facility, PID data are not recorded to disk at F2. Due to inexperience, the author did not request these data in December 2006, and so the data only exist as ANAPAW histogram files, so here the PID is only reproduced for the charge-states $^{30}S^{14+,16+}$ from May 2008. However, as $^{30}S^{15+}$ is in between these two charge-states, the method used for its PID will be clear after considering the other two cases. As $B\rho$ selects particles of different species on their momentum to charge ratio $\frac{p}{q}$ (see Equation 5.2), for a given $B\rho$, particles of different species with a higher charge must also have more energy and a longer flight time than particles of lower charge that arrive faster with lower energy. For a given ion, the charge-to-mass ratio $\frac{A}{q}$ is fixed, and for given dipole settings, $B\rho$ is necessarily fixed, and thus only those ions of a particular species with the correct velocity may pass through the magnets to F2. One may calculate the anticipated energy and flight time for a specified $B\rho$ for each species, but such a task is time consuming, particularly when the beam cocktail involves many species and the $B\rho$ value is changed frequently. As such, we use computer programs to predict and plot the results.

Under the run May 2008 conditions, $^{30}S^{14+}$ transmission was optimized at $B\rho_1$=0.57516 Tm and $B\rho_2$=0.57575 Tm. We found the LISE++ simulation to agree well with the CRIB Optimizer predictions, so we only refer to CRIB Optimizer predictions here (Figure 6.2), enabling the confident PID of $^{30}S^{14+}$ in the experimental data (see Figure 6.3).

Under the run May 2008 conditions, $^{30}S^{16+}$ transmission was optimized at $B\rho_1$=0.51528 Tm and $B\rho_2$=0.51593 Tm. The LISE++ simulation does not display the fully stripped charge states of reaction products (only the primary beam), and so PID is made using only the CRIB Optimizer predictions (Figure 6.4), which is not a concern because the LISE++ simulation and CRIB Optimizer predictions are found to agree for lower charge-states. One probably does not even need simulations to perform PID of $^{30}S^{16+}$, as it lies at the top of the $B\rho$ line for this primary

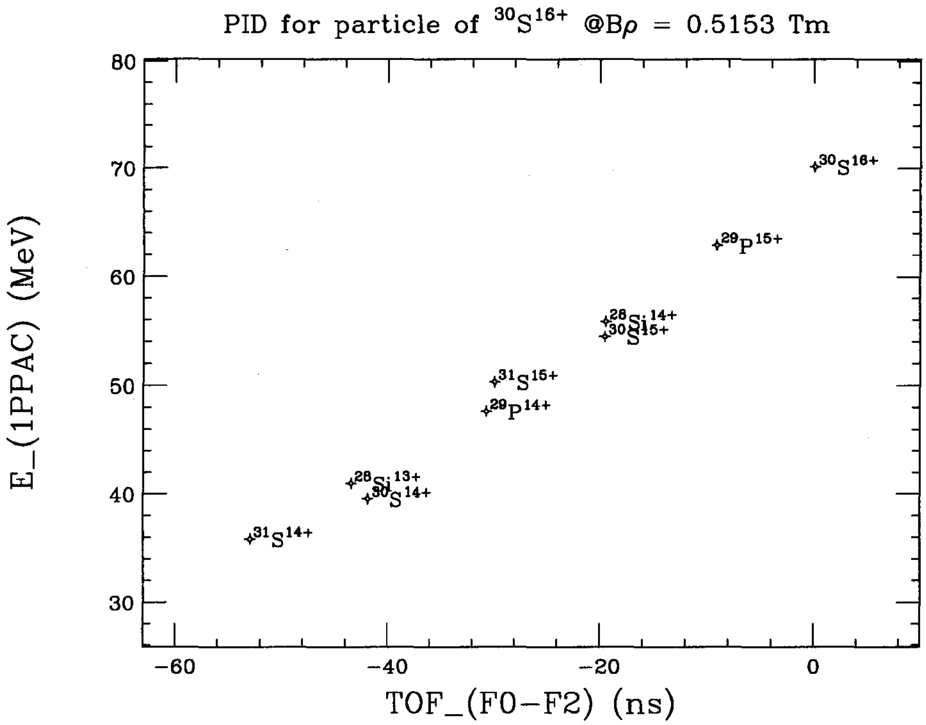

Figure 6.4: The plot shows predicted time of flight (corresponding to $RF0$) on the abscissa and energy on the ordinate for various charge-states of nuclear species in the cocktail beam after traversing the dipoles D1 and D2 and the F2 PPAC. The plot is calculated and generated by the CRIB Optimizer program. The species of interest, $^{30}S^{16+}$, is isolated from other beam particles. The CRIB Optimizer does not predict the intensity of beam ions.

beam and production target, although one should recall that $^{30}S^{16+}$ is populated at a very low rate and wait for good reaction statistics before making the $^{30}S^{16+}$ PID. PID of $^{30}S^{16+}$ in the experimental data (see Figure 6.5) is straight-forward with good reaction statistics.

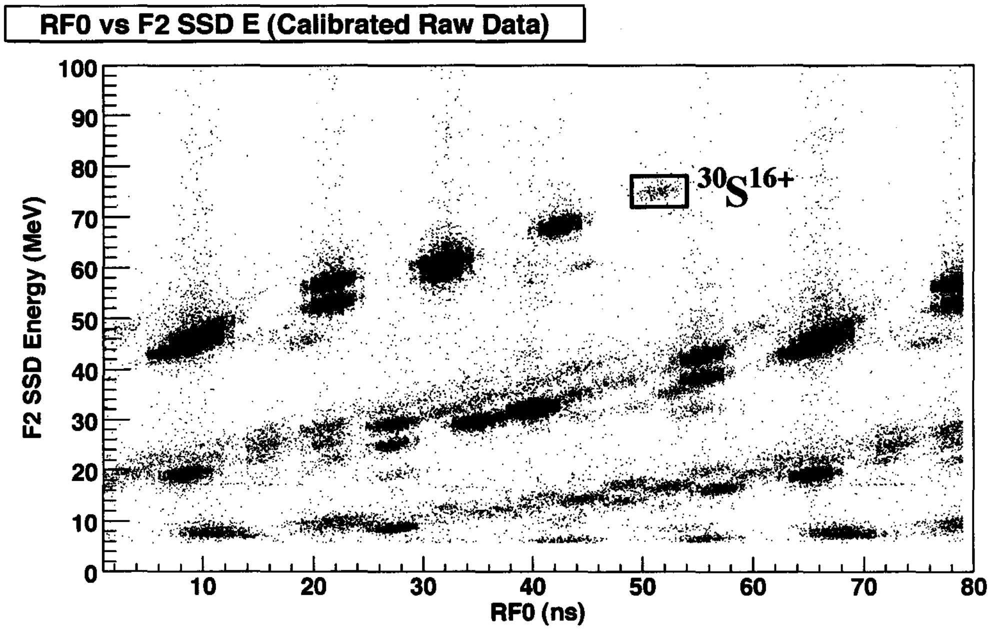

Figure 6.5: The plot shows *RF time* in nanoseconds on the abscissa and SSD energy in million electron volts on the ordinate for various charge-states of nuclear species in the cocktail beam after traversing the dipoles D1 and D2 and the F2 PPAC during run 119 in May 2008. The species of interest, $^{30}S^{16+}$, is indicated. The data collection period is 117 seconds, and a total of 177,200 particles are detected.

6.3 $^{30}S^{15+}$ Results

Once PID is made at F2, the beam is transmitted to the experimental scattering chamber F3. PID must also be confirmed at F3, because the *RF time* shifts from measuring the flight time from F0 $\rightarrow$ F2 PPAC to F0 $\rightarrow$ F3 PPACa. Once PID was made for $^{30}S^{15+}$ from the December 2006 experiment, a *ToF*-RF gate is drawn around the particle group of interest (see Figure 6.6). In December 2006, we achieved $^{30}S^{15+}$ beams on target at F3 with 3×10^3 pps per 100 pnA, 14.1 $\pm$ 1.5 MeV and 1.7% purity.

It is experimentally more challenging to make high-purity RIBs of even-A nuclei than odd-A nuclei employing this separation technique, as even-A charge-states are less likely to have unique $\frac{A}{q}$ values, and as a result contaminants are more difficult

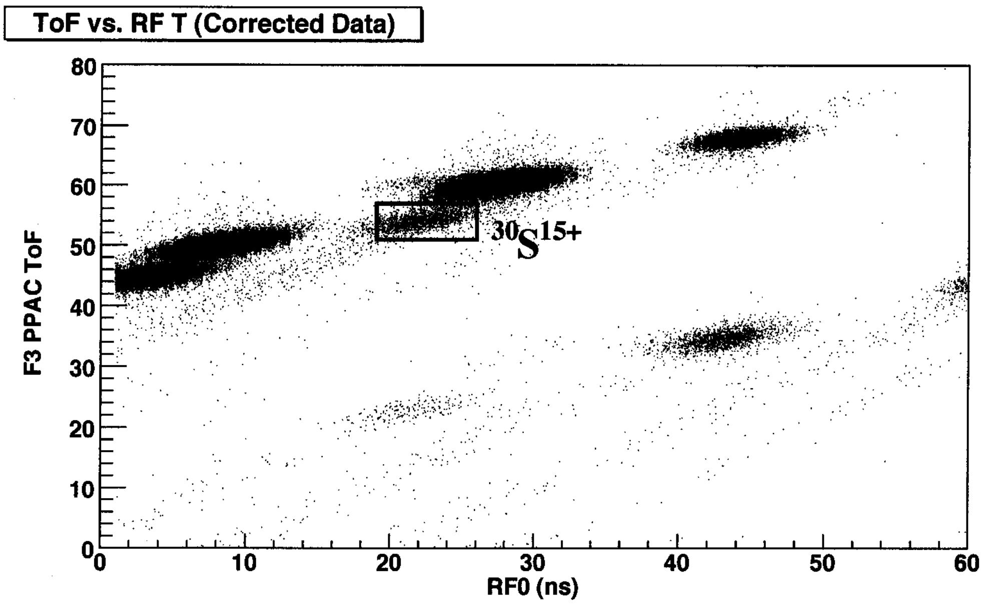

Figure 6.6: The plot shows the raw spectrum of beam particle ToF plotted against RF for Run 9. CRIB settings during this run were optimized for $^{30}S^{+15}$. Particles are grouped on charge-to-mass ratio $\frac{A}{q}$.

to separate out. In the case of ^{30}S, although $^{30}S^{+15}$ is a moderately populated charge-state ($\frac{A}{q} = 2$), there is leaky-beam contamination via $^{28}Si^{+14}$ ($\frac{A}{q} = 2$), and we were unable to fully separate these two ions using F3 PPAC ToF vs. *RF time* during our December 2006 beam development run.

By measuring the energy of beam particles with the 0° F3 PSD (69 μm of silicon is thick enough to fully stop these heavy ions), it is possible to distinguish ions of the same ToF-RF characteristics but differing momentum (thus different mass). The physics of this technique is elementary: if two particles with different masses have the same ToF (velocity), then they cannot possess the same kinetic energy. However, the beam particles must be fully stopped within a detector to measure energy, so this method cannot be used during an experiment to distinguish beam particles bombarding a target. During RIB development, it is possible to get the energy E of beam particles from the 0° F3 PSD. We may then plot *RF time* vs. E (see Figure 6.8). Most of the beam particles do not reach the PSD but are instead

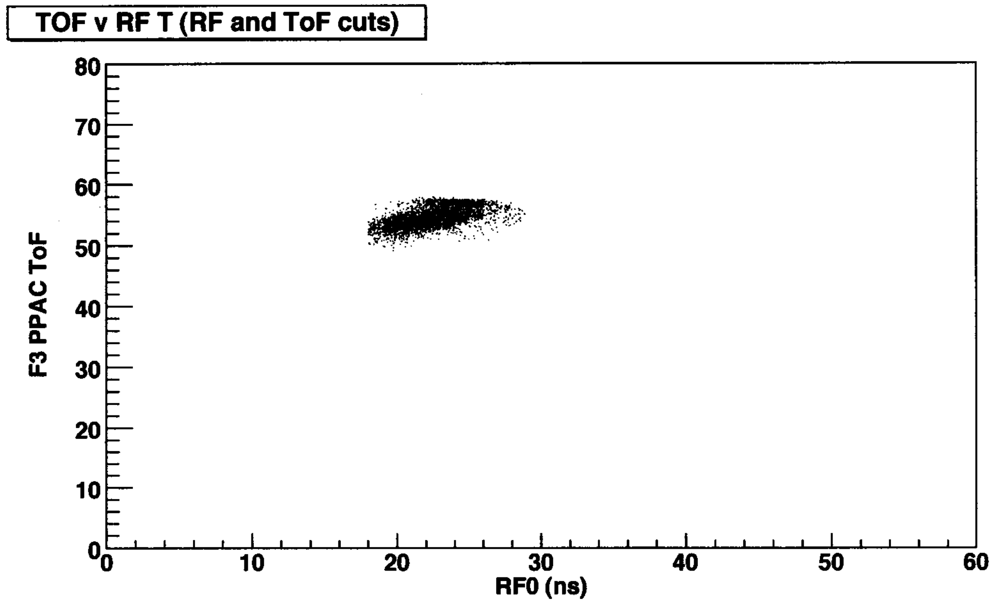

Figure 6.7: The plot shows the raw spectrum of beam particle *ToF* plotted against RF for Run 9. CRIB settings during this run were optimized for $^{30}S^{+15}$. A gate is applied to both *ToF* and RF to include only particles with $\frac{A}{q} \approx 2$. Particles satisfying this criteria comprise 1.5% of the raw data.

stopped in a 2.5 μm Havar foil between F3 PPACb and the PSD. We use a 2.5 μm Havar foil target, because we wish to determine the beam energy on target for helium gas (related to the future work), which will be confined in a gas cell with a 2.5 μm Havar entrance window. However, by plotting only data points on the *ToF* vs. *RF time* spectrum in coincidence with the PSD, inspection confirms there is not a systematic bias in the energy data collection (see Figure 6.9). To see the energy distribution of particles within the *ToF-RF time* gate, that gate is applied to the raw *RF time* vs. *E* plot (resulting in Figure 6.10), which allows us to separate $^{30}S^{+15}$ from $^{28}Si^{+14}$ in the beam production experimental data.

It is useful to distinguish between concepts of purity and contamination in RIB physics. *Beam purity* is simply the intensity of the desired radioactive ion charge-state within the (secondary) beam divided by the total (secondary) beam intensity. Low beam purity will not hamper the success of an experiment, provided

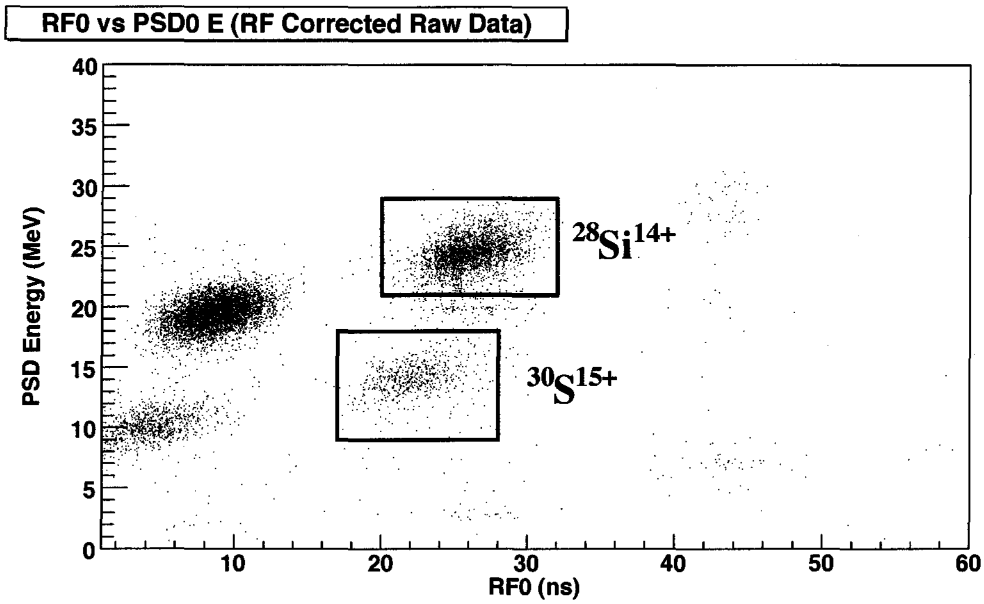

Figure 6.8: The plot shows the raw spectrum of beam particle E plotted against RF for Run 9. CRIB settings during Run 9 were optimized for $^{30}S^{+15}$. A majority of beam particles are stopped within a 2.5 μm Havar foil upstream from the PSD.

a number of conditions are met: 1) Good reaction statistics may be gathered during the course of allotted beam-time; 2) The species of interest can be separated by *RF time* vs. *ToF*; 3) The total (secondary) beam intensity does not surpass the counting rate of F3 delay-line PPACs ($\sim 10^6$ Hz). *Beam contamination* is the number of leaky (primary) beam ions possessing *ToF-RF time* characteristics indistinguishable from the radioactive ion of interest, divided by the total number of particles with said *ToF* and *RF time*.

Any beam contamination must be detected and quantified, so that adequate corrections are made during event-by-event off-line analysis of the future reaction cross-section. Even if the leaky beam does not induce any nuclear reactions within the secondary target, it may easily be mistaken as a good event for ^{30}S statistics. In the case where the leaky beam induces reactions identical to the reaction of interest within the secondary target, the experiment becomes insurmountable. Beam contamination may also result from other primary reaction products, but due to

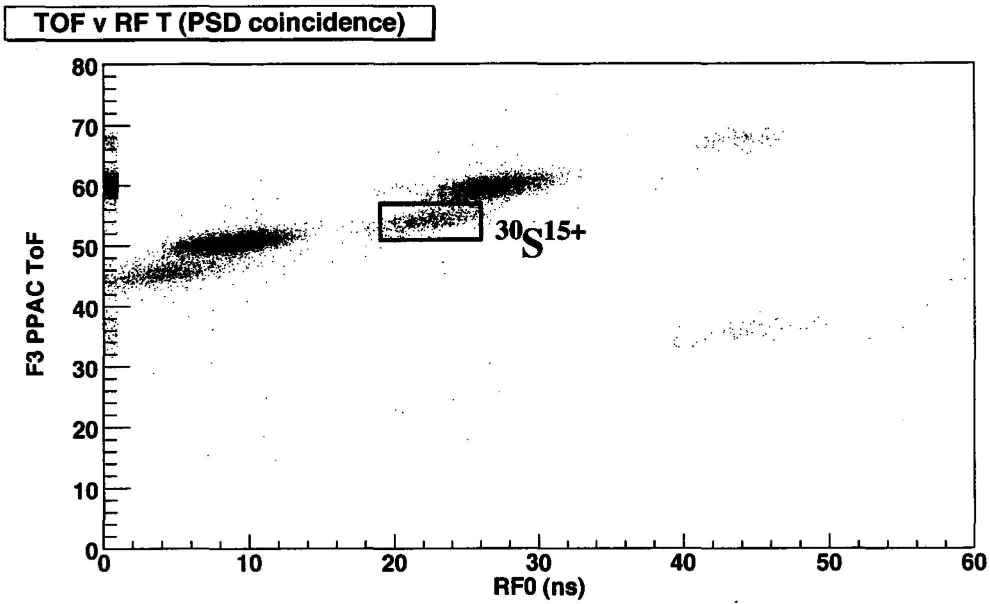

Figure 6.9: The plot shows the spectrum of beam particle *ToF* plotted against RF in coincidence with PSD trigger for Run 9. CRIB settings during Run 9 were optimized for $^{30}S^{+15}$. Particles are grouped on charge-to-mass ratio $\frac{A}{q}$.

the low intensity of the secondary beam compared with the primary beam (10^4 or greater), this is less of a problem in practice; however, this point must not be overlooked when determining possible sources of $\frac{A}{q}$ contaminants and background subtraction.

One may reasonably ask if we really observe leaky-beam contamination for $^{30}S^{+15}$, or if we just did a poor job drawing the *ToF-RF time* gate on the raw data. First, it is useful to see a gated *ToF* vs. *RF time* spectrum coincident with the PSD (see Figure 6.11). Then, one may consider only the lower-energy ^{30}S particles (see Figure 6.12) or higher-energy ^{28}Si particles (see Figure 6.13) separately by applying gates to the raw *RF time* vs. PSD *E* data (raw data is otherwise ungated) and viewing the corresponding gated *ToF* vs. *RF time* spectra. While the bulk of the $^{28}Si^{+14}$ particles in the *ToF*-RF gate appear in a particular region, one also notices that a small fraction contaminate the $^{30}S^{+15}$ *ToF*-RF space.

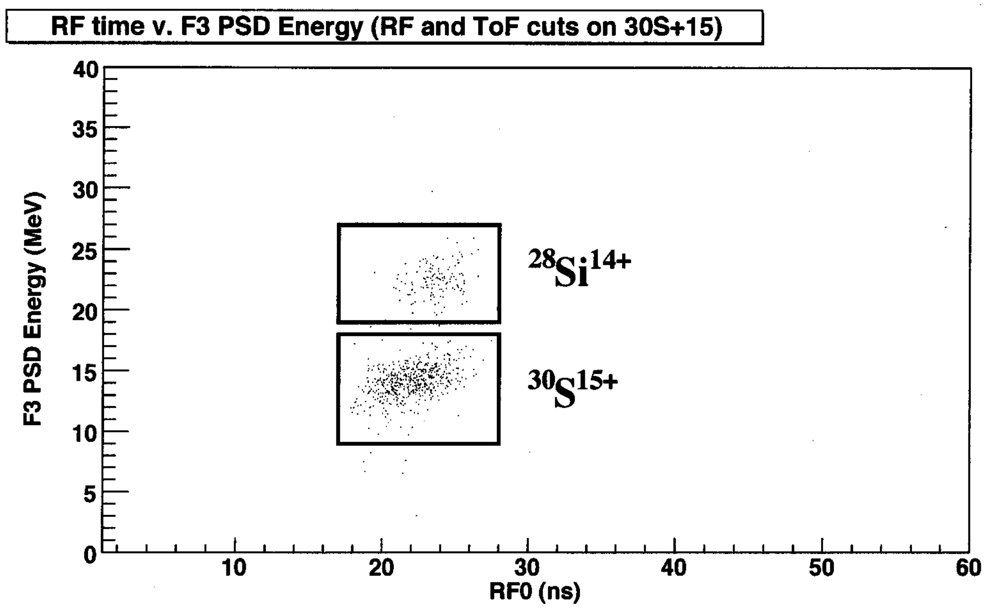

Figure 6.10: The plot shows the spectrum of beam particle E plotted against RF for Run 9, gated on ToF-RF. CRIB settings during Run 9 were optimized for $^{30}S^{+15}$. The same gate from Figure 6.7 is applied to both RF and ToF to include only particles with $\frac{A}{q} \approx 2$. Here two distinct particle groups are observed. The upper group is the leaky-beam contaminant $^{28}Si^{+14}$, while the lower group is $^{30}S^{+15}$.

In our case, we wish to inversely measure the $^{30}S(\alpha,p)^{33}Cl$ cross-section, which is expected to be many orders of magnitude smaller than the leaky-beam reaction $\alpha(^{28}Si,p)^{31}P$ cross-section (of order 0.1 mb at this energy [BUC84]). The $^{28}Si^{+14}$ leaky-beam $\frac{A}{q}$ contamination necessarily precludes the $^{30}S^{+15}$ charge-state from use in a $\alpha(^{30}S,p)^{33}Cl$ cross-section measurement using our technique without higher orders of $\frac{A}{q}$ separation capability, or perhaps a thin Mylar degrader placed at F1.

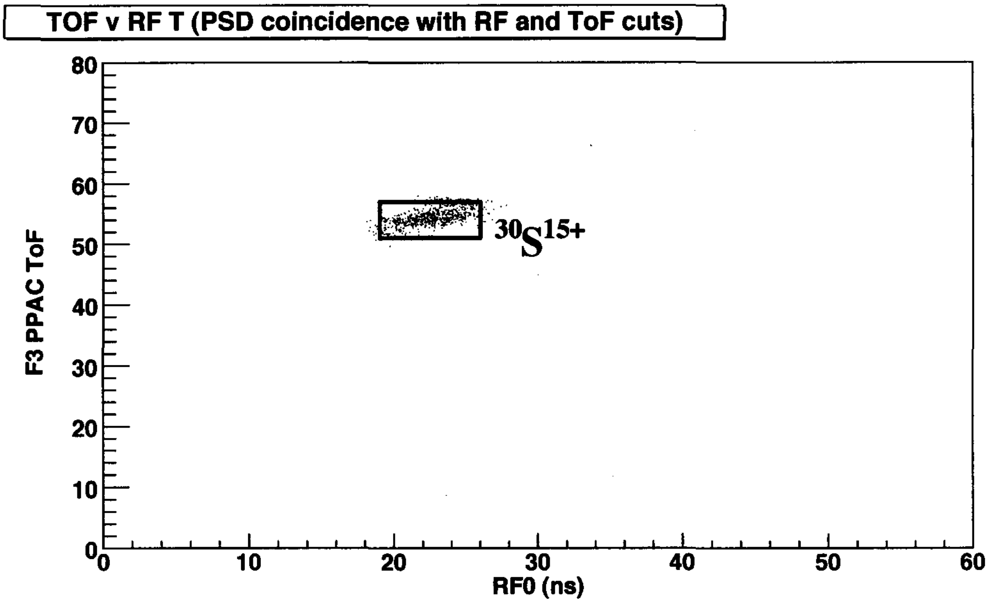

Figure 6.11: The plot shows the spectrum of beam particle ToF plotted against RF in coincidence with PSD trigger for Run 9, gated on ToF-RF. CRIB settings during Run 9 were optimized for $^{30}S^{+15}$.

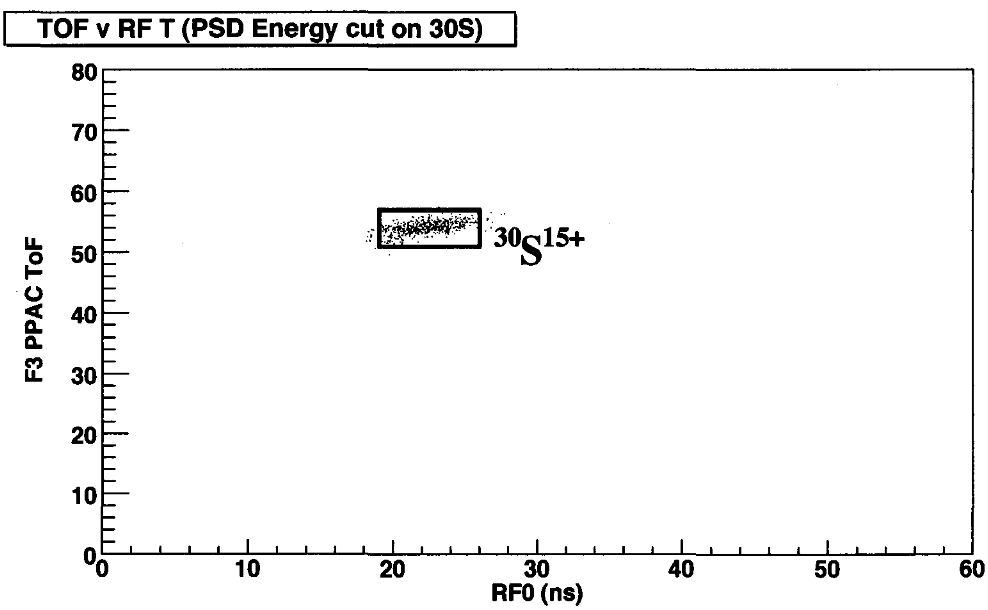

Figure 6.12: The plot shows the spectrum of beam particle ToF plotted against RF in coincidence with PSD trigger for Run 9, gated on ToF-RF and E coresponding to $^{30}S^{+15}$. CRIB settings during Run 9 were optimized for $^{30}S^{+15}$.

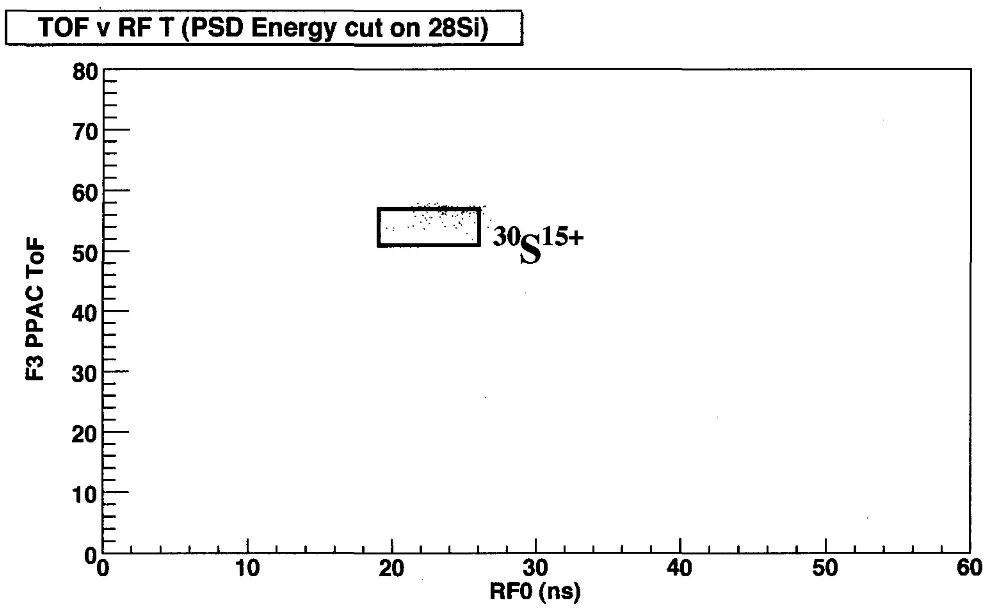

Figure 6.13: The plot shows the spectrum of beam particle ToF plotted against RF in coincidence with PSD trigger for Run 9, gated on ToF-RF and E coresponding to $^{28}Si^{+14}$. CRIB settings during Run 9 were optimized for $^{30}S^{+15}$.

6.4 $^{30}S^{16+}$ Results

$^{30}S^{+16}$ is particularly appealing for use in the $\alpha(^{30}S,p)$ cross-section measurement employing the $^{3}He(^{28}Si,n)^{30}S$ production reaction. Sulfur is the highest accessible nuclear charge (Z) to the $^{28}Si+^{3}He$ production mechanism, and the 16+ charge-state (fully stripped of electrons) has $\frac{A}{q}$ = 1.875 (lower than the fully stripped beam $^{28}Si^{+14}$ with $\frac{A}{q}$ = 2), so there is no possibility of leaky-beam contamination. For example, if one compares the PID of $^{30}S^{+16}$ to $^{30}S^{+14}$ (see Section 6.2), the 16+ charge state is well isolated from all other reaction products, making $^{30}S^{+16}$ not only easier to identify but also easier to separate. For these reasons, we gathered

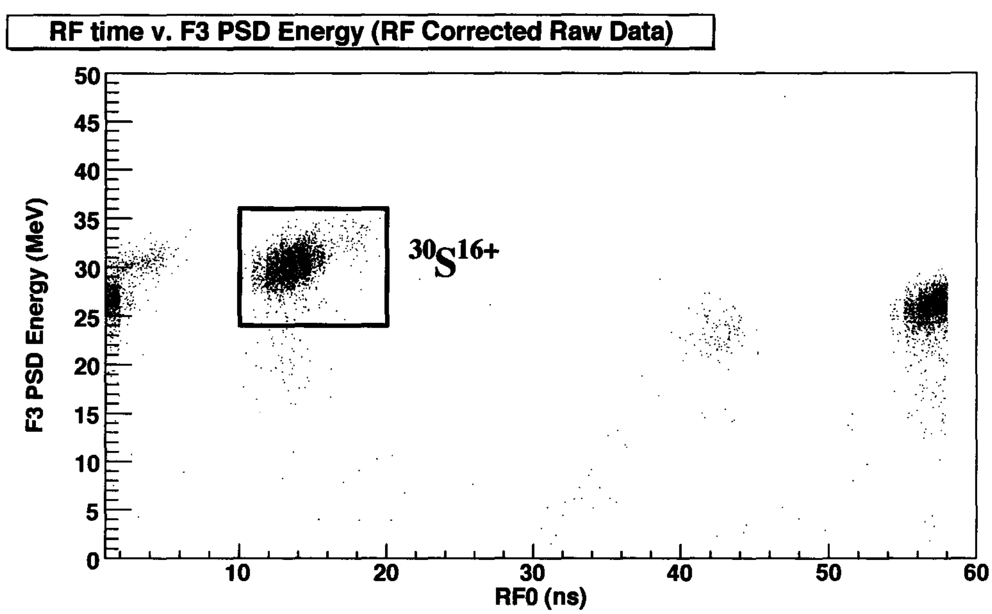

Figure 6.14: The plot shows *RF time* in nanoseconds on the abscissa and PSD energy in million electron volts on the ordinate for the beam after traversing the CRIB, including both F3 PPACs and a 2.5 μm Havar target, and with the Wien Filter set to 60 kV for runs 124–126 in May 2008. The species of interest, $^{30}S^{16+}$, is indicated. The summed data collection period is 2265 seconds, a total of 8,169 particles are detected, 2458 of which are identified as $^{30}S^{16+}$. The unlabeled particles near 0 and 60 ns are $^{29}P^{15+}$ (these particles show up at apparently different *RF times* because the cyclotron RF is ~59 ns), and the group near 40 ns is the leaky-beam $^{28}Si^{14+}$.

data on $^{30}S^{+16}$ in both December 2006 and May 2008. Unluckily, there was an error in how the Barbarl DAQ saved the $^{30}S^{+16}$ data to disk in December 2006, and most of the raw data was lost. The online results for $^{30}S^{+16}$ in December 2006 are still recorded in the log book[1], and we achieved a beam on target at F3 with 1.8×10^3 pps per 100 pnA and purity 13.2% (no energy information is available). In May 2008 we achieved $^{30}S^{+16}$ beams on target at F3 with 7×10^2 pps per 10 pnA, 30.5 $\pm$ 1.5 MeV, and 30% purity (see Figure 6.14). While it is possible to uniquely identify $^{30}S^{+16}$ by *ToF-RF time* at F3, the beam intensity is rather low.

Another important parameter to the RI beam yield is the amount of ^{3}He gas in the cryogenic production target. One can imagine that for very low gas pressure, there are not many target nuclei for the primary beam to interact with. Conversely, for very high gas pressure, there are plenty of target nuclei, but the primary beam and reaction products are slowed down through energy loss to the gas particles (or ultimately stopped for extremely high gas pressures). As the beam energy decreases, the theoretical production cross section drops rapidly, and as reaction products lose energy, the probability to escape the production target decreases. The optimum gas pressure is very difficult to calculate, because the ^{3}He(^{28}Si,^{30}S)n cross-section is not known at the high beam energy used in this work, and so we do not really know at what point in the gas cell a majority of the ^{30}S ions are predominantly produced.

The author attempted a number of theoretical approaches to the problem, which indicated the optimum ^{3}He gas pressure is somewhere between 200 and 500 Torr. We tested gas pressures of 200, 300, and 400 Torr in May 2008 and found that the $^{30}S^{16+}$ intensity increased with increasing gas pressure up to at least 400 Torr. As the CRIB cryogenic gas target can safely hold up to 450 Torr of LN_2 cooled gas, in the future the ^{30}S intensity should be measured with 450 Torr of ^{3}He gas in the production target.

[1] Without the ability to re-analyze the data, these results must be interpreted with some caution.

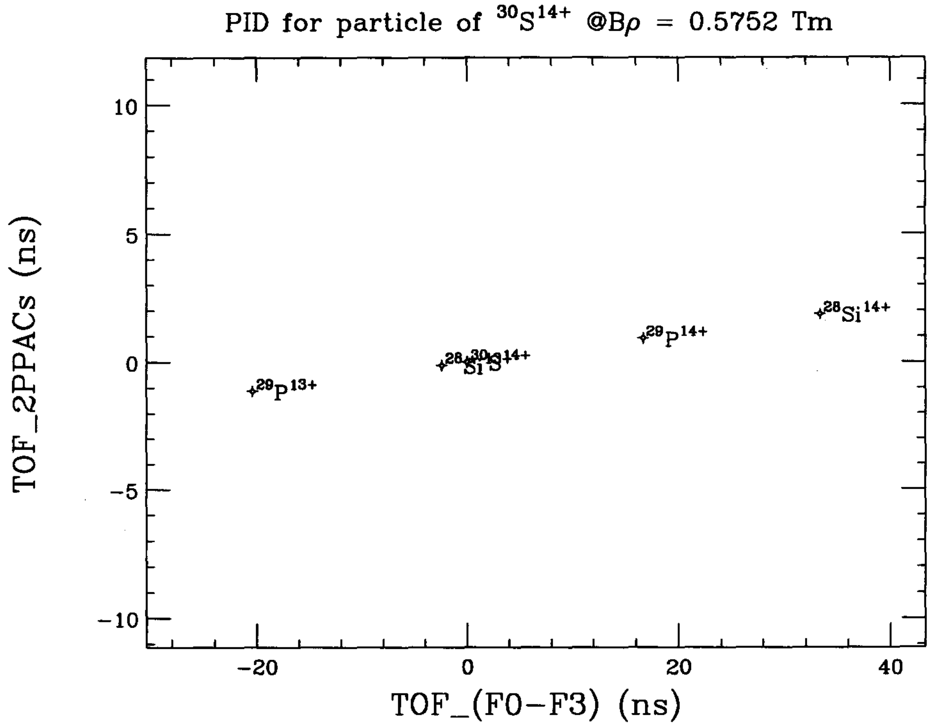

Figure 6.15: The plot shows predicted time of flight from F0 $\rightarrow$ F3 PPACa (corresponding to $RF0$) on the abscissa and time of flight between F3 PPACa and PPACb on the ordinate for various charge-states of nuclear species under the run conditions. The plot is calculated and generated by the CRIB Optimizer program. The species of interest, $^{30}S^{14+}$, is very close to the primary beam charge-state $^{28}Si^{13+}$ due to similar $\frac{A}{q}$. The CRIB Optimizer does not predict the intensity of beam ions.

6.5 $^{30}S^{14+}$ Results

Due to time constraints, we only had the chance to begin scanning the $^{30}S^{+14}$ charge-state in our December 2006 run. However, we separated $^{30}S^{+14}$ in May 2008 and we achieved beams on target with 1.2×10^4 pps per 10 pnA, 32 ± 2 MeV, and 0.8% purity. It is quite likely the purity of $^{30}S^{+14}$ can be increased by optimizing CRIB facility parameters, but we did not have ample time to do so in May 2008. The predicted spectrum for *RF time* vs. *ToF* is shown in Figure 6.15, and the run data are shown in Figure 6.16. Knowing that the leaky-beam will have the highest intensity, we identify the particle group above the most intense

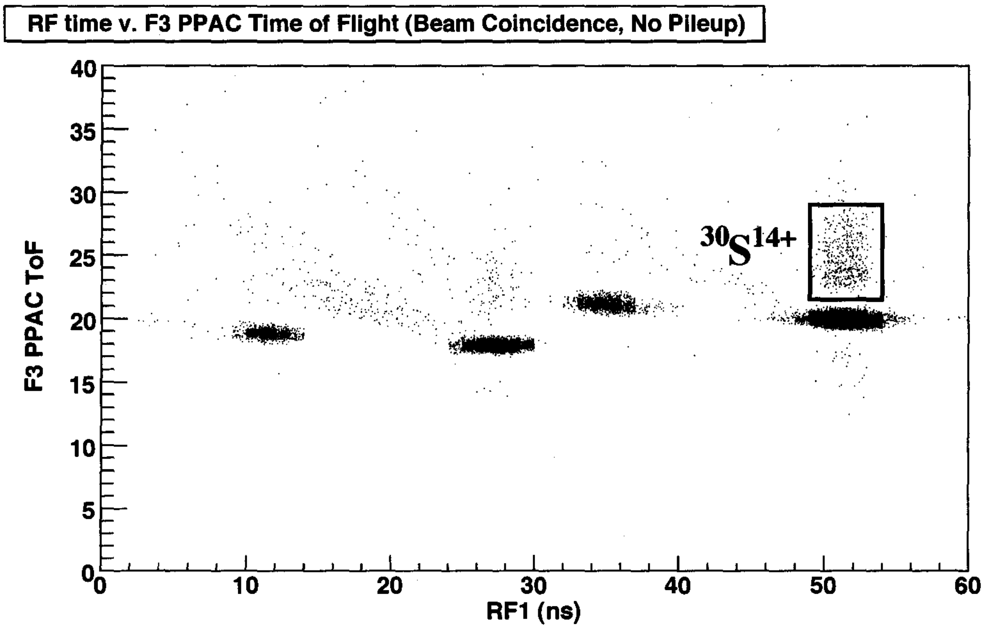

Figure 6.16: The plot shows *RF time* in nanoseconds on the abscissa and F3 PPAC ToF in nanoseconds on the ordinate for the beam after traversing the CRIB, and the Wien Filter is set to ~60 kV for run 154 in May 2008. The species of interest, $^{30}S^{14+}$, is indicated. The data collection period is 640 seconds, a total of 93,714 particles are detected, 586 of which are identified as $^{30}S^{14+}$.

group as $^{30}S^{+14}$, consistent with the CRIB Optimizer predictions. This PID is also consistent with the ratio of the intensity of $^{30}S^{+14}$ to $^{28}Si^{+13}$ measured at F2, corroborating the F2 PID (see Section 6.2). $^{30}S^{+14}$ shows up at *RF time* = 0 in the CRIB optimizer prediction because it is defined as the reference particle. The absolute value of the *RF time* for any particle is not of consequence — only the relative *RF time* spacing between particles is used for PID in such a case.

We tested a 1.5 μm aluminized Mylar degrader at F1 for $^{30}S^{+14}$, based on the December 2006 results, which indicate that ^{30}S charge states, with the exception of the fully stripped 16+ state, are highly contaminated by the leaky beam. However, without the degrader, we were surprised to be able to separate $^{30}S^{+14}$ at F3 in the *RF time* vs. *ToF* spectrum. Using the F1 degrader reduced the $^{30}S^{+14}$ intensity by 80%, because after the energy straggling in the Mylar degrader, only 20% of the initial $^{30}S^{+14}$ ions entering the F1 degrader still had the correct $B\rho$ to be focused at F2.

6.6 ^{30}S RI Beam Production Remarks

In May 2008, although the primary beam intensity is an order of magnitude lower than in December 2006, the higher primary beam energy appears to enhance the RI beam production cross sections, consistent with nuclear reaction theory. If all numbers reported here are normalized to the same primary beam intensity[2], one observes that the ^{30}S beam intensities are nearly an order of magnitude higher in May 2008 compared to December 2006 if both experiments had the same primary beam intensity. The intensity difference may not be a full order of magnitude, and it is difficult to quote a firm number, as only $^{30}S^{+16}$ was measured in both experiments (and the December 2006 results for $^{30}S^{+16}$ may not be reliable).

The primary beam energy increase from December 2006 to May 2008, by accelerating a higher charge state of ^{28}Si, was 0.6 MeV/u, which gave notably higher ^{30}S intensities for the same primary beam intensity. The future hope to accelerate $^{28}Si^{+10}$ with an additional 0.5 MeV/u suggests we may obtain yet another order of magnitude energy increase in ^{30}S yield. Furthermore, the $^{28}S^{+10}$ intensity from the ECRIS ought be stable up to at least 30 pnA, yielding a further factor of 3 in ^{30}S yield on target. Thus, extracting a $^{28}Si^{+10}$ beam from the ECRIS at 30 pnA and accelerating the beam to 8 MeV/u in the AVF cyclotron should give a $^{30}S^{+14}$ beam intensity on the order of 1×10^5 pps on target, provided the $^{30}S^{+14}$ purity may be increased above $\sim$1%. Given the entire time spent optimizing the CRIB for $^{30}S^{+14}$ was a mere 6 hours in May 2008, most of which was spent with the F1 Mylar degrader in place, one expects optimizing parameters will increase the $^{30}S^{+14}$ purity significantly (more than 24 hours were spent optimizing the CRIB for $^{30}S^{+16}$ in May 2008, which is a much easier charge state to separate).

Although we could analyze $^{30}S^{+15}$ using a degrader at F1 in the future, the 80%

[2]December 2006 results are normalized to 100 pnA and May 2008 results are normalized to 10 pnA.

transmission loss from momentum straggling in the degrader observed for $^{30}S^{+14}$ indicates that even if the separation of $^{30}S^{+15}$ and $^{28}Si^{+14}$ is possible, the $^{30}S^{+15}$ intensity is still too low for experimental use.

6.7 Charge State Distribution

Although the beam production results presented here are highly stripped charge states of ^{30}S, these charge states are not populated equally. It is not probable for atoms to emerge from the production target in a highly ionized state, as the inner-most (1s orbital) electrons are tightly bound, with binding energy increasing proportionally to Z. As fast ions pass through a medium, electrons are captured by and knocked out of any given ion many times so that a charge-state statistical equilibrium is realized, which does not favor fully stripped atoms. The location and width of the equilibrium peak depends on the specific properties of the ions and target material, and there is no satisfactory theoretical model predicting ion-beam charge-state distributions. Higher energy ions attain a higher charge-state equilibrium, and the more electrons in the target material (which scales with the target Z value), the lower the charge-state equilibrium. But other than these general properties, if one wishes to predict results in the experimental hall, he must rely on previous experimental data and empirical fits.

Intuition indicated that adding a carbon foil after the cryogenic production target in order to strip more electrons from the cocktail beam may result in preferentially populating higher charge-states of interest. The author considered a model by Sayer [SAY77] to compare the charge-state distribution of ^{30}S ions passing through two different materials: ^{3}He gas and carbon foil. Sayer's model predicts the charge-states within a single medium follow an asymmetric Gaussian function depending only on ion velocity and nuclear charge, which he parameterizes for dilute light gases and carbon foils. However, the author was reminded by Professor Kubono that the cocktail beam particles will come into a charge-state equilibrium

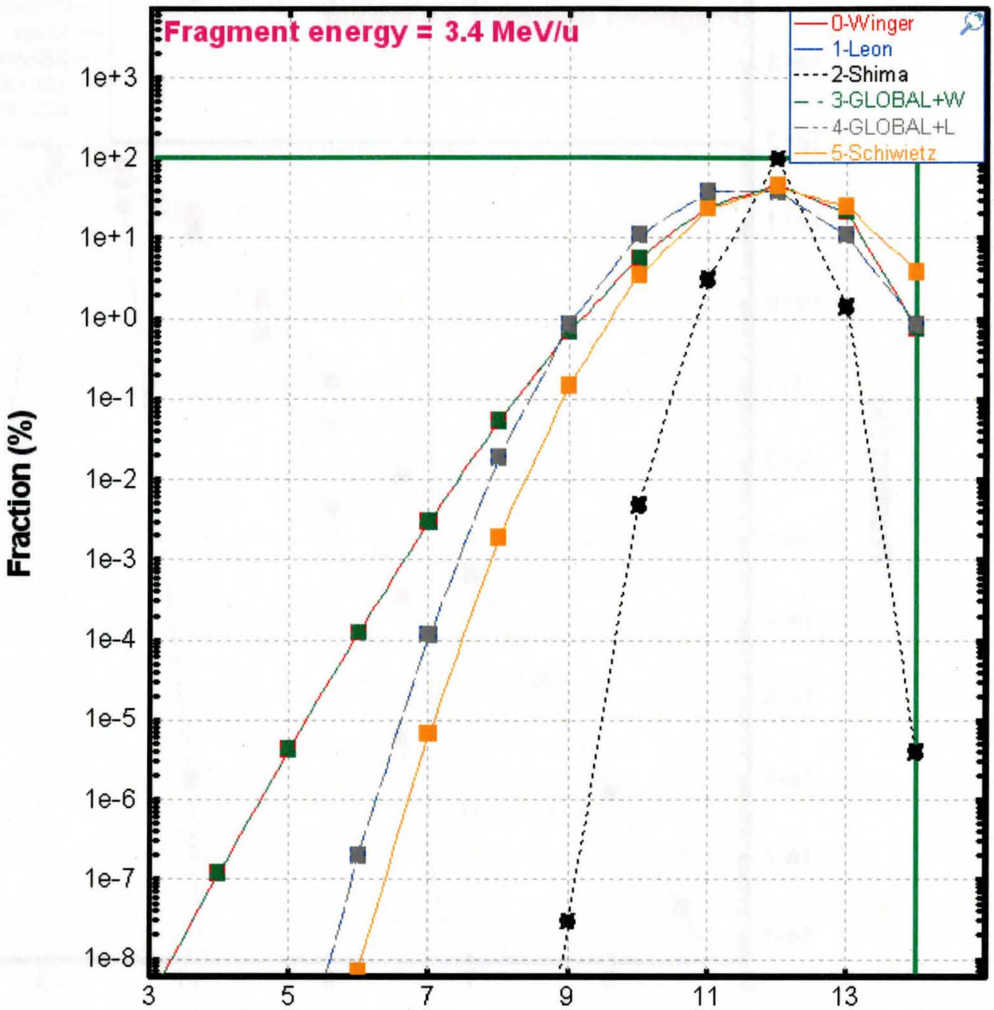

Figure 6.17: The plot shows ^{28}Si charge states on the abscissa against predicted charge state fraction from the LISE++ program in Havar for various theoretical models on the ordinate.

within the cryogenic gas target exit Havar window, and so the charge-state distribution in helium gas is not relevant to the charge-states of particles emerging from the production target. The DRAGON group at TRIUMF used the Sayer model to predict charge-state distribution with good results [VOC07], because the model is applicable to their case due to their use of a low pressure gas in a windowless target. Details of the application of Sayer's model to this case are given in [OUE07].

As Havar foil is a nickel-group alloy, it should still have a lower charge-state

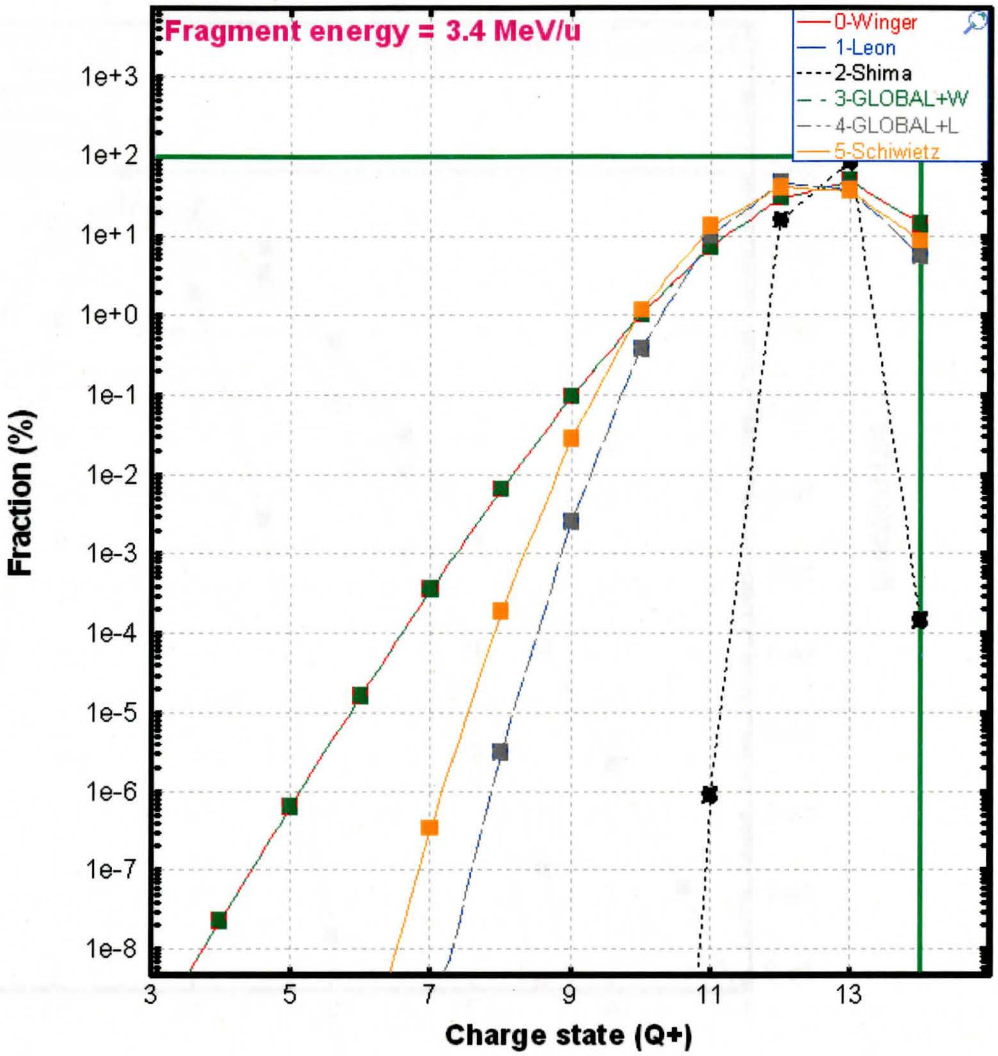

Figure 6.18: The plot shows ^{28}Si charge states on the abscissa against predicted charge state fraction from the LISE++ program in carbon for various theoretical models on the ordinate.

equilibrium than carbon foil. We can then use the LISE++ program to predict charge state distributions of ions in Havar foil compared to carbon foil. Although we attempted to measure charge-state distributions of ^{30}S in Havar and carbon foil in May 2008, a fluctuating primary beam current made normalization of the data impossible. Thus, we decided to measure the charge-state distribution of ^{28}Si ions in Havar and carbon in July 2008. The LISE++ charge-state predictions of ^{28}Si ions of ~95 MeV are shown for Havar in Figure 6.17 and for carbon in Figure

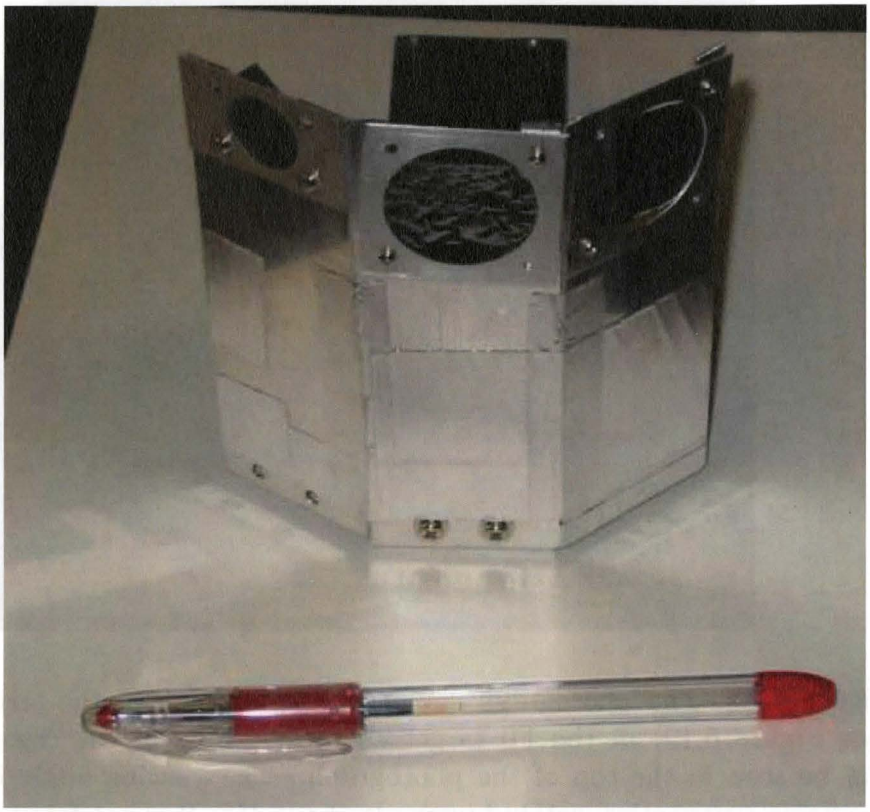

Figure 6.19: The photograph shows the newly designed stripper foil mount, which can hold up to three different foils; a red ball-point pen is also in the image for scale. From left to right, the targets are a carbon foil of 550 μm cm^{-2} thickness, a carbon foil of 508 μm cm^{-2} thickness, and a Havar foil 2.2 μm thick. The mount is designed to affix to a rotating wheel below the F0 cryogenic gas target cell, so that different foils may be rotated behind the production target, or all the foils may be rotated out of the beam line. The different individual target mounts are connected by flexible, yet strong, aluminum tape, so that the beam's normal angle with respect to the foil may be changed during installation, changing the effective target thickness, if desired.

6.18. The author designed and machined a foil mount (see Figure 6.19), which was successfully installed behind the F0 cryogenic production target on a rotating wheel (see Figure 6.20) so that the foils could be changed or removed safely during beam operation.

Because charge state distribution depends on the ion nuclear charge Z and energy, silicon and sulfur ion beams ought have comparable charge-state distri-

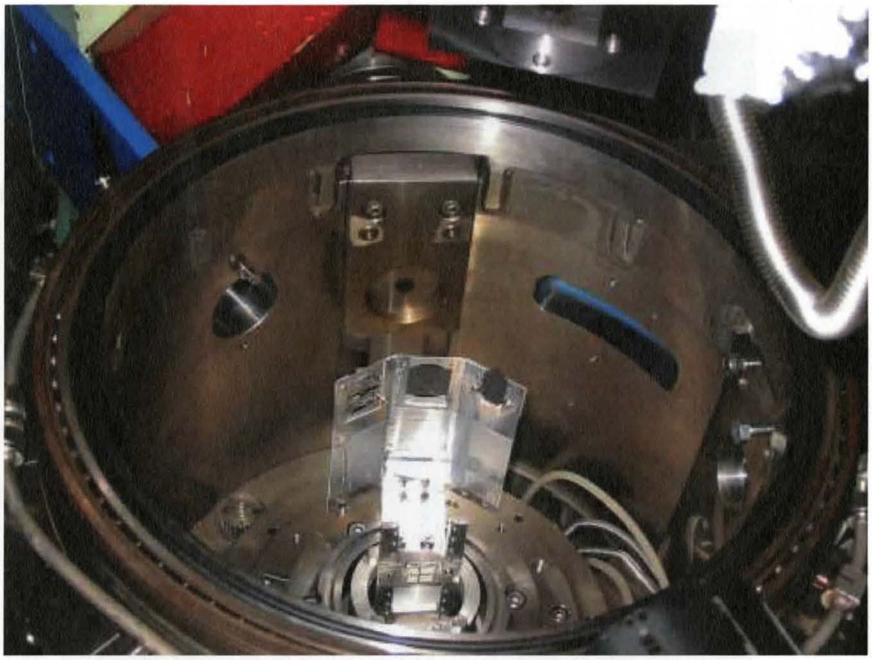

Figure 6.20: The photograph shows the installation of the stripper foil mount (see Figure 6.19) in the F0 target chamber. Part of the cryogenic gas target can be seen in the top of the photograph. The viewing angle is approximately the beam perspective, rotated upwards about 45°. It is not feasible to take a good photograph of both the cryogenic gas target and the stripper foil mount installation simultaneously, because the cryogenic target is affixed to the F0 chamber lid. There are transparent viewing ports, but due to glare and narrow view angles, the view from the F0 viewing ports does not photograph readily.

butions. The ^{28}Si beam energy ($\sim$95 MeV) is comparable to the optimized ^{30}S transmission energies ($\sim$75 MeV) from May 2008. The primary beam intensity was much more stable in July 2008, and so normalization to compare various charge states is possible. The data are listed in Table 6.7 and plotted in Figure 6.21. The results show that silicon has a higher charge-state equilibrium in carbon compared to Havar. Thus, it is postulated that for future experiments, we may increase the charge-state equilibrium of ^{30}S by putting a carbon stripper foil immediately after the F0 cryogenic gas target before reaction products enter the first magnetic dipole D1.

Run number	Target	Species	Time seconds	Counts particles	$\langle I \rangle$ enA	Attn. matter	Normalized pps @ 10 enA
35	Havar	$^{28}Si^{12+}$	541.4	58,178	10	10^{-7}	1.075×10^8
36	Havar	$^{28}Si^{13+}$	615.9	27,775	7.5	10^{-7}	6.013×10^7
37	Havar	$^{28}Si^{14+}$	569.2	155,420	7	10^{-5}	3.901×10^6
38	Carbon	$^{28}Si^{12+}$	564.0	69,409	7	10^{-7}	1.758×10^8
39	Carbon	$^{28}Si^{13+}$	600.6	54,647	7	10^{-7}	1.300×10^8
40	Carbon	$^{28}Si^{14+}$	600.7	18,354	7	10^{-7}	4.365×10^7

Table 6.2: Intensity of highly-stripped charge states of the stable nucleus ^{28}Si after passing through Havar foil or carbon foil. The Havar foil thickness is 2.2 μm, and the carbon foil thickness is 550 μm/cm^2. The ^{28}Si beam energy emerging from the AVF cyclotron is 134.6 MeV, but the beam energy is reduced by impinging first on a 6.47 μm Havar foil, reducing the average beam particle energy to 94.6 MeV. The ^{28}Si particles emerge from the 2.2 μm Havar foil with an average of 77.7 MeV and the 550 μm/cm^2 carbon foil with an average of 85.2 MeV. The intensity of ^{28}Si from the ECR ion source decreased slightly during the experiment. The emerging particles are separated with the D1 magnet and detected with the F1 PPAC. The PPAC cannot handle much above 10^6 pps, so the beam is highly attenuated prior to entering the CRIB. Run times are roughly 10 minutes each, and the data are normalized for comparison. The data indicate that the charge state equilibrium is higher in carbon compared to Havar for ^{28}Si ions with 3.4 MeV/u.

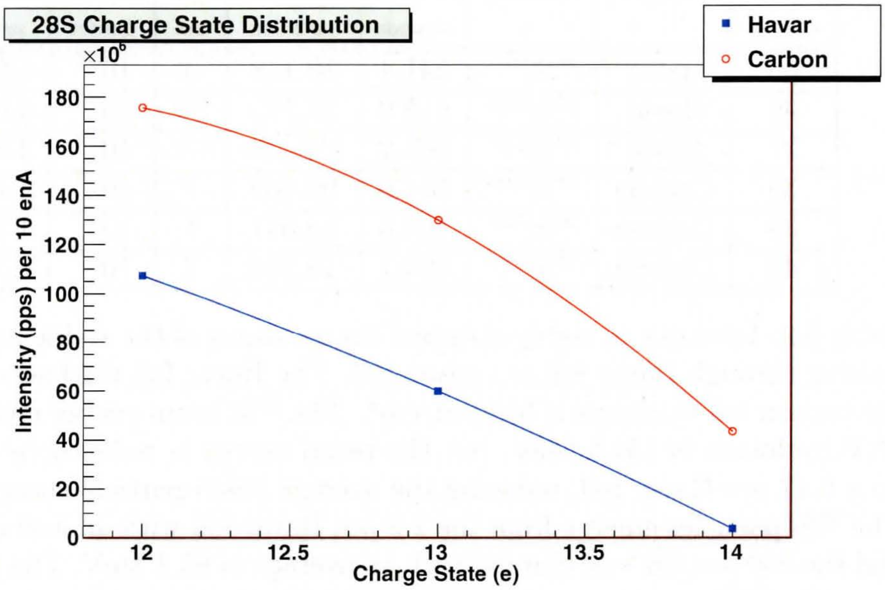

Figure 6.21: The plot shows ^{28}Si charge states on the abscissa against beam intensity in particles per second normalized to primary beam intensity 10 enA on the ordinate. The data are recorded in Table 6.7. To make firm conclusions about the charge state equilibrium, we should also measure lower charge states of ^{28}Si to find the mean charge state; however, during the July 2008 experiment we did not consider this fact.

Chapter 7

Future Work

It is anticipated that with a $^{28}Si^{10+}$ beam accelerated to 8 MeV/u at 30 pnA and with a carbon stripper foil placed after the cryogenic production target of ^{3}He gas of pressure $\geq$ 400 Torr at F0, the requisite ^{30}S beam of 32.3 MeV at 1×10^5 pps required by the Hauser-Feshbach statistical model (see Section 3.6.1) can be produced to successfully measure the $^{4}He(^{30}S,p)$ cross-section in 2009. However, there is still much work to do with regard to the (α,p) reaction technique development, which is anticipated to be part of the author's Ph.D. thesis work at the University of Tokyo under the supervision of Professor KUBONO Shigeru in collaboration with the McMaster University group, where Dr. Alan CHEN will continue to be the $^{30}S(\alpha$,p) experiment spokesperson.

7.1 Present (α,p) Technique

We have seen that many (α,p) reactions are of great importance to astrophysical phenomena as a mechanism to by-pass β-decay waiting point nuclei, particularly the explosive nuclear burning in X-ray bursts and novæ, such as $^{14}O(\alpha$,p), $^{18}Ne(\alpha$,p), $^{22}Mg(\alpha$,p), $^{30}S(\alpha$,p), $^{34}Ar(\alpha$,p), among many others. However, only $^{18}Ne(\alpha$,p) has been experimentally measured [BRA99a, BRA99b, GRO02] at Louvain-la-Neuve in Belgium. RI beam development and (α,p) cross-section measurement technique for astrophysics have proven to be very challenging tasks in the experimental nuclear physics community. Currently at CNS of the University of Tokyo, a number of (α,p) experiments are in the works, such as ^{11}C(α,p), ^{14}O(α,p), ^{21}Na(α,p), and ^{30}S(α,p), and provided this thesis is correct, all four of these (α,p) reactions have RI beams ready to go (the other three were developed independent of the author) for the cross-section measurements once a successful (α,p) technique is developed.

The proposed (α,p) technique will reconstruct event-by-event beam ions as they traverse the F3 PPACs. When a ^{30}S ion is identified, we will look for protons in the downstream $\Delta E - E$ silicon telescopes for each ^{30}S event (see Figure 7.3). By considering the individual ^{30}S ion trajectories obtained from the F3 PPACs and the position of reaction protons, we plan to geometrically determine the position of the reaction within the F3 helium gas target to determine the individual reaction centre-of-mass energy. Thus, our energy resolution is dependent on our ability to reconstruct the position of the reaction within the target, because the beam energy decreases as it passes through the helium gas. However, for the originally proposed (α,p) technique (see Section 5.5) a gas target merely 30 mm in length at pressures above an atmosphere (1100 Torr ^{4}He gas is required in a 30 mm gas cell to scan both the 1 GK and 2 GK Gamow window for ^{30}S(α,p), see Section 3.6.1), the energy straggling of the beam and ejecta in the target may result in significant uncertainties. Indeed, a similar experiment attempting to measure ^{4}He(^{14}O,p) in December 2006 has not yet arrived at conclusive cross-section results.

In principle, the originally proposed setup allows one to obtain an integrated cross-section over the entire Gamow window, but because we scan beginning at 2 GK, and yet X-ray burst peak temperatures only achieve 1.3 GK, if there are α-cluster resonances in the compound nucleus ^{34}Ar, we might have difficulty determing if those resonances are at astrophysically accessible temperatures (see Figure 3.12). Furthermore, as the solid angle of each of the three $\Delta E - E$ detectors is on the order of 0.05 sr each (see Figure 5.7), naïvely assuming the ejecta are emitted isotropically in the laboratory reference frame, the detectors only cover $\frac{0.15}{4\pi} \sim 1.2\%$ of the 4π solid angle, if the Hauser-Feshbach cross-section is correct, we would detect 50 of the 4,213 protons predicted to be ejected under our planned run conditions over the course of 11 days of beam time. Of course, the ejecta are forward focused due to reaction kinematics, increasing the yield by perhaps a factor of four allowing the detection of 200 events. 200 events will likely give us good enough statistics to calculate an integrated cross-section, but the Hauser-Feshbach model predicts all those protons are from reactions above astrophysically relevant temperatures.

As a result, the setup described in Section 5.5 has since been modified to include an extended gas cell of a new design, 87.5 mm in length and 8.1 mm in width, allowing for lower pressures of helium gas in a larger volume to scan the Gamow window with the same ^{30}S RI beam. The extended gas cell length to the RI beam will make our reaction position projections more precise and thus more precise determination of individual reaction energies. The new design was proposed by Professor KUBONO Shigeru, and fabricated in the summer of 2008 for another measurement of ^{14}O+α (the author collaborated on this June 2008 experiment). A very similar setup was then used in July 2008 for a measurement of the previously measured ^{28}Si+α reaction; the author proposed this experiment after Dr. Chris WREDE suggested in 2007 that we calibrate our (α,p) technique with a known reaction to confirm our detection efficiency. The ^{28}Si+α experiment was chosen as a calibration reaction to take place during the ^{30}S(α,p) cross-section measurement experiment in 2009 because it involves the primary beam ^{28}Si used in the ^{30}S RI beam production (and then we could also be assured that the physical setup is identical for the two measurements), but the ^{28}Si+α calibration reaction was deemed important enough to merit a two day experiment in July 2008. These results are currently under analysis, and it is hoped the analysis will be complete before the ^{4}He(^{30}S,p) experiment is conducted in 2009, at which time we may also spend some beam time calibrating the exact experimental setup with ^{28}Si+α.

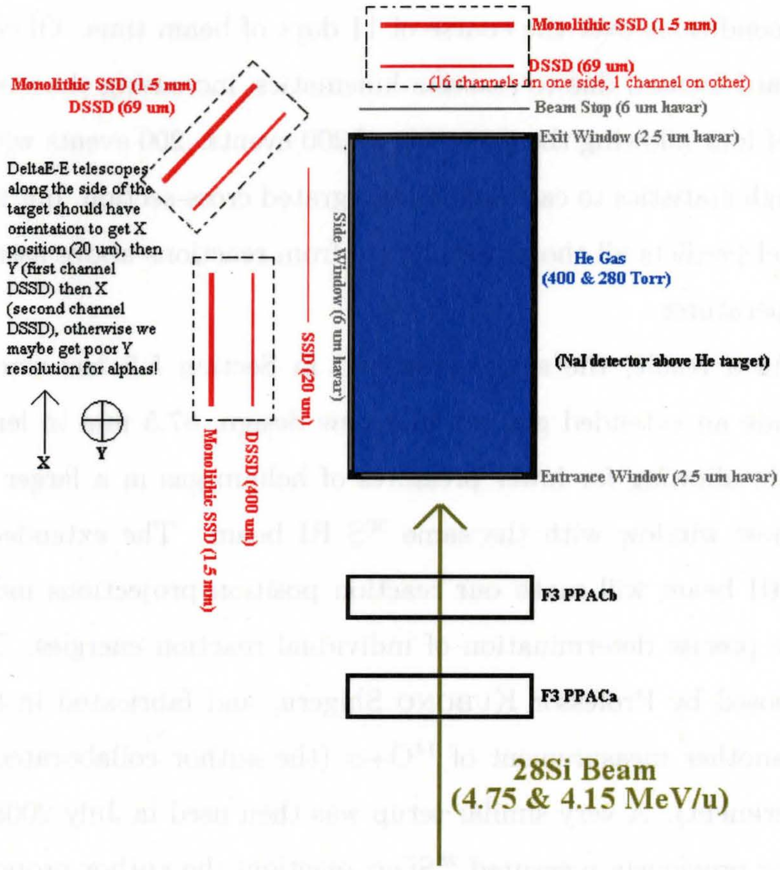

Figure 7.1: New (α,p) experimental setup used in July 2008 for the ^{28}Si+α reaction. The gas cell is extended in length, and has windows on the front, back, and one side. Detectors are placed very close to the exit windows to maximize the detection solid angle. More silicon detectors are available, but we did not want to risk damaging them in this test run with the recently designed gas target. The schematic is not to scale.

7.2 ^{28}Si+^{4}He Experiment Conducted in July 2008

We measured ^{28}Si(α,p) and concurrently ^{28}Si(α,α') in inverse kinematics at three beam energies, two of which have overlapping E_{cm} in the helium gas (held at between 345 and 400 Torr), allowing us to scan E_{cm} 10.3–5.4 MeV and 3.8–1.8 MeV

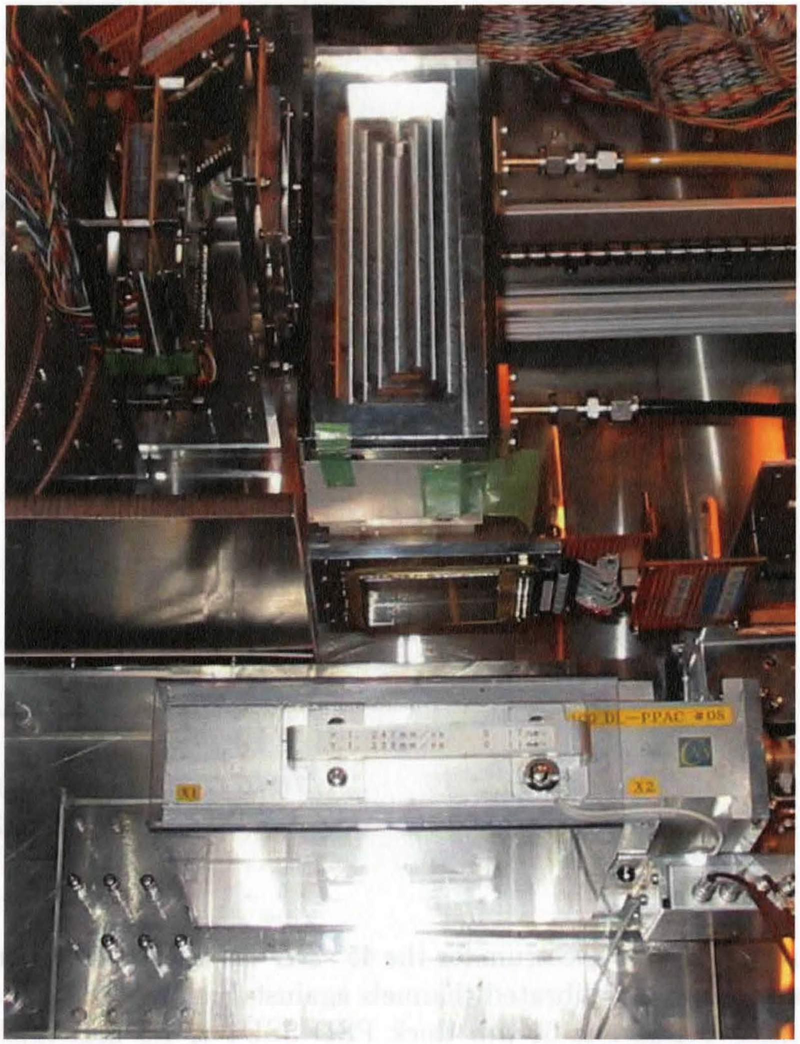

Figure 7.2: Photographic birds-eye-view of the F3 chamber for the July 2008 ^{28}Si experiment, corresponding to the schematic in Figure 7.1. Only the F3 PPACb is visible at the bottom of the picture, and the gas cell is clearly visible, surrounded closely by silicon detectors.

($Q_{\alpha,p} = -1.916$, so we scan down to the lowest energy the ^{4}He(^{28}Si,p) reaction can occur), or equivalently the excitation energy range E_x 17.3–12.4 MeV and 10.8–8.8 MeV in the compound nucleus ^{32}S. Once the data are analyzed, we may compare the ^{28}Si(α,p) results to 21 data points reported in [BUC84] from $5.47 \leq E_{cm} \leq$ 10.06 MeV and 46 reported levels in the compound nucleus ^{32}S reported from ^{28}Si elastic α-scattering reported with computed Γ, Γ_α, and l values [KÄL03] from

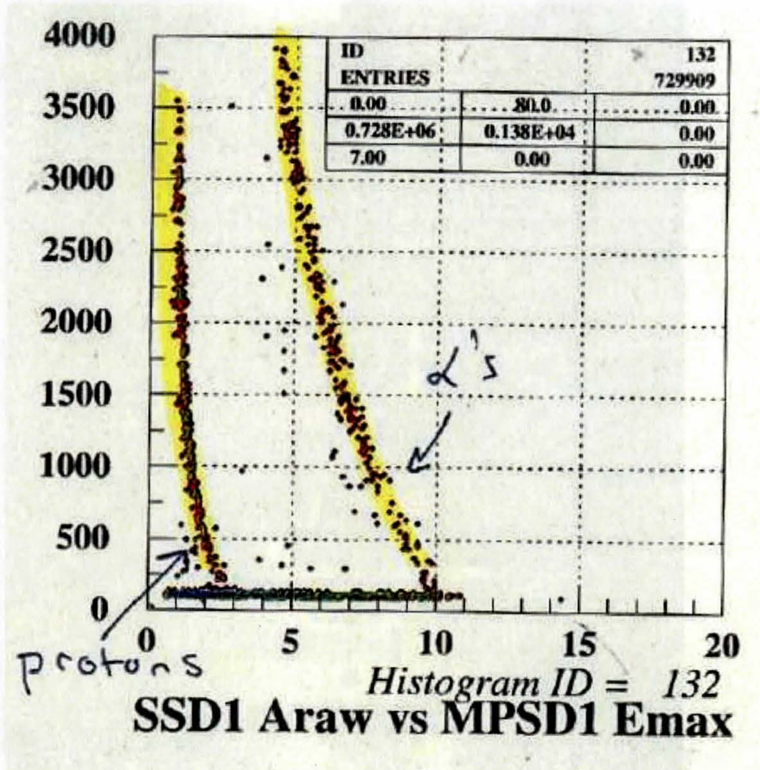

Figure 7.3: Online spectrum for the 45° $\Delta E - E$ telescopes, where ΔE is plotted on the abscissa in uncalibrated channels against E along the ordinate in uncalibrated channels. MPSD1 is 69 μm thick PSD SSD1 is 1.5 mm thick. Because energy loss of radiation matter goes as Z^2, α particles lose more energy in the thin PSD than protons, making a clear ejecta PID using the $\Delta E - E$ method. The run number is 15, for the high energy (relative to other energies tested) ^{28}Si beam with $E_{beam} = 82.3$ MeV on target. There is 400 Torr of helium in the gas target.

$12.93 \leq E_x \leq 17.25$ MeV, allowing us to obtain a good understanding of what resolution our (α,p) and elastic α-scattering setup is able to achieve. The low energy, $8.8 \leq E_x \leq 10.8$, in the ^{32}S compound nucleus, also corresponds to the early phases of silicon burning in massive stars via ^{28}Si(α,γ)^{32}S at T = 3 GK, which is not measured by [KÄL03] by elastic scattering, but is directly measured at astrophysical energies [BAB02].

There are also some previously unmeasured astrophysical applications of the

^{28}Si+α experiment. The $1.82 \leq E_{cm} \leq 3.84$ MeV energy scan corresponds to ^{28}Si(α,p) energies which occur during explosive carbon burning at $1.8 \leq T_9 \leq 2.2$ (where T_9 is temperature in GK) [CLA74], although the 'simmering' of carbon prior to the Type Ia supernova explosion of a white dwarf that has exceeded the Chandrasekhar limit (see Equation 2.8) occurs at a temperature $T = 0.7$ GK [BRO08], which we do not scan. One may also deduce properties of the time-reversal reaction ^{31}P(p,α)^{28}Si, which is astrophysically important in the SiP hydrogen burning cycle (see Equation A.14) up to $T = 0.4$ GK until the ^{31}P(p,γ) breaks out of the SiP cycle [ILI93] (see Section A.3). The Gamow window for ^{31}P(p,α)^{28}Si (the 'forward' reaction) at $T = 0.4$ GK is $0.26 \leq E_{cm\rightarrow} \leq 0.53$ MeV, corresponding to energies $2.18 \leq E_{\leftarrow cm} \leq 2.45$ MeV for the time-reversed ('backwards') reaction ^{28}Si(α,p). Since our experiment scans down to the proton threshold in ^{32}S, our measurement covers all important astrophysical energies for ^{31}P(p,α), which is still uncertain at the lowest energies.

A new detector system, where the detectors reside inside the helium gas target chamber, was recently developed at KEK, called the gated multiple-sampling and tracking proportional chamber (GMSTPC) [HAS06], and the primary investigator (PI) of the GMSTPC, Dr. HASHIMOTO, is now a research associate in the CNS astrophysics group, so this detection method may be implemented for future CRIB experiments. In this setup, the detector and target are combined, leading to the ability to track reactions as they occur by tracking charged particle tracks with a large solid angle coverage.

7.3 Outlook for ^{30}S(α,p) and ^{34}Ar States

The author is also working on a proposal to investigate the structure of ^{34}Ar via ^{36}Ar(α,^{6}He)^{34}Ar at a high resolution spectrometer, such as the Enge Spectrograph at the WNSL of Yale University, pending the results of current experimental work investigating the structure of ^{30}S (the structure of ^{30}S itself is not related to the

^{30}S(α,p) reaction) using the thin target method (see Section 3.6.1). The structure of ^{30}S is currently being investigated by the McMaster group (PI Kiana SETOODEH NIA) at the WNSL via ^{32}S(p,t)^{30}S. One experimental run was already conducted in May 2008, where one of the ^{32}S targets used was implanted ^{32}S in natural carbon foil from the University of Washington at Seattle. Kiana SETOODEH NIA has been working with Professor William LENNARD of the University of Western Ontario to implant ^{32}S in an isotopically pure ^{12}C foil. The structure of ^{34}Ar is difficult to analyze through normal spectrometry methods because it is a noble gas and not easily made into a thin target, as the confining windows in a gas cell would likely induce unacceptable straggling of the ejecta and beam. However, because ^{36}Ar is a noble gas, it cannot be accelerated by a Tandem accelerator (see Section 4.2.1), such as the one at Western Ontario, and we would need to go elsewhere to attempt implanting ^{36}Ar in carbon foil to produce the thin ^{36}Ar target required for a ^{36}Ar(α,^{6}He)^{34}Ar measurement. ^{36}Ar also has a very low natural abundance (0.34%) and is thus expensive.

Noble gases are notoriously difficult to implant, because the sublimation energy is very low and much gas may leak out over time, although the author is aware of a ^{20}Ne implanted target in carbon foil which was used successfully in experiments at the WNSL. Professor Lennard has suggested the implantation of ^{36}Ar is difficult enough to warrant a Master's thesis project of its own, and it is hoped that this thesis, in support of investigating the ^{30}S XRB waiting point proposed by Fisker, Thielemann and Wiescher [FIS04], will lead to the undertaking of this project. If a thin target of ^{36}Ar implanted in carbon foil (isotopically pure or natural) is fabricated, one could also measure the ^{36}Ar(p,t)^{34}Ar reaction. Using the (p,t) reaction to populate states in ^{34}Ar may be advantageous, as the (α,^{6}He) mechanism preferentially populates unnatural partiy states in the compound nucleus (compared to the (p,t) reaction) [TAN81], and we are interested in any natural parity, α-cluster resonances that may exist in ^{34}Ar. The Coulomb barrier for the (p,t) reaction is also smaller than the Coulomb barrier for (α,^{6}He) reaction, meaning we could expect a higher (p,t) reaction cross section, and hence collect better statistics over the same experiment time compared to the (α,^{6}He) mechanism.

The author has discussed the possibility of studying the structure of ^{34}Ar by gamma-ray spectroscopy with David CROSS, a graduate student at TRIUMF. It should be possible to populate excited states of ^{34}Ar via the β-delayed proton decay of ^{35}Ca [TRI99], although at this time it is uncertain if the excitation energy in ^{34}Ar would correspond to the X-ray burst Gamow window.

The structure of ^{33}Ar was studied by the ^{1}H(^{34}Ar,d)^{33}Ar at the NSCL, where the ^{34}Ar beam is made by fragmentation (see Section 4.1.2.1) of a ^{36}Ar beam of 150 MeV/u impinging on a ^{9}Be target [CLE04], and one could make a ^{35}Ar beam and perform a similar experiment to study the structure of ^{34}Ar via ^{1}H(^{35}Ar,d)^{34}Ar, though this method is less likely than other methods to populate α-cluster resonances relevant to the ^{30}S(α,p) stellar reaction rate.

A second proposal (see Section 4.2.1) to study ^{30}S(α,p) via the time-inversed reaction ^{1}H(^{33}Cl,^{4}He)^{30}S at ANL was independently proposed by Dr. Catherine DEIBEL, working with Dr. K. Ernst REHM, who supervised the author as a summer student in 2005 and served as an excellent resource of information for this thesis work. The author hopes that if the Argonne PAC approves the experiment, we may have fruitful discussions about the astrophysical reaction ^{30}S(α,p), or that a collaborative effort will emerge between CNS, ANL, and McMaster.

It is also possible to study the structure of the ^{34}Ar nucleus via ^{12}C(^{28}Si,^{6}He)^{34}Ar or ^{28}Si(^{12}C,^{6}He)^{34}Ar at a high resolution spectrograph [CHE99, CHE01, SET07], although the Coulomb barrier for this nuclear structure probe for ^{34}Ar is quite high, as well as the energy straggling of beam and ejecta, which go as Z^2, in the silicon target ought to be very large and is much less for a carbon target with a silicon beam. Out of all the proposed probes of ^{34}Ar, the (^{12}C,^{6}He) mechanism seems the least promising, but the experimental setup is the least complicated, and the experiment could be carried out with available beams and targets at WNSL.

With the wealth of available mechanisms to study the structure of the compound nucleus ^{34}Ar, and the well-documented importance of the ^{30}S(α,p) reaction in X-ray bursts, it comes as quite a surprise that so little information is known about ^{34}Ar above the α-threshold. The lack of information about ^{34}Ar above the α-threshold is certainly not a consequence of a shortage of viable experimental options, which need only be pursued by present or future experimental nuclear astrophysicsits. However, it is believed that the ^{30}S beam development results presented in this thesis will lead to a successful direct measurement of the ^{4}He(^{30}S,p) cross section at X-ray burst energies at the CRIB facility, so that others may be motivated to confirm or refute the results by using indirect nuclear structure probes of the ^{34}Ar nucleus or perform other direct measurements of ^{30}S(α,p) in time-reversal or inverse laboratory kinematics. Probing nuclear structure with indirect measurements is very important for identifying the energy of resonances. Such an eventuality is welcomed and encouraged by the author and his collaborators and colleagues in the scientific pursuit of understanding the nucleosynthetic energy generation in Type I X-ray bursts.

Appendix A

Hydrogen Burning

A basic understanding of hydrogen burning is critical in nuclear astrophysics, because 90% of the atoms in the universe are hydrogen [CLA03], and stars spend a majority of their nucleosynthetic lives on the main sequence supported by core hydrogen fusion.

Except for the *rp* process, hydrogen fusion may be accomplished through many cycles, or catalytic loops, which convert ^{1}H to ^{4}He and are represented schematically as either

$$4p \rightarrow \ ^4He + 2e^+ + 2\nu_e \ \ (Q = 25.71\ MeV) \tag{A.1}$$

or

$$4p + 2e^- \rightarrow \ ^4He + 2\nu_e \ \ (Q = 26.73\ MeV) \tag{A.2}$$

where the leptons are necessary to conserve charge and lepton number when two protons are converted to neutrons, and the Q value is the energy released in these exothermic reactions[1]. Reaction A.1 involves two β^+ decays and reaction A.2 involves two electron captures (EC), where the latter is more likely to occur in volumes of high density.

[1] Endothermic reactions have negative Q values.

A.1 The Proton-Proton Chains

In the first generation of stars (massive low metallicity Population III), there are no CNO catalysts available, because only primordial elements from the Big Bang are available (up to ^{7}Li). Due to the Coulomb barrier between charged particles, some lower mass main-sequence stars like the sun ($M < 1.5M_{\odot}$) cannot achieve core temperatures high enough for the operation of the CNO cycles for core hydrogen burning [WIE99]. In both cases, hydrogen fusion proceeds through the proton-proton (*pp*) chains.

All the *pp* chains begin by converting hydrogen into ^{3}He via

$$p(p, e^{+}\nu_{e})d(p,\gamma)^{3}He \tag{A.3}$$

or in environments of higher density

$$p(e^{-}, \nu_{e})n(p,\gamma)d(p,\gamma)^{3}He \tag{A.4}$$

and ^{4}He is then produced through a number of competing branches

$$^{3}He(^{3}He, pp)\alpha \tag{A.5a}$$

$$^{3}He(^{4}He,\gamma)^{7}Be(e^{-},\nu_{e})^{7}Li(p,\gamma)\alpha \tag{A.5b}$$

$$^{3}He(^{4}He,\gamma)^{7}Be(p,\gamma)^{8}B(e^{+}\nu_{e})^{8}Be(\alpha)\alpha \tag{A.5c}$$

which are denoted as the *pp* I branch (A.5a), *pp* II branch (A.5b), and *pp* III branch (A.5c), respectively. (Note that ^{8}Be is unbound and spontaneously α decays.) In massive Population III stars, the *pp* chains may be linked to the *rp* process via the so-called *rαp* process [WIE89], but otherwise core hydrogen burning in stars above $1.5M_{\odot}$ proceeds via the cold CNO cycle.

A.2 The CNO Cycles

The CNO cycles utilize carbon, nitrogen, oxygen, and fluorine as catalysts to burn hydrogen into helium. These reaction chains can generally be grouped into two sets according to the temperature regimes in which they are active. The cold CNO cycles occur in static stellar hydrogen burning, whereas the hot CNO cycles occur explosive hydrogen burning.

A.2.1 Cold CNO Cycles

Conditions for the cold CNO cycles are $T \approx 2 - 13\ x\ 10^7$ K in main sequence stars with densities $\rho \approx 2\ x\ 10^3 - 2\ x\ 10^5$ kg m^{-3} [HAN94, LUNA06], and $T \approx 5 - 8\ x\ 10^7$ K in hydrogen shell burning off the main sequence at densities $\rho \approx 20$ kg m^{-3} [FOR97]. The cold CNO cycles take place on timescales where β^+ decays are faster than proton capture rates. Thus, the individual cycles have timescales set by the lowest Q_p value, or nuclear species with the lowest energy released by proton capture. The cold CNO reaction network is

$$^{12}C(p,\gamma)^{13}N(e^+\nu_e)^{13}C(p,\gamma)^{14}N(p,\gamma)^{15}O(e^+\nu_e)^{15}N(p,\alpha)^{12}C \tag{A.6a}$$

$$^{15}N(p,\gamma)^{16}O(p,\gamma)^{17}F(e^+\nu_e)^{17}O(p,\alpha)^{14}N \tag{A.6b}$$

$$^{17}O(p,\gamma)^{18}F(e^+\nu_e)^{18}O(p,\alpha)^{15}N \tag{A.6c}$$

$$^{18}O(p,\gamma)^{19}F(p,\alpha)^{16}O \tag{A.6d}$$

The limiting reaction in the CN cycle A.6a is ^{14}N(p,γ) [LUNA06], which is about two orders of magnitude stronger than the limiting reaction in the ON cycles A.6b-d ^{16}O(p,γ) [WIE99]. The branching ratio between the CN and ON cycles is thus determined by the ratio of the rates of the reactions ^{15}N(p,γ)^{16}O/^{15}N(p,α)^{12}C [RED82], and an equilibrium is established [CAU62].

Material can escape, or break-out[2] from, the CNO cycles via

$$^{19}F(p,\gamma)^{20}Ne \tag{A.7}$$

because the reaction flow past ^{20}Ne is irreversible. At higher temperatures, one must also include the hot CNO reaction paths.

A.2.2 β-Limited Hot CNO Cycles

The hot CNO (HCNO) cycles occur in electron degenerate gases in hydrogen-rich, runaway thermonuclear explosive environments found in novæ and x-ray bursts. Novæ conditions at peak are $T \approx 2 - 3.5\ x\ 10^8$ K [TRU90, STA98] with densities $\rho \approx 5\ x\ 10^5 - 5\ x\ 10^6$ kg m^{-3} [WIE99], and x-ray burst triggering conditions are $T \approx 1 - 2\ x\ 10^8$ K at extreme densities $\rho \approx 10^9 - 10^{10}$ kg m^{-3} [TAA96]; less than half the energy released in x-ray bursts originates from the HCNO cycles [WAL81], which is why the triggering conditions (instead of peak conditions) are provided here for x-ray bursts. Due to the high temperatures and densities in novæ and x-ray bursts, the burning takes place on timescales where β^+ lifetimes are less than proton capture rates, and hence the fusion is β-limited. Although weak decays are insensitive to temperature, proton capture rates are highly temperature dependent. When the temperature is high enough, the proton capture rates exceed the decay half-lives of radioactive nuclei in the cycles. Thus, the individual cycles have timescales set by the slowest β^+ decays in the sequence, called *waiting point nuclei*, ^{14}O ($t_{1/2}$=70.641 seconds), ^{15}O ($t_{1/2}$=122.24 seconds), and ^{18}Ne ($t_{1/2}$=1.672 seconds). As a result, the hydrogen burning rate is a fixed function of the CNO mass fraction Z_{CNO}

$$\epsilon_{CNO} = 4.6x10^{11} Z_{CNO}\ (J\ kg^{-1}\ s^{-1}) \tag{A.8}$$

[2]Break-out reactions from the CNO cycles indicate that via hydrogen burning and weak decays, the material cannot re-enter the CNO cycles as catalyst material.

as detailed in [HOY65, WIE99]. The time to consume all the hydrogen is then $\approx \frac{790s}{Z_{CNO}}$, which is only 1 day for solar metallicity [SCH99], indicating the HCNO cycle is not a form of quiescent hydrogen burning.

The HCNO reaction network is, in addition to the catalytic cycles A.6a-d:

$$^{12}C(p,\gamma)^{13}N(p,\gamma)^{14}O(e^+\nu_e)^{14}N(p,\gamma)^{15}O(e^+\nu_e)^{15}N(p,\alpha)^{12}C \tag{A.9a}$$

$$^{15}N(p,\gamma)^{16}O(p,\gamma)^{17}F(p,\gamma)^{18}Ne(e^+\nu_e)^{18}F(p,\alpha)^{15}O(e^+\nu_e)^{15}N \tag{A.9b}$$

$$^{18}F(p,\gamma)^{19}Ne(e^+\nu_e)^{19}F(p,\alpha)^{16}O \tag{A.9c}$$

At neutron star envelope densities and $T = 4\ x\ 10^8$ K [TAA80], the ^{14}O(α,p)^{17}F reaction may also link the cycles [SCH99] via

$$^{14}O(\alpha,p)^{17}F(p,\gamma)^{18}Ne(e^+\nu_e)^{18}F(p,\alpha)^{15}O(e^+\nu_e)^{15}N \tag{A.10}$$

^{14}O, ^{15}O, and ^{18}Ne are at the proton drip line, and so there are no alternative burning paths circumventing the HCNO cycle as outlined above, although there are possible break-out paths via di-proton capture shown below in A.11c-d. There are many more break-out paths from the HCNO cycles (compared to the cold CNO cycles):

$$^{15}O(\alpha,\gamma)^{19}Ne(p,\gamma)^{20}Na \tag{A.11a}$$

$$^{14}O(\alpha,p)^{17}F(p,\gamma)^{18}Ne(\alpha,p)^{21}Na \tag{A.11b}$$

$$^{15}O(2p,\gamma)^{17}Ne \tag{A.11c}$$

$$^{18}Ne(2p,\gamma)^{20}Mg \tag{A.11d}$$

where the latter two reactions A.11c-d involve proton-unbound intermediary compound nuclei [GÖR95, WIE99]. If the break-out channels are strong enough in the

HCNO cycles, then material flow and hydrogen burning may continue with heavier catalysts.

A.3 Hydrogen Burning in Novæ

As the temperature increases in degenerate explosive environments, the burning will break-out from the HCNO cycles. In x-ray bursts, the hydrogen burning is not generally accomplished by catalytic loops that increase the abundance of helium, and instead hydrogen burning proceeds by the *rp* process, detailed in Chapter Blah; although early break-out from the HCNO cycles in x-ray bursts may resemble the novæ burning pathway [THI94]. However, in the lower (relative to x-ray bursts) temperature and density environments found in novæ, hydrogen continues to be fused into helium through cyclic burning. The distinction between novæ burning and the *rp* process for $A < 40$ is not clear, and at low temperatures, the *rp* process is dominated by such cycles [THI94], and so some authors describe novæ nucleosynthesis as occuring via the *rp* process [ILI99].

These cycles all begin from seed nuclei with an even number of proton and neutrons (even-even) capturing two protons, a β^+-decay, another proton capture and β^+-decay, and then a final (p,α) reaction to close the cycle [THI94]. This cycling is slightly different from the HCNO cycles because the ^{18}F(p,α) reaction is possible [because the alpha threshold in ^{19}Ne is lower than the proton threshold [VAN94]], so the CNO cycles require break-out to the NeNa cycle because ^{19}F(p,γ) is by-passed [THI01]. These cycle closures usually happen at α-nuclei (see Section 2.3), such as ^{12}C, ^{16}O, ^{20}Ne, ^{24}Mg, ^{28}Si, ^{32}S, and ^{36}Ar [THI94]. The (p,α) reactions then happen on targets with $T_z = +\frac{1}{2}$ ($T_z \equiv \frac{N-Z}{2}$): ^{15}N, ^{19}F, ^{23}Na, ^{27}Al, ^{31}P, and ^{35}Cl [THI94]. This creates NeNa-, MgAl-, SiP-, SCl-cycles *etc.*, some of which are explained in more detail presently.

The NeNa cycles (also called the NeNaMg cycles [BOY08]) contain two pathways:

$$^{20}Ne(p,\gamma)^{21}Na(e^+\nu_e)^{21}Ne(p,\gamma)^{22}Na(p,\gamma)^{23}Mg(e^+\nu_e)^{23}Na(p,\alpha)^{20}Ne \quad \text{(A.12a)}$$

$$^{20}Ne(p,\gamma)^{21}Na(p,\gamma)^{22}Mg(e^+\nu_e)^{22}Na(p,\gamma)^{23}Mg(e^+\nu_e)^{23}Na(p,\alpha)^{20}Ne \quad \text{(A.12b)}$$

which are the classical and hot NeNa cycles, respectively [CHE99], and the burning flow is limited either by the β^+ decay of ^{21}Na ($t_{1/2}$=22.49 seconds) in A.12a or the β^+ decay of ^{23}Mg ($t_{1/2}$=11.317 seconds) in A.12b. The two cycles are linked by the proton capture rate ^{21}Na(p,γ) [BIS03a, BIS03b]. Material need not enter from the CNO breakout reaction ^{19}F(p,γ)^{20}Ne, but may also arise through breakout mechanisms such as ^{19}Ne(p,γ)^{20}Na(e^+ ν_e)^{20}Ne or ^{19}Ne(p,γ)^{20}Na(p,γ)^{21}Mg(e^+ ν_e)^{21}Na*(p)^{20}Ne. The NeNa cycles are linked through ^{23}Na(p,γ)^{24}Mg and ^{23}Mg(p,γ)^{24}Al(e^+ ν_e)^{24}Mg to the MgAl cycles.

The MgAl cycles (also called the MgAlSi cycles [BOY08]) contain three pathways, due to the short-lived isomer ^{26}Al^m ($t_{1/2}$=6.345 seconds) populated by the β^+ decay of ^{26}Si (^{26}Al^g ($t_{1/2}$=7.17 x 10^5 years))

$$^{24}Mg(p,\gamma)^{25}Al(e^+\nu_e)^{25}Mg(p,\gamma)^{26}Al^g(p,\gamma)^{27}Si(e^+\nu_e)^{27}Al(p,\alpha)^{24}Mg \quad \text{(A.13a)}$$

$$^{24}Mg(p,\gamma)^{25}Al(p,\gamma)^{26}Si(e^+\nu_e)^{26}Al^m(e^+\nu_e)^{26}Mg(p,\gamma)^{27}Al(p,\alpha)^{24}Mg \quad \text{(A.13b)}$$

$$^{24}Mg(p,\gamma)^{25}Al(p,\gamma)^{26}Si(e^+\nu_e)^{26}Al^m(p,\gamma)^{27}Si(e^+\nu_e)^{27}Al(p,\alpha)^{24}Mg \quad \text{(A.13c)}$$

Burning may break-out from the MgAl cycles via reactions like ^{27}Al(p,γ)^{28}Si. The burning may store material in the SiP cycle, .

$$^{28}Si(p,\gamma)^{29}P(p,\gamma)^{30}S(e^+\nu_e)^{30}P^m(p,\gamma)^{31}S(e^+\nu_e)^{31}P(p,\alpha)^{28}Si \quad \text{(A.14)}$$

depending on the reaction branching ratio ^{31}P(p,γ)/(p,α) [ILI91]

For novæ, where $T = 1 - 3\ x\ 10^8$ K, the $^{31}P(p,\alpha)^{28}Si$ reaction plays an important role and leads to an increased enrichment of Si and S nuclei [ILI93].

In novæ, the burning pathway may continue up to ^{40}Ca in catalytic loops similar to the SiP cycle, such as the SCl cycle [VAN94], depending on the (p,γ)/(p,α) branching ratios on odd-Z, $T_z = +\frac{1}{2}$ nuclei. However, higher temperature *rp* process nucleosynthesis begins to deviate significantly from nova nucleosynthesis beyond the NeNa and MgAl cycles; break-out from these CNO-type cycles above Ne occur at 3 x 10^8 K [THI01]. The list of detailed novæ cycles has been truncated so as not to deviate significantly from the scope of the present work. Typical novæ conditions are $\rho \sim 10^6 kgm^{-3}$ and 1-4 x 10^8 K [THI05].

Appendix B

CRIB Electronics

1

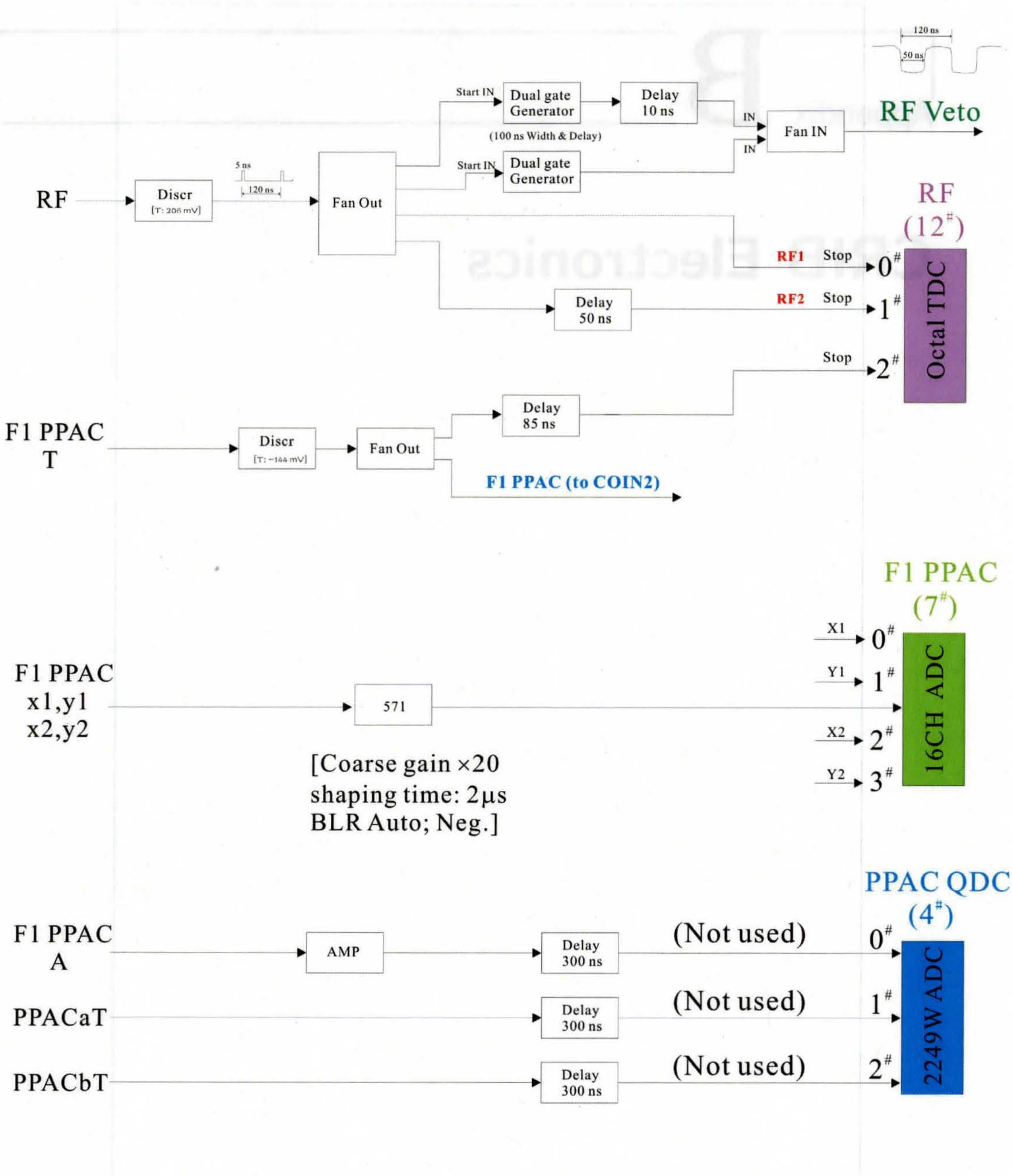

RF
Discr
5 ns
120 ns
Fan Out
Start IN
Dual gate Generator
(100 ns Width & Delay)
Delay 10 ns
IN
Fan IN
RF Veto
120 ns
50 ns
RF (12#)
RF1 Stop 0#
Delay 50 ns
RF2 Stop 1#
Stop 2#
Octal TDC
F1 PPAC T
Discr
Fan Out
Delay 85 ns
F1 PPAC (to COIN2)
F1 PPAC (7#)
F1 PPAC x1,y1 x2,y2
571
[Coarse gain ×20 shaping time: 2μs BLR Auto; Neg.]
X1 0#
Y1 1#
X2 2#
Y2 3#
16CH ADC
PPAC QDC (4#)
F1 PPAC A
AMP
Delay 300 ns
(Not used)
0#
PPACaT
1#
PPACbT
2#
2249W ADC

Figure B.1

2

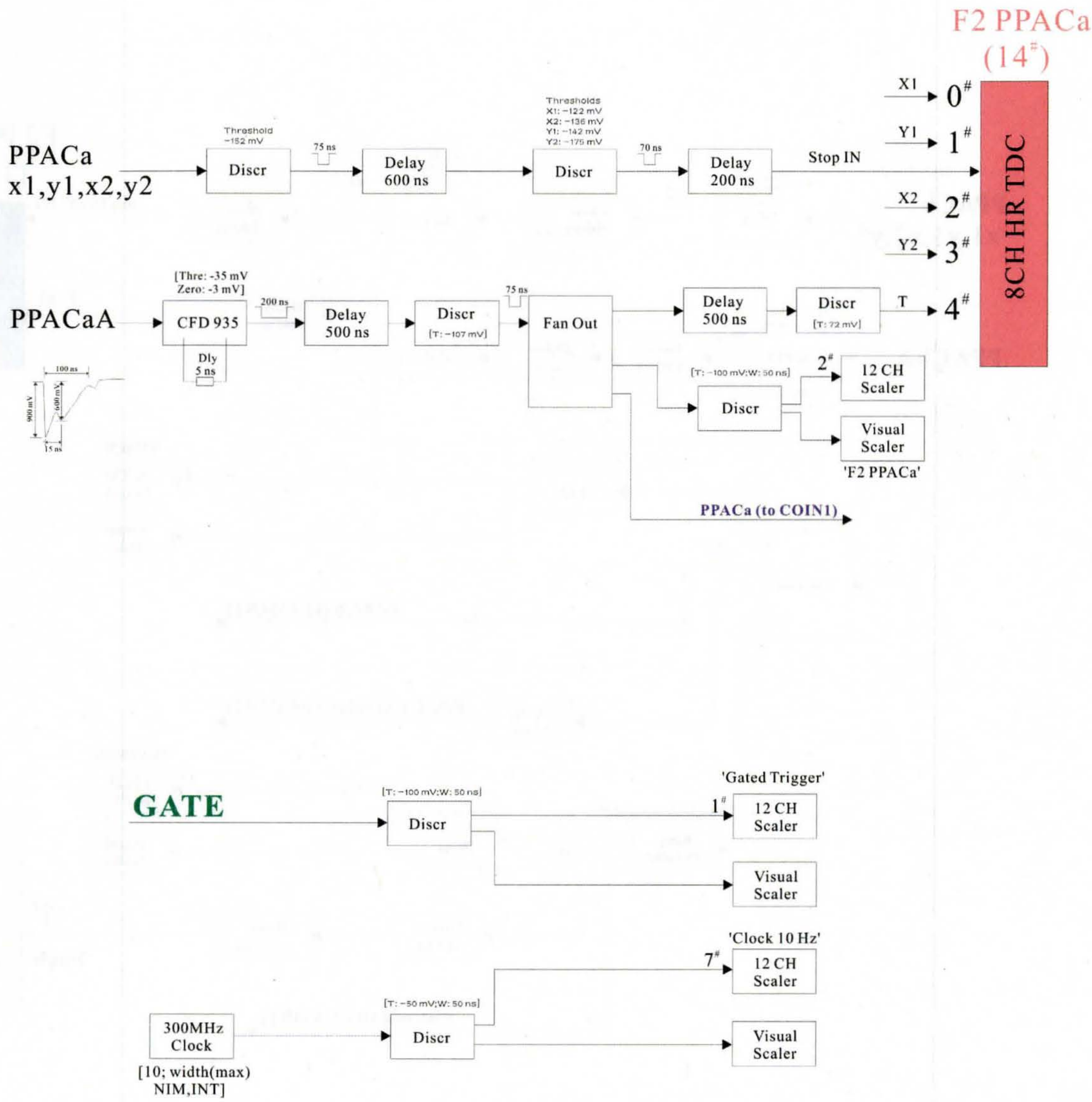
F2 PPACa
(14#)
PPACa
x1,y1,x2,y2
Threshold
−152 mV
Discr
75 ns
Delay
600 ns
Thresholds
X1: −122 mV
X2: −136 mV
Y1: −142 mV
Y2: −175 mV
Discr
70 ns
Delay
200 ns
Stop IN
X1
0#
Y1
1#
X2
2#
Y2
3#
T
4#
8CH HR TDC
PPACaA
[Thre: -35 mV
Zero: -3 mV]
CFD 935
Dly
5 ns
200 ns
Delay
500 ns
Discr
[T: −107 mV]
75 ns
Fan Out
Delay
500 ns
Discr
[T: 72 mV]
100 ns
900 mV
600 mV
15 ns
[T: −100 mV; W: 50 ns]
Discr
2#
12 CH
Scaler
Visual
Scaler
'F2 PPACa'
PPACa (to COIN1)
GATE
[T: −100 mV; W: 50 ns]
Discr
'Gated Trigger'
1#
12 CH
Scaler
Visual
Scaler
'Clock 10 Hz'
7#
12 CH
Scaler
300MHz
Clock
[10; width(max)
NIM,INT]
[T: −50 mV; W: 50 ns]
Discr
Visual
Scaler

Figure B.2

3

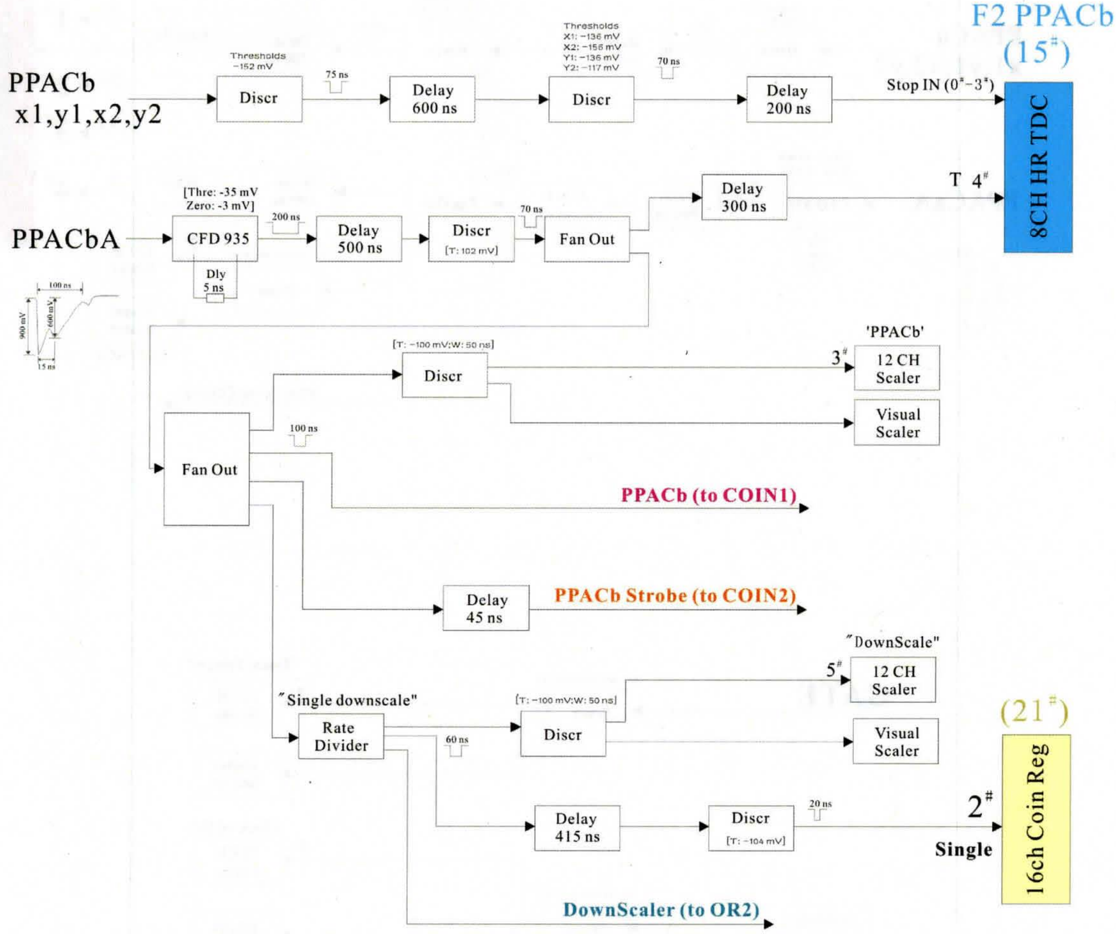
F2 PPACb
(15#)
PPACb
x1,y1,x2,y2
Thresholds
-152 mV
Discr
75 ns
Delay
600 ns
Thresholds
X1: -136 mV
X2: -156 mV
Y1: -136 mV
Y2: -117 mV
Discr
70 ns
Delay
200 ns
Stop IN (0#-3#)
8CH HR TDC
T 4#
Delay
300 ns
PPACbA
[Thre: -35 mV
Zero: -3 mV]
CFD 935
Dly
5 ns
200 ns
Delay
500 ns
Discr
[T: 102 mV]
70 ns
Fan Out
100 ns
900 mV
600 mV
15 ns
'PPACb'
[T: -100 mV;W: 50 ns]
Discr
3#
12 CH
Scaler
Visual
Scaler
Fan Out
100 ns
PPACb (to COIN1)
Delay
45 ns
PPACb Strobe (to COIN2)
"DownScale"
5#
12 CH
Scaler
"Single downscale"
Rate
Divider
60 ns
[T: -100 mV;W: 50 ns]
Discr
Visual
Scaler
(21#)
Delay
415 ns
Discr
[T: -104 mV]
20 ns
2#
Single
16ch Coin Reg
DownScaler (to OR2)

Figure B.3

4

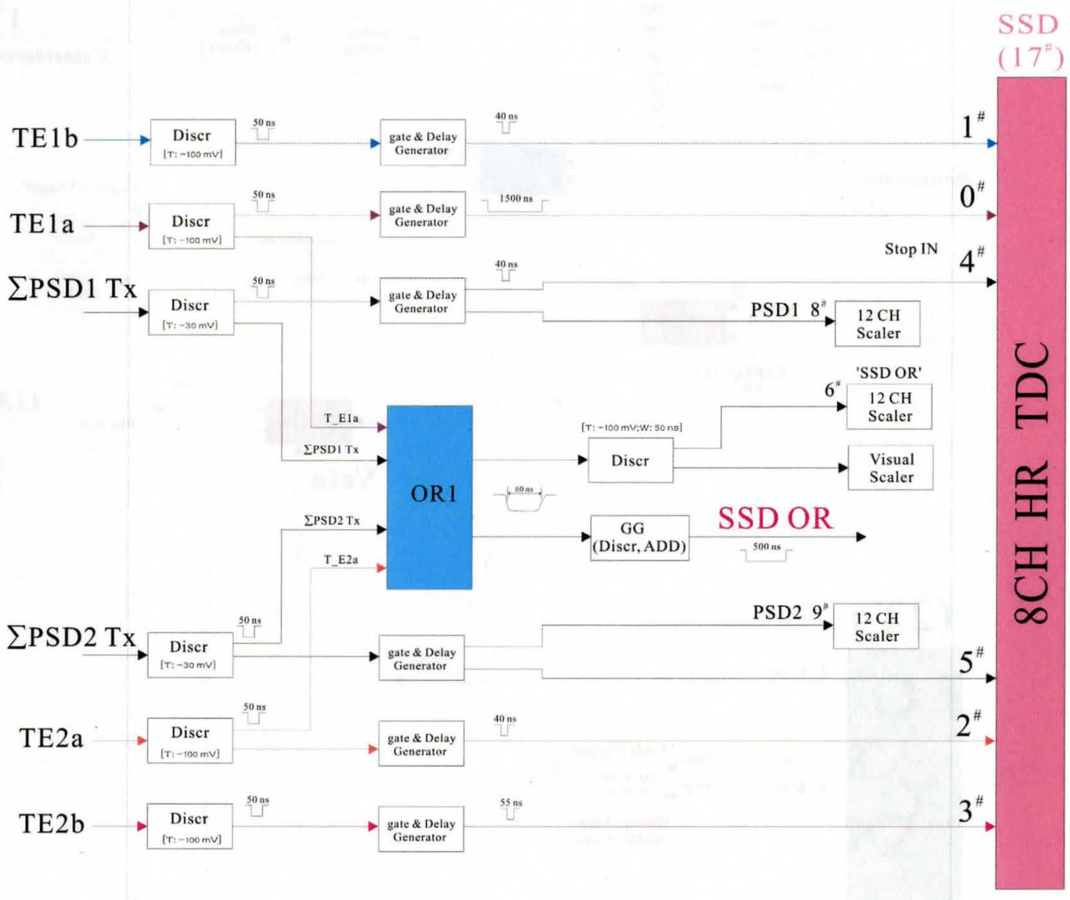
SSD
(17#)
8CH HR TDC
TE1b
TE1a
ΣPSD1 Tx
ΣPSD2 Tx
TE2a
TE2b
Discr
gate & Delay Generator
1#
0#
Stop IN
4#
PSD1 8#
12 CH Scaler
'SSD OR'
6#
Visual Scaler
OR1
GG (Discr, ADD)
SSD OR
PSD2 9#
5#
2#
3#

Figure B.4

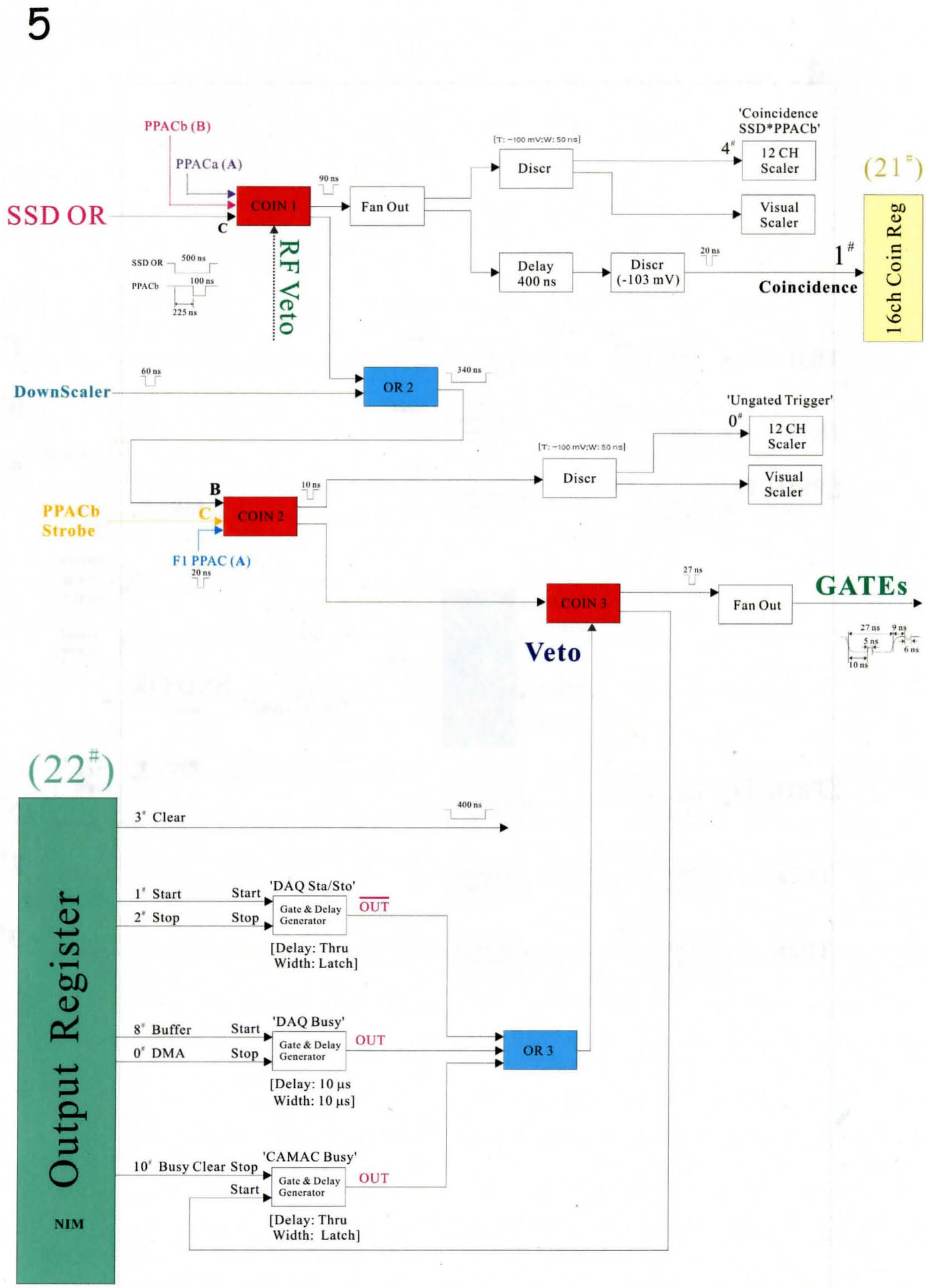
5
PPACb (B)
PPACa (A)
SSD OR
C
COIN 1
90 ns
Fan Out
RF Veto
SSD OR
500 ns
PPACb
100 ns
225 ns
[T: -100 mV; W: 50 ns]
Discr
'Coincidence SSD*PPACb'
4#
12 CH Scaler
Visual Scaler
(21#)
16ch Coin Reg
Delay 400 ns
Discr (-103 mV)
20 ns
1#
Coincidence
DownScaler
60 ns
OR 2
340 ns
'Ungated Trigger'
0#
12 CH Scaler
[T: -100 mV; W: 50 ns]
Discr
Visual Scaler
B
PPACb Strobe
C
COIN 2
10 ns
F1 PPAC (A)
20 ns
27 ns
COIN 3
Fan Out
GATEs
Veto
27 ns
9 ns
5 ns
6 ns
10 ns
(22#)
3# Clear
400 ns
1# Start
Start
'DAQ Sta/Sto'
Gate & Delay Generator
OUT
2# Stop
Stop
[Delay: Thru Width: Latch]
8# Buffer
Start
'DAQ Busy'
Gate & Delay Generator
OUT
0# DMA
Stop
OR 3
[Delay: 10 μs Width: 10 μs]
10# Busy Clear Stop
'CAMAC Busy'
Start
Gate & Delay Generator
OUT
[Delay: Thru Width: Latch]
Output Register
NIM

Figure B.5

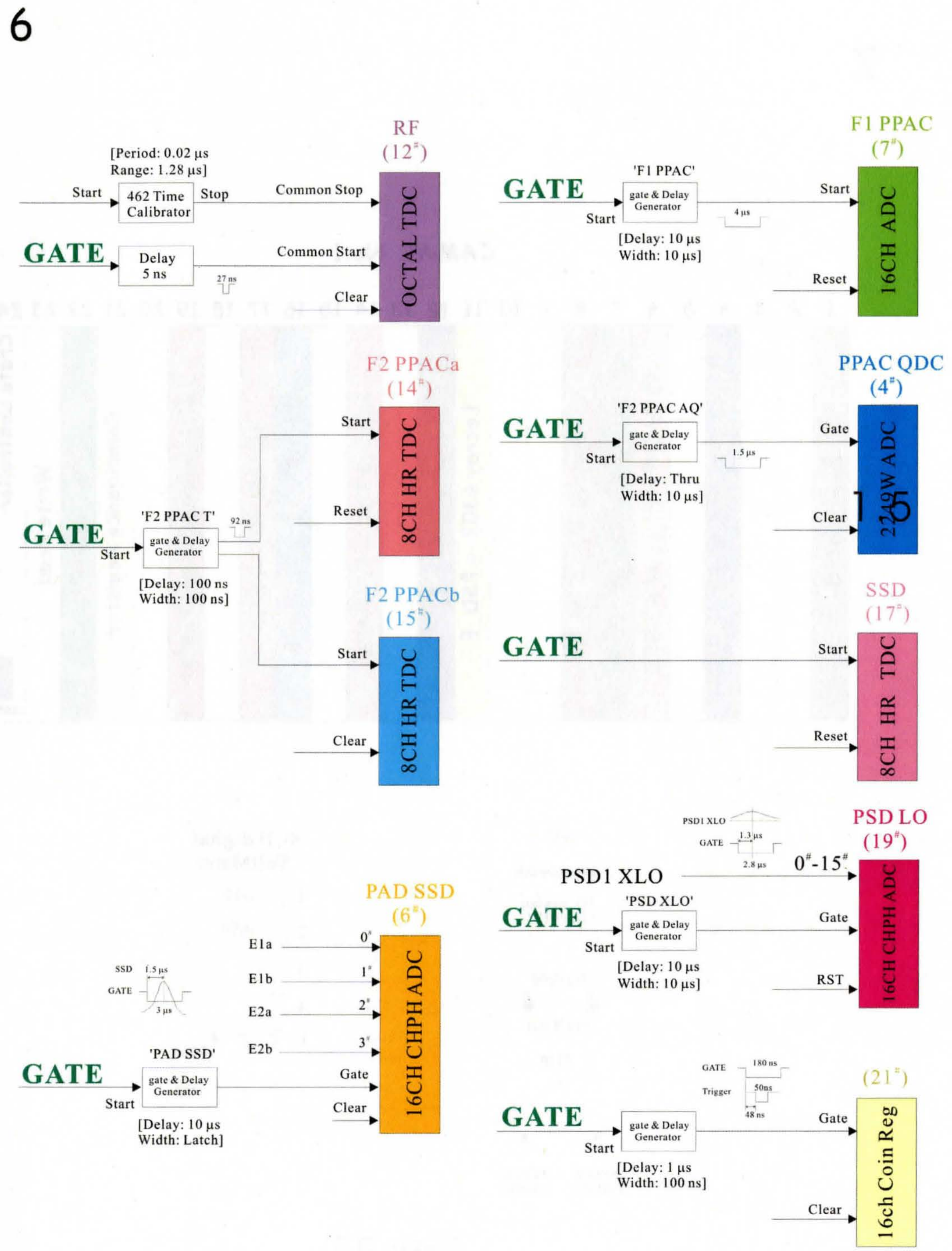
6
RF
(12#)
[Period: 0.02 μs
Range: 1.28 μs]
Start
462 Time Calibrator
Stop
Common Stop
GATE
Delay 5 ns
Common Start
Clear
OCTAL TDC
F1 PPAC
(7#)
'F1 PPAC'
gate & Delay Generator
[Delay: 10 μs
Width: 10 μs]
Reset
16CH ADC
F2 PPACa
(14#)
Start
Reset
8CH HR TDC
'F2 PPAC T'
[Delay: 100 ns
Width: 100 ns]
F2 PPACb
(15#)
Clear
8CH HR TDC
PPAC QDC
(4#)
'F2 PPAC AQ'
[Delay: Thru
Width: 10 μs]
Gate
Clear
22/9W ADC
SSD
(17#)
8CH HR TDC
PSD LO
(19#)
PSD1 XLO
0#-15#
'PSD XLO'
[Delay: 10 μs
Width: 10 μs]
RST
16CH CHPH ADC
PAD SSD
(6#)
E1a
E1b
E2a
E2b
'PAD SSD'
[Delay: 10 μs
Width: Latch]
16CH CHPH ADC
(21#)
[Delay: 1 μs
Width: 100 ns]
16ch Coin Reg

Figure B.6

7

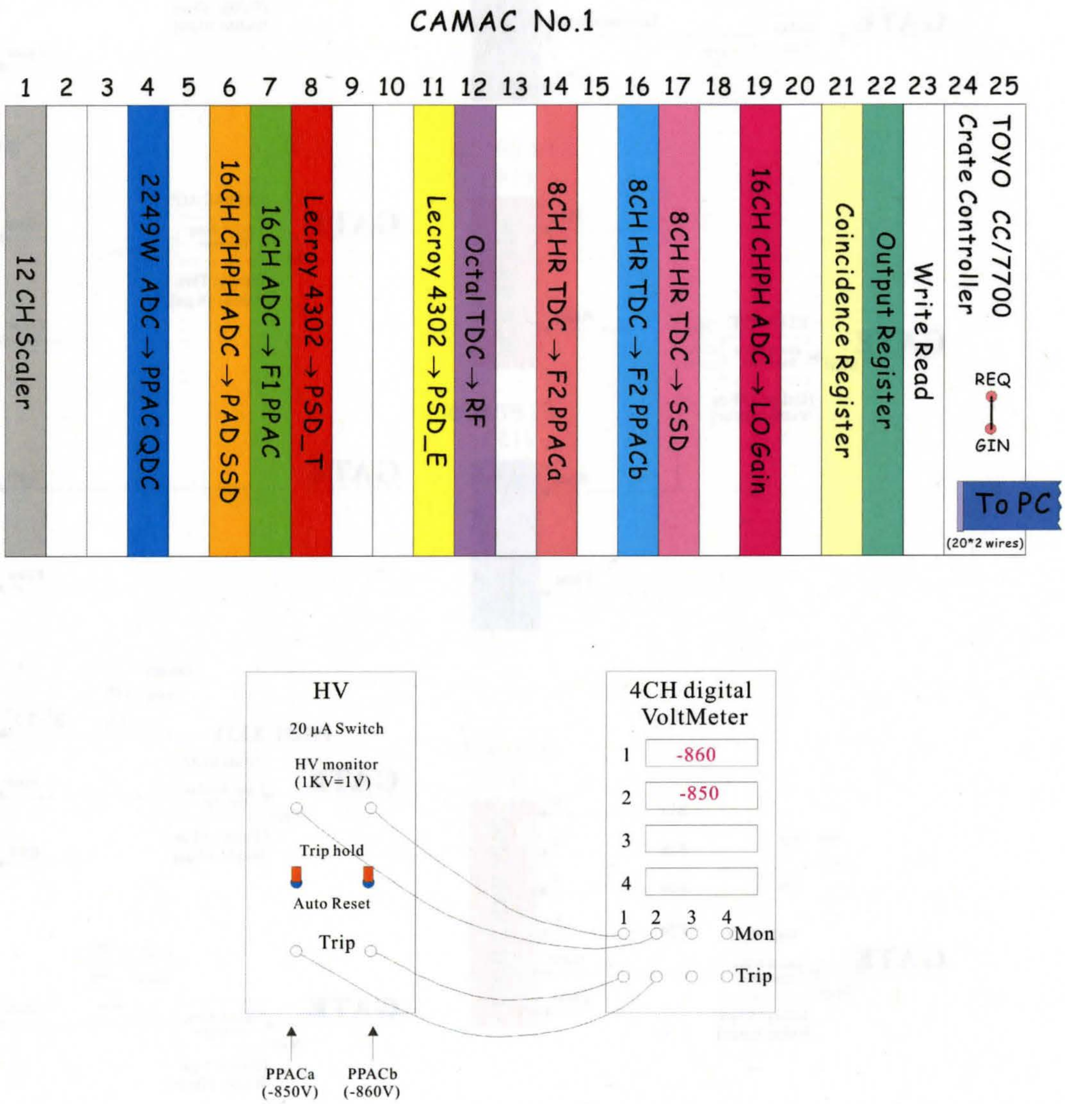
CAMAC No.1
1 2 3 4 5 6 7 8 9 10 11 12 13 14 15 16 17 18 19 20 21 22 23 24 25
12 CH Scaler
2249W ADC → PPAC QDC
16CH CHPH ADC → PAD SSD
16CH ADC → F1 PPAC
Lecroy 4302 → PSD_T
Lecroy 4302 → PSD_E
Octal TDC → RF
8CH HR TDC → F2 PPACa
8CH HR TDC → F2 PPACb
8CH HR TDC → SSD
16CH CHPH ADC → LO Gain
Coincidence Register
Output Register
Write Read
TOYO CC/7700
Crate Controller
REQ
GIN
To PC
(20*2 wires)
HV
20 μA Switch
HV monitor
(1KV=1V)
Trip hold
Auto Reset
Trip
PPACa
(-850V)
PPACb
(-860V)
4CH digital
VoltMeter
1 -860
2 -850
3
4
1 2 3 4
Mon
Trip

Figure B.7

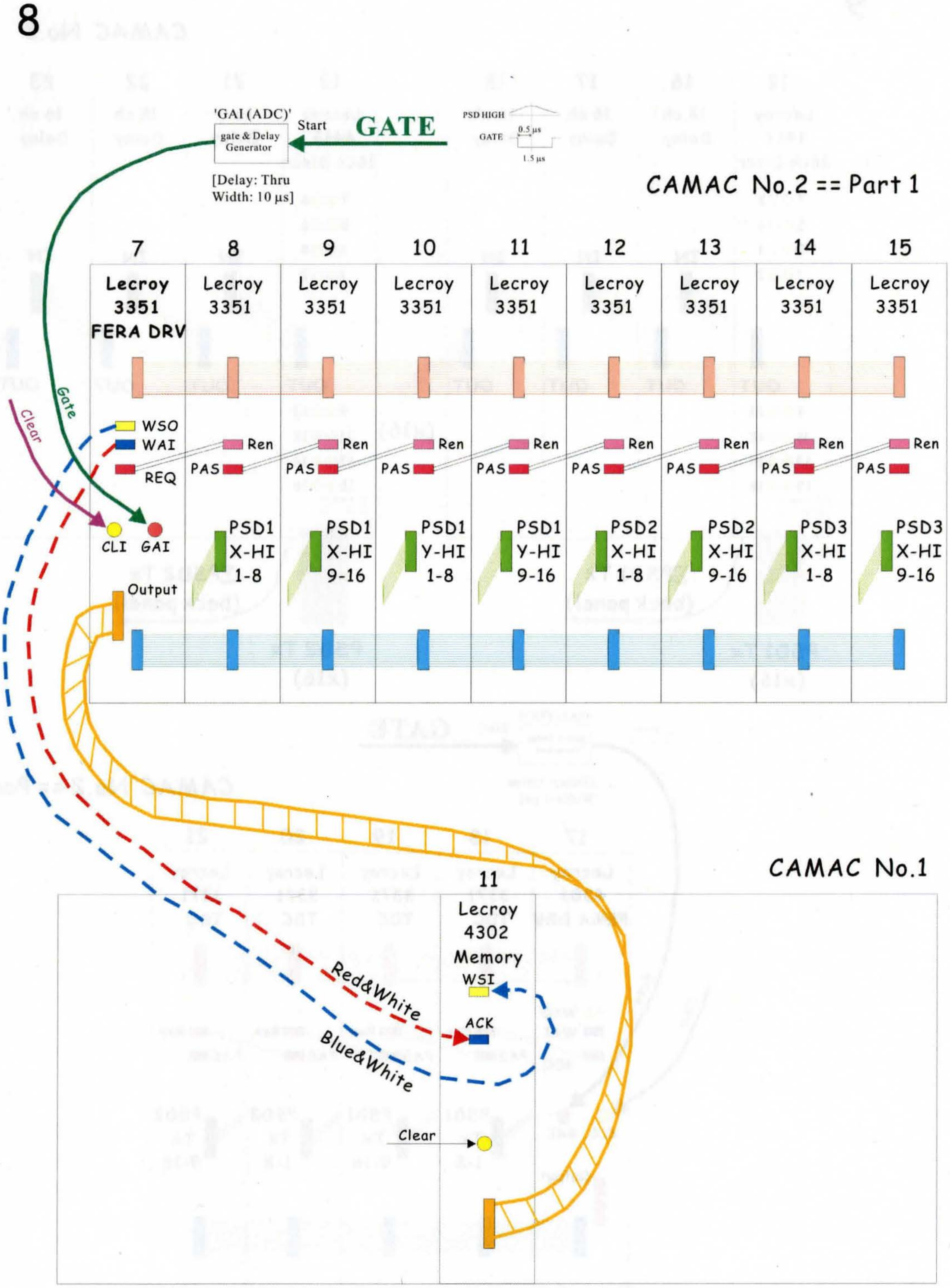
8
'GAI (ADC)'
gate & Delay Generator
Start
GATE
PSD HIGH
GATE
0.5 μs
1.5 μs
[Delay: Thru Width: 10 μs]
CAMAC No.2 == Part 1
7
8
9
10
11
12
13
14
15
Lecroy 3351 FERA DRV
Lecroy 3351
Gate
Clear
WSO
WAI
REQ
Ren
PAS
CLI
GAI
PSD1 X-HI 1-8
PSD1 X-HI 9-16
PSD1 Y-HI 1-8
PSD1 Y-HI 9-16
PSD2 X-HI 1-8
PSD2 X-HI 9-16
PSD3 X-HI 1-8
PSD3 X-HI 9-16
Output
CAMAC No.1
11
Lecroy 4302 Memory
WSI
ACK
Red&White
Blue&White
Clear

Figure B.8

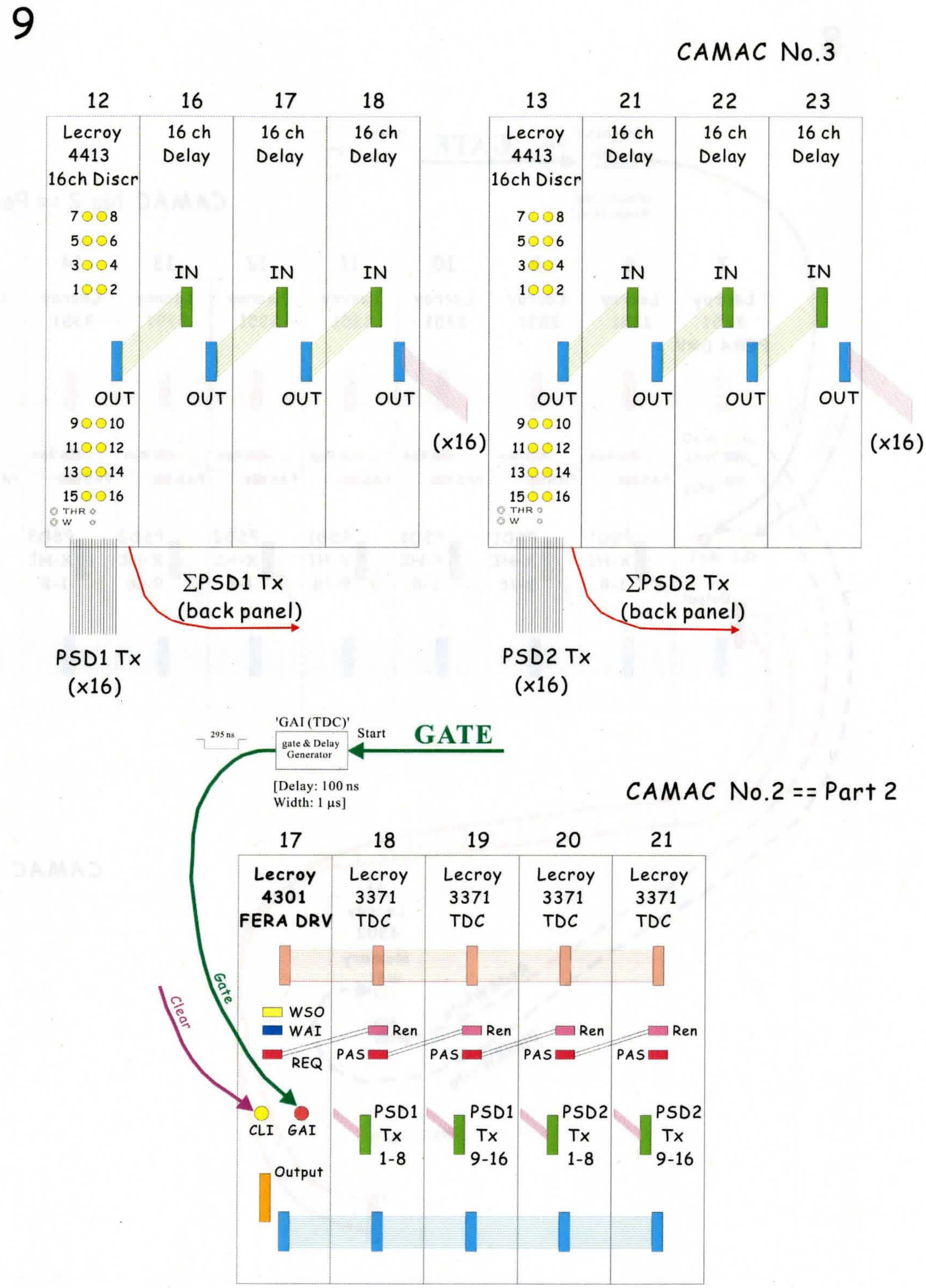
9
CAMAC No.3
12
16
17
18
13
21
22
23
Lecroy 4413 16ch Discr
16 ch Delay
16 ch Delay
16 ch Delay
Lecroy 4413 16ch Discr
16 ch Delay
16 ch Delay
16 ch Delay
IN
OUT
THR
W
(x16)
(x16)
ΣPSD1 Tx (back panel)
ΣPSD2 Tx (back panel)
PSD1 Tx (x16)
PSD2 Tx (x16)
'GAI (TDC)'
gate & Delay Generator
295 ns
Start
GATE
[Delay: 100 ns Width: 1 μs]
CAMAC No.2 == Part 2
17
18
19
20
21
Lecroy 4301 FERA DRV
Lecroy 3371 TDC
Lecroy 3371 TDC
Lecroy 3371 TDC
Lecroy 3371 TDC
Gate
Clear
WSO
WAI
REQ
Ren
PAS
CLI
GAI
Output
PSD1 Tx 1-8
PSD1 Tx 9-16
PSD2 Tx 1-8
PSD2 Tx 9-16

Figure B.9

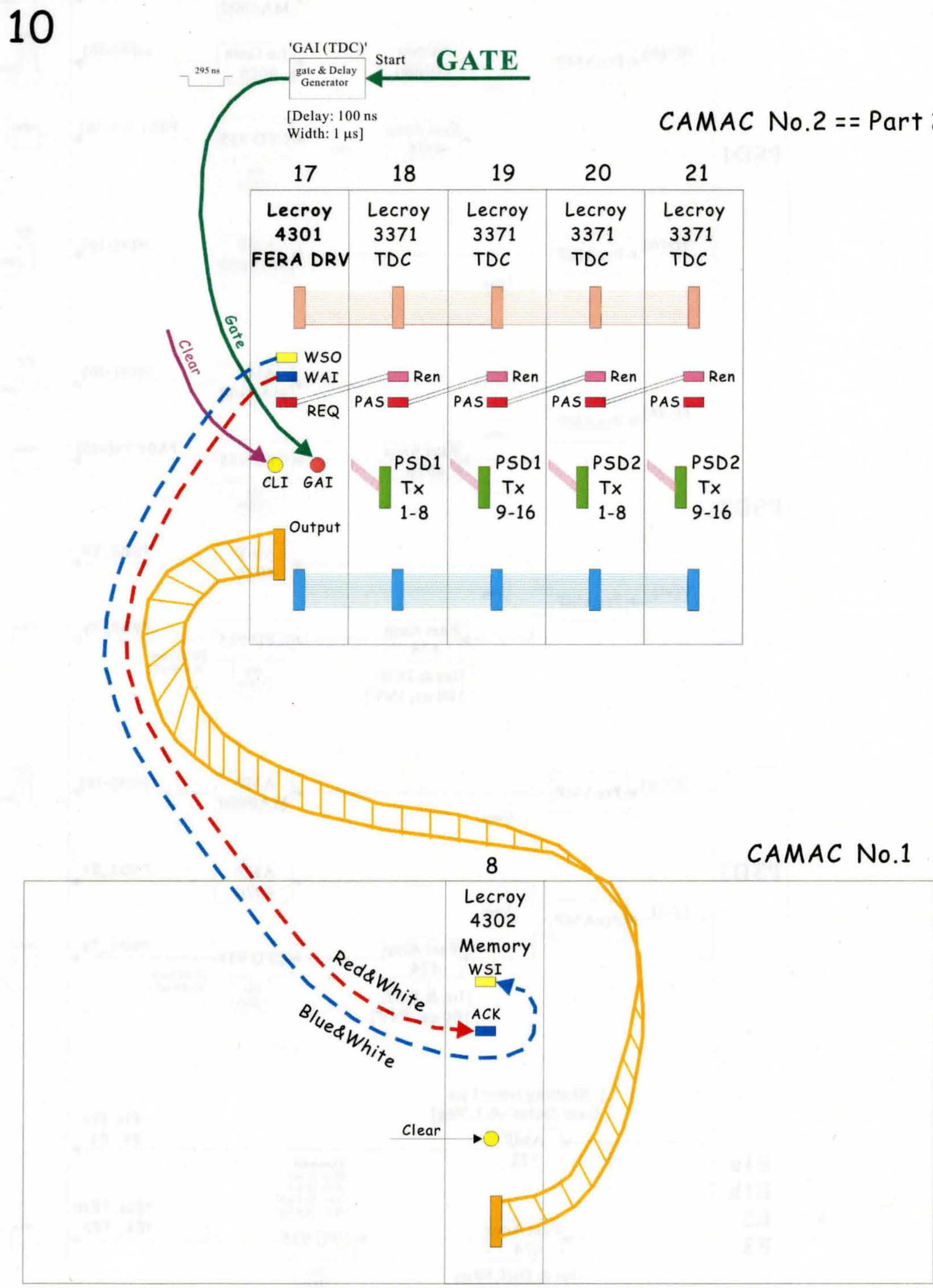
10
'GAI (TDC)'
gate & Delay Generator
295 ns
Start
GATE
[Delay: 100 ns
Width: 1 μs]
CAMAC No.2 == Part 2
17
18
19
20
21
Lecroy 4301 FERA DRV
Lecroy 3371 TDC
Lecroy 3371 TDC
Lecroy 3371 TDC
Lecroy 3371 TDC
Gate
Clear
WSO
WAI
REQ
Ren
PAS
CLI
GAI
PSD1 Tx 1-8
PSD1 Tx 9-16
PSD2 Tx 1-8
PSD2 Tx 9-16
Output
CAMAC No.1
8
Lecroy 4302 Memory
WSI
ACK
Red&White
Blue&White
Clear

Figure B.10

11

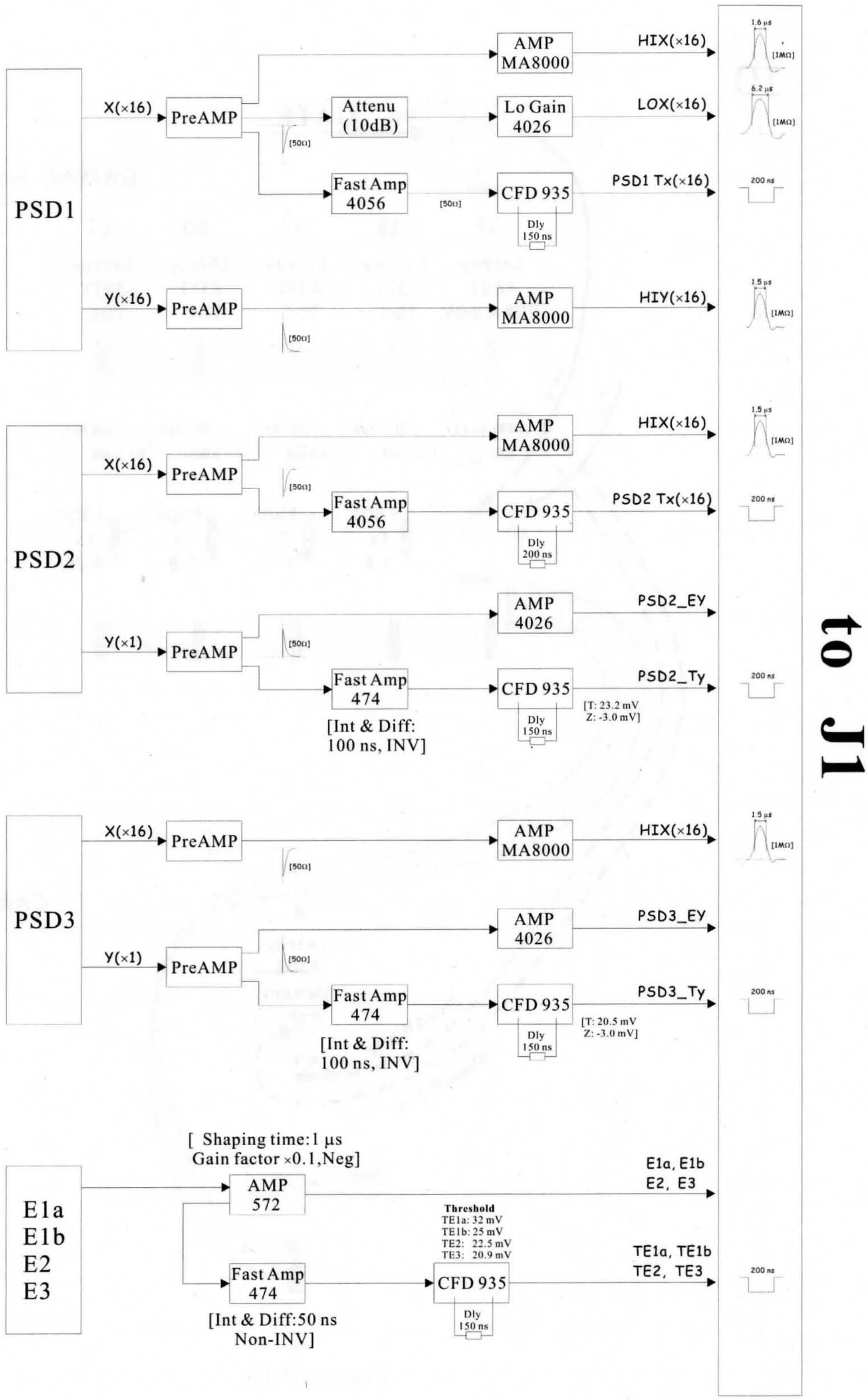

Figure B.11

12

Electronics in E7 Room

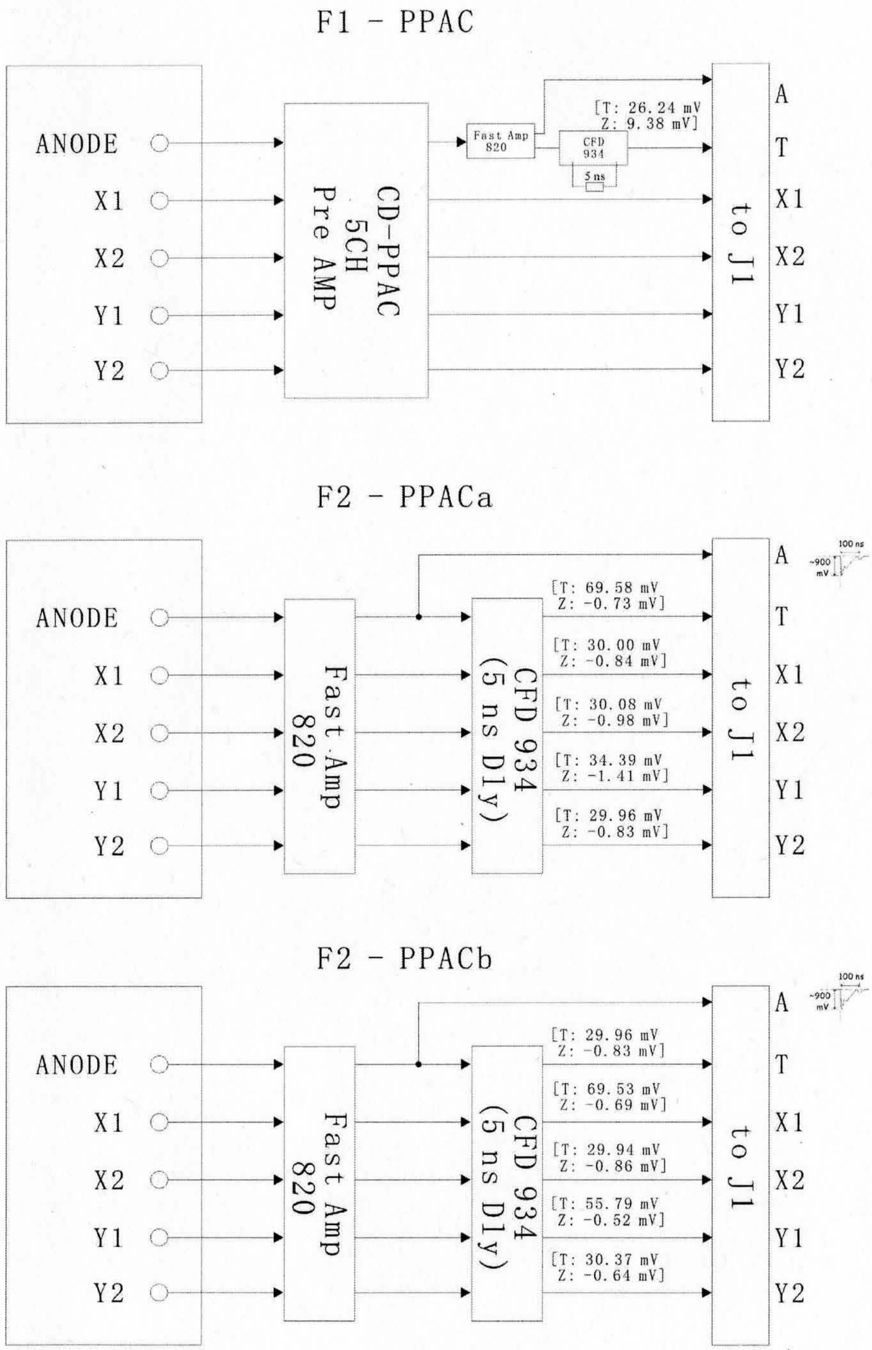

Figure B.12

Bibliography

[ADA14] Adams, W. S. "An A-Type Star of Very Low Luminosity." *Publications of the Astronomical Society of the Pacific*, **26** (1914), 198.

[ADA15] Adams, W. S. "The Spectrum of the Companion of Sirius." *Publications of the Astronomical Society of the Pacific*, **27** (1915) 236–7.

[ALP48] Alpher, R. A., Bethe, H. and Gamow, G. "The Origin of Chemical Elements." *Physical Review*, **73** (1948) 803–4.

[ALP49] Alpher, R. A. and Herman, R. C. "Remarks on the Evolution of the Expanding Universe." *Physical Review*, **75** (1949) 1089–95.

[AND89] Anders, E. and Grevesse, N. "Abundances of the elements - Meteoritic and solar." *Geochimica et Cosmochimica Acta*, **53** (1989) 197–214.

[ANG99] Angulo, C., Arnould, M., Rayet, M., Descouvemont, P., Baye, D., Leclercq-Willain, C., Coc, A., Barhoumi, S., Aguer, P., Rolfs, C., Kunz, R., Hammer, J. W., Mayer, A., Paradellis, T., Kossionides, S., Chronidou, C., Spyrou, K., Degl'Innocenti, S., Fiorentini, G., Ricci, B., Zavatarelli, S., Providencia, C., Wolters, H., Soares, J., Grama, C., Rahighi, J., Shotter, A. and Lamehi Rachti, M. "A compilation of charged-particle induced thermonuclear reaction rates." *Nuclear Physics A*, **656** (1999) 3—183.

[ANG05] Angulo, C., Champagne, A. E. and Trautvetter, H.-P. "R-matrix analysis of the ^{14}N(p,γ)^{15}O astrophysical S-factor *Nuclear Physics A*, **758** (2005) 391–4.

[ANL08] *Argonne Physics Division – ATLAS* website. (URL: `http://www.phy.anl.gov/atlas/facility/stable_beams.html`) Last updated 16 August 2004 (*Access date: 4 July 2008*).

[APA73] Apard, P., Bliman, S., Geller, R., Jacquot, B. and Jacquot, C. "Multiply Charged Ion Source." *Japan Journal of Applied Physics* **12** (1973) 1099–1100.

[APA75] Apard P., Bliman S., and Geller R. "A Multipurpose Highly Charged Ion Source." *Nuclear Instruments and Methods in Physics Research* **129** (1975) 357–63.

[APR05] Aprahamian, A. and Langanke, K. and Wiescher, M. "Nuclear structure aspects in nuclear astrophysics." *Progress in Particle and Nuclear Physics*, **54** (2005) 535–613.

[ATK29] Atkinson, R. D. E. and Houtermans, F. G. "Zur Frage der Aufbaumöglichkeit der Elemente in Sternen." *Zeitschrift für Physik*, **54** (1929) 656–65.

[ATK31a] Atkinson, R. d'Escourt "Atomic Synthesis and Stellar Energy. I." *The Astrophysical Journal*, **73** (1931) 250–95.

[ATK31b] Atkinson, R. d'Escourt "Atomic Synthesis and Stellar Energy. II." *The Astrophysical Journal*, **73** (1931) 208–47.

[ATK36] Atkinson, R. d'Escourt "Atomic Synthesis and Stellar Energy. III." *The Astrophysical Journal*, **84** (1931) 73–84.

[AYA82] Ayasli, S. and Joss, P. C. "Thermonuclear processes on accreting neutron stars - A systematic study." *The Astrophysical Journal*, **256** (1982) 637–65.

[B^{2}FH] Burbidge, E. M., Burbidge, G. R., Fowler, W. A. and Hoyle, F. "Synthesis of the Elements in Stars." *Reviews of Modern Physics*, **29** (1957) 547–650.

[BAA34] Baade, W and Zwicky, F. "Remarks on Supernovæ and Cosmic Rays." *Physical Review*, **46** (1934) 76–7.

[BAA42] Baade, W. "The Crab Nebula." *The Astrophysical Journal*, **96** (1942) 188–98.

[BAB02] Babilon, M., Bayer, W., Galaviz, D., Hartmann, T., Hutter, C., Mohr, P., Rochow, W., Sonnabend, K., Vogt, K., Volz, S. and Zilges, A. "Resonance strengths for the reaction ^{28}Si(α,γ)^{32}S at low energies." *Physical Review C*, **66** (2002) 028801:1–4.

[BAL90] Balbus, S. A. and Hawley, J. F. "A Powerful Local Shear Instability in Weakly Magnetized Disks: I. Linear Analysis." *Bulletin of the American Astronomical Society*, **22** (1990) 1209.

[BAL91a] Balbus, S. A. and Hawley, J. F. "A powerful local shear instability in weakly magnetized disks. I - Linear analysis. II - Nonlinear evolution." *The Astrophysical Journal* **376** (1991) 214–22.

[BAL91b] Balbus, S. A. and Hawley, J. F. "A Powerful Local Shear Instability in Weakly Magnetized Disks. II. Nonlinear Evolution." *The Astrophysical Journal* **376** (1991) 223–33.

[BAL92a] Balbus, S. A. and Hawley, J. F. "A powerful local shear instability in weakly magnetized disks. III - Long-term evolution in a shearing sheet." *The Astrophysical Journal* **400** (1992) 595–609.

[BAL92b] Balbus, S. A. and Hawley, J. F. "A Powerful Local Shear Instability in Weakly Magnetized Disks. IV. Nonaxisymmetric Perturbations." *The Astrophysical Journal* **400** (1992) 610–21.

[BAR65] Bardet, R. and Consoli, T. "Excitation et Detection D'ondes Ioniques Das un Plasma de Diffusion." *Physics Letters* **16** (1965) 117–9.

[BAR07] Bardayan, D. W., Blackmon, J. C., Fitzgerald, R. P., Hix, W. R., Jones, K. L., Kozub, R. L., Liang, J. F., Livesay, R. J., Ma, Z., Roberts, L. F., Smith, M. S., Thomas, J. S. and Visser, D. W. "^{30}S studied with the ^{32}S(p,t)^{30}S reaction and the ^{29}P(p,γ)^{30}S reaction rate." *Physical Review C*, **76** (2007) 045803:1–7.

[BAU07] Baumann, T. "Working Group One: Beam Optics." *Sixth Summer School on Exotic Beam Physics Lecture Notes* (2007)

[BEC03] Becker, W., Swartz, D. A., Pavlov, G. G., Elsner, R. F., Grindlay, J., Mignani, R., Tennant, A. F., Backer, D., Pulone, L., Testa, V. and Weisskopf, M. C. "Chandra X-Ray Observatory Observations of the Globular Cluster M28 and Its Millisecond Pulsar PSR B1821-24." *The Astrophysical Journal*, **594** (2003) 798–811.

[BEL76] Belian, R. D., Conner, J. P. and Evans, W. D. "The discovery of X-ray bursts from a region in the constellation Norma." *The Astrophyiscal Journal*, **206** (1976) L135–8.

[BEN98] Benlliure, J., Farget, F., Junghans, A. R. and Schmidt, K.-H. "Possibilities for the production of neutron-rich isotopes," ENAM 98, *AIP Conference Proceedings* **455** (1998) 960–4

[BER03] Berg, G. P. A., Hatanaka, K., Wiescher, M., Schatz, H., Adachi, T., Bacher, A. D., Foster, C. C., Fujita, Y., Fujita, H., Fujita, K., Görres, J., Herman, C., Kamiya, J., Sakamoto, N., Sakemi, Y., Shimbara, Y., Shimizu, Y., Stephenson, E. J., Wakasa, T. and Yosoi, M. "Resonance states in ^{22}Mg for reaction rates in the rp-process." *Nuclear Physics A*, **718** (2003) 608–10.

[BET38] Bethe, H. A. and Critchfield, C. L. "The Formation of Deuterons by Proton Combination." *Physical Review*, **54** (1938) 248–54 and 862.

[BET39] Bethe, H.A. "Energy Production in Stars." *Physical Review* **55** (1939) 103 and 434–56.

[BHA97] Bhattacharya, D. "Millisecond pulsars." *X-ray Binaries*, ed. W. H. G. Lewin, J. van Paradijs and P. J. Van den Heuvel. Cambridge University Press, 1997.

[BIL92] Bildsten, L., Salpeter, E. E. and Wasserman, I. "The fate of accreted CNO elements in neutron star atmospheres - X-ray bursts and gamma-ray lines." *The Astrophysical Journal*, **384** (1992) 143–76.

[BIL95] Bildsten, L. "Propagation of nuclear burning fronts on accreting neutron stars: X-ray bursts and sub-hertz noise." *The Astrophysical Journal*, **438** (1995) 852–75.

[BIL97] Bildsten, L. and Brown, E. F. "Thermonuclear Burning on the Accreting X-Ray Pulsar GRO J1744-28." *The Astrophysical Journal*, **477** (1997) 897–904.

[BIL98] Bildsten, L. and Cumming, A. "Hydrogen Electron Capture in Accreting Neutron Stars and the Resulting g-Mode Oscillation Spectrum." *The Astrophysical Journal*, **506** (1998) 842–62.

[BIS03a] Bishop, S., Azuma, R. E., Buchmann, L., Chen, A. A., Chatterjee, M. L., D'Auria, J. M., Engel, S., Gigliotti, D., Greife, U., Hernanz, M., Hunter, D., Hussein, A., Hutcheon, D., Jewett, C., José, J., King, J., Kubono, S., Laird, A. M., Lamey, M., Lewis, R., Liu, W., Michimasa, S., Olin, A., Ottewell, D., Parker, P. D., Rogers, J. G., Strieder, F. and Wrede, C. "^{21}Na(p,γ)^{22}Mg Reaction and Oxygen-Neon Novæ." *Physical Review Letters*, **90** (2003) 162501–4.

[BIS03b] Bishop, S., Azuma, R. E., Buchmann, L., Chen, A. A., Chatterjee, M. L., D'Auria, J. M., Engel, S., Gigliotti, D., Greife, U., Hunter, D., Hussein, A., Hutcheon, D., Jewett, C., King, J., Kubono, S., Lamey, M., Lewis, R., Liu, W., Michimasa, S., Olin, A., Ottewell, D., Parker, P. D., Rogers, J. G., and Wrede, C. "Nuclear astrophysics studiesat dragon: The ^{21}Na(p,γ)^{22}Mg reaction and oxygen-neon novae." *Nuclear Physics A*, **718** (2003) 263–6.

[BLA62] Blatt, J. M and Weisskopf, V. F. *Theoretical Nuclear Physics* John Wiley & Sons, 1962.

[BOH37] Bohr, N. "Transmutations of Atomic Nuclei." *Science*, **86** (1937) 161–5.

[BOH82] Bohne, W., Büchs, K. D., Fuchs, H., Grabisch, K., Hilscher, D., Jahnke, U., Kluge, H., Masterson, T. G., Morgenstern, H. and Wildenthal, B.

H. "Study of the Reactions ^{24,26}Mg(^{3}He,n)^{26,28}Si and ^{28}Si(^{3}He,n)^{30}S." *Nuclear Physics A* **378** (1982) 525–38.

[BOY08] Boyd, R. N. *An Introduction to Nuclear Astrophysics.* University of Chicago Press, 2008.

[BRA99a] Bradfield-Smith, W., Davinson, T., Dipietro, A., Laird, A. M., Ostrowski, A. N., Shotter, A. C., Woods, P. J., Cherubini, S., Galster, W., Graulich, J. S., Leleux, P., Michel, L., Ninane, A., Vervier, J., Görres, J., Wiescher, M., Rahighi, J. and Hinnefeld, J. "Investigation of (α,p) reactions using a radioactive beam." *Nuclear Instruments and Methods in Physics Research A*, **425** (1999) 1–7.

[BRA99b] Bradfield-Smith, W., Davinson, T., Dipietro, A., Laird, A. M., Ostrowski, A. N., Shotter, A. C., Woods, P. J., Cherubini, S., Galster, W., Graulich, J. S., Leleux, P., Michel, L., Ninane, A., Vervier, J., Görres, J., Wiescher, M., Rahighi, J. and Hinnefeld, J. "Breakout from the hot CNO cycle via the ^{18}Ne(α,p)^{21}Na reaction." *Physical Review C*, **59** (1999) 3402–9.

[BRI75] Briand, P., Geller, R., Jacquot, B., Jacquot, C. and Theiss, A. "Production and Abundance Measurements of Multicharged Xenon Ions in ECR Produced Plasmas." *Nuclear Instruments and Methods in Physics Research* **127** (1975) 441–3.

[BRI08] **fission fragment** (2008) *Encyclopædia Britannica* (URL: `http://www.britannica.com/EBchecked/topic/208789/fission-fragment`) (*Access date: 7 July 2008*).

[BRO98] Brown, E. F., Bildsten, L. and Rutledge, R. E. "Crustal Heating and Quiescent Emission from Transiently Accreting Neutron Stars." *The Astrophysical Journal*, **504** (1998) L95–8.

[BRO02] Brown, B. A., Clement, R. R., Schatz, H., Volya, A. and Richter, W. A. "Proton drip-line calculations and the rp process." *Physical Review C*, **65** (2002) 045802-1–12.

[BRO08] Brown E. F. *Private communication*, 2008.

[BUC84] Buckby M. A. and King J. D. "Cross sections and thermonuclear reaction rates for the ^{28}Si(α,p)^{31}P and ^{54}Fe(α,p)^{57}Co reactions." *Canadian Journal of Physics*, *62* (1984) 134–40.

[CAM57] Cameron, A. G. W. "Stellar evolution, nuclear astrophysics, and nucleogenesis; a series of lectures given at Purdue University, March 25 to April 5, 1957 with supplemental notes added January, 1958." Chalk River Laboratories, 1957.

[CAM59] Cameron, A. G. W. "Pycnonuclear Reations and Nova Explosions." *The Astrophysical Journal*, **130** 916–40.

[CAR66] Carlson, T. A., Hunt, W. E., Krause, M. O. "Relative Abundances of Ions Formed as the Result of Inner-Shell Vacancies in Atoms." *Physical Review* **151** (1966) 41–7.

[CAR00] Carretta, E., Gratton, R. G, Clementini, G. and Fusi Pecci, F. "Distances, Ages, and Epoch of Formation of Globular Clusters." *The Astrophysical Journal*, **533** (2000) 215–35.

[CAR06] Carroll B. W. and Ostlie D.A. *An Introduction to Modern Astrophysics.* Benjamin Cummings, 2006.

[CAU62] Caughlan, G. R. and Fowler, W. A. "The Mean Lifetimes of Carbon, Nitrogen, and Oxygen Nuclei in the CNO Bicycle." *The Astrophysical Journal*, **136** (1962) 453–64.

[CHA31] Chandrasekhar, S. "The Highly Collapsed Configurations of a Stellar Mass." *Monthly Notices of the Royal Astronomical Society* **91** (1931) 456–66

[CHA60] Chandrasekhar, S. "The stability of non-dissipative Couette flow in hydromagnetics." *Proceedings of the National Academy of Science*, **46** (1960) 253–7.

[CHA32] Chadwick, J. "Possible Existence of a Neutron." *Nature* **129** (1932) 312

[CHE99] Chen, A. A. *The Structure of ^{22}Mg and Its Implications of Explosive Nucleosynthesis.* Ph. D. thesis, Yale University, USA, 1999.

[CHE01] Chen, A. A., Lewis, R., Swartz, K. B., Visser, D. W. and Parker, P. D. "Structure of ^{22}Mg and its implications for explosive nucleosynthesis." *Physical Review C*, **63** (2001) 065807

[CHE08] Chen, J. *Private communication*, 2008.

[CHA95] Chaboyer, B., Demarque, P., Kernan, P. J., and Krauss, L. M. "A lower limit on the age of the Universe.." *Science*, **271** (1995) 957–61.

[CIE08] *7 Ciencia de Accíon* website.
(URL:
`http://www.cienciaenaccion.org/material/trabajos_cas/id_054/`)
(*Access date: 10 July 2008*).

[CLA74] Clayton, D. D. and Woosley, S. E. "Thermonuclear astrophysics." *Reviews of Modern Physics*, **46** (1974) 755–71.

[CLA03] Clayton, D. D. *Handbook of Isotopes in the Cosmos: Hydrogen to Gallium.* Cambridge University Press, 2003.

[CLE04] Clement, R. R., Bazin, D., Benenson, W., Brown, B. A., Cole, A. L., Cooper, M. W., Deyoung, P. A., Estrade, A., Famiano, M. A., Frank, N. H., Gade, A., Glasmacher, T., Hosmer, P. T., Lynch, W. G., Montes, F., Mueller, W. F., Peaslee, G. F., Santi, P., Schatz, H., Sherrill, B. M., van Goethem, M.-J. and Wallace, M. S. "New Approach for Measuring Properties of rp-Process Nuclei." *Physical Review Letters*, **92** (2004) 172502:1–4.

[COC69] Cocke, W. J. and Disney, M. J. and Taylor, D. J. "Discovery of Optical Signals from Pulsar NP 0532." *Nature*, **221** (1969) 525.

[COR00] Cornelisse, R. and Heise, J. and Kuulkers, E. and Verbunt, F. and in't Zand, J. J. M. "The longest thermonuclear X-ray burst ever observed? A BeppoSAX Wide Field Camera observation of 4U 1735-44." *Astronomy and Astrophysics*, **357** (2000) L21–4.

[CUM01] Cumming, A. and Bildsten, L. "Carbon Flashes in the Heavy-Element Ocean on Accreting Neutron Stars." *The Astrophysical Journal*, **559** (2001) L127–30.

[CUM08] Cumming, A. "New results on nuclear burning on accreting neutron stars." Oral presentation at the *10th International Symposium on Nuclei in the Cosmos*, 1 August 2008.

[DAB03] Dababneh, S., Heil, M., Käppeler, F., Görres, J., Wiescher, M., Reifarth, R. and Leiste, H. "Stellar He burning of ^{18}O: A measurement of low-energy resonances and their astrophysical implications." *Physical Review C*, **68** (2003) 025801:1–11.

[DAY90] Day, C. S. R. and Tawara, Y. "The Rising Phase of X-Ray Bursts from MXB:1728-34 - Constraints on the Spreading of Thermonuclear Flashes Over the Surface of the Neutron Star." *Monthly Notices of the Royal Astronomical Society*, **245** (1990) 31P–35P.

[DEB08] De Bernardis, F., Melchiorri, A., Verde, L. and Jimenez, R. "The cosmic neutrino background and the age of the Universe." *Journal of Cosmology and Astroparticle Physics*, **03** (2008) 020:1–9.

[DIC46] Dicke, R. H., Beringer, R., Kyhl, R. L. and Vane, A. B. "Atmospheric Absorption Measurements with a Microwave Radiometer." *Physical Review*, **70** (1946) 340–8.

[DIE08] Diehl, R. "Abundance Constraints on Sources of Nucleosynthesis, and on the Chemical evolution of the Universe and its Components (I)." *JINA School: Nuclear Astrophysics of the Cosmos 2008* (URL: `http://www.jinaweb.org/events/argonne08/talks.html`). Image credit is attributed to A. Davis of University of Chicago.

[DOM08] Dombsky, M. "List of Radioactive Ion Beams at ISAC as of February 2008." *ISAC Yield Measurements* website. (URL: `http://www.triumf.info/facility/research_fac/yield.php`) Last updated 6 February 2008 (*Access date: 7 July 2008*).

[DRE94] Drentje, A. G. "Review of the Eleventh International Workshop on ECR ion sources (invited)." *Review of Scientific Intruments* **65** (1994) 1045–50.

[DUF86] Dufour, J. P., del Moral, R. Emmermann, H., Hubert, F., Jean, D., Poinot, C., Pravikoff, M. S., Fleury, A., Delagrange, H. and Schmidt, K.-H. "Projectile Fragments Isotopic Sepeartion: Application to the LISE Spectrometer at GANIL." *Nuclear Instruments and Methods in Physics Research A* **248** (1986) 267–81.

[DUY42] Duyvendak, J. J. L. "Further Data Bearing on the Identification of the Crab Nebula with the Supernova of 1054 A.D. Part I. The Ancient Oriental Chronicles." *Publications of the Astronomical Society of the Pacific*, **54** (1942) 91–4.

[EBI83] Ebisuzaki, T., Hanawa, T. and Sugimoto, D. "Mass loss from the neutron stars associated with X-ray bursts." *Publications of the Astronomical Society of Japan*, **35** (1983) 17–32.

[EBI84] Ebisuzaki, T., Sugimoto, D. and Hanawa, T. "Are X-ray bursts really of super-Eddington luminosities?" *Publications of the Astronomical Society of Japan*, **36** (1984) 551–566.

[EDD19] Eddington, A. S. "The Sources of Stellar Energy." *The Observatory* **42** (1919) 371–6.

[EDD20] Eddington, A. S. "The Internal Constitution of the Stars." *The Observatory* **43** (1920) 341–58.

[EIC89] Eichler, D., Livio, M., Piran, T. and Schramm, D. N. "Nucleosynthesis, neutrino bursts and gamma-rays from coalescing neutron stars." *Nature*, **340** (1989) 126–8.

[END90] Endt, P. M. "Energy levels of A = 21-44 nuclei (VII)." *Nuclear Physics A*, **521** (1990) 1–400.

[END98] Endt, P. M. "Supplement to Energy levels of A = 21-44 nuclei (VII)." *Nuclear Physics A*, **633** (1998) 1–220.

[FIS03] Fisker, J. L.. Raphael Hix, W., Liebendörfer, M. and Thielemann, F.-K. "The transition to stable burning on an accreting neutron star." *Nuclear Physics A*, **718** (2003) 614–6.

[FIS04] Fisker, J. L., Thielemann, F.-K. and Wiescher, M. "The Nuclear Reaction Waiting Points: ^{22}Mg, ^{26}Si, ^{30}S, and ^{34}Ar and Bolometrically Double-peaked Type I X-Ray Bursts." *The Astrophysical Journal*, **608** (2004) L61–4.

[FIS05] Fisker, J. L., Brown, E. F., Liebendörfer, M., Thielemann, F.-K. and Wiescher, M. "The reactions and ashes of thermonuclear explosions on neutron stars." *Nuclear Physics A*, **752** (2005) 604–7.

[FIS06] Fisker, J. L., Görres, J., Wiescher, M. and Davids, B. "The Importance of ^{15}O(α,γ)^{19}Ne to X-Ray Bursts and Superbursts." *The Astrophysical Journal*, **650** (2006) 332–7.

[FIS08a] Fisker, J. L., Schatz, H. and Thielemann, F.-K. "Explosive Hydrogen Burning during Type I X-Ray Bursts." *The Astrophysical Journal Supplement Series*, **172** (2008) 261–76.

[FIS08b] Fisker J. L. *Private communication*, 2008.

[FOR97] Forestini, M. and Charbonnel, C. "Nucleosynthesis of light elements inside thermally pulsing AGB stars: I. The case of intermediate-mass stars." *Astronomy and Astrophysics Supplement Series* **123** (1997) 241–72.

[FOW26] Fowler, R. H. "On dense matter." *Monthly Notices of the Royal Astronomical Society*, **87** (1926) 114–22.

[FRE99] Freiburghaus, C., Rosswog, S. and Thielemann, F.-K. "R-Process in Neutron Star Mergers." *The Astrophysical Journal*, **525** (1999) L121–4.

[FRI73] Fricke, K. J. "Dynamical Phases of Supermassive Stars." *Astrophysical Journal* **183** (1973) 941–58.

[FRY99] Fryxell, B., Zingale, M., Timmes, F. X., Olson, K., Lamb, D., Calder, A., Dursi, J., Ricker, P., Rosner, R. and Tufo, H. "Helium Burning on Neutron Stars: 2-dimensional Results." *Bulletin of the American Astronomical Society*, **31** (1999) 1431.

[FUJ81] Fujimoto, M. Y., Hanawa, T. and Miyaji, S. "Shell flashes on accreting neutron stars and X-ray bursts." *The Astrophysical Journal*, **247** (1981) 267–78.

[FUJ87] Fujimoto, M. Y., Sztajno, M., Lewin, W. H. G. and van Paradijs, J. "On the theory of type I X-ray bursts - The energetics of bursts and the nuclear fuel reservoir in the envelope." *The Astrophysical Journal*, **319** (1987) 902–15.

[FUJ88] Fujimoto, M. Y., Sztajno, M., Lewin, W. H. G. and van Paradijs, J. "The interpretation of a multi-peaked structure observed in some X-ray bursts from 4U/MXB 1636-53." *Astronomy and Astrophysics*, **199** (1988) L9–12.

[FUS87] Fushiki, I. and Lamb, D. Q. "New insights from a global view of X-ray bursts." *The Astrophysical Journal*, **323** (1987) L55–60.

[GAM28] Gamow, G. "Zur Quantentheorie des Atomkernes." *Zeitschrift für Physik*, **51** (1928) 204–12.

[GEL80] Geller, R., Jacquot, B. and Pauthenet, R. "Micromafios source d'ions multichargés basée sur la résonance cyclotronique des électrons *Revue de Physique Appliquée* **15** (1980) 995–1005.

[GEN03a] Gendre, B., Barret, D. and Webb, N. A. "An XMM-Newton observation of the globular cluster Omega Centauri." *Astronomy and Astrophysics*, **400** (2003) 521–31.

[GEN03b] Gendre, B., Barret, D. and Webb, N. "Discovery of a quiescent neutron star binary in the globular cluster M 13." *Astronomy and Astrophysics*, **403** (2003) L11–4.

[GIA62] Giacconi, R., Gursky, H., Paolini, F. R. and Rossi, B. B. "Evidence for x Rays From Sources Outside the Solar System." *Physical Review Letters*, **9** (1962) 439–43.

[GIA71] Giacconi, R., Gursky, H., Kellogg, E., Schreier, E. and Tananbaum, H. "Discovery of Periodic X-Ray Pulsations in Centaurus X-3 from UHURU." *The Astrophysical Journal*, **167** (1971) L67–73.

[GIA71] Giacconi, R., Gursky, H., Kellogg, E., Schreier, E. and Tananbaum, H. "Discovery of Periodic X-Ray Pulsations in Centaurus X-3 from UHURU." *The Astrophysical Journal*, **167** (1971) L67–73.

[GOL68] Gold, T. "Rotating Neutron Stars as the Origin of the Pulsating Radio Sources." *Nature*, **218** (1968) 731.

[GÖR95] Görres, J., Wiescher, M and Thielemann, F.-K. "Bridging the waiting points: The role of two-proton capture reactions in the rp process." *Physical Review C* **51** (1995) 392–400.

[GOT86] Gottwald, M., Haberl, F., Parmar, A. N. and White, N. E. "The bursting behavior of the transient X-ray burst source EXO 0748-676 - A dependence between the X-ray burst properties and the strength of the persistent emission." *The Astrophysical Journal*, **308** (1986) 213–24.

[GRI76] Grindlay, J. E., Schnopper, H., Schreier, E., Gursky, H., Parsignault, D. R. "Improved position for the X-ray source associated with the globular cluster NGC 6441." *The Astrophysical Journal*, **206** (1976) L23–4.

[GRO02] Groombridge, D., Shotter, A. C., Bradfield-Smith, W., Cherubini, S., Davinson, T., di Pietro, A., Görres, J., Graulich, J. S., Laird, A. M., Leleux, P., Musumarra, A., Ninane, A., Ostrowski, A. N., Rahighi, J., Schatz, H., Wiescher, M., Woods, P. J. "Breakout from the hot CNO cycle via the ^{18}Ne(α,p)^{21}Na reaction. II. Extended energy range $E_{c.m.}$ ~1.7-2.9 MeV." *Physical Review C*, **66** (2002) 055802:1–10.

[GUR29] Gurney, R. W. and Condon, E. U. "Quantum Mechanics and Radioactive Disintegration." *Physical Review*, **33** (1929) 127-40.

[HAG68] Hagen, M, Maier, K. H., and Michaelsen, R. "The Level Schemes of ^{26}Si, ^{30}S, ^{34}Ar and ^{42}Ti Studied with the (^{3}He,n) Reaction." *Physics Letters* **26B** (1968) 432–6.

[HAL48] Hall, R. N. "High Frequency Proton Source." *The Review of Scientific Instruments* **19** (1948) 905–10.

[HAN75] Hansen, C. J. and van Horn, H. M. "Steady-state nuclear fusion in accreting neutron-star envelopes." *The Astrophysical Journal*, **195** (1975) 735–41.

[HAN82] Hanawa, T. and Sugimoto, D. "Helium Shell Flash on Accreting Neutron Stars - Effects of Hydrogen-Rich Envelope and Recurrence of X-Ray Bursts." *Publications of the Astronomical Society of Japan*, **34** (1982) 1–20.

[HAN83] Hanawa, T., Sugimoto, D. and Hashimoto, M.-A. "Nucleosynthesis in explosive hydrogen burning and its implications in ten-minute interval of X-ray bursts." *Publications of the Astronomical Society of Japan*, **35** (1983) 491–506.

[HAN84] Hanawa, T. and Fujimoto, M. Y. "Thermal response of neutron stars to shell flashes." *Publications of the Astronomical Society of Japan*, **36** (1984) 199–214.

[HAN94] Hansen, C.J., Kawaler, S.D, and Trimble, V. *Stellar Interiors – Physical Principles, Structure, and Evolution.* Springer, 2004.

[HAS06] Hashimoto, T., Ishiyama, H., Ishikawa, T., Kawamura, T., Nakai, K., Watanabe, Y. X., Miyatake, H., Tanaka, M. H., Fuchi, Y., Yoshikawa, N., Jeong, S. C., Katayama, I., Nomura, T., Furukawa, T., Mitsuoka, S., Nishio, K., Matsuda, M., Ikezoe, H., Fukuda, T., Das, S. K., Saha, P. K., Mizoi, Y., Komatsubara, T., Yamaguchi, M. and Tagishi, Y. "Gated multiple-sampling and tracking proportional chamber." *Nuclear Instruments and Methods in Physics Research A*, **556** (2006) 339–49.

[HAU52] Hauser, W. and Feshbach, H. "The Inelastic Scattering of Neutrons." *Physical Review*, **87** (1952) 366–73.

[HEI06] Heinke, C. O., Rybicki, G. B.;, Narayan, R. and Grindlay, J. E. "A Hydrogen Atmosphere Spectral Model Applied to the Neutron Star X7 in the Globular Cluster 47 Tucanæ." *The Astrophysical Journal*, **644** (2006) 1090–1103.

[HER85] Herschel, F. W. "Catalogue of Double-Stars." *Philosophical Transactions of the Royal Society of London*, **75** (1785) 40–126.

[HER44] Herschel, J. F. W. "On the Variations of the Proper Motions of Procyon and Sirius." *Monthly Notices of the Royal Astronomical Society*, **6** (1844) 136–41.

[HEW68] Hewish, A., Bell, S. J., Pilkington, J. D., Scott, P. F. and Collins, R. A. "Observation of a Rapidly Pulsating Radio Source." *Nature*, **217** (1968) 709.

[HOF77a] Hoffman, J. A., Lewin, W. H. G. and Doty, J. "Observations of the X-ray burst source MXB 1636-53." *The Astrophysical Journal*, **217** (1977) L23–28.

[HOF77b] Hoffman, J. A., Lewin, W. H. G. and Doty, J. "Further observations of the burst source MXB 1728-34." *Monthly Notices of the Royal Astronomical Society*, **179** (1977) 57P–64P.

[HOF78] Hoffman, J. A., Marshall, H. L., Lewin, W. H. G. "Dual character of the rapid burster and a classification of X-ray bursts." *Nature*, **271** (1978) 630–3.

[HOF80] Hoffman, J. A., Cominsky, L. and Lewin, W. H. G. "Repeatable, multiple-peaked structure in Type I X-ray bursts." *The Astrophysical Journal*, **240** (1980) L27–31.

[HOY46a] Hoyle, F. "The chemical composition of the stars." *Monthly Notices of the Royal Astronomical Society*, **106** (1946) 255–59.

[HOY46b] Hoyle, F. "The synthesis of the elements from hydrogen." *Monthly Notices of the Royal Astronomical Society*, **106** (1946) 343–83.

[HOY54] Hoyle, F. "On Nuclear Reactions Occuring in Very Hot STARS.I. the Synthesis of Elements from Carbon to Nickel." *The Astrophysical Journal Supplement*, **1** (1954) 121.

[HOY65] Hoyle, F. and Fowler, W. A. "Report on the Properties of Massive Objects. *Quasi-Stellar Sources and Gravitational Collapse, Proceedings of the 1st Texas Symposium on Relativistic Astrophysics*, ed. I. Robinson, A. Schild and E.L. Schucking. University of Chicago Press, (1965) 17–28.

[HRIBF07] *HRIBF RIB Intensities (2008)* website. (URL: `http://www.phy.ornl.gov/hribf/beams/rib-intensity-2008.shtml`) Last updated 1 March 2007 (*Access date: 7 July 2008*).

[HUB29] Hubble, E. "A Relation between Distance and Radial Velocity among Extra-Galactic Nebulæ." *Proceedings of the National Academy of Sciences of the United States of America*, **15** (1929) 168–73.

[HYD88] Hyder, H. R. McK., Baris, J., Gingell, C. E. L., McKay, J., Parker, P. D., and Bromley, D. A. "The ESTU accelerator at Yale." *Nuclear Instruments and Methods in Physics Research in Physics Research Section A* **268** (1988) 285–94.

[ILI91] Iliadis, C., Giesen, U., G{orres, J., Graff, S., Wiescher, M., Azuma, R. E., King, J., Buckby, M., Barnes, C. A. and Wang, T. R. "The reaction branching ^{31}P(p,γ)^{31}P(p,α) in the rp-process." *Nuclear Physics A*, **533** (1991) 153–69.

[ILI93] Iliadis, C., Görres, J., Ross, J. G., Scheller, K. W., Wiescher, M., Grama, C., Schange, T., Trautvetter, H. P. and Evans, H. C. "Explosive hydrogen burning of ^{31}P." *Nuclear Physics A*, **559** (1993) 83–99.

[ILI99] Iliadis, C., Endt, P. M., Prantzos, N. and Thompson, W. J. "Explosive Hydrogen Burning of ^{27}Si, ^{31}S, ^{35}Ar, and ^{39}Ca in Novæ and X-Ray Bursts." *The Astrophysical Journal*, **524** (1999) 434–53.

[ILI07] Iliadis, C. *Nuclear Physics of Stars.* Wiley-VCH, 2007.

[ISH75] Ishizuka, H., Ohyama, M., Kamada, K., Ôno, H., and Kojima, S. "ECR Ion Source Using Mesh Electrodes and a Space Charge Neutralizer." *Japanese Journal of Applied Physics* **14** (1975) 1217–22.

[JOS77] Joss, P. C. "X-ray bursts and neutron-star thermonuclear flashes." *Nature*, **270** (1977) 310–4.

[JOS78] Joss, P. C. "Helium-burning flashes on an accreting neutron star - A model for X-ray burst sources." *The Astrophysical Journal*, **225** (1978) L123–7.

[JOS80] Joss, P. C. and Li, F. K. "Helium-burning flashes on accreting neutron stars - Effects of stellar mass, radius, and magnetic field." *The Astrophysical Journal*, **238** (1980) 287–95.

[KÄL03] Källman, K.-M., Brenner, M., Goldberg, V. Z., Lönnroth, T., Manngård, P., Pakhomov, A. E. and Pankratov, V. V. "Narrow α + ^{28}Si elastic-scattering states at high excitation in ^{32}S." *European Physical Journal A*, **16** (2003) 159–69.

[KAT83] Kato, M. "Neutron star wind." *Publications of the Astronomical Society of Japan*, **35** (1983) 31–46.

[KIM06] Kim, A. *Private communication*, 2006.

[KNO00] Knoll, G. F. *Radiation Detection and Measurement*, 3rd Ed. Wiley, 2000.

[KOI99] Koike, O., Hashimoto, M., Arai, K. and Wanajo, S. "Rapid proton capture on accreting neutron stars - effects of uncertainty in the nuclear process." *Astronomy and Astrophysics*, **342** (1999) 464–73.

[KOI04] Koike, O., Hashimoto, M.-a., Kuromizu, R. and Fujimoto, S.-i. "Final Products of the rp-Process on Accreting Neutron Stars." *The Astrophysical Journal*, **603** (2004) 242–51.

[KOY81] Koyama, K., Inoue, H., Makishima, K., Matsuoka, M., Murakami, T., Oda, M., Osgawara, Y., Ohashi, T., Shibazaki, N., Tanaka, Y., Marshall, F. J., Kondo, I. S., Hayakawa, S., Kunieda, H., Makino, F., Masai, K., Nagase, F., Tawara, Y., Miyamoto, S., Tsunemi, H. and Yamashita, K. "Discovery of X-ray bursts from Aquila X-1." *The Astrophysical Journal*, **247** (1981) L27–9.

[KRA03] Krauss, L. M. and Chaboyer, B. "Age Estimates of Globular Clusters in the Milky Way: Constraints on Cosmology." *Science*, **299** (2003) 65-9.

[KUB02] Kubono, S., Yanagisawa, Y., Teranishi, T., Kato, S., Kishida, Y., Michimasa, S., Ohshiro, Y., Shimoura, S., Ue, K., Watanabe, S. and Yamazaki, N. "New low-energy RIB separator CRIB for nuclear astrophysics." *European Journal of Physics A* **13** (2002) 217–20.

[KUM01] Kumagai, H., Ozawa, A., Fukuda, N., Sümmerer, K. and Tanihata, I. "Delay-line PPAC for high-energy light ions." *Nuclear Instruments and Methods in Physics Research A*, **470** (2001) 562–70.

[KUU02] Kuulkers, E., Homan, J., van der Klis, M., Lewin, W. H. G. and Méndez, M. "X-ray bursts at extreme mass accretion rates from GX 17+2." *Astronomy and Astrophysics*, **382** (2002) 947–73.

[LAM78] Lamb, D. Q. and Lamb, F. K. "Nuclear burning in accreting neutron stars and X-ray bursts." *The Astrophysical Journal*, **220** (1978) 291–302.

[LAM00] Lamb, D. Q. "Some Startling Discoveries about X-Ray Bursts." *The Astrophysical Journal Supplement Series*, **127** (2000) 395–408.

[LAT77] Lattimer, J. M., Mackie, F., Ravenhall, D. G. and Schramm, D. N. "The decompression of cold neutron star matter." *The Astrophysical Journal*, **213** (1977) 225–33.

[LAW30] Lawrence, E. O. and Edlefson, N. E. *Science* **72** (1930) 376.

[LAW34] Lawrence, E. O. *Method and apparatus for the acceleration of ions.* U.S. Patent 1948384 (1934).

[LAW83] Lawrence, A., Cominsky, L., Engelke, C., Jernigan, G., Lewin, W. H. G., Matsuoka, M., Mitsuda, K., Oda, M., Ohashi, T., Pedersen, H., van Paradijs, J. "Simultaneous U, B, V, and X-ray measurements of a burst from 4U/MXB 1636-53." *The Astrophysical Journal*, **271** (1983) 793–803.

[LET99] Lettry, J. A. "Review of ion-source developments for radioactive ion-beam facilities." *Proceedings of the 1999 Particle Accelerator Conference*, New York (1999) 92–6. 0-7803-5573-3 IEEE.

[LEW76a] Lewin, W. H. G., Doty, J., Clark, G. W., Rappaport, S. A., Bradt, H. V. D., Doxsey, R., Hearn, D. R., Hoffman, J. A., Jernigan, J. G., Li, F. K., Mayer, W., McClintock, J., Primini, F. and Richardson, J. "The discovery of rapidly repetitive X-ray bursts from a new source in Scorpius." *The Astrophysical Journal*, **207** (1976) L95–9.

[LEW76b] Lewin, W. H. G. and Hoffman, J. A. and Doty, J. and Hearn, D. R. and Clark, G. W. and Jernigan, J. G. and Li, F. K. and McClintock, J. E. and Richardson, J. "Discovery of X-ray bursts from several sources near the galactic centre." *Monthly Notices of the Royal Astronomical Society*, **177** (1976) 83–92.

[LEW77] Lewin, W. H. G. "X-ray burst sources." *Monthly Notices of the Royal Astronomical Society*, **179** (1976) 43–53.

[LEW93] Lewin, W. H. G., van Paradijs, J. and Taam, R. E. "X-Ray Bursts." *Space Science Reviews*, **62** (1993) 223–389.

[LEW95] Lewin, W. H. G, van Paradijs, J. and Taam, R. E. "X-ray bursts." *X-ray Binaries*, ed. W. H. G. Lewin, J. van Paradijs and P. J. Van den Heuvel. Cambridge University Press, 1997.

[LON94] Longair, M. S. *High Energy Astrophysics.* Cambridge University Press, 1994.

[LUNA06] LUNA Collaboration, Bemmerer, D., Confortola, F., Lemut, A., Bonetti, R., Broggini, C., Corvisiero, P., Costantini, H., Cruz, J., Formicola, A., Fülöp, Zs., Gervino, G., Guglielmetti, A., Gustavino, C., Gyürky, Gy., Imbriani, G., Jesus, A., Junker, M., Limata, B., Menegazzo, R., Prati, P., Roca, V., Rolfs, C., Rogalla, D., Romano, M., Rossi-Alvarez, C., Schümann, F. Somorjai, E. Straniero, O. Strieder, F. Terrasi, F. and Trautvetter, H. P. "Low energy measurement of the $^{14}N(p,\gamma)^{15}O$ total cross section at the LUNA underground facility." *Nuclear Physics A* **779** (2006) 297–317.

[MAR77] Maraschi, L and Cavaliere, A. *Highlights in Astronomy*, ed. E. A. Müller, Dordrecht: Reidel, 1977, 127.

[MAR08] Marranghello, G. F., de Araujo, J. C. N. and Miranda, O. D. "Hydrodynamical collapse of neutron stars due to hadron-quark phase transition." *Journal of Physics Conference Series*, *122* (2008) 012039:1–6.

[MAY42] Mayall, N. U. and Oort, J. H. "Further Data Bearing on the Identification of the Crab Nebula with the Supernova of 1054 A.D. Part II. The Astronomical Aspects." *Publications of the Astronomical Society of the Pacific*, **54** (1942) 95–104.

[MEL87] Melia, F. "Multipeaked X-ray bursts from 4U/MXB 1636-53 - Evidence for burst-induced accretion disk coronae." *The Astrophysical Journal*, **315** (1987) L43–7.

[MCG07] McGraw J.D. *Private communication*, 2007.

[MOS13] Moseley, H. "The High Frequency Spectra of the Elements." *Philosophical Magazine*, **26** (1913) 1024–34.

[MIL01] Mills, A., Simon, H., Nilsson, T. and Georg, U. "Radioactive Ion Beam Intensities at ISOLDE." *ISOLDE WEB* website. (URL: `http://isolde.web.cern.ch/ISOLDE/`) Last updated 24 July 2001 (*Access date: 7 July 2008*).

[MIN42] Minkowski, R. "The Crab Nebula." *The Astrophysical Journal*, **96** (1942) 199–213.

[NAK08] Nakazato, K., Sumiyoshi, K. and Yamada, S. "Astrophysical implications of equation of state for hadron-quark mixed phase: Compact stars and stellar collapses." *Physical Review D*, **77** 103006:1–12.

[NEW06] Newman, W. R. *Atoms and Alchemy: Chymistry and the Experimental Origins of the Scientific Revolution.* University of Chicago Press, 2006.

[NUC08] *NucAstroData* (URL: `www.nucastrodata.org`)

[ODA71] Oda, M., Gorenstein, P., Gursky, H., Kellogg, E., Schreier, E., Tananbaum, H., Giacconi, R. "X-Ray Pulsations from Cygnus X-1 Observed from UHURU." *The Astrophysical Journal*, **166** (1971) L1–7.

[OGA62] Ogawa, I. and Abe, N. "Electron Cyclotron Resonances in a Radiofrequency Ion Source." *Nuclear Instruments and Methods in Physics Research* **16** (1962) 227–32.

[OKA72] Okamoto, Y. and Tamagawa, H. "Some Features of an Electron Cyclotron Resonance Plasma Produced by Means of a Lisitano-Coil." *Japanese Journal of Applied Physics* **11** (1972) 726-31.

[OHS03] Oshiro, Y., Watanabe, S., Higurashi, Y., Kageyama, T., Kidera, M., Nakagawa, T., Kase, M., Kubono, S. and Katayama, T. "First beam injection from the Hyper ECR ion source to the RIKEN AVF cyclotron." *RIKEN Accelerator Progress Report* **36** (2003) 279–80.

[OPP39] Oppenheimer, J. R. and Volkoff, G. M "On Massive Neutron Cores." *Physical Review*, **55** (1939) 374–81.

[OUE07] Ouellet, C. V. *The* $^{40}Ca(\alpha,\gamma)^{44}Ti$ *Nuclear Reaction Using DRAGON.* Ph. D. thesis, McMaster University, Canada, 2007.

[PAC83] Paczyński, B. "Models of X-ray bursters with radius expansion." *The Astrophysical Journal*, **267** (1983) 315–21.

[PAG97] Pagel, B. E. J. *Nucleosynthesis and Chemical Evolution of Galaxies.* Cambridge University Press, 1997

[PAR08] Parikh, A., Josè, J., Moreno, F. and Iliadis, C. "The Sensitivity of Nucleosynthesis in Type I X-ray Bursts to Thermonuclear Reaction-Rate Variations." *ArXiv e-prints*, **806** (2008) 0806.2975. Accepted for publication in *the Astrophysical Journal*, **178** (2008).

[PAV91] Pavlov, G. G., Shibanov, Iu. A. and Zavlin, V. E. "Spectra of X-ray bursts at near-Eddington luminosities." *Monthly Notices of the Royal Astronomical Society*, **253** (1991) 193–97.

[PET95] Pethick, C. J. and Ravenhall, D. G. "Matter at large neutron excess and the physics of neutron-star crusts." *Annual Review of Nuclear and Particle Science*, **45** (1995) 429–84.

[PEN65] Penzias, A. A. and Wilson, R. W. "A Measurement of Excess Antenna Temperature at 4080 Mc/s." *The Astrophysical Journal*, **142** (1965) 419–21.

[PEN87] Penninx, W., Lewin, W. H. G. and van Paradijs, J. "Multipeaked X-ray bursts from 4U/MXB 1636-53 - Evidence against burst-induced accretion disk coronae." *The Astrophysical Journal*, **321** (1987) L67–9.

[PEN89] Penninx, W., Damen, E., van Paradijs, J., Tan, J. and Lewin, W. H. G. "EXOSAT observations of the X-ray burst source 4U 1608-52." *Astronomy and Astrophysics*, **208** (1989) 146–52.

[POP00] Popov, S. B., Colpi, M., Treves, A., Turolla, R., Lipunov, V. M. and Prokhorov, M. E. "The Neutron Star Census." *The Astrophysical Journal*, **530** (2000) 896–903.

[RAU00] Rauscher, T. and Thielemann, F.-K. "Astrophysical Reaction Rates From Statistical Model Calculations." *Atomic Data and Nuclear Data Tables*, **75** 2000 1–2.

[RAU01] Rauscher, T. and Thielemann, F.-K. "Tables of Nuclear Cross Sections and Reaction Rates: AN Addendum to the Paper "ASTROPHYSICAL Reaction Rates from Statistical Model Calculations"" *Atomic Data and Nuclear Data Tables*, **79** 2001 47–64.

[RAU04] Rauscher, T. and Thielemann, F.-K. "Predicted cross-sections for photon-induced particle emission." *Atomic Data and Nuclear Data Tables*, **88** 2004 1–81.

[RAU08] Rauscher, T. and Thielemann, F.-K. "NON-SMOKER(web)." (URL `http://nucastro.org/nonsmoker.html`) (*Access date: 24 October 2007*).

[RAY83] Rayleigh "Investigation of the character of the equilibrium of an incompresible heavy fluid of variable density." *Proceedings of the London Mathematical Society*, **14** (1883) 170–7.

[RAV92] Ravn, H. L. "Status and future development of ion sources for on-line mass separators." *Nuclear Instruments and Methods in Physics Research in Physics Research B* **70** (1992) 107–17.

[RAV94] Ravenhall, D. G. and Pethick, C. J. "Neutron star moments of inertia." *The Astrophysical Journal*, **424** (1994) 846–51.

[RED82] Redder, A., Becker, H. W., Lorenz-Wirzba, H., Rolfs, C., Schmalbrock, P. and Trautvetter, H. P. "The ^{15}N(p,α)^{12}C reaction at stellar energies." *Zeitschrift fur Physik A Hadrons and Nuclei*, **305** (1982) 325–33.

[REG84] Regev, O. and Livio, M. "Thermal cycles from a two-zone accreting model - X-ray bursts and shell flashes." *Astronomy and Astrophysics*, **134** (1984) 123–8.

[REH08] Rehm, K.E. *Private communication* (2008).

[ROO08] *ROOT User's Guide, v. 5.20* 30 July 2008. (URL `http://root.cern.ch/root/doc/RootDoc.html`)

[ROS73] Rosenbluth, M. N., Ruderman, M., Dyson, F., Bahcall, J. N., Shaham, J. and Ostriker, J. "Nuclear Fusion in Accreting Neutron Stars." *The Astrophysical Journal*, **184** (1973) 907–910.

[RR88] Rolfs, C. E. and Rodney, W. S.. *Cauldrons in the Cosmos.* The University of Chicago Press, 1988.

[RUT11] Rutherford, E. "The Scattering of Alpha and Beta Particles by Matter and the Structure of the Atom." *Philosophical Magazine*, **21** (1911) 669–88.

[RUT47] Rutherglen, J. G. and Cole, J. F. I. "A Radio-Frequency Ion Source With High Percentage Yield of Protons." *Nature* **160** (1947) 545–6.

[RUT02] Rutledge, R. E., Bildsten, L., Brown, E. F., Pavlov, G. G. and Zavlin, V. E. "A Possible Transient Neutron Star in Quiescence in the Globular Cluster NGC 5139." *The Astrophysical Journal*, **578** (2002) 405–12.

[RUT05] Rutledge, R. "Neutron Star Radii: At the Crossroads." *Proceedings of Neutron Stars at the Crossroads of Fundamental Physics*, 2005 (URL: `http://www.physics.ubc.ca/˜heyl/ns2005`).

[SAK93] Sakurai, J. J. *Modern Quantum Mechanics (Revised Edition).* 2nd Ed., Addison Wesley, 1993.

[SAL64] Salpeter, E. E. "Accretion of Interstellar Matter by Massive Objects." *The Astrophysical Journal*, **140** (1964) 796–800.

[SAL69] Salpeter, E. E. and van Horn, H. M. "Nuclear Reaction Rates at High Densities." *The Astrophysical Journal*, **155** (1969) 183–202.

[SAY77] Sayer R. O. "Semi-Empirical Formulas for Heavy-Ion Stripping Data." *Revue de Physique Appliquée, 12* (1977) 1543–46.

[SCH99] Schatz, H., Bildsten, L., Cumming, A. and Wiescher, M. "The Rapid Proton Process Ashes from Stable Nuclear Burning on an Accreting Neutron Star." *The Astrophysical Journal*, **524** (1999) 1014–29.

[SCH01a] Schatz, H., Aprahamian, A., Barnard, V., Bildsten, L., Cumming, A., Ouellette, M., Rauscher, T., Thielemann, F.-K., Wiescher, M. "End Point of the rp Process on Accreting Neutron Stars." *Physical Review Letters*, **86** (2001) 3471–4.

[SCH01b] Schatz, H., Aprahamian, A., Barnard, V., Bildsten, L., Cumming, A., Ouellette, M., Rauscher, T., Thielemann, F.-K., Wiescher, M. "The endpoint of the rp-process on accreting neutron stars." *Nuclear Physics A*, **688** (2001) 150–3.

[SCH03] Schatz, H., Bildsten, L. and Cumming, A. "Photodisintegration-triggered Nuclear Energy Release in Superbursts." *The Astrophysical Journal*, **583** (2003) L87–90.

[SCH16] Schwarzschild, K. "Uber das Gravitationsfeld eines Massenpunktes nach der Einsteinschen Theorie." *Sitzungsberichte der Deutschen Akademie der Wissenschaften zu Berlin, Klasse fur Mathematik, Physik, und Technik*, (1916) 189–96.

[SCH71] Schreier, E., Levinson, R., Gursky, H., Kellogg, E., Tananbaum, H., Giacconi, R. "Evidence for the Binary Nature of Centaurus X-3 from UHURU X-Ray Observations." *The Astrophysical Journal*, **172** (1972) L79–89.

[SCH99] Schatz, H., Bildsten, L., Cumming, A., and Wiescher, M. "The Rapid Proton Process Ashes from Stable Nuclear Burning on an Accreting Neutron Star." *The Astrophysical Journal* **524** (1999) 1014–29.

[SET07] Setoodeh nia, K. *Studies of* $20 < A < 30$ *Nucleosynthesis in AGB Stars and Novæ.* M. Sc. thesis, McMaster University, Canada, 2007.

[SHK67] Shklovsky, I. S. "On the Nature of the Source of X-Ray Emission of SCO XR-1." *The Astrophysical Journal*, **148** (1967) L1–L4.

[SNE00] Sneden, C., Cowan, J. J., Ivans, I. I., Fuller, G. M., Burles, S., Beers, T. C. and Lawler, J. E. "Evidence of Multiple R-Process Sites in the Early Galaxy: New Observations of CS 22892-052." *The Astrophysical Journal*, **533** (2000) L139–42.

[SNE55] Snell, A. H. and Pleasonton, F. "Spectrometry of the Neutrino Recoils of Argon-37." *Physical Review* **100** (1955) 1396–1403.

[SNE58] Snell, A. H. and Pleasonton, F. "Charge Spectrometry for Xe^{133}-Cs^{133}." *Physical Review* **111** (1958) 1338–43.

[SPI02] Spitkovsky, A., Levin, Y. and Ushomirsky, G. "Propagation of Thermonuclear Flames on Rapidly Rotating Neutron Stars: Extreme Weather during Type I X-Ray Bursts." *The Astrophysical Journal*, **566** 2002 1018–38.

[STA98] Starrfield, S., Truran, J. W., Wiescher, M. C. and Sparks, W. M. "Evolutionary sequences for Nova V1974 Cygni using new nuclear reaction rates and opacities." *Monthly Notices of the Royal Astronomical Society*, **296** (1998) 502–22.

[STR01] Strohmayer, T. E. "Oscillations during thermonuclear X-ray bursts: A new probe of neutron stars." *X-ray Astronomy: Stellar Endpoints, AGN, and the Diffuse X-ray Background*, **599** (2001) 377–86.

[SWA77] Swank, J. H., Becker, R. H., Boldt, E. A., Holt, S. S., Pravdo, S. H. and Serlemitsos, P. J. "Spectral evolution of a long X-ray burst." *The Astrophysical Journal*, **212** (1977) L73–6.

[SZT85] Sztajno, M., van Paradijs, J., Lewin, W. H. G., Trumper, J., Stollman, G., Pietsch, W. and van der Klis, M. "Unusual X-ray burst profiles from 4U/MXB 1636-53." *The Astrophysical Journal*, **299** (1985) 487–95.

[TAA78] Taam, R. E. and Picklum, R. E. "Nuclear fusion and carbon flashes on neutron stars." *The Astrophysical Journal*, **224** (1978) 210–16.

[TAA79] Taam, R. E. and Picklum, R. E. "Thermonuclear runaways on neutron stars." *The Astrophysical Journal*, **233** (1979) 327–33.

[TAA80] Taam, R. E. "X-ray bursts from thermonuclear runaways on accreting neutron stars." *The Astrophysical Journal*, **241** (1980) 358–66.

[TAA82] Taam, R. E. "Helium and combined hydrogen-helium shell flashes in the envelope of an accreting neutron star." *The Astrophysical Journal*, **258** (1982) 761–69.

[TAA85] Taam, R. E. "Nuclear processes at neutron star surfaces." *Annual Review of Nuclear and Particle Science*, *35* (1985) 1–23.

[TAA93] Taam, R. E., Woosley, S. E., Weaver, T. A. and Lamb, D. Q. "Successive X-ray bursts from accreting neutron stars." *The Astrophysical Journal*, **413** (1993) 324–32.

[TAA96] Taam, R. E., Woosley, S. E. and Lamb, D. Q. "The Effect of Deep Hydrogen Burning in the Accreted Envelope of a Neutron Star on the Properties of X-Ray Bursts." *The Astrophysical Journal* **459** (1996) 271–7.

[TAM72] Tamagawa, H, Okamoto, Y and Akutagawa, C. "A Proposal on Multiply Charged Ion Source." *Japan Journal of Applied Physics* **11** (1972) 1226–7.

[TAN81] Tanaka, M. H., Kubono, S., Kato, S., Hayakawa, S. I., Morita, K., Nakagawa, T., Asano, R. and Igarashi, M. "Allowed excitation of unnatural-parity states in the ^{208}Pb(^{4}He, ^{6}He) reaction." *Physics Letters B*, **104** (1981) 265–8.

[THI94] Thielemann, F.-K., Kratz, K.-L.;, Pfeiffer, B., Rauscher, T., van Wormer, L., and Wiescher, M. C. "Astrophysics and Nuclei far from Stability." *Nuclear Physics A*, **570** (1994) 329c–44c.

[THI01] Thielemann, F.-K., Brachwitz, F., Freiburghaus, C., Kolbe, E., Martinez-Pinedo, G., Rauscher, T., Rembges, F., Hix, W. R., Liebendrfer, M., Mezzacappa, A., Kratz, K.-L.;, Pfeiffer, B., Langanke, K., Nomoto, K., Rosswog, S., Schatz, H., Wiescher, M. "Element synthesis in stars." *Progress in Particle and Nuclear Physics*, **46** (2001) 5–22.

[THI05] Thielemann, F.-K., Argast, D., Brachwitz, F., Fisker, J. L., Fröhlich, C., Hirschi, R., Kolbe, E., Mocelj, D. and Rauscher, T. "Nuclear Physics: A Key Ingredient in Astrophysical Modeling." *Nuclear Physics A*, **751** (2005) 301–26.

[THI07] Thielemann, F.-K. *Private communication*, 2007.

[THO46] Thonemann, P. C. "High-frequency Discharge as an Ion Source." *Nature* **158** (1946) 61.

[THO99] Thorsett, S. E. and Chakrabarty, D. "Neutron Star Mass Measurements. I. Radio Pulsars." *The Astrophysical Journal*, **512** (1999) 288–99.

[THO01] Thompson, I. B., Kaluzny, J., Pych, W., Burley, G., Krzeminski, W., Paczyǹski, B., Persson, S. E. and Preston, G. W. "Cluster AgeS Experiment: The Age and Distance of the Globular Cluster ω Centauri Determined from Observations of the Eclipsing Binary OGLEGC 17." *The Astronomical Journal*, **121** (2001) 3089–99.

[THO78] Thorstensen, J., Charles, P. and Bowyer, S. "The optical counterpart of Aquila X-1 3U 1908+00." *The Astrophysical Journal, 220* (1978) L131–4.

[TRI99] Trinder, W., Angélique, J. C., Anne, R., Äystö, J., Borcea, C., Daugas, J. M., Guillemaud-Mueller, D., Grévy, S., Grzywacz, R., Jokinen, A., Lewitowicz, M., Lopez, M. J., de Oliveira, F., Ostrowski, A. N., Siiskonen, T.

and Saint-Laurent, M. G. "β-decay of ^{35}Ca." *Physics Letters B*, **459** (1999) 67–72.

[TRU90] Truran, J.W. "Theoretical Implications of Nova Abundances." *Physics of Classical Novæ*, ed. A. Cassatella, R. Viotti Springer-Verlag, 1990 373–85.

[VAN74] van Horn, H. M. and Hansen, C. J. "A Model for the Transient X-Ray Sources." *The Astrophysical Journal*, **191** (1974) 479–82.

[VAN78] van Paradijs, J. "Average properties of X-ray burst sources." *Nature*, **274** (1978) 650–3.

[VAN80] van Paradijs, J., Verbunt, F., van der Linden, T., Pedersen, H. and Wamsteker, W. "Spectroscopic observations of the optical counterpart of Centaurus X-4." *The Astrophysical Journal*, **241** (1980) L161–4.

[VAN86] van Paradijs, J., Sztajno, M., Lewin, W. H. G., Trumper, J., Vacca, W. D., and van der Klis, M. "A unique triple-peaked type-1 X-ray burst from 4U/MXB 1636-53." *Monthly Notices of the Royal Astronomical Society*, **221** (1986) 617–23.

[VAN94] van Wormer, L., Göerres, J., Iliadis, C., Wiescher, M. and Thielemann, F.-K. "Reaction rates and reaction sequences in the rp-process." *The Astrophysical Journal*, **432** (1994) 326–350.

[VEL59] Velikhov, E. P. "Stability of an Ideally Conducting Liquid Flowing Between Cylinders Rotating in a Magnetic Field." *Soviet Journal of Experimental and Theoretical Physics*, **36** (1959) 1398–1404.

[VIS08] Vishniac, E. T. *Private communication*, 2008.

[VOC07] Vockenhuber C., Ouellet C. O., The L.-S., Buchmann L., Caggiano J., Chen A. A., Crawford H., D'Auria J. M., Davids B., Fogarty L., Frekers D., Hussein A., Hutcheon D. A., Kutschera W., Laird A. M., Lewis R., O'Connor E., Ottewell D., Paul M., Pavan M. M., Pearson J., Ruiz C., Ruprecht G., Trinczek M., Wales B., and Wallner A. "Measurement of the ^{40}Ca(α,γ)^{44}Ti reaction relevant for supernova nucleosynthesis." *Physical Review C*, *76* (2007) 035801:1–13.

[WAH65] Wahl, A. C. *Symposium on Physics and Chemistry of Fission* (1965) International Atomic Energy Agency, Vienna.

[WAL81] Wallace, R. K. and Woosley, S. E. "Explosive Hydrogen Burning." *The Astrophysical Journal Supplement Series* **45** (1981) 389–420.

[WAL82] Wallace, R. K., Woosley, S. E. and Weaver, T. A. "The thermonuclear model for X-ray transients." *The Astrophysical Journal*, **258** (1982) 696–715.

[WAS96] Wasserburg, G. J., Busso, M. and Gallino, R. "Abundances of Actinides and Short-lived Nonactinides in the Interstellar Medium: Diverse Supernova Sources for the r-Processes." *The Astrophysical Journal*, **466** (1996) L109–13.

[WEI37] von Weizsäcker C. F. *Physikalische Zeitschrift* **38** (1938) 176.

[WEI38] von Weizsäcker C. F. *Physikalische Zeitschrift* **39** (1938) 633.

[WEI06] Weinberg, N. N., Bildsten, L. and Brown, E. F. "Hydrodynamic Thermonuclear Runaways in Superbursts." *The Astrophysical Journal*, **650** (2006) L119–22.

[WEI07] Weinberg, N. N. and Bildsten, L. "Carbon Detonation and Shock-Triggered Helium Burning in Neutron Star Superbursts." *The Astrophysical Journal*, **670** (2007) 1291–1300.

[WHE66] Wheeler J. A. "Superdense Stars." *Annual Review of Astronomy and Astrophysics* **4** (1966) 393–432.

[WHE98] Wheeler, J. C., Hoeflich, P., Harkness, R. P. and Spyromilio, J. "Explosion Diagnostics of Type IA Supernovae from Early Infrared Spectra." *The Astrophysical Journal*, **496** (1998) 908–14.

[WID28] Wideroe, R. *Archiv Elektronik und Uebertragungstechnik* **21** (1928) 387.

[WIE89] Wiescher, M., Görres, J., Graff, S., Buchmann, L. and Thielemann, F.-K. "The hot proton-proton chains in low-metallicity objects." *The Astrophysical Journal*, **343** (1989) 352–64.

[WIE99] Wiescher, M., Görres, J. and Schatz, H. "Break-out reactions from the CNO cycles." *Journal of Physics G Nuclear Physics* **25** (1999) R133–61.

[WIE00] Wiescher, M. and Schatz, H. "Ignition and Cooling of X-Ray Bursts." *Progress of Theoretical Physics Supplement*, **140** (2000) 11–32.

[WIK08b] *Image: Binding energy curve*, hosted by Wikimedia Commons. (URL: `http://en.wikipedia.org/wiki/Image:Binding_energy_curve_-_common_isotopes.svg`) File uploaded 7 January 2007 *(Access date: 15 August 2008).*

[WIK08c] *Image: Bragg Curve for Alphas in Air*, hosted by Wikimedia Commons. (URL: `http://en.wikipedia.org/wiki/Image:Bragg_Curve_for_Alphas_in_Air.png`) File uploaded 9 May 2006 *(Access date: 7 July 2008).*

[WIK08d] *Image: Pulsar schematic*, hosted by Wikimedia Commons. (URL: `http://en.wikipedia.org/wiki/Image:Pulsar_schematic.svg`) File uploaded 23 August 2007 (*Access date: 15 August 2008)*.

[WIK08e] *Image: Cyclotron patent*, hosted by Wikimedia Commons. (URL: `http://en.wikipedia.org/wiki/Image:Cyclotron_patent.png`) File uploaded 29 January 2006 (*Access date: 5 July 2008)*.

[WNSL08] *A. W. Wright Nuclear Structure Laboratory* website. (URL: `http://wnsl.physics.yale.edu`) Last updated 22 April 2008 (*Access date: 3 July 2008*).

[WOO76] Woosley, S. E. and Taam, R. E. "Gamma-ray bursts from thermonuclear explosions on neutron stars." *Nature*, **263** (1976) 101–3.

[WOO84] Woosley, S. E. and Weaver, T. A. "Repeated Thermonuclear Flashes on an Accreting Neutron Star." *American Institute of Physics Conference Series*, **115** (1984) 273–97.

[WOO04] Woosley, S. E., Heger, A., Cumming, A., Hoffman, R. D., Pruet, J., Rauscher, T., Fisker, J. L., Schatz, H., Brown, B. A., and Wiescher, M. "Models for Type I X-Ray Bursts with Improved Nuclear Physics." *The Astrophysical Journal Supplement Series*, **151** (2004) 75–102.

[YAK05] Yakovlev, D. G., Levenfish, K. P. and Gnedin, O. Y. "Pycnonuclear reactions in dense stellar matter." *European Physical Journal A Supplement*, **25** (2005) 669–72.

[YAM07] Yamaguchi, H., Wakabayashi, W., Hayakawa, S. Amadio, G., Fujikawa, H., Kubono, S. and Binh, D. N. "Intense RI Beam Production using a Cryogenic Gas Target at CRIB." *CNS Annual Report 2006* **CNS-REP-76** (2007) 59–60.

[YAM08] Yamaguchi, H. *Private communication*, 2008.

[YAN05] Yanagisawa, Y., Kubono, S., Teranishi, T., Ue, K., Michimasa, S., Notani, M., He, J. J., Ohshiro, Y., Shimoura, S., Watanabe, S., Yamazaki, N., Iwasaki, H., Kato, S., Kishida, T., Morikawa, T. and Mizoi, Y. "Low-energy radioisotope beam separator CRIB." *Nuclear Instruments and Methods in Physics Research in Physics Research A* **539** (2005) 74–83.

[YUE08] Yue, Y. and Xu, R. "PSR B1257+12: a quark star with planets?" *AIP Conference Proceedings*, **968** (2008) 206–8.

[XU06] Xu, R. "Pulsars and Quark Stars." *Chinese Journal of Astronomy and Astrophysics, Supplement*, **6** (2006) 279–86.

[XU08] Xu, R. "Possible evidence that pulsars are quark stars." *AIP Conference Proceedings*, **968** (2008) 197–202.

[ZAV96] Zavlin, V. E., Pavlov, G. G. and Shibanov, Yu. A. "Model neutron star atmospheres with low magnetic fields. I. Atmospheres in radiative equilibrium." *Astronomy and Astrophysics*, **315** (1996) 141–52.

[ZEL64] Zel'dovich, Ya. B. *Soviet Physics*, *9* (1964). Reprinted in *Neutron Stars, Black Holes and Binary X-ray Sources*, R. Giacconi and R Ruffini. Reidel, (1975) 329.

[ZHA07a] Zhang, C. M., Yin, H. X., Kojima, Y., Chang, H. K., Xu, R. X., Li, X. D., Zhang, B. and Kiziltan, B. "Measuring neutron star mass and radius with three mass-radius relations." *Monthly Notices of the Royal Astronomical Society*, **374** (2007) 232–36.

[ZHA07b] Zhang, C. M., Yin, H. X., Zhao, Y. H., Wei, Y. C. and Li, X. D. "Does Submillisecond Pulsar XTE J1739-285 Contain a Weak Magnetic Neutron Star or Quark Star?" *The Publications of the Astronomical Society of the Pacific*, **119** (2007) 1108–13.

[ZIN01] Zingale, M., Timmes, F. X., Fryxell, B., Lamb, D. Q., Olson, K., Calder, A. C., Dursi, L. J., Ricker, P., Rosner, R., MacNeice, P. and Tufo, H. M. "Helium Detonations on Neutron Stars." *The Astrophysical Journal Supplement Series*, **133** (2001) 195–220.